High-fidelity, compact readout of spins in silicon quantum dots

Virginia Ciriano Tejel

a thesis submitted for the degree of

Doctor of Philosophy

London Centre for Nanotechnology

University College London

August 14, 2022

I, Virginia Natalia Ciriano Tejel, confirm that the work presented in this thesis is my own. Where information has been derived from other sources, I confirm that this has been indicated in the thesis.

High-fidelity, compact readout of spins in silicon quantum dots

Abstract

Silicon has become one of the leading platforms for quantum computation, having demonstrated qubits with long coherence times and high fidelity operations. Moreover, the similarities between silicon quantum dots and transistors give hope for mass production of qubits easily integrable with control electronics. However, to fully leverage their scalability potential, the footprint of the additional circuits for control and readout needs to be minimised.

Here, we introduce a compact spin-readout method based on spin-dependent tunnelling combined with a dispersive charge sensor: the radio-frequency single-electron box (SEB). Opposite to traditional charge sensors, the SEB only requires a single lead, reducing its footprint. Using this sensing technique, we demonstrate spin readout of a single electron spin in a CMOS device manufactured at the 300mm wafer-scale using industrial processes, in which we measure long single spin relaxation times (up to 9 s).

Next, we focus on achieving a high readout fidelity, since it is essential to perform error correction and ultimately sets the fidelity of qubit operations. The readout fidelity is partly set by the ability of the sensor to detect rapid events with high accuracy. We demonstrate that a low-loss high-impedance resonator highly coupled to the SEB, together with a Josephson Parameter Amplifier, are central for optimal performance. With these modifications, we obtain an integration time $\tau_{\mathrm{m}} = 100$ ns for a signal to noise ratio equal to 1, which facilitates single-shot spin readout, reaching a measurement fidelity $F_{\mathrm{M}} = 99.54\%$, above the fault-tolerant threshold, in a readout time $\Delta t = 250$ μs.

We identify that the readout time is limited by the choice of the spin-to-charge conversion mechanism. In the last part of the thesis, we work towards performing Pauli spin blockade spin readout, which does not have such time limitation.

Impact statement

Quantum computation proposes a change of paradigm in the way that algorithms are envisioned and performed. This new computing approach will have major implications in any field that relies on understanding many-body quantum systems such as material science, chemistry or the discovery of new drugs. Moreover, quantum computation could speed up certain tasks that classical computers struggle with, which could unravel further technological advances.

This thesis pushes forwards toward the creation of a large-scale silicon-based quantum processor. The results demonstrated in this thesis show that industrially manufactured silicon transistors possess some of the properties that high-quality qubits must have. At the same time, the work presented on scalable and high fidelity spin readout places dispersive charge sensing at the forefront of readout methodologies for scalable semiconductor spin-based quantum processors.

The fast and reliable charge and capacitance sensor presented in this thesis can also have applications in other fields such as axionic dark matter detection, nano-electromechanical systems or astronomy instrumentation. Moreover, the addition of a Josephson Parametric Amplifier, typically used in superconducting qubits, bridges the gap between both communities. The positive results in spin readout motivate further cross-disciplinary work, in which techniques developed for other quantum applications can be integrated with a silicon quantum processor.

Acknowledgments

I would like to give a massive thanks to the following people who helped and supported me during my PhD:

To **John Morton** for being such a supportive and understanding supervisor whose broad knowledge is truly inspiring. His scientific intuition is extremely valuable to subtly guide students in the right direction (although I can always tell if I'm saying something crazy by looking at his characteristic arching eyebrow). John has the rare skill of being able to calm me down when I am in panic mode, which kept me going during these years. However, I feel like I have to say the sentence, just to continue the tradition: "The PhD has been an amazing experience, even though the group skiing trip that John promised at the beginning never took place"[1].

To **Fernando González Zalba** for being the best second supervisor anyone could ask for. He would always find some time to help me, regardless of the other thousand things he is involved with. His dedication, motivation and insight make all of us believe that everything is possible when he is in the lab. He's really a wizard when it comes to physics. Gracias por tu paciencia infinita, tus consejos y por ser una persona maravillosa con la que es un placer trabajar. Sí, los acknowledgementes también tenían que estar an Spanglish. Thank you so much too for carefully reading and add corrections to this manuscript.

To **Simon Schaal**, who is always willing to help, for explaining all the details of his research and baring me while I was shadowing him in the lab. I aspire to apply his methodical approach to problem-solving. Although I usually fail, since I am not as constant and optimistic as him. Simon also knows how to organise a good party, like when we finished dancing on top of the tables in that German-themed bar.

To all the **old lab gang** with who I shared such good moments, discussions about the best way to brew the coffee and pub trips. *Michael Fogarty*, with who is always fun to be in the lab and has the unique skill of seeing the physics behind really noisy data. *Oscar Kennedy*, who made me feel welcomed to the group and slightly overrates delicious food (the only true delicatessen is his liquid nitrogen ice cream). *Gavin Dold*, also known as the "Gavinator" or "Gavin do1d". I love his made-up gossip and how supportive he is, without him I probably would have quit at some point. *Pier Andrea Conti* who always finds a way to improve stuff that was already working. *David Wise* for having the wittiest comments in all of England and introducing me to Rugby. Forgive me if I do not pick up the hobby after you. Also to *Michael Fogarty*, *Mantas Simenas* and *Siddarth Dhomkar* for being such a good postdocs. And especially *Christoph Zollitsch* for being the best lab desk partner and for your constant effort for stopping making things kaput! Finally, to *James O'Sullivan* who is a brilliant person that would shine with his own light anywhere he goes. I am extremely grateful for his very patient explanations about the physics and the lab even though I was a stubborn and difficult student. He kept me sane during the Covid lockdown with a routine that included an extremely geeky but very fun game we always finished having arguments about.

---

[1] Due to Covid19, but still valid.

To the **PhD students that started at the same time as me** for all our shared memories. *Sofia Patomäki*, who knows how to work hard and party hard. *Jingyu Duan* who is like a remember ball with an amazing memory. I loved all the moments we shared, the chats in the lab, the pret coffee trips, the calls trying to motivate each other to write, but most of all I adore your new acquired sassy personality and your famous sentence 'I am not drunk', which I have never heard you saying when being sober even once.

To the **new lab gang**, who are now the heart of the group. *Joe Alexander*, who started the Pret club. His obsession to mix with the locals and middle part hairstyles are certainly unique qualities. But most importantly, Joe is a really good friend that helped me tons through a difficult time. *Felix Donaldson* for being a bad baby with who is always fun to chat with. *Ed Thomas* who is an example of perseverance and knows so many obscure facts. *James Williams* for being the soul of the group, the glue that keeps us together and the best of the best[2]. He can turn a dull evening into a comedy show with his presence, although it seems like he attracts bizarre people who will talk about babies.

---

[2] I could not have made his part more over the top

To the **new members of QSD** *Paddy Hogan*, *Mathieu de Kruijf*, *Ross Leon*, *Nathan Johnson* and *Jacob Chittock-Wood*[3], I hope you much luck and a fruitful future. *Frederic Schlattner* for being the sophisticate 'Frenchie' everyone needs in their life. *Thomas Swift*, who runs too fast and too much in football. *Ana Villanueva Ruiz de Temino* por ser más maja que las pesetas y la mejor maña del grupo.

To the **Centre for Doctoral Training and the EPSRC** for providing training and funding throughout my PhD. To *Paul Warburton* for being a caring and great director. Thanks to all the academics that created and are part of such an immersive and enriching experience. I also would like to thank my CDT cohort for basically teaching me English and making moving to London way less scary. To **Hitachi Cambridge Laboratory** for co-funding this PhD and to *David Ibberson* and *Giovanni Oakes* for being so helpful, friendly and good at their jobs. To **Quantum Motion Limited** for providing the opportunity of developing this research with them and helping to deliver these results to a broader audience.

To the people of **CEA Leti** for fabricating excellent devices, the MOSQUITO consortium who have been exceptional partners and to **Irfan Siddiqqi's group** for fabricating a superb Josephson parametric amplifier. To the **British-Spanish society** and **Telefónica** for awarding me the BritishSpanish Society Scholarship.

A mis **amigos**, que aunque vivan muy lejos, siempre encontramos tiempo para vernos o llamarnos. *Mila*, *Javi* y *Alejandra*, sois un soplo de aire fresco traído de las islas canarias (aunque ninguno seamos canarios). *Guille*, experto cultivador de células y rastreador de queso de mercadona. *Nico*, I never thought we would get so close after a conference. Thank you for all your help with the noise in my setup. We still need those cocktails!. *Clavero*, que es como una especie de adorable científico loco al que intento imitar. Las amigas del *Goya* que aunque sean muy divertidas, son un poco feíllas [4]. Y finalmente a *Violeta*, que es mi mejor amiga del mundo mundial. Gracias por todas esas charlas sobre el cómo afrontar el doctorado y porque siempre podemos confiar la una en la otra y apoyarnos mutuamente.

To **Aidan**, who always knows how to make me smile. You understand me and make problems seem smaller. I hope we keep running around because we are late[5] for a very long time. Thanks as well to your family and friends who received me with

---

[3] Specially Jacob for being so annoying, haha

[4] En realidad son muy guapas

[5] Even inside museums

open arms.

A mis **padres**, quienes son una fuente de inspiración desde que les escribí esa postal de ‘bailando con las moleculas’ cuando tenía 5 años. Ellos me han enseñado que con sacrificio y dedicación cualquier meta es posible. Gracias también a *Marta*, que es como mi segunda madre, por ser tan comprensiva y buena escuchando.

Contents

List of Symbols and Abreviations **2**

1 Introduction **7**
- 1.1 Transistor miniaturisation 7
- 1.2 Quantum computation 7
- 1.3 Qubit realisations 11
- 1.4 Extensibility in quantum computing 13
- 1.5 Silicon as a scalable quantum platform 15
- 1.6 This thesis 16

2 Background **18**
- 2.1 Quantum Confinement in Silicon 18
  - 2.1.1 Silicon Quantum Dots 18
  - 2.1.2 Dopants in silicon 20
  - 2.1.3 Physics of Quantum dots 21
  - 2.1.4 Double quantum dots 27
- 2.2 Spin qubits in silicon 28
  - 2.2.1 Single spin qubit manipulation 28
  - 2.2.2 Two-qubit gates 29
  - 2.2.3 Spin Readout and initialisation 35
- 2.3 Charge sensors 39
  - 2.3.1 Quantum point contact and Single-electron transistor 40
  - 2.3.2 Radio-frequency reflectometry 41
  - 2.3.3 rf-SET and rf-QPC 46
  - 2.3.4 Single electron box (SEB) 47

2.3.5 In-situ readout 50
2.4 Amplification 51
2.4.1 Noise in amplifiers 51
2.4.2 Noise quantum limits 53
2.4.3 Parametric amplification 54
2.4.4 Josephson parametric amplifier (JPA) 56
2.4.5 Superconducting parametric amplifiers for qubit readout . . . 60

3 EXPERIMENTAL METHODS **64**
3.1 Device description 64
3.1.1 Device advantages 66
3.1.2 PCB 68
3.2 Measurement setup 69
3.2.1 rf-reflectometry setup 70
3.2.2 Homodyne detection 71
3.3 Setup optimisation 74
3.3.1 Fast pulse generation 74
3.3.2 Reducing setup interferences 75

4 OPTIMISATION OF GATE-BASED SINGLE ELECTRON BOX **79**
4.1 SNR and minimum integration time 79
4.2 Maximising the signal 81
4.2.1 Strong and weak sensitive regime 81
4.2.2 Circuit and simulations 82
4.2.3 Power to the device 84
4.2.4 Device capacitance 85
4.2.5 Minimum integration time dependency on the experimental parameters 87
4.3 Setup and implementation 87
4.3.1 SEB characterisation 90
4.3.2 Resonator characterisation 95
4.4 Reducing noise 97
4.4.1 JPA setup 99
4.4.2 JPA tuning 99
4.4.3 JPA and LC resonator 101

4.5 Effect of the external magnetic fields 103
4.6 SNR improvements 104
4.7 SNR and τ_{m} extraction 106
4.7.1 Experimental bandwidth 107
4.8 Conclusions 109

5 Readout of a single spin using a SEB **112**
5.1 Spin readout 113
5.1.1 Readout offset tuning 114
5.1.2 Effect of the rf-carrier on spin readout 122
5.2 Spin relaxation 123
5.2.1 T_1 dependence on the magnetic field 124
5.3 Excited states spectroscopy (qubit dot) 126
5.3.1 The spin-valley mixing impact on the relaxation time 129
5.3.2 Excited state nature 130
5.4 Reservoir excited states 131
5.5 Single shot spin readout fidelity 132
5.5.1 Single-shot spin-dependent tunneling readout traces 132
5.5.2 Trace identification and electrical fidelity 133
5.5.3 Measurement fidelity, F_{M} 138
5.5.4 F_{M} dependence on Δt and the measurement bandwidth 141
5.5.5 Machine learning spin labelling approach 142
5.6 Conclusions 144

6 Towards singlet-triplet readout using a SEB **146**
6.1 Motivation for Pauli Spin blockade readout 146
6.1.1 Measurement fidelity for asymmetric tunneling rates 148
6.2 SEB as a DQD charge sensor 149
6.3 Evidence of Pauli Spin blockade 150
6.4 Conclusions 153

7 Conclusions and outlook **155**
7.1 Achievements 155
7.1.1 CMOS foundry-based quantum devices 155
7.1.2 Highly sensitive compact charge sensing 156

7.1.3 Single-shot readout 157
7.2 Next steps 157
  7.2.1 CMOS devices 157
  7.2.2 Sensor improvements 159
  7.2.3 Scalability 160

APPENDICES **161**

A SILICON QUBIT READOUT BENCHMARKING **162**

B LJPA MATHEMATICAL DESCRIPTION **164**

C DEPENDENCE OF SPIN RELAXATION (T_1) ON MAGNETIC FIELD **167**

REFERENCES **189**

List of Symbols and Abreviations

α	Lever arm 24, 48, 49, 85, 87, 88, 90, 93, 94, 104, 109, 159
B	Bandwidth 45, 51, 52, 80, 101, 105, 109, 157
β	Coupling constant 45, 46, 83–85, 87, 95, 97
C	Capacitance 56, 164, 165
C_t	Tunneling capacitance 48, 49, 80, 82
Δt	Readout time 35, 37, 132, 134, 135, 138, 139, 141, 142, 144–146, 154, 157
δ	Phase difference across Josephson junction 56, 165, 166
$\Delta\omega$	Frequency difference between pump and signal 59, 60, 165, 166
DOS	Density of states 23
Γ_d	Resonator dumping rate 165
E	Energy 55
e	Electron charge 21, 22, 47–49, 56, 85, 87, 165
E_C	Charging energy 22, 26, 31, 32
E_Z	Zeeman Energy 28, 30
EDSR	Electron Dipole Spin Resonance 29, 30, 34
ESR	Electron Spin Resonance 29, 30, 34
F_E	Electrical fidelity 132, 134, 135, 138, 140, 142
$f_\mathrm{eff,BW}$	Effective noise bandwidth/measurement bandwidth 106, 108, 133–136, 139, 141, 142
F_M	Measurement fidelity 138–142, 144, 154, 157

f_{pump}	Pump frequency 101, 102
f_{res}	Resonant frequency 44–46, 83, 87, 88, 95–97, 101, 102, 107, 109
f_{rf}	rf probe frequency 63, 85, 98, 99, 101, 102, 107, 109, 110
F_{STC}	Spin to charge conversion fidelity 132, 138, 140, 141
FET	Field-Effect-Transistor 15, 18
G_{s}	Signal power gain of parametric amplifier 51, 52, 58, 61
Γ	Reflection coefficient 43, 44, 46, 47, 71, 72, 80, 81, 83–85, 95–97, 101, 102, 104, 159
γ_0	Characteristic tunneling rate between SEB and reservoir 48, 49, 63, 85–88, 90, 94, 98, 99
Γ_{s}	Sample rate 133–136, 138
Γ_{t}	Inter-dot tunneling rate 147, 151, 153
H	Filter transfer function 74, 75, 107, 108
$\hbar$	Reduced Planck's constant 28, 48, 49, 53–55, 85, 165
HEMT	High-electron-mobility-transistors 40, 52, 60, 62, 97, 98, 156
I	Electrical current 42, 43, 56, 164, 165
I_0	Critical current of a Josephson junction 56, 164, 165
I_{d}	Parametric amplifier driving current 56, 165
I_{J}	Electrical current though a Josephson junction 165
ICT	Inter dot charge transition 150–152
JBA	Josephson Biphurcation Amplifier 57
JPA	Josephson Parametric Amplifier 17, 53, 56–59, 61–63, 71, 86, 98–107, 110, 133, 135, 141, 142, 144, 159, 164, 165
k_{B}	Boltzman constant 22, 48, 49, 51–54, 80, 81, 85, 87, 94

L_{J}	Induction across a Josephson junction 56, 165
LJPA	Lumped Josephson Parametric Amplifier 56, 164, 166
MOS	Metal-Oxide-Semiconductor 18, 19, 64
NISQ	Noisy Intermediate-Scale Quantum 14
ω_{idler}	Idler frequency 55, 58, 166
ω_{JPA}	LJPA linear resonant frequency 56, 57, 61, 99, 100, 165, 166
ω_{pump}	Pump frequency in radians 55, 56, 58–60, 99, 101, 165, 166
Ω_{R}	Rabi frequency 28, 29
ω_{rf}	rf probe frequency in rad/s 48, 49, 85, 87
ω_{signal}	Signal frequency 55, 58–60, 166
P_0	Power applied to the matching network 80, 81, 84–87, 90, 94, 102, 103, 122, 123
P_{c}	Critical power for bifurcation of the LJPA 57
P_{JPA}	Power arriving to the JPA 56, 99, 101
P_{n}	Noise power 51
PCB	Printed Circuit Board 68, 69, 72, 74, 84, 88, 89, 104, 109
Φ_0	Flux quantum $h/2e$ 165
PSB	Pauli Spin Blockade 17, 145, 147, 149–151, 153, 154
Q_{int}	Internal Q-factor 45, 83, 84, 87, 105
Q_{L}	Load quality factor 45, 80, 95, 97, 103, 109
QD	Quantum dot 16
QEC	Quantum Error Correction 15, 17, 35, 39, 112
QPC	Quantum point contact 39–41, 46, 47, 50, 53, 110, 156
$S(\omega)$	Power spectrum density 51, 53
SEB	Single Electron Box II, 16, 17, 37, 39, 47–49, 62, 63, 73, 79–85, 87–94, 96–99, 102, 104–106, 109, 110, 112, 113, 122, 123, 132, 135, 136, 144–146, 148–150, 153, 156–159

SET	Single Electron Transistor 20, 22, 37, 39–41, 46, 47, 49, 53, 63, 98, 99, 110, 145, 156
SNR	Signal to Noise Ratio 51, 52, 58, 62, 63, 75, 79–82, 84, 87, 88, 90, 93, 94, 96, 97, 106–110, 112, 114, 133, 135, 141, 156, 159
SQUID	Superconducting Quantum Interference Device 56, 61, 164
T	Temperature 22, 53, 54
T_1	Relaxation time 112, 123–125, 130, 140, 141, 147, 153
t_c	Tunneling rate between dots 31–33
T_e	Electron temperature 23, 48, 49, 85, 87, 90, 94
T_eff	Noise effective temperature 53
$t_\mathrm{in}^{\downarrow}$	Tunneling time for a spin-down electron to come back to the qubit dot 131, 133–136, 138, 146, 147
T_n	Noise temperature 51, 52, 80, 87, 97, 98
$t_\mathrm{out}^{\uparrow}$	Tunneling time for a spin-up electron to leave the qubit dot 131, 133–136, 138–140, 145–147
T_sys	Noise temperature of the device under test 52
τ_m	Minimum integration time to obtain a SNR=1 79, 80, 87, 101, 102, 104, 105, 107, 109, 157
TWPA	Traveling-Wave Parametric Amplifier 61–63, 110, 159
V	Voltage 42, 43, 71, 72, 165
V_Q	Quantum Volume 13, 14
V_rf	Normalised rf response 133, 134
V_T	Selected threshold voltage 134, 135, 138
VNA	Vector network analyser 43
VQE	Variational Quantum Eigensolver 14
Z_0	Intrinsic transmission line impedance 41–43, 45, 46, 56, 83, 84, 95, 97, 164, 165
Z_D	Device impedance 42
Z_L	Load impedance 42–46, 82, 83, 95

1

Introduction

1.1 TRANSISTOR MINIATURISATION

At the heart of the digital revolution is a single piece of technology – the silicon transistor. The exponential speed-up of computers, enabled by transistor miniaturization [1], has now reached a point where the electrical characteristics of transistors start to be affected by unique quantum mechanical effects such as quantum tunneling [2]. Whilst this limits the exponential scaling up in classical computer power, it opens up a new era of quantum computing. Quantum computers hold the promise of a paradigm shift in computation with possible applications in machine learning [3], database searches [4], cryptoanalysis [5] and molecular modelling [6], among others.

1.2 QUANTUM COMPUTATION

In the same way that bits are the building blocks of classical computers, qubits are the unit cell of quantum computers. A bit, or binary digit, has only two possible states defined by a transistor through which electrical current can flow (1) and a closed transistor (0). On the other hand, a qubit is a 2-level system formed by a ground state, $|0\rangle$, and excited state, $|1\rangle$. Although the measurement of a qubit has only two possible outcomes ('0' for $|0\rangle$ and '1' for $|1\rangle$), the reiterative measurement of a qubit in a given state results in a probabilistic distribution. For example, if a qubit is prepared in the state $|\phi\rangle = \frac{1}{\sqrt{2}}|0\rangle - \frac{1}{\sqrt{2}}|1\rangle$, the outcome will be '0' half of the times that it is measured. This way, a qubit state is most generally described as a **superposition** of the ground state and the excited state as:

$$|\phi\rangle = \alpha\,|0\rangle + \beta\,|1\rangle\,, \tag{1.1}$$

where $|\phi\rangle$ is the wave function that describes the qubit state and α and β, so-called probability amplitudes, are complex numbers. The probability of measuring '0' is given by $|\alpha|^2$ whereas the probability of measuring '1' is $|\beta|^2$ and, as probabilities, they can be normalised so their sum is equal to one: $|\alpha|^2 + |\beta|^2 = 1$.

α and β not only describe the probability of each outcome, but also the phase difference between states. This phase is a consequence of the wave-particle duality that allows quantum states to interfere constructively and destructively. An example of an interference pattern with quantum particles would be the double-slit experiment with electrons, where two electron beams are made to go through different paths, acquiring a phase difference and are later combined as a single wave. Although the position of each electron measured at the end of the experiment appears as a single point, the final position of many electrons as a whole form an interference pattern, like the one shown in Fig. 1.2.1.

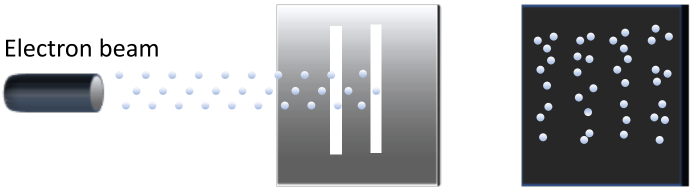

Figure 1.2.1: Double-slit experiment. An electron beam throws electrons that pass through a double-slit aperture. Although the position where they hit the final screen is discrete, as a whole they form an interfere pattern.

Given that the global phase of a quantum state is undetectable, the description of a qubit state can be simplified as:

$$|\phi\rangle = \cos(\theta/2)\,|0\rangle + \sin(\theta/2)e^{i\phi}\,|1\rangle\,, \tag{1.2}$$

where θ quantifies the probability of measuring '0' or '1' and ϕ is the phase difference between states. Due to its parallelism with the spherical coordinates, the state of a qubit is commonly represented as a point in the Bloch sphere, in which the north and south pole correspond to the $|0\rangle$ and $|1\rangle$ states, respectively (See Fig. 1.2.2).

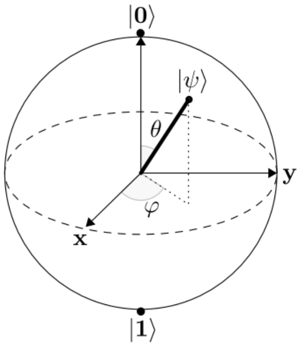

Figure 1.2.2: Bloch sphere. A pure qubit state is represented as a point in a sphere of radius one, where θ is the polar angle and ϕ is the azimuthal angle. Retrieved from [7].

The phase between states is something purely quantum and the key of quantum computing speed up. Most quantum algorithms are based on the possibility of having "negative probabilities", produced by a π phase. An example would be Grover's algorithm to search in a database [4]. Classically, to find the 'winner' element in a list of N items, $N/2$ elements would need to be checked, on average. In the quantum version, N qubits are placed in superposition so all the states are present at the same time with equal probability $1/\sqrt{N}$ (see Fig. 1.2.3a). The quantum algorithm is configured so when acting on the superposition, only the 'winner' state finishes with its phase inverted. At this point, if the superposition is measured, the probability of getting any entry is still $1/N$ (see Fig. 1.2.3b). Additional quantum operations can produce a reflection of the phase about the average amplitude that amplifies the probability of finding the correct entry (see Fig. 1.2.3c). Repeating this process increases the probability of finding the correct answer. After repeating the process $\sqrt{N}$ times, the probability of finding the correct answer is very closed to one. This way, the number of cycles has been reduced from $N/2$ to $\sqrt{N}$ by making use of the quantum phase and the ability to act on all the states at the same time (quantum parallelism). Quantum algorithms are an active line of research (see [8] for more information). Another examples are the Shor's algorithm for integer factorisation, with major implications in cryptography [9], or the Harrow, Hassidim and Lloyd algorithm to solve systems of linear equations [10].

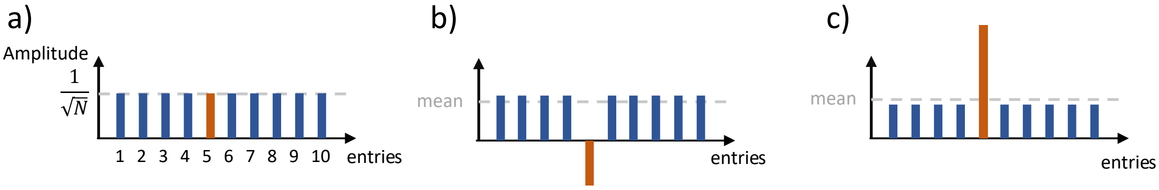

Figure 1.2.3: Grover's algorithm. a) Superposition of 10 quantum states with the same amplitude. b) The phase of the correct entry is inverted by the search algorithm. c) Inversion of all of the states amplitudes about their overall mean. The steps described in b) and c) are repeated until the amplitude of the correct entry is amplified. Figure inspired on [11]

However, quantum computers were initially postulated to simulate physical systems [12–14], a challenging task for conventional computers. As more qubits are put together, the complexity to describe the system increases exponentially as 2^n, where n is the number of qubits. Moreover, qubits can be entangled, meaning that the state of a qubit depends on the other. Under these conditions, qubits cannot be described individually any longer, but as a group. These quantum specific effects are the root of the complexity in simulating quantum systems by supercomputers, where the largest system simulated has around 50 qubits [15]. Quantum computing would allow studying large quantum many-body physical systems. This new tool would open a new understanding of condensed matter, with direct applications in chemistry, material design and medicine, among others.

Moreover, indirect quantum computing applications arise as the field works towards building large quantum processors. For example, quantum computing requires extensive research on cryogenics since qubits work at low temperatures. As a consequence, quantum computing has pushed the boundaries for the detection of small signals at low temperatures, applicable to other fields such as astrophysics instrumentation, metrology, or electron spin resonance detection [16].

1.3 QUBIT REALISATIONS

Although a qubit can be realised by any 2-level quantum system, not any 2-level system is a good candidate for a qubit. To quantify what would be a suitable qubit realisation, Divincenzo introduced five criteria that experimental qubits should satisfy [17]: firstly, we need a *scalable system with well-characterized qubits*, where the system can be described in the qubits Hilbert space with a well-known Hamiltonian. This task becomes more and more complicated as the number of qubits increases. Furthermore, the qubits of such a system need to be *initialisated to a known state*, which should be isolated from the environment to have *long coherence times*, but whose interaction with the environment can be switched on on-demand to perform one or two-qubit gates. Finally, to perform any quantum algorithm, the qubit gates should form a *universal set of quantum gates* [18], where the final state of those qubits can be *read-out fast and with a high fidelity.* Additional requirements would be the ability to transfer information between different stationary qubit modules using flying qubits.

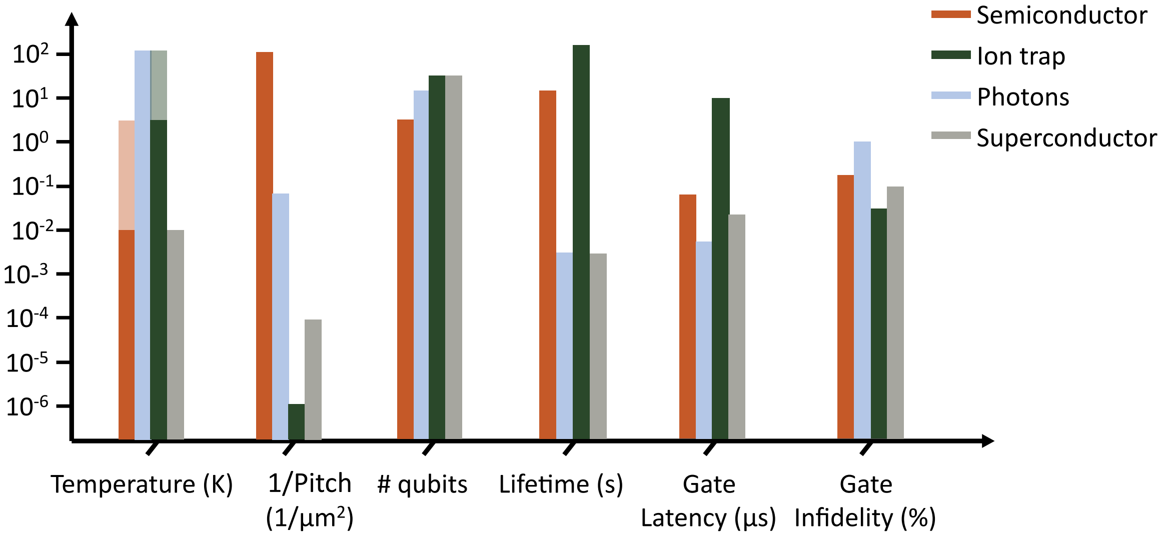

Figure 1.3.1: Qubits implementation figure of merit. Comparative figure of merit for different qubit implementations. Data retrieved from [7, 19, 20]. These numbers are a good assessment of the quality of the system for small qubit implementations. However, as systems scale up the comparative metric should include more parameters such as cross-talk, connectivity, circuit depth, etc... To take into account these factors some groups are introducing the concept of quantum volume [21].

There are many qubit realisations: the spin of an electron, the polarization of a photon, the orbital states in an ion, etc... One of the first demonstration was the outer electron of ions trapped with electric fields in vacuum, called ion traps [22]. Currently, there are several quantum processors based on ion traps [23, 24] with extraordinary high single and two-qubit gates fidelities [25, 26], as well as readout fidelities [27]. Moreover, although the best performance is at 4K, they can operate at room temperature. The main disadvantage of ion traps is their large size, which would lead to a quantum computer of a size of a football pitch [28]. This scalability issues motivated the use of solid materials as hosts, producing solid-state qubits.

Solid-state qubits come in different flavours depending on the material they are made of and can be separated into superconductors, semiconductors or Majorana fermion qubits. Superconducting qubits store information in the eigenvalues of circuits made of Josephson junctions [29]. One of their main advantages against ion traps is that their fabrication is compatible with already developed methods such as circuit printing [30]. As a disadvantage, superconductors display shorter coherence times. However this disadvantage is overcome by their faster single and two-qubit gates, so that superconducting gates still display high fidelities [31] with shorter computing times. Superconducting qubits are one of the leading technologies, with examples of working and accessible quantum processors like the IBM Quantum experience [32], Intel [33], Riggeti [34] and the Google processor with which quantum supremacy was demonstrated in 2019 [35].

Due to their smaller size, research in semiconductor qubits expanded as the nanofabrication methods developed. In semiconductor qubits, the information is saved in the charge distribution of confined electrons (charge qubits) [36], or in its spin state (spin qubits) [37]. Semiconductor qubits have a smaller footprint in comparison to other qubit realisations, which, in principle, has the potential to place millions of qubits in a small chip. Moreover, their fabrication is based on gate electrodes, just like field-effect transistors, so that they could be integrated with classical circuitry for signal processing and distribution [38]. Electrons (or holes) can be trapped in impurities placed in a semiconductor or in an artificial atom, so-called quantum dot – a potential well that can be self-assembled or electrically defined with electrostatic gates. The first demonstrations of semiconductor spin qubits were achieved in AlGaAs/GaAs heterostructures [39], where the interface between the different materials forms a 2-dimensional electron gas and deposited electrostatic gates further confine the electron to a 0-dimensional quantum dot. The almost perfect lattice matching, previous experience in mesoscopic devices [40], and its high mobility [41] made possible the fabrication of quantum dots in GaAs. However, Ga and As most common isotopes have a nuclear spin of 3/2 that fluctuates randomly even at high magnetic fields [42]. The nuclear spin of millions of atoms surrounding the qubit creates a fluctuating field that couples with the electron spin leading to short decoherence times of the order of $T_2^* = 10$ ns [43]. Moreover, its high spin-orbit coupling makes the electron spin sensitive to electric noise, present in semiconductor structures. Although during the last decade, advances in dynamical nuclear decoupling [44], notching filtering of the nuclear environment [45] and decoherence pulses have led to demonstrations of long relaxation times (T_1=57 s at 100 mK and 0.6 Tesla) [46] and decoherences times of hundreds of microseconds [47], the field has moved towards silicon structures.

Photons are another attractive technology for quantum computation, with the advantage that they can use existing technology as optic fibres. In 2020, a photon quantum processor proved quantum advantage in boson sampling [48]. However, the chip was not reconfigurable, and therefore, can only execute that one algorithm. On the other hand, the Canadian company Xanadu recently released an X8 qubit reprogrammable chip [49]. Photons natural isolating properties delay the decoherence process and make possible operation at room temperature, however, they pose a challenge for the realisation of two-qubit gates [50]. For this reason, photons have been proposed as a vehicle for coherent information, connecting entangled states between long distances [51].

1.4 EXTENSIBILITY IN QUANTUM COMPUTING

The main challenge that the quantum community faces is to scale up current quantum processors, since not only putting together an enormous amount of uniform qubits is an obstacle, but also scaling up the interconnections between qubits and digital electronics represents a great challenge [52].

As the quantum processor size keeps increasing, the number of qubits becomes as important as the number of operations that can be performed before an error occurs [52]. This so-called circuit depth depends on other parameters like the gate fidelity and the rate between gate latency and coherence time. Because of this, researchers introduced the quantum volume, V_{Q}, as a way to quantify a quantum processor quality. Fig. 1.4.1a show a colour plot of V_{Q} calculated as $V_{\mathrm{Q}} = \min(N, d)^2$, where N is the number of qubits and d is the circuit depth. The red area in Fig. 1.4.1a includes quantum processors that can still be simulated by classical computers. As the V_Q increases, quantum processors become too complex to be simulated by classical computers [53] (yellow region in Fig. 1.4.1a). At the moment, there are specific algorithms that are more easily solved by small quantum processors than supercomputers [54], demonstrating quantum supremacy in that instance [35]. Moreover, there are already small noisy quantum processors with dozens of qubits that allow proof-of-concept demonstrations of quantum algorithms [8]. These so-called Noisy Intermediate-Scale Quantum (NISQ) processors have proven to be more useful than initially thought. They can be used in combination with a classical computer so that the quantum processor performs the challenging bit of the computation. An example is the variational quantum eigensolvers (VQE), in which a conventional computer finds an optimised guess for a problem and the quantum processor does a fine-tuning searching between all nearby options [55]. VQE has proven successful to find molecular ground states [56, 57] and to investigate some material magnetic properties [58].

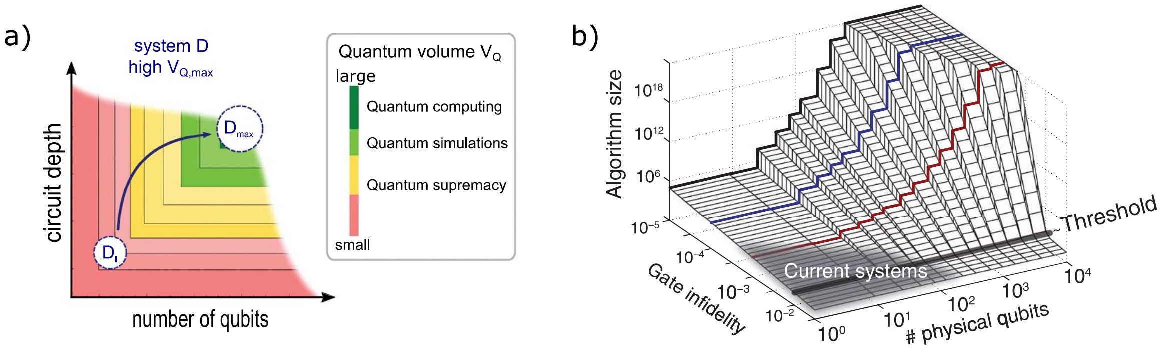

Figure 1.4.1: Errors and scalability. a) Colour plot of quantum volume, V_{Q} as a function of the number of qubits and the qubit depth. Here, both axes are in logarithm scale. b) Number of gates applicable to the logical qubits as a function of the gate infidelity and the number of physical qubits. As the fidelity increases, larger algorithms can be performed with the same amount of physical qubits. Figures retrieved from [20, 52]

The green area in Fig. 1.4.1a encompasses functional quantum computers for practical applications, which should include error correction algorithms. The non-binary nature of the qubit leads to more complicated errors than a simple bit flip, like, for example, an additional phase between states after a 1-qubit gate. This is why the realisation of quantum computers was thought to be impossible until the invention of quantum error correction (QEC) [59]. QEC working principle is based on encoding the logical information across several physical qubits that are constantly readout as a whole, so errors are corrected without losing information. QEC requires high fidelities for qubit gates and readout, being the fault tolerance threshold 99% for the surface code. However, maybe even higher fidelities are necessary so that the physical qubits overhead can be reduced (see Fig. 1.4.1b).

1.5 Silicon as a scalable quantum platform

The development of spin qubits in silicon was delayed compared to GaAs dots because silicon requires smaller dots to confine charges due to its larger electron effective mass, imposing further restrains in their fabrication.

The appeal of silicon as a host for qubits grew as the semiconductor industry fabricated even larger transistors [60]. The possibility of manufacturing qubits in the same way as Field Effect Transistors (FETs) opens the door to using the existent foundry industry capabilities with mass production experience and previous knowledge in the material. At the same time, silicon offers some inherent physical advantages. Natural silicon is composed mostly by three isotopes; ^{28}Si, ^{29}Si, and ^{30}Si. Of the three of them, only ^{29}Si has a non-zero nuclear spin with an abundance of 5% that can be reduced to 60 ppm [61]. The low abundance of nuclear spins together with silicon's weak spin-orbit coupling leads to large coherent times, demonstrating coherence times of $T_2^* = 120\ \mu$s (in a quantum dot) that can be extended up to 28 ms [62] and 560 ms in donors [63]. Such long coherent times in comparison to the manipulation times led to high-fidelity qubit manipulation [64, 65], and 2-qubit gates [66–69] with fidelities above the quantum threshold error in silicon and silicon-germanium (Si\SiGe) dots [70, 71] and nuclear spins of phosphorus atoms [72].

So far, there are working silicon quantum processors of 2, 4 and up 6 qubits with devices fabricated in academic cleanrooms [68, 73]. However, the moderately low levels of yield and reproducibility from these devices motivate manufacturing qubits in well-controlled facilities operating with 300-mm fabrication techniques [74–76].

Besides the fabrication challenges, scaling up also encompasses the integration of qubits with the classical circuitry that controls each qubit and handles the input/output signals between the qubits and room temperature instruments [77]. Although using many terminals per qubit allows for high versatility, the extra wiring becomes a bottleneck as the number of qubits increases [52]. This challenge is similar to the one faced by the transistor industry in the 60s, which was resolved thanks to the invention of integrated circuits. Using similar principles, different architectures envision how to structure silicon-based quantum processors [38, 78–82]. However, these proposals include share control, readout, tuning and manipulation which demands a high device uniformity.

The effort to produce scalable silicon processors has led to successful experimental demonstrations of global control [83], long-distance readout [84, 85], readout multiplexing [86, 87] and device uniformity. There are also advances for moving towards a modular architectures [79, 81] by using spin shuttling [88–91], photon mediators [92, 93] or QD couplers [94] for long distance 2-qubit gates or to move the information between modules.

Moreover, recent demonstrations of 2-qubit processors at more than 1 K promise to lift the very demanding heating restrictions, which would allow to produce a cheaper quantum processor (potentially operable in a lower budget ^{4}He system) integrable with the hotter classical electronics layer [95, 96]. At the same time, the high magnetic fields at which spin qubits normally work, $B \sim 1$ T, could be relaxed to 150 mT [97].

1.6 THIS THESIS

As stated above, to scale up, silicon qubits should be uniform and have high levels of yield and reproducibility. Moreover, the footprint of the additional circuitry for control and readout needs to be minimised. This thesis tries to tackle both challenges: on one hand, we store long-lived electron spin states in quantum dots fabricated using CMOS-compatible manufacturing processes performed at the scale of 300mm wafers and, on the other hand, we measure the electron spin polarisation with high fidelity using a compact readout method.

This thesis is divided as follows. Chapter 2 contains some background introducing the concepts necessary to understand the following chapters, whereas Chapter 3 describes the methodology and experimental setup.

Chapter 4 focuses on the single-electron box (SEB) as a sensor that can detect small changes in their surrounding potential. To do so, a small oscillating radiofrequency is continuously attempting to move an electron between the SEB and the reservoir, so that any perturbation of the electrochemical potential would result in the breakdown of the SEB\reservoir dynamic equilibrium. The chapter describes how to improve the SEB signal to noise ratio by reducing the temperature noise with the help of a Josephson Parameter Amplifier (JPA) and optimising both the resonator and its coupling to the SEB . The main advantage of the SEB is that it only requires a single lead, leading to a very compact readout method that can be operated without dissipation under certain conditions. Moreover, in the nanowire configuration, the additional footprint introduced by the SEB becomes almost negligible because SEB and qubit dot are integrated into a single nanowire and share the same reservoir.

In Chapter 5, a SEB is used to measure the electron spin of a nearby quantum dot using spin-dependent tunneling. High readout fidelities above the error threshold for the surface error correction code are demonstrated thanks to the SEB performance and the exceptionally long single spin relaxation times (up to 9 s). The results presented in Chapters 4 and 5 are included within the publications [98, 99].

In addition to the fidelity, the readout time is also an important figure of merit since QEC requires that qubits are routinely read. In the case of spin-dependent tunneling, the readout time is limited by the tunneling time between qubit and reservoir. Chapter 6 follows the first steps towards using the SEB as a charge sensor for Pauli spin blockade (PSB) readout, whose readout time does not have that limitation.

Finally, Chapter 7 summarises the key outcomes of this thesis and suggests future research directions.

2

Background

2.1 QUANTUM CONFINEMENT IN SILICON

Electrons (or holes) can be confined in silicon either bound to impurities with an extra (or missing) electron or in artificial 0-dimensional quantum wells called quantum dots.

2.1.1 SILICON QUANTUM DOTS

To form a quantum dot in silicon, first, a 2-dimensional electron gas is formed in the interface between two materials with different levels of conduction band minima. Based on the materials used to create the 2D electron gas, silicon quantum dots can be divided into SiMOS dots [62, 100, 101], where MOS stands for metal-oxide-semiconductor, and Si/SiGe heterostructures [102, 103]. SiMOS use the same technology concept as MOS field-effect transistors (FETs) in digital circuits, where a Si substrate is covered by a SiO_2 insulating layer and, on top of that, a metal gate covers the oxide. Electrons or holes are trapped in the Si/SiO_2 interface depending on the voltage applied to the metal gate.

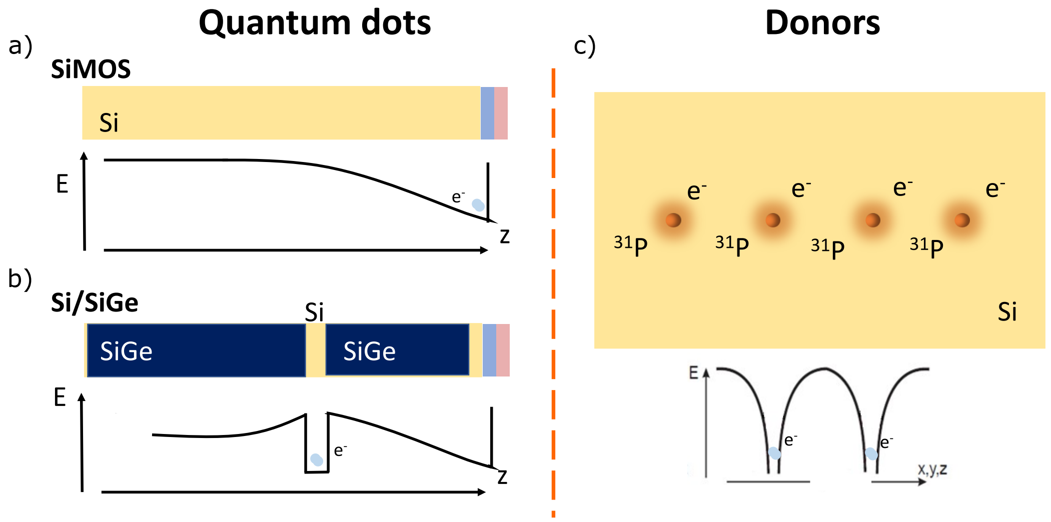

Figure 2.1.1: Electron confinement. Three main ways to confine electrons in silicon. Material layer structure and potential landscape in the vertical direction for SiMOS (a) and Si/SiGe (b) quantum dots. The colors of the structure sketches symbolise the materials, where light blue stands for SiO_2, light red for the gate stack, yellow for Silicon and dark blue for SiGe. Here, the blue balls mark the position where the electron is confined. c) Same for donors.

On the other hand, Si/SiGe heterostructures trap electrons when silicon is confined by SiGe in a SiGe/Si/SiGe structure [65, 67, 75, 99, 104]. Trapping holes requires the opposite structure, with Ge placed in between SiGe as SiGe/Ge/SiGe [105, 106]. Fig. 2.1.1a and b show the material structure and the confinement potential for SiMOS and Si/SiGe dots, respectively.

The main difference between Si/SiGe and SiMOS quantum dots is how far the 2-D gas is formed with respect to the surface and the quality of the interface. In SiMOS dots, the gas is formed closer to the surface, so that the lateral gates can shape the potential more easily. However, at the same time, electrons are sitting just next to the amorphous SiO_2 structure that can contain charge traps and defects.

Quantum dots can be further differentiated by how charges are confined in the other directions. In planar structures, additional electrostatic gates shape the potential to further confine the electrons laterally. Quantum dots can also be formed using the material geometry: if the heterostructure is assembled in a nanowire shape, quantum dots can form in the corners of the nanowire due to the corner effect when some voltage is applied on an overarching gate [20, 74, 104, 107]. The nanowire geometry is especially relevant since modern CMOS foundries like Samsung, TSMC or Intel have moved from planar MOS to patterned Si technology such as finFETs, nanowireFETs or Gate-All-Around structures [108, 109]

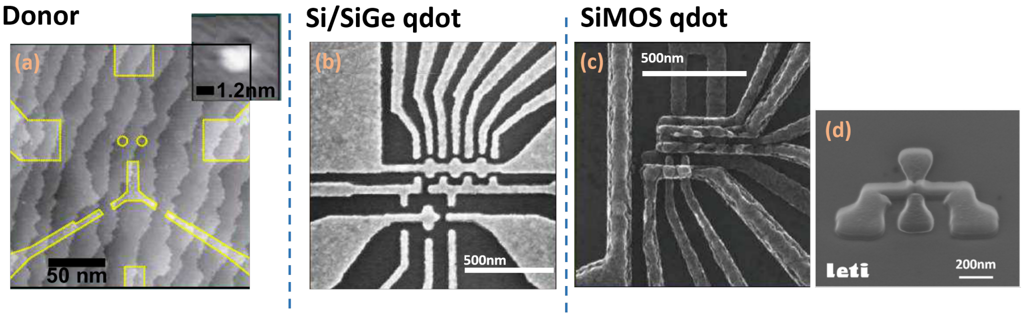

Figure 2.1.2: Nanodevice structures. Micrographs of silicon nanodevice structures. a) STM image of phosphorus donors implanted by STM lithography and a single electron transistor (SET) for readout. The top layer gates are outlined by yellow dashed lines and the top right shows a zoom-in. The white area in the zoom-in is the exposed region of the monolayer hydrogen resist where the donor is later implanted. b) SEM image of a triple dot structure in a Si/SiGe heterostructures with overlayed gates for confinement. c) SEM image of a MOS triple-dot structure. d) CMOS technology double dot nanowire. Adapted from [110]

2.1.2 DOPANTS IN SILICON

Impurities implanted in silicon with an extra (donor) or a missing (acceptor) electron can confine electrons or holes, respectively. One of the advantages is that the potential landscape is completely reproducible since it is determined by the impurity atomic species, although the potential gets deformed close to interfaces.

The most popular impurity is phosphorus [111, 112], which has have shown extremely long coherent times and whose nuclear spin can be used as a quantum memory [113]. Other atomic impurities are ^{209}Bi [114], ^{123}Sb [115] and ^{75}As [116] as donors and ^{11}B as an acceptor [117].

The behaviour of donors is very similar to quantum dots, differing in the fact that impurities hold electrons tighter, display different excited states (valley states) physics and have fewer charge transitions, which, in the case of group V donors, are no electron, D^+, one electron, D^0, or two electrons D^- [118].

To produce predictable interactions between qubits, phosphorus impurities need to be positioned with atomic precision and, even at present, ion implantation techniques are not developed enough to reach that level of precision. However, methods based on hydrogen lithography with scanning tunneling microscopy (STM) allow phosphorus atoms implanted within 6 atomic site accuracy [119, 120]. A detailed review of donors can be found in [112].

2.1.3 PHYSICS OF QUANTUM DOTS

Semiconductor quantum dots are artificial structures with a size of around 100nm^2. Although these structures are formed by millions of atoms, most electrons are tightly bound to the nuclei of the host material and there is only a small number of free electrons [121]. The behaviour of the free electrons in quantum dots is very similar to an electron bound to an atom: the confinement in every direction produces a 0-dimensional discrete energy spectrum similar to atomic orbitals, and the Coulomb repulsion between electrons creates a similar effect to ionisation in atoms.

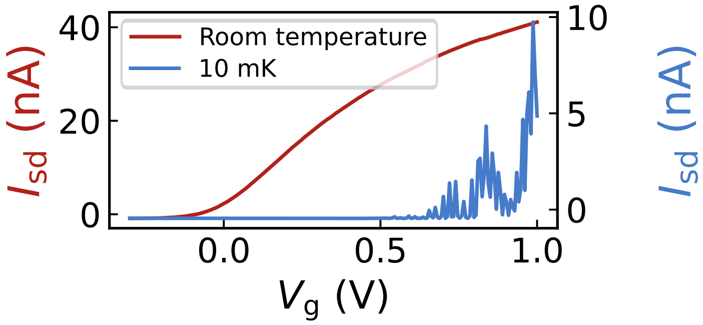

Figure 2.1.3: Coulomb blockade. Current at room temperature (red) and 10mK (blue) through a silicon nanowire fabricated in a CMOS compatible manner in a 300mm wafer.

We firstly describe the dot behaviour in a purely classical way, taking into account only the Coulomb repulsion between electrons. The dot can be considered as an isolated conductive island, in which the total charge of the dot, Q, produces a repulsion energy

$$E_{el} = \frac{Q^2}{2C} = \frac{N^2 e^2}{2C}. \tag{2.1}$$

Here, N is the number of electrons inside the island, e is the electron charge and C is the island capacitance. Adding an extra electron requires providing a charging energy $E_\mathrm{C} = \frac{e^2}{2C}$, which depends on the dot size. The smaller the dot is, the larger the charging energy is. Only if the charging energy is larger than the thermal energy, $\frac{e^2}{2C} > k_\mathrm{B}T$, the charge in the dot would be a discrete number of electrons.

The quantum properties of these devices can be tested by measuring the electronic transport through the dot. To do so, the dot is connected via tunnel coupling to two reservoirs, called source and drain, with which the dot can exchange electrons. The tunneling barriers can be simulated as a resistance and capacitance in parallel – C_S and R_S in the case of the source and C_D and R_D for the drain. To show signs of charge quantisation in transport, the resistance of the tunneling barriers must be large compared with the quantum resistance, so that electrons are localised either in the dot or the reservoir. The dot is also capacitively coupled (with capacitance C_g) to a gate electrode to tune its electrostatic potential (See Fig. 2.1.4a). This structure is called a single electron transistor (SET) because of its equivalent behaviour to a transistor: a tunable channel that connects two electronic reservoirs. Fig. 2.1.3 shows the drain-source current in a silicon transistor as a function of the gate voltage at room temperature and at 10 mK, at which, the current shows the so-called quantum oscillations due to charge quantisation.

Neglecting second-order effects and assuming that the capacitances remain constant, the dot electrostatic energy depends on the number of electrons, N, and the voltage applied to each terminal as [122]:

$$E_\mathrm{el} = \frac{(|e|N - C_\mathrm{S}V_\mathrm{S} - C_\mathrm{D}V_\mathrm{D} - C_\mathrm{g}V_\mathrm{g})^2}{2C}, \tag{2.2}$$

where $|e|$ is the electronic charge and V_g, V_S and V_D are the voltages applied to gate, source and drain, respectively. C, the dot capacitance, is the sum of capacitances expressed as $C = C_\mathrm{g} + C_\mathrm{D} + C_\mathrm{S}$. The voltage applied to the gates modifies E_el in a continuous manner. However, due to the quantisation of electronic change, the addition of a new electron produces a discrete jump in energy. Fig. 2.1.4b shows the energy as a function of V_g, where each parabola corresponds to an electron occupation, N. The gate voltages at which the parabolas cross are degenerate charge configurations ($E_\mathrm{el}(N) = E_\mathrm{el}(N-1)$). At the degeneracy points, the number of electrons in the dot can fluctuate between $N-1$ and N, allowing current between source and drain as

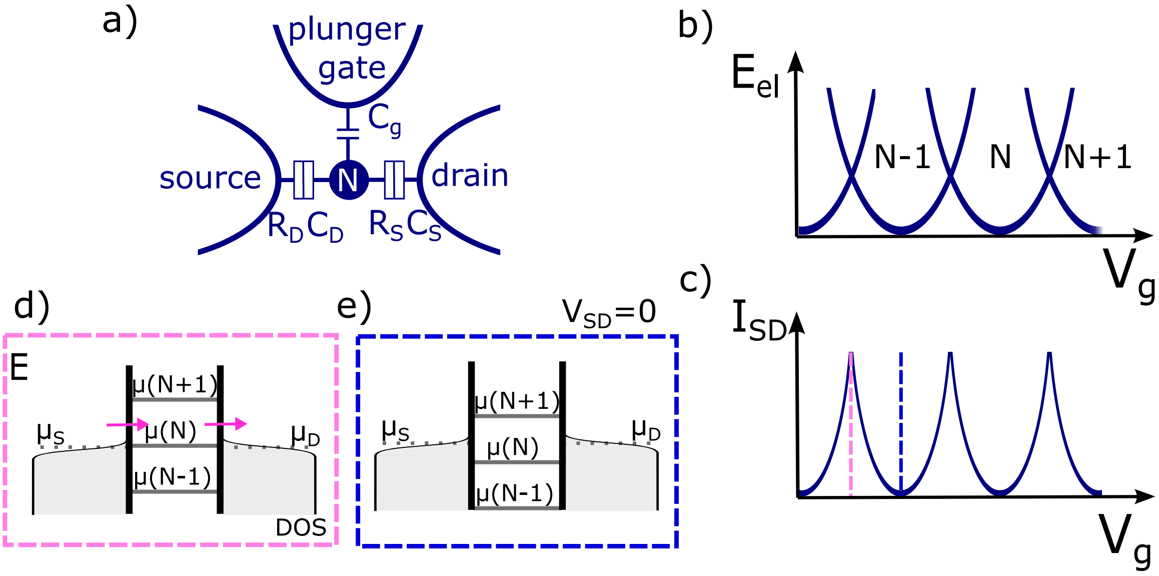

Figure 2.1.4: Quantum dot schematics. (a) Quantum dot with N electrons capacitively coupled to a plunger gate and tunneled coupled to two electronic reservoirs called source and drain. b) Electrostatic energy as a function of the gate voltage. c) Electrical current between source and drain as a function of the gate voltage. The pink dashed line corresponds to the situation shown in (d), whereas the blue dashed line indicates the voltage for Coulomb blockade, corresponding with the energy spectrum shown in (e). d) Transport is possible when the dot potential lies in between the source and drain potential. The horizontal axis is the density of states (DOS), which follows a Fermi distribution for the reservoirs and a set of Dirac functions for the 0-D quantum dot. The width of the Fermi function is determined by the electron temperature, T_e. e) Transport is suppressed when there is not an available dot state between source and drain (Coulomb blockade).

consecutive electrons tunnel through the path source-dot-drain with no energy cost. This behaviour leads to the so-called Coulomb oscillations, where transport is only permitted at the degeneracy points (see Fig. 2.1.4c).

The figure of merit to describe transport is the electrochemical potential, μ_{N}, defined as the energy necessary to add the Nth electron when there are already $N-1$ electrons in the dot. Mathematically $\mu(N)$ reads as:

$$\mu(N) = E_{\mathrm{el}}(N) - E_{\mathrm{el}}(N-1) = \frac{e^2}{C}\left(N - \frac{1}{2}\right) - \frac{|e|}{C}(C_{\mathrm{S}}V_{\mathrm{S}} + C_{\mathrm{D}}V_{\mathrm{D}} + C_{\mathrm{g}}V_{\mathrm{g}}). \quad (2.3)$$

The potential is very useful to represent the conditions for transport graphically as shown in Fig 2.1.4d) and e). Tunneling through a barrier can happen when it is energetically favourable. This situation is graphically represented by the condition that the potential at the initial side of the barrier is above the potential on the final side. This way, we can observe transport between source and drain when the potential of the dot lies in between them, so electrons can continuously flow from source to dot and finally to drain (see Fig. 2.1.4d). If there is not any dot level available between the source and drain Fermi energy, transport is suppressed (see Fig. 2.1.4e).

Applying a bias voltage between source and drain increases the range of gate voltage at which a dot state is available for transport. If the range is large enough, even two states will be available (See right upper corner from Fig. 2.1.5). By sweeping the gate voltage and the source-drain bias the current forms the so-called "Coulomb diamonds" (see Fig.2.1.5). Inside the diamond, current is forbidden and its borders correspond to an alignment in the electrochemical potential between the source/drain reservoirs and the dot state. Coulomb diamonds enclose much information such as the energy necessary to add a new electron, $E_{\mathrm{add}}(N) = \mu(N+1) - \mu(N)$, or the dot lever arm: the relation between the voltage applied to the gate and the dot electrochemical potential ($E = \alpha_{\mathrm{g}}V_{\mathrm{g}}$), calculated as $\alpha_{\mathrm{g}} = \frac{C_{\mathrm{g}}}{C}$.

As stated above, quantum dots have a single particle level spectrum similar to orbital states in atoms due to the small size of the dot in comparison with the Fermi wavelength (λ = 35 nm for silicon). On top of that, silicon quantum dots have an additional fine structure due to the electron spin degree of freedom and silicon properties. Bulk silicon has an indirect bandgap and cubic symmetry, leading to a

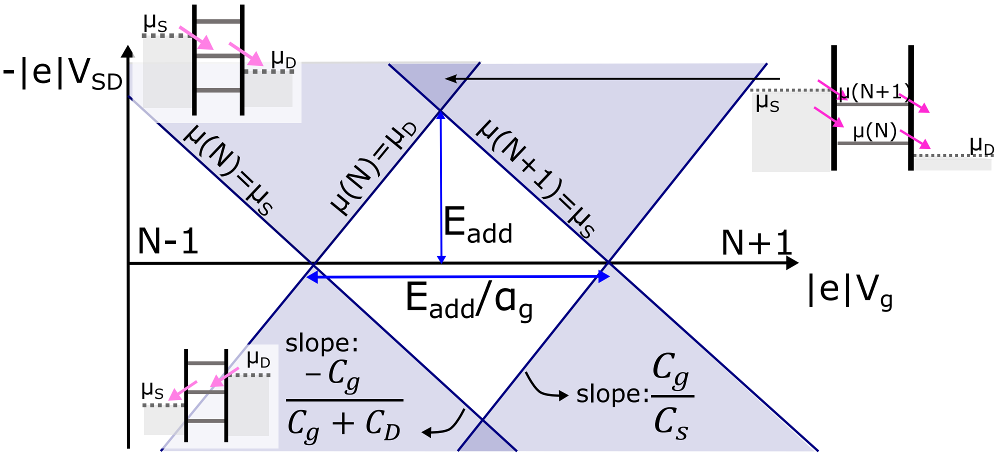
-|e|V_SD
μS
μD
μ(N)=μS
μ(N)=μD
μ(N+1)=μS
μS
μ(N+1)
μ(N)
μD
E_add
N-1
N+1
|e|V_g
E_add/α_g
slope: $\frac{-C_g}{C_g + C_D}$
slope: $\frac{C_g}{C_S}$
μD
μS

Figure 2.1.5: Coulomb diamonds. Current through the quantum dot as a function of the gate voltage, V_g, and the source/drain voltage, $V_{SD} = V_S - V_D$. Transport is only allowed in the regions between diamonds, whereas inside each diamond there is a constant number of electrons, $N-1$, N or $N+1$. As depicted in the electronic level sketches, electrons flow from source to drain in the upper half and from drain to source in the lower half. The diamond height determines $E_\mathrm{add}(N)$ since at this point the bias window is equal to the energy difference between two levels ($\mu_S - \mu_D = \mu(N+1) - \mu(N)$). At an even larger bias voltage, the bias window is larger than the level spacing and there is no Coulomb blockade, as depicted in the upper right sketch. Adapted from [123].

six-fold degenerate manifold in its band structure. In nanodevices, the degeneracy is lifted using electric fields and strain [62], creating the so-called valley states. This way, the energy spectrum of electrons confined in silicon includes orbital excited states together with spin states and valley states.

The excited states are included in the energy as:

$$E(N) = E_{\mathrm{el}} + \sum_{N} E_{\mathrm{n}}, \tag{2.4}$$

where E_{n} is the single-particle spectrum. This way, the adding energy, E_{add}, depends on the number of electrons in the dot as

$$E_{\mathrm{add}} = E(N+1) - E(N) = E_{\mathrm{C}} + \Delta E, \tag{2.5}$$

where $\Delta E = E_{\mathrm{N+1}} - E_{\mathrm{N}}$ is the energy difference between two consecutive excited states. As electrons are added sequentially to the dot, the first orbital/valley fills up until it is full. The extra energy necessary to start filling a new orbital/valley produces an increment in E_{add}. This effect leads to the electron filling sequence shown in Fig. 2.1.6a. Excited states can also be observed in Coulomb diamonds since, if the bias window exceeds ΔE, we can see an increment in current (See Fig. 2.1.6b).

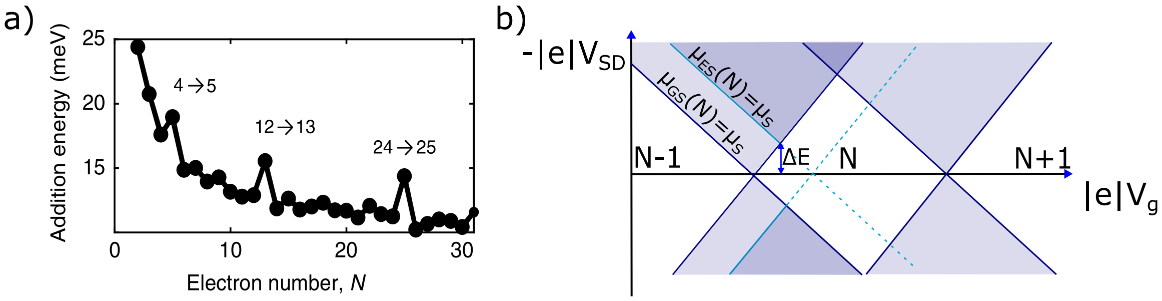

Figure 2.1.6: Excited states in Coulomb diamonds. a) Adding energy as a function of the number of electrons in a silicon quantum dot. Image retrieved from [124]. b) Schematic of Coulomb diamonds with excited states. The current increases when both the dot ground state and excited state potential lie in the bias window.

2.1.4 DOUBLE QUANTUM DOTS

Now we analyse the behaviour of two quantum dots coupled electrostatically via their mutual capacitance, C_m, where a small interdot tunnel coupling between the dots allows transport between them. In this regime, the system can be described within the Coulomb blockade frame.

The electrostatic potential of each dot called *quantum dot 1* and *quantum dot 2* can be controlled independently by the voltage applied to *gate 1* and *2*, respectively. The dots can be placed in a series distribution, with each of them connected to one lead (see Fig. 2.1.7a), or a parallel distribution, with both dots connected to both leads (see Fig. 2.1.7b).

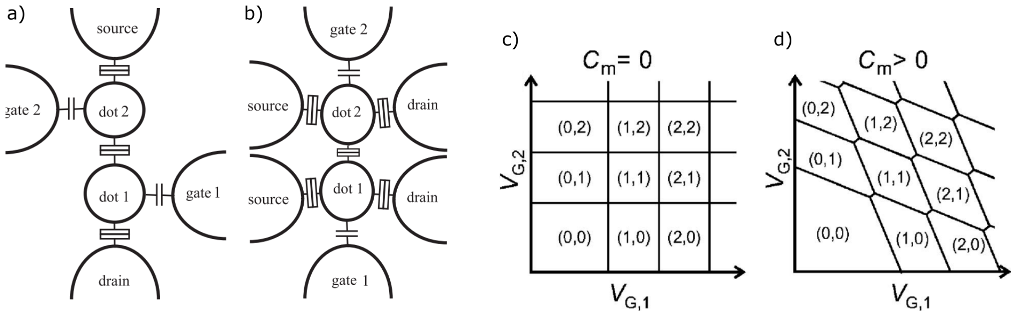

Figure 2.1.7: Double quantum dot. Schematic of a double quantum dot arranges in series (a) and in parallel (b). Stability diagram of an uncoupled (c) and a coupled (d) double quantum dot. The occupation number in each dot is included as (N_1, N_2). Images retrieved from [123, 125].

The number of electrons in the system can be described as (N_1, N_2), where $N_{1(2)}$ is the number of electrons in *dot 1(2)*. Like in single quantum dots, the voltage applied to *gate 1* and *2* (V_{g1} and V_{g2}, respectively) varies each dot potential. Fig. 2.1.7c and d shows the equilibrium electron number against V_{g1} and V_{g2}. This representation is called **stability map** and it is characterised by voltage regions where the equilibrium electron number is constant.

When the dots are not coupled to each other, $C_m = 0$, the electrochemical potential in one dot is independent of the other and the borders of the constant occupation regions are vertical and horizontal straight lines (see Fig. 2.1.7c). On the other hand, for a finite coupling capacitance, $C_m \neq 0$, the voltage applied to one of the gates will affect both dots, tilting the stability diagram lines. Moreover, the addition of a new electron in one dot produces a shift in the electrochemical potential of the other dot. This way, each cross point is split in two, separated by the coupling energy. A point shared by three different electron occupations is called a triple point and is an important feature for quantum dots in series since transport through a double-dot system in series is only possible around these points.

For a more complete and in-depth description of quantum dots and, specifically, silicon quantum dots we refer the reader to Refs. [121, 123, 125, 126].

2.2 SPIN QUBITS IN SILICON

Spin qubits in silicon come in different flavours, the simplest two-level system is formed by the spin polarisation of a single electron. However, a spin qubit can also be formed by the combined spin state of two electrons each one confined in a different dot (singlet-triplet qubits) [127], three electrons in three dots (exchange only qubits) [128] and three electrons in two dots (quantum-dot hybrids) [129]. Here, the discussion is focused on single electron spin qubits.

2.2.1 SINGLE SPIN QUBIT MANIPULATION

A single spin qubit is formed by the spin states $|\uparrow\rangle = |1\rangle$ and $|\downarrow\rangle = |0\rangle$ of a confined electron in the presence of a static magnetic field, B_z. The states are separated by the Zeeman energy, $E_\mathrm{Z} = g\mu_\mathrm{B}B_\mathrm{z}$. Here, g is the electron g factor and μ_B is the Bohr magneton.

Electron spins can be manipulated using an AC magnetic field, B_ac (applied perpendicularly to B_z) that oscillates at the Larmor frequency, $\omega_0 = g\mu_B B_\mathrm{z}/\hbar$.

The complete hamiltonian including static and rotating magnetic field is equal to:

$$H = \frac{\hbar\omega_0}{2}\sigma_\mathrm{z} + \hbar\Omega_\mathrm{R}\cos(\omega t + \delta)\sigma_\mathrm{x}. \tag{2.6}$$

The first part comes from the static magnetic field that separates ground ($|\downarrow\rangle$) and excited ($|\uparrow\rangle$) states by the Zeeman energy, whereas the second part is related to B_ac. Here, ω is the oscillating frequency of B_ac and δ is the initial phase of B_ac. The magnitude of B_ac is included in the Rabi frequency, which quantifies how fast the spin state rotates around the Bloch sphere, as $\Omega_\mathrm{R} = \frac{g\mu_\mathrm{B}B_\mathrm{ac}}{\hbar}$.

Qubit manipulation is normally described in the rotational frame of the rotating magnetic field, B_{ac}. In this frame, and applying the rotational wave approximation, the total Hamiltonian simplifies to:

$$H_{rot} = (-\omega_0 + \omega)\sigma_z/2 - \Omega_{\mathrm{R}}\left(\cos(\delta)\sigma_x/2 - \sin(\delta)\sigma_y/2\right), \tag{2.7}$$

A mismatch between the Larmor and the microwave frequency would produce a rotation along the Z-axis. On the other hand, the rotation speed is dictated by Ω_{R} and the specific axis along which the spin will rotate is controlled by δ.

In electron spin resonance (ESR) the B_{ac} can be delivered through a transmission line placed near the qubit, where the current through the antenna produces an AC magnetic field. The heating produced by the alternating current limits the speed of the qubit manipulation to a few MHz [62], reaching fidelities of up to 99.96% [130]. This method poses a challenge in terms of scalability since the number of antennas generating heat would increase linearly with the number of qubits. Moreover, the magnetic field created in an antenna can interact with multiple qubits at the same time, leading to cross-talk. To avoid that issue, individual spins would need to have their resonant frequency shifted relative to their neighbours. A more scalable option for ESR is to put the qubits in a microwave cavity resonating at a given frequency [83]. In this approach B_{ac} is applied globally and, to control a given qubit, its Larmor frequency is switched on and off the cavity resonance.

Another approach for qubit control is electric dipole spin resonance (EDSR), where an AC voltage applied to the gate induces the electron to oscillate back and forth. If the electron is moving in a magnetic gradient produced naturally via spin-orbit coupling [131] or artificially by placing micromagnets [64], the electron movement is equivalent to applying an oscillating magnetic field. EDSR leads to faster spin manipulations (30MHz), reaching a fidelity of 99.9% [64].

2.2.2 TWO-QUBIT GATES

Quantum computing requires to have a universal set of quantum gates, which include qubit rotations, like the ones described in the previous section, and interactions between two qubits to generate entanglement. Two-qubit gates are normally realised between two neighbour dots. To do so, voltage pulses can bring close the electronic

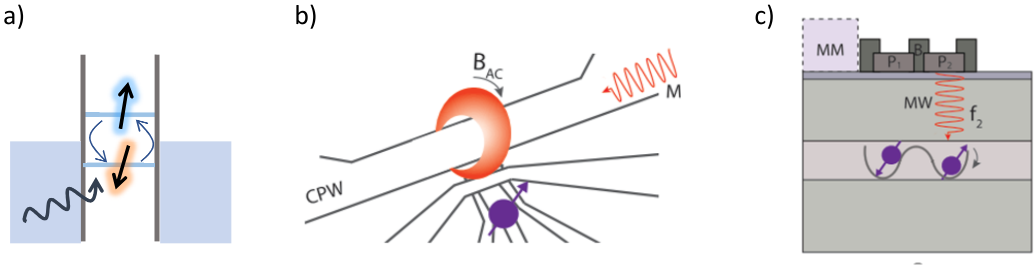

Figure 2.2.1: ESR and EDSR. a) Diagram of the spin manipulation of a single electron confined in a quantum dot. The spin can manipulated via an AC magnetic field delivered directly through a stripline placed near the dot (ESR) (b) or by shaking the electron in a magnetic gradient produced naturally or artificially with micromagnets (EDSR) (c). Images adapted from [132].

wavefunctions, increasing the strength of its exchange interaction. At the same time, long-distance 2-qubit gates in which single spins can be coupled to a resonator via circuit quantum electrodynamics cQED [133] have also been proposed.

In this section, we firstly introduce the physics of a double quantum dot occupied by two electrons to later explain how to use them to create two-qubit gates.

Two electron spin states in a single quantum dot

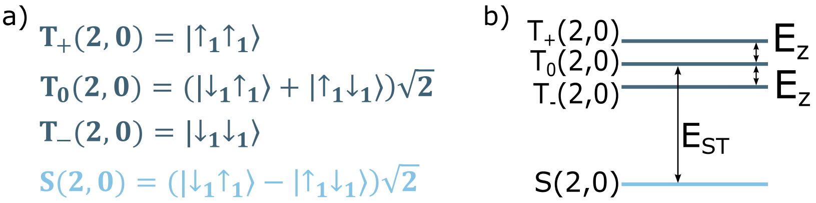

a)

$$\mathbf{T_{+}(2,0)} = |\uparrow_1\uparrow_1\rangle$$

$$\mathbf{T_{0}(2,0)} = (|\downarrow_1\uparrow_1\rangle + |\uparrow_1\downarrow_1\rangle)\sqrt{2}$$

$$\mathbf{T_{-}(2,0)} = |\downarrow_1\downarrow_1\rangle$$

$$\mathbf{S(2,0)} = (|\downarrow_1\uparrow_1\rangle - |\uparrow_1\downarrow_1\rangle)\sqrt{2}$$

Figure 2.2.2: Spin states in a single quantum dot. a) Wave function of a doubly occupied single quantum dot eigenstates. b) Corresponding energy diagram. The triplet states are separated by the Zeeman energy, E_{Z}, when a magnetic field is applied. E_{ST} is the energy difference between $S(2,0)$ and $T_0(2,0)$ and it is equal to $E_{\mathrm{ST}} = \Delta E_{\mathrm{orb(valley)}} - E_{\mathrm{k}}$, where $\Delta E_{\mathrm{orb(valley)}}$ is the energy of the next available orbital or valley state and E_{k} is the change in Coulomb repulsion produced by the antisymmetric part of the orbital part of the wave function.

If both of the electrons are in the same dot (occupancy (2,0) or (0,2)), the situation is equivalent to having a doubly occupied single quantum dot. The ground state is the singlet state, in which both electrons occupy the same orbital(valley) state and the spin has an antiparallel configuration $S(2,0) = (|\uparrow_1\downarrow_1\rangle - |\downarrow_1\uparrow_1\rangle)/\sqrt{2}$, where the sub-index designates the quantum dot number 1(2). The consequently excited states correspond to the symmetric triplet states: T_-, T_0 and T_+, with spin number S=1. In the triplet configuration, the second electron must occupy the next orbital because, due to the fermionic nature of the electron, its global wave function has to be antisymmetric. Fig. 2.2.2 shows a graphic representation of these states.

TWO ELECTRON SPIN STATES IN A DOUBLE QUANTUM DOT

In the case that the occupation is (1,1) and the inter-dot coupling is negligible, each electron is in a different dot with eigenstates $|\downarrow_1\downarrow_2\rangle$, $|\uparrow_1\downarrow_2\rangle$, $|\downarrow_1\uparrow_2\rangle$ and $|\uparrow_1\uparrow_2\rangle$. As the tunneling rate between dots, t_c, becomes significant, the electrons are not fully localised in either of the dots and orbital bonding and antibonding states are formed. The spin ground state is the singlet $S(1,1)$, which is separated from the triplet states by the exchange energy $J = \frac{4{t_\mathrm{c}}^2}{E_\mathrm{C}}$.

Fig. 2.2.3a shows the stability diagram in the (1,1) to (2,0) region, where a combination of gate voltages can move the system along the detuning axis ϵ. Near the degeneracy point between the (1,1) and (2,0) configurations, the electrons are delocalised due to the tunneling coupling and both configurations hybridise, resulting in an avoided crossing with an energy separation of $2\sqrt{2}t_\mathrm{c}$

Since the transport is spin preserving, the singlet state S(1,1) hybridise only with S(2,0) and the triplets T(1,1) with T(2,0). However, due to the different energy splitting between singlet and triplet, we obtain an energy diagram like the one in Fig. 2.2.3b. Here, transport between singlet S(1,1) and S(2,0) is allowed at a lower detuning than between the triplets T(1,1) and T(2,0) due to Pauli spin blockade [134]. This property can be explored to determine the spin state using charge sensing (See Sec. 2.2.3 for more information). As shown in Fig. 2.2.3c, applying a magnetic field breaks the degeneracy between the triple states. If the magnetic field surpasses the value $B > E_\mathrm{ST}/g\mu_\mathrm{B}$, the hybridisation detuning between singlets is no longer lower than the one for the triplets.

To describe the whole system, we use the computing base $|\uparrow\uparrow\rangle$, $|\downarrow\uparrow\rangle$, $|\uparrow\downarrow\rangle$, $|\downarrow\downarrow\rangle$ with one electron in each dot without mixing. Here, for simplicity, we consider that the first term of the wavefunction corresponds to the spin state in *dot* 1 and the second

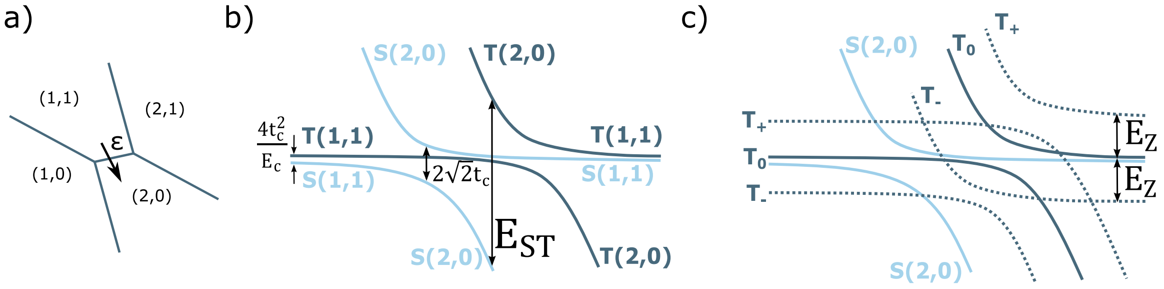

Figure 2.2.3: Two-electron spin states in a double quantum dot. a) Stability diagram in the (1,1), (2,0) region. ϵ is the axis of the detuning. b) Spectrum of a double quantum dot near the (1,1) to (2,0) charge transition. c) Same as b) when a magnetic field is applied.

to *dot* 2. The strong Coulomb interaction and the large valley splitting characteristic in silicon dots [66] allows to consider only the five lowest energy states: {(1,1): $|\uparrow\uparrow\rangle$, $|\downarrow\uparrow\rangle$, $|\uparrow\downarrow\rangle$, $|\downarrow\downarrow\rangle$; S(0,2): $\frac{1}{\sqrt{2}}|0,\uparrow\downarrow-\downarrow\uparrow\rangle$ }. The Hamiltonian acting on such a base reads as [66]:

$$H = \begin{pmatrix} \bar{E}_z & 0 & 0 & 0 & 0 \\ 0 & \delta E_z/2 & 0 & 0 & t_c \\ 0 & 0 & -\delta E_z/2 & 0 & -t_c \\ 0 & 0 & 0 & -\bar{E}_z & 0 \\ 0 & t_c & -t_c & 0 & U-\epsilon \end{pmatrix} \begin{pmatrix} |\uparrow\uparrow\rangle \\ |\uparrow\downarrow\rangle \\ |\downarrow\uparrow\rangle \\ |\downarrow\downarrow\rangle \\ \frac{1}{\sqrt{2}}|0,\uparrow\downarrow-\downarrow\uparrow\rangle \end{pmatrix}, \tag{2.8}$$

where $\bar{E}_z$ is the average Zeeman energy, δE_Z is the Zeeman energy difference between dots, $U \sim E_\mathrm{C}$ is the Coulomb repulsion for adding the second electron to a dot and ϵ is the detuning, controlled by the gate voltages. Due to the spin conservation nature of tunneling between dots, the singlet (0,2) state hybridise only with the states $|\downarrow\uparrow\rangle$ and $|\uparrow\downarrow\rangle$.

Using the Schrieffer-Wolff transformation and assuming that $U-\epsilon >> t_c$ the Hamiltonian can be reduced to the four single dot occupied states [62, 135], leading to the Heisenberg exchange interaction Hamiltonian ($J\hat{S}_1\hat{S}_2$):

$$H = \begin{pmatrix} \bar{E}_z & 0 & 0 & 0 \\ 0 & \delta E_z/2 - \frac{J}{4} & J/2 & 0 \\ 0 & J/2 & -\delta E_z/2 - \frac{J}{4} & 0 \\ 0 & 0 & 0 & -\bar{E}_z \end{pmatrix} \begin{pmatrix} |\uparrow\uparrow\rangle \\ |\uparrow\downarrow\rangle \\ |\downarrow\uparrow\rangle \\ |\downarrow\downarrow\rangle \end{pmatrix}, \tag{2.9}$$

where, in first-order approximation, the exchange, J is equal to $J = \frac{2{t_{\mathrm{c}}}^2}{U-\epsilon-dE_z} + \frac{2{t_{\mathrm{c}}}^2}{U-\epsilon+dE_z}$. The exchange is highly dependent on the detuning and the tunneling coupling, which are controllable through gate pulsing. Modifying the tunneling coupling is the preferred method to implement 2-qubit gates because it makes the gate less sensitive to charge noise [67, 136].

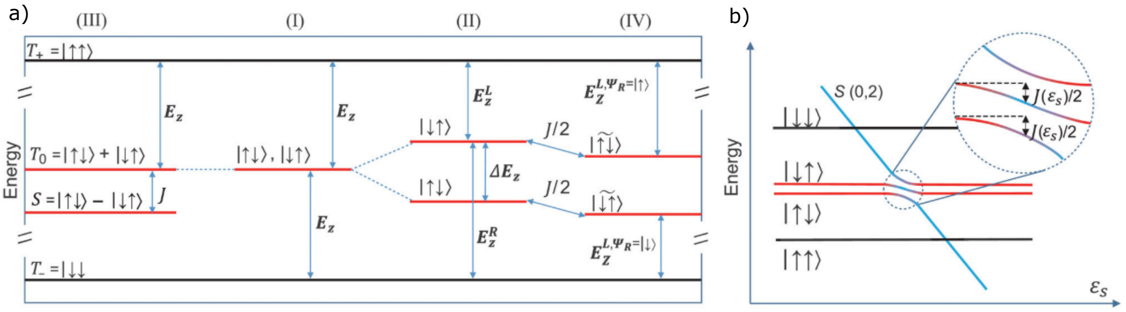
a)
(III)
(I)
(II)
(IV)
$T_+ = |\uparrow\uparrow\rangle$
E_z
E_z
E_Z^L
$E_Z^{L,\Psi_R=|\uparrow\rangle}$
$|\downarrow\uparrow\rangle$
$J/2$
$\widetilde{|\uparrow\downarrow\rangle}$
Energy
$T_0 = |\uparrow\downarrow\rangle + |\downarrow\uparrow\rangle$
$|\uparrow\downarrow\rangle, |\downarrow\uparrow\rangle$
ΔE_z
$|\uparrow\downarrow\rangle$
$J/2$
$\widetilde{|\downarrow\uparrow\rangle}$
$S = |\uparrow\downarrow\rangle - |\downarrow\uparrow\rangle$
J
E_z
E_Z^R
$E_Z^{L,\Psi_R=|\downarrow\rangle}$
$T_- = |\downarrow\downarrow\rangle$
b)
S (0,2)
$J(\varepsilon_S)/2$
$J(\varepsilon_S)/2$
$|\downarrow\downarrow\rangle$
Energy
$|\downarrow\uparrow\rangle$
$|\uparrow\downarrow\rangle$
$|\uparrow\uparrow\rangle$
ε_S

Figure 2.2.4: Hamiltonian eigenstates. a) Eigenstates of two spins in a double quantum dot depending on the exchange interaction, J, and the Zeeman energy difference, δE_Z. (I) δE_Z and J are equal to zero. (II) δE_Z is non zero. (III) δE_Z and J are non-zero with $\delta E_Z >> J$. The eigenstates are approximately the same as in (II) but with different energy gaps. (IV) δE_Z and J are non-zero with $\delta E_Z << J$. b) Energy levels depending on the detuning ϵ. The left part of the graph corresponds to situation (IV), whereas the enlarged area leads to (III). Image retrieved from [137].

The ratio between the exchange, J, and the difference in the Zeeman energy, δE_Z, determines the eigenstates of the Hamiltonian of Eq. 2.9. When J and E_Z are equal to zero, both dots have the same Zeeman energy and the single electron spin states are not mixed. In this situation the states $|\uparrow\downarrow\rangle$ and $|\downarrow\uparrow\rangle$ are degenerate as it is shown in Fig. 2.2.4(I). On the other hand, a non zero δE_Z breaks the degeneracy (See Fig. 2.2.4(II)). In the case both J and δE_Z are non-zero and $J >> \delta E_Z$, the system eigenstates are a mixture of the dot defined spin states forming singlet and triplet states (See Fig. 2.2.4(III)). In this condition, **exchange 2-qubit gates** can be realised. Here, the double quantum dots are brought to the inter-charge dot transition, where J is maximal. The off-diagonal terms from Eq.2.9 interchange the spin states producing a $\sqrt{\mathrm{SWAP}}$ gate [43, 111, 138, 139].

On the other hand, when $\delta E_Z >> J$ the single dot occupied states can still be considered eigenstates with small corrections due to spin-charge hybridisation. The

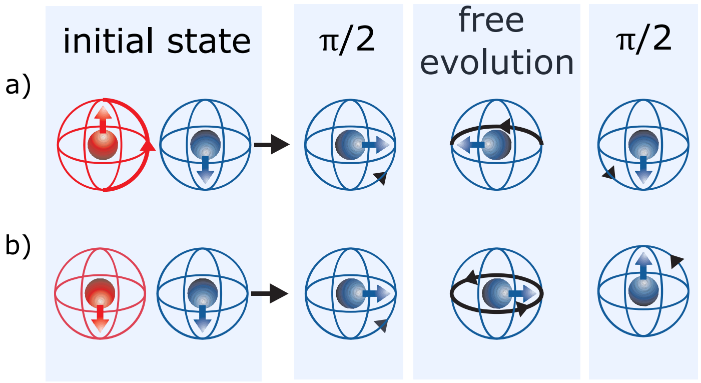

Figure 2.2.5: CNOT gate. Bloch sphere sketches of a CNOT gate realised as a combination of $\pi/2$ pulses and CPhase gate. a) The final position of the spin is the same as the initial state. b) Qubit final state is the opposite of the initial one due to the faster free rotation of the spin around the Z-axis in free evolution. The speed is different depending on the control qubit (red) due to the effect of the exchange interaction. Image retrieved from [66].

small J makes the energy between spin up and down in one dot dependent on the qubit state in the other dot (See Fig. 2.2.4(IV)). This property can be used to create a **resonant gate** since the frequency for a qubit rotation realised via ESR or EDSR depends on the ancilla qubit state [67, 140] producing a CROT gate. Qubit rotations using ESR are normally slow, limiting the maximum fidelity (with an implementation of a CROT in the order of the microsecond and a fidelity of 98% [140]). Alternatively, EDSR can be used for a faster qubit rotation, reducing the gate latency to 103 ns and demonstrating a fidelity of 99.5% [71].

In this same regime ($\delta E_Z >> J$) CNOT gates are possible by combining single-qubit rotation with a control phase gate (CPhase) [66, 68]. As shown in Fig. 2.2.5, firstly one of the qubits is rotated $\pi/2$. In this position, the free evolution of the spin produces a rotation around the Z-axis whose speed depends on the other spin polarisation. After some wait time, the spin acquires a different phase depending on the state of the other qubit (control qubit). Another $\pi/2$ rotation is necessary to complete the CNOT gate. CPhase gates have been realised with a fidelity of 99.5% in 100 ns [70].

In summary, traditionally CPhase gates and $\sqrt{\text{SWAP}}$ gates are faster since they do not rely on single-qubit rotations. However, the rapid control of the exchange strength requires a complex engineering of high-frequency pulses. On the other hand, CROT gates are usually slower but do not require a complex pulse engineering.

2.2.3 Spin Readout and initialisation

The spin magnetic moment of a single electron is approximately two times the Bohr magnetron, $\mu_B = 9.274\times10^{-24}$ J/T, being too small to be resolved using spin magnetic resonance [141] or microresonators [142, 143]. Although NV centres can directly measure single spins [144], the preferred method to measure the spin polarisation is to use spin to charge conversion- making a tunneling event dependent on the spin polarisation.

Two factors characterise the quality of the readout: the readout time, Δt and the fidelity. The readout time is defined as the total time during which the measurement is acquired. QEC requires short readout times so errors can be corrected faster than the decoherence time. On the other hand, the fidelity determines the percentage of readout traces that are classified correctly. Therefore, the desirable conditions are to have the maximum amount of spin polarisation correctly identified in the minimum readout time, Δt. A benchmark of the readout demonstrations in silicon can be found in Appendix. A.

Spin to charge conversion

Spin dependent tunneling: In a single-spin qubit, the 2-level system is formed by the spin-up ($|\uparrow\rangle$) and down ($|\downarrow\rangle$) electron states, separated by the Zeeman energy. To convert the spin polarisation to a tunneling event, the dot is tunnel coupled to a reservoir, whose Fermi energy is placed in between the spin up and down electrochemical potential as shown in Fig. 2.2.6a. A $|\uparrow\rangle$ electron will tunnel out from the dot to the reservoir and be subsequently replaced by a spin $|\downarrow\rangle$ electron, whereas a spin $|\downarrow\rangle$ electron will remain in the dot [145, 146]. The changes in the dot occupation can be registered with a charge sensor. This way, a readout trace from a spin $|\downarrow\rangle$ state is a constant noisy background (the light blue trace in Fig. 2.2.6a). On the other hand, a spin $|\uparrow\rangle$ readout trace, like the one displayed in dark blue in Fig. 2.2.6a, is characterised by a 'blip' that starts when the spin $|\uparrow\rangle$ electron leaves the dot ($t^{\uparrow}_{\text{out}}$), and lasts until a spin $|\downarrow\rangle$ electron tunnels back into the dot ($t^{\downarrow}_{\text{in}}$). The spin is initialised in the $|\downarrow\rangle$ state after each readout.

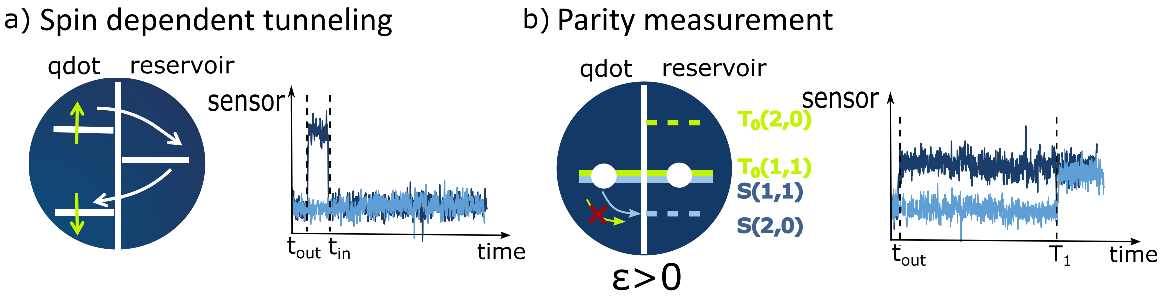
a) Spin dependent tunneling
qdot
reservoir
sensor
t_{out}
t_{in}
time
b) Parity measurement
qdot
reservoir
$T_0(2,0)$
$T_0(1,1)$
S(1,1)
S(2,0)
ε>0
sensor
t_{out}
T_1
time

Figure 2.2.6: Readout schematic. a) **Spin dependent tunneling.** The reservoir Fermi energy is placed between the spin up and down states. The $|\downarrow\rangle$ state remains in the dot, whereas a $|\uparrow\rangle$ state tunnels out with time $t^{\uparrow}_{\mathrm{out}}$, and consequently a $|\downarrow\rangle$ electron tunnels in from the reservoir. A charge sensor capacitively couple to the dot senses the dot occupancy so that the $|\uparrow\rangle$ state is detected as a blip in the signal (dark blue). b) **Parity measurement.** When a double quantum dot is set from the (1,1) to the (0,2) charge configuration, the Pauli exclusion principle forbids the state $T_0(1,1)$ to tunnel to the ground state S(2,0). On the other hand, a singlet state S(1,1) can tunnel to the S(2,0). A charge sensor can sense the different occupation so that a singlet S(1,1) leaves a measurement trace like the one in dark blue trace. If the initial state is $T_0(1,1)$ the system will stays in the (1,1) configuration until it decays to $S(1,1)$ and consequently tunnel to S(2,0), leading to the measurement trace in light blue.

Spin-dependent tunneling requires high magnetic fields since, to correctly determine the spin polarisation, the bath temperature has to be smaller than the Zeeman splitting. Moreover, this method imposes a limit on the readout time, Δt, which needs to be necessarily larger than the $t^{\uparrow}_{\text{out}}$ to include the 'blip' in the measurement.

The fidelity of the readout is a combination of the charge sensor accuracy and the duration of the blip. On one hand, the longer the blip is, the easier is to discern, but on the other hand, a better sensor can differentiate between blip and background faster, reducing the readout time while maintaining a high fidelity. Another factor in the fidelity is the relaxation time, T_1, defined as the time that a $|{\uparrow}\rangle$ electron takes to decay to a $|{\downarrow}\rangle$ state. In single electron spins T_1 increases as the applied magnetic field, B_z, decreases. This creates a trade-off between applying a strong enough the magnetic field to create a large energy separation, but not too strong so that the relaxation time compromises the fidelity [147].

Spin dependent tunneling has a simple realisation since it does not require an ancilla dot. However, it cannot be realised at high temperatures and the readout time is limited by $t^{\uparrow}_{\text{out}}$. For this reason, the demonstrations of spin dependent tunneling have longer Δt. For example, [68] reached a fidelity of $F_{\text{M}} = 99.8\%$ in $\Delta t = 58$ ms using an SET in donors. One of the fastest implementations is [147] with $F_{\text{M}} = 97.8\%$ in $\Delta t = 1.5\ \mu s$ and the one presented in this thesis $F_{\text{M}} = 99.54\%$ in $\Delta t = 250\ \mu$s using an SEB and low temperature amplification.

Pauli Spin blockade:

The spin state can also be measured in the singlet-triplet ($S(1,1)$-$T_0(1,1)$) basis. To do so, a static magnetic field splits off $T_+(1,1)$, and $T_-(1,1)$, so they don't contribute to the readout. If starting in a $T_0(1,1)$, the Pauli exclusion principle will forbid the electron to tunnel from $T_0(1,1)$ to $S(2,0)$. However, if the initial state is S(1,1), the electron can tunnel to the other dot, as shown in Fig. 2.2.6b. The conditional tunneling holds only for magnetic fields smaller than the (2,0) singlet-triplet splitting, E_{ST}.

A charge sensor can measure whether the dots are in the (1,1) or the (2,0) occupation. This way, a triplet measurement corresponds to a constant value, until the triplet relaxes to a singlet, allowing tunneling. On the other hand, the trace of a singlet will change when the electron tunnels to S(2,0). Tunneling time between dots is normally very short (too small to be detected) compared to the relaxation time (typically in the scale of hundreds of microseconds) [148–150].

The readout time for Pauli spin readout is normally shorter than spin-dependent tunneling due to the fast tunneling time between dots, allowing a fidelity of $F_{\mathrm{M}} = 99.2\%$ in 6 μs in a SiMOS nanowire [98]. The limiting factor in the fidelity is normally the ability of the sensor to differentiate between spin states faster than the relaxation time. For a higher fidelity, the relaxation time can be extended using Latching Pauli Spin blockade as explained below.

Pauli spin readout does not require as large magnetic fields as spin-dependent tunneling. Moreover, it does not use a reservoir, so the readout is not affected by the reservoir electron temperature, and can potentially be realised at higher temperatures.

The state S(2,0) can be initialised by allowing the dot to exchange electrons with the reservoir when the reservoir Fermi level is placed below the states T(2,0) and above S(2,0) [43]. Then, the system is pulsed to the (1,1) configuration fast (non adiabatically) compared to the nuclear mixing, but slow (adiabatically) compared to the exchange interaction, finishing with a state S(1,1). If the system is ramped slowly to even more negative detunings, where the exchange interaction is almost negligible, the singlet state adiabatically becomes a $|\uparrow\downarrow\rangle$ state. In the same manner, a triplet $T_0(1,1)$ can be transformed into a $|\downarrow\uparrow\rangle$ state [43, 138]. On this basis, singlet qubit operations can be applied to each individual spin [151].

Spin Pauli Blockade can also be used for parity readout, necessary in quantum error correction codes. In this case, the mixing between T_0(1,1) and S(1,1) is too fast to be measured so that any combination of $|\uparrow\downarrow\rangle$ and $|\downarrow\uparrow\rangle$ is allowed to tunnel to $S(2,0)$. On the other hand, the T_-(1,1) and T_+(1,1) cannot tunnel to the (2,0) configuration. This way, we can differentiate between odd parity ($|\uparrow\downarrow\rangle$, $|\downarrow\uparrow\rangle$) and even parity ($|\uparrow\uparrow\rangle$, $|\downarrow\downarrow\rangle$) [152].

Latching Pauli Spin blockade:

The fidelity of Pauli spin blockade measurements can be improved by adding a reservoir to the readout that has a higher tunneling coupling to one of the dots. This way, the transition to the state (1,2) is much faster from the state (0,2) than from (1,1). To do a parity measurement with latching enhancement, the electronic sequence is (1,1)-(0,2)-(1,2). If the system was initially in a $S(1,1)$ state, it will firstly tunnel to the (0,2) state and shortly after to (2,1). However, a triplet T_0(1,1) is not allowed to transition to (0,2) so the tunneling to (2,1) will be much slower than for a singlet [150, 153, 154].

Although this readout requires a more difficult fabrication [155] and the addition

	Resistive	Reactive
DC	SET (2) QPC (2)	
rf-reflectometry	rf-SET (2) rf-QPC (2)	SEB (1) in-situ (0)

Table 2.3.1: Sensor classification. Sensors classification based on whether the sensor registers changes in its resistance or capacitance and on whether that change is detected by directly measuring current through the sensor (DC) or by connecting the sensor to a resonator (rf-reflectometry). The numbers between brackets correspond to the number of leads that each type of sensor requires.

of a reservoir might pose some problems in terms of scalability, it shows higher readout fidelities. This is because, on one hand, the latching mechanism involves a change in the system total charge, which is normally more easily detected and, on the other hand, the blockade lifetimes are now determined by the different tunneling rates to the reservoir, which are normally longer than the relaxation time from $T_0(1,1)$ to $S(1,1)$ [150, 155]. Spin latching mechanism holds the highest fidelities reaching $F_\mathrm{M} = 99\%$ in 1.6 μs [156] using an rf-SET and $F_\mathrm{M} = 99.9\%$ in 6 μs [150, 157] with an SET and amplification at millikelvin temperatures.

2.3 CHARGE SENSORS

In order to implement QEC protocols, the readout fidelity has to be larger than 99.9% and faster than the qubit decoherent time. In the previous section, we saw how the readout method and tunneling times can affect the readout time and fidelity. However, another crucial factor is the charge sensor, which must be highly sensitive and with a bandwidth larger than the involved tunneling rates.

Charge sensors have a complex impedance that is very sensitive on their surrounding electrochemical potential. The different kinds of charge sensors can be divided by what is measured (reactive changes or resistive changes) and how it is measured (as a direct measurement or using rf-reflectometry). Another way to classify charge sensors is by the number of leads that the sensor requires, which determines their suitability for scalability. Table 2.3.1 summarises the sensor classification.

This section presents a small review of the current state of charge sensors and their working principles. At the moment, there is not a unify method to quantify the sensor sensitivity (see Sec 4.1 for a detailed description). So that, for the sake of simplicity, this section refers exclusively to charge sensitivity, defined as how much difference in charge can be sensed in a second, measured in $e/\sqrt{\mathrm{Hz}}$. For a deeper description of charge sensors we direct the reader to the review recently published in Ref. [158].

2.3.1 QUANTUM POINT CONTACT AND SINGLE-ELECTRON TRANSISTOR

The first demonstration of charge sensors were single-electron transistors (SETs) [159] and quantum point contacts (QPCs) [160] as the ones shown in Fig. 2.3.1a and b. Both of them have quantised conductances that are very sensitive on the electrostatic environment (see Fig. 2.3.1c). This way, any changes in the charge occupation of a nearby quantum dot can be measured as a drop in the current through a SET or a QPC. Moreover, since the behaviour of a quantum dot is very similar to a SET, quantum dots can also be used as charge sensors in a similar manner.

Direct measurement of the current through the sensor have a bandwidth limited to few kHz, which makes measuring fast tunneling events in quantum dots challenging [161]. The low bandwidth is produced by the RC low-pass filter formed by the sensor large resistance and the capacitance from the cables that join the cold stage in a cryostat with the room-temperature electronics.

Moreover, although the theoretical limit for the SET sensitivity calculated for common experimental values is 1 $\mu e/\sqrt{\mathrm{Hz}}$ [162], the minimum charge sensitivity achieved with an SET is 20 $\mu e/\sqrt{\mathrm{Hz}}$ at 4.4 kHz [163]. This is because the theoretical limit is based on the shot noise produced by the current through the sensor, but it does not take into account noises that dominate at low frequencies. An example of this is charge noise, which originates from the collective behaviour of defects or charge traps trapping and releasing electrons [164]. The density spectrum of charge noise depends on the frequency as 1/f dominates at frequencies below 10kHz.

To increase the bandwidth and get rid of low frequency noise, the cable capacitance can be reduced by placing an amplifier like a HEMT [165] or a SiGe Heterojunction-Bipolar-Transistor [157] as current amplifiers in the mixing chamber (100 mK), close to the charge sensor. However, in this demonstrations, the measurement bandwidth was only increased to up to hundreds of kiloHertzs achieving the rather modest sensitivity of 300 $\mu e/\sqrt{\mathrm{Hz}}$.

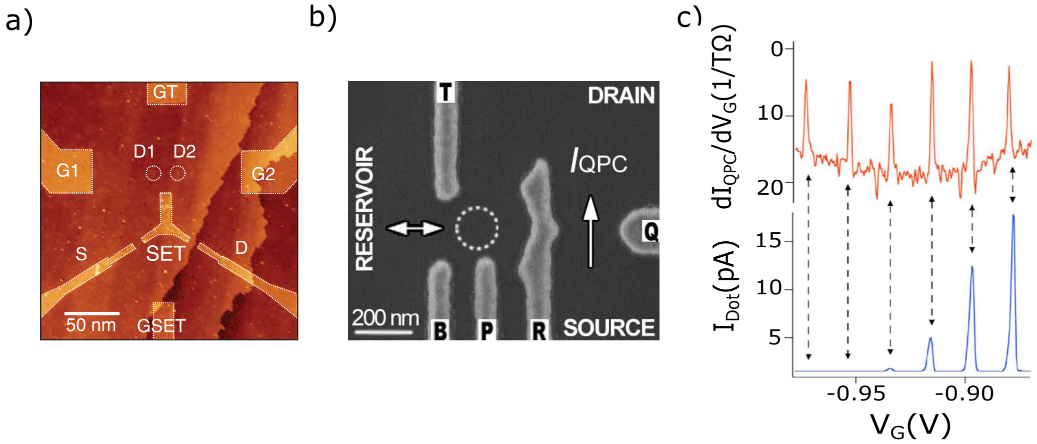

Figure 2.3.1: Charge sensors. a) STM picture of a SET used for spin readout in phosphorus donors. b) SEM picture of a QPC used for spin dependent tunneling in a Si/SiGe quantum dot. c) Top: derivative of the current through a QPC with respect to the dot gate voltage, the peaks correspond to a charge transition. Bottom: Current through the quantum dot at the same gate voltage. Adapted from [118, 166, 167]

2.3.2 Radio-frequency reflectometry

Another approach to increase the bandwidth is to use an impedance matching network on resonance that transforms the high resistance of the sensor into the fridge line impedance ($Z_0 = 50$). Changes in the sensor impedance are observed in the power reflected by the resonator formed by the matching network and the sensor. This method allows bandwidths of 100 MHz, more suitable to spin measurement [168].

The following describes how rf-reflectometry works, starting with a revision of how waves propagate in transmission lines, what is a matching network and how to use it to measure changes in the sensor impedance.

Waves in transmission lines

Transmission lines allow the propagation of microwave electromagnetic fields within their boundaries. They are formed by two conductors (signal and ground) that con-

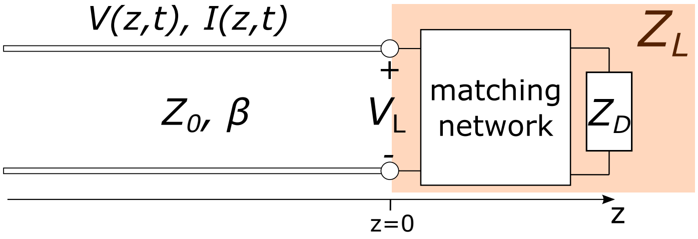

Figure 2.3.2: Transmission line. Transmission line terminated in a Z_{L} impedance at $z = 0$ formed by the matching network and the sensor impedance, Z_{D}. Image adapted from [169].

fine the electromagnetic field within the dielectric material between them. Although Fig. 2.3.2 sketches a transmission line as two parallel wires (representing the conductors), they come in different shapes, like parallel plates or coaxial cables.

The wave propagating can be described as a voltage difference between the conductors that depends on time, t, and position, z. The specific waveform is obtained by solving the *telegraph equations* that describe the physics in the transmission line [169]. This way, an incident voltage waveform generated at a source position $z < 0$ and travelling through a transmission line has the form:

$$V_{\mathrm{in}}(z,t) = |V_0^+| \cos(\omega t - \beta z + \phi^+), \tag{2.10}$$

where z is the position on the line as pictured in Fig. 2.3.2, β is the propagation constant, ω is the frequency of the rf-signal, $|V_0^+|$ is the voltage amplitude and ϕ^+ is the phase angle of the complex voltage V_0^+. Here, we have assumed that the transmission line is lossless.

For simplicity, we can drop the time dependency and express the wave using phasors as

$$V_{\mathrm{in}}(z) = V_0^+ \mathrm{e}^{-j\beta z}. \tag{2.11}$$

Now, we shall see what happens when we terminate the transmission line with an arbitrary load impedance, $Z_{\mathrm{L}}(\omega)$, at $z = 0$. The relation between current and voltage in the line ($z < 0$) is given by the intrinsic impedance, Z_0, that is normally designed to be $Z_0 = 50\ \Omega$. However, at $z = 0$, voltage and current have to satisfy the condition $V(z = 0)/I(z = 0) = Z_{\mathrm{L}}$. To do so, a reflected wave is created, so that the voltage waveform in the line is a sum of the incident and reflected wave:

$$V(z) = V_0^+ \mathrm{e}^{-j\beta z} + V_0^- \mathrm{e}^{j\beta z}, \tag{2.12}$$

related to the current by the factor Z_0:

$$I(z) = \frac{V_0^+}{Z_0} \mathrm{e}^{-j\beta z} - \frac{V_0^-}{Z_0} \mathrm{e}^{j\beta z}. \tag{2.13}$$

At the load position (z=0), the constant of proportionality between voltage and current is Z_L, leading to

$$\frac{V(z=0)}{I(z=0)} = Z_\mathrm{L} = \frac{V_0^+ + V_0^-}{(V_0^+ - V_0^-)} Z_0. \tag{2.14}$$

This way we can extract the relation between the input and output voltages as

$$\Gamma(\omega) = \frac{V_0^-}{V_0^+} = \frac{Z_\mathrm{L} - Z_0}{Z_\mathrm{L} + Z_0}, \tag{2.15}$$

where Γ the reflection coefficient.

When performing rf-reflectometry for charge sensing, Z_L corresponds to the matching network plus the device, as shown in Fig. 2.3.2. Small changes in the sensor impedance are observable by extracting the reflection coefficient at different wave frequencies, ω. This can be done using a vector network analyser (VNA) that compares the incident and reflected power (normally measured in Decibels as $S_{11} = 20\log(V_0^-/V_0^+)$) or with homodyne detection. The latter is specially related to this thesis and a deeper explanation can be found in the experimental methods chapter (Sec. 3.2.2).

In the absence of a matching network, Z_L is equal to the device resistance (usually larger than the quantum resistance $R_Q = 26$ kΩ). In this case, the measurable reflection coefficient, Γ, would be almost one and we would not observe small changes in Z_L.

RESONATOR IMPEDANCE

The combination of matching network and sensor is created to act as a resonator since, near the resonant frequency, small variations of the charge sensor impedance produces large changes in the reflection coefficient.

Any resonator can be transformed into an equivalent LCR circuit, like the one shown in Fig. 2.3.3a, with an inductance L, a capacitance, C, and a resistance, R in series. The equivalent impedance of that circuit is:

$$Z_{\mathrm{L}} = R + j\omega L + \frac{1}{j\omega C}, \tag{2.16}$$

where ω is the frequency in radians ($f = \omega/2\pi$) and j is the imaginary unit.

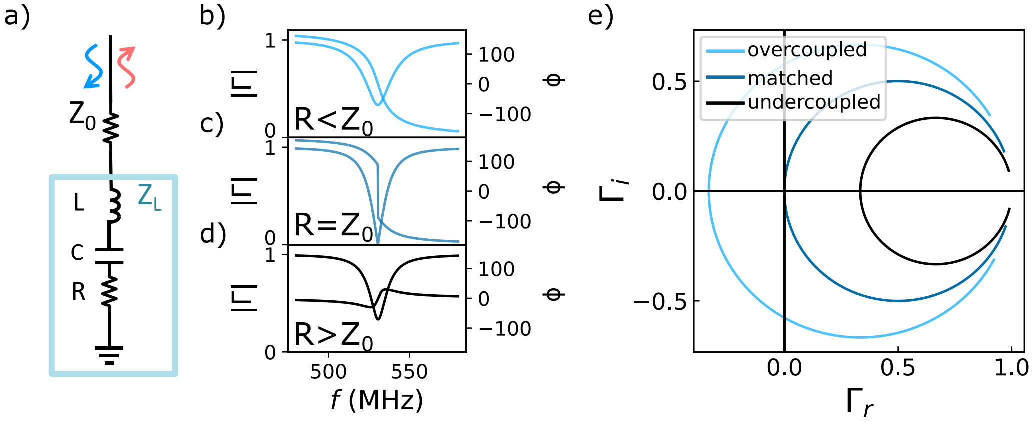

Figure 2.3.3: LCR resonator. a) Sketch of a transmission line terminated in a LCR resonator. b) c) and d) simulation of Γ in phase (ϕ) and magnitude ($|\Gamma|$) in an overcoupled, matched and undercoupled resonator, respectively. e) Reflection coefficient from the resonators simulated in b), c) and d) in cartesian coordinates.

Assuming that the resistance, R, is invariant with respect to the frequency near the resonance frequency, the real part of the resonator impedance stays constant over frequency, whereas the imaginary part (admittance) pass along different values. Such behaviour produces a reflection coefficient with a circular shape in the complex plane when plotted as a function of the frequency. The whole circle, so-called resistance circle, has its center on the real axis $\Im\{\Gamma\} = 0$ and crosses it twice: firstly at the resonant frequency, f_{res}, corresponding to the circle closest point to the origin and a second time when the frequency tends to infinity and zero: $f \to \infty$ and $f \to 0$, at which $\Gamma = 1$ (see circles in Fig. 2.3.3b).

The reflection coefficient in resonators is usually presented in polar coordinates (magnitude, $|\Gamma|$ and phase, $\angle(\Gamma) = \phi$), as shown in Fig. 2.3.3b,c and d). Here, we can observe very clearly how the magnitude has a minimum at the resonant frequency, f_{res}, at which the imaginary part of the reflection coefficient is equal to zero ($\Im\{Z_\mathrm{L}(\omega = 2\pi f_\mathrm{res})\} = 0$). From Eq. 2.16 we can extract that the resonant frequency is:

$$f_\mathrm{res} = \frac{1}{2\pi\sqrt{LC}}. \tag{2.17}$$

One of the factors that characterises the sensor is its bandwidth, which determines how fast a change in the reflection coefficient appears in the reflected signal. This is measured as the full width at half maximum (FWHM) of the lorentzian shape of the resonator magnitude.

The resonator bandwidth is related to the energy lost, which is a combination of the internal losses (within the resonator) and external losses (in the transmission line). To quantify the losses we use the quality factor, Q, defined as the inverse of energy lost in one radian of oscillation [158]. The quality internal and external quality factors are:

$$Q_\mathrm{int} = \frac{1}{R}\sqrt{\frac{L}{C}} \tag{2.18}$$

$$Q_\mathrm{ext} = \frac{1}{Z_0}\sqrt{\frac{L}{C}}. \tag{2.19}$$

The load quality factor is a sum of both lossy channels an it is calculated as:

$$\frac{1}{Q_\mathrm{L}} = \frac{1}{Q_\mathrm{int}} + \frac{1}{Q_\mathrm{ext}}. \tag{2.20}$$

The load Q-factor is related to the resonator bandwidth, B, as:

$$Q_\mathrm{L} = \frac{f_\mathrm{res}}{B}. \tag{2.21}$$

Eq. 2.21 shows the trade-off between having a sharp resonance, very sensitive to Z_L (large Q_L), and the fast bandwidths require for spin measurement (lower Q_L).

The bandwidth can be limited by the external or internal losses. To compare their contribution, we use the so-called coupling, defined as:

$$\beta = \frac{Q_\mathrm{int}}{Q_\mathrm{ext}} = \frac{Z_0}{R}. \tag{2.22}$$

Undercoupled	Overcoupled
$\beta < 1$ $R > Z_0$ $< 2\pi$ shift in $\angle(\Gamma)$ BW limited by resonator	$\beta > 1$ $R < Z_0$ 2π shift in $\angle(\Gamma)$ BW limited by transmission line

Table 2.3.2: Overcoupled and undercoupled resonators. Characteristics of an overcoupled and undercoupled resonator.

Depending on the value of the coupling, β, the resonator is said to be overcoupled or undercoupled. Fig. 2.3.3b,c and d) show the shape of an overcoupled ($R < Z_0$), matched ($R = Z_0$) and undercoupled ($R > Z_0$) resonator in polar coordinates, whereas Fig. 2.3.3e shows the reflection coefficient of the same resonators plotted in the complex plane. In the case of perfect matching, $\Re\{Z_\mathrm{L}\} = Z_0$, the circle is centered at the position $\Gamma = 0.5$ and crosses the origin, leading to $\Gamma = 0$ at f_res. If the resonator is overcoupled ($\Re\{Z_\mathrm{L}\} < Z_0 = 50$), the center of the circle is nearer the origin, making it is radius larger in order to pass through $\Gamma = 1$. In this case, the magnitude of the reflection coefficient $|\Gamma|$ does not tend to zero at the resonant frequency, but it is phase, $\angle\Gamma$, completes a whole 2π rotation as the frequency is varied across f_res. The different characteristics of resonators depending on their coupling are compactly summarised in Table. 2.3.2.

2.3.3 RF-SET AND RF-QPC

To use a QPC or a SET together with rf-reflectometry, one of the leads is connected to the matching network, while the other is grounded. This way, the sensor acts as a resistive element with a setup like the one shown in Fig. 2.3.2.

Although the theoretical limit for charge sensitivity for rf-SETs is 1.4 times worse than for SETs [170], rf-SETs and rf-QPCs are the most sensitive sensors with charge sensitivities reaching 1 $\mu e/\sqrt{\mathrm{Hz}}$ and below [171] and measurement bandwidths in the order of few megahertzs. This is because the high bandwidths allow to work at higher frequencies, where 1/f noise does not play a role. However, rf-SETs and rf-QPCs are still limited by the noise produced during the amplification stages (See Sec. 2.4.2 for more information about noise in amplifiers).

The main disadvantage of rf-SETs and rf-QPCs is that they require two reservoirs located close to the qubit [104], impacting in dense qubit arrays. Moreover, in the case of rf-SETs shot-noise dominates. The shot noise in a SET has the power density $S_{\mathrm{II}} = e\langle I\rangle$, where $\langle I\rangle$ is the average current [172]. Usual values for the average current through a SET are around 1 nA, leading to a corresponding shot-noise temperature of 1.0 K [173]. Due to their sensitivity limitation and its footprint impact, the semiconductor community is moving from SETs towards sensors based on capacitance shifts (dispersive readout), where the readout requires one or no leads. Fig. 2.3.4 shows the effect of capacitive and resistive changes on the resonator reflection coefficient.

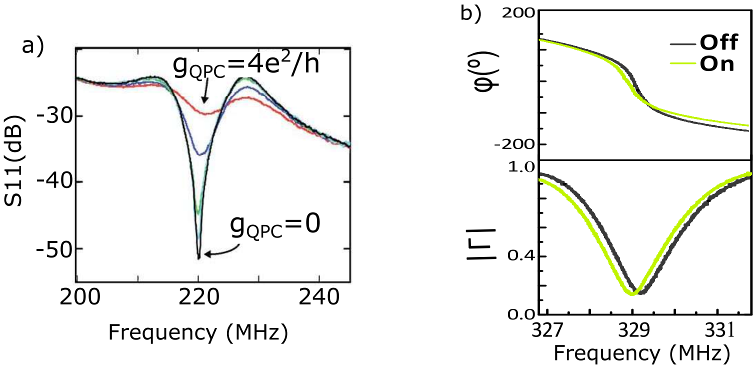

Figure 2.3.4: Dispersive and dissipative charge sensors. a) Magnitude of the reflection coefficient measured as $S_{11} = |\Gamma|^2$ in dB for different values of the QPC conductance. Image retrieved from [174]. b) Reflection coefficient in phase and magnitude of a resonator connected to a SEB at the charge degeneracy (on) and far from it. Retrieved from [175].

2.3.4 SINGLE ELECTRON BOX (SEB)

The single electron box (SEB) is formed by a quantum dot tunnel coupled to a single lead (see Fig. 2.3.5a) [85, 99, 107, 155, 176–178]. The SEB is operated close to the degeneracy between two dot charge states, which for simplicity we considered them to be the dot empty, E_0, and the dot occupied with one electron, E_1. Fig. 2.3.5b shows the energy level as a function of the reduced gate voltage, $n_{\mathrm{g}} = \frac{C_{\mathrm{g}}V_{\mathrm{g}}}{e}$, where V_{g} is the voltage applied to the gate, C_{g} is the gate capacitance and e is the electron charge. At $n_{\mathrm{g}} < 0.5$, E_0 is the ground state, whereas at $n_{\mathrm{g}} > 0.5$, the ground state is E_1.

Both states are related by the tunneling rates between a three-dimensional (reservoir) and a zero-dimensional (dot), which depend on n_g and the electron temperature, T_e, following a Fermi-Dirac distribution as shown in Fig. 2.3.5c, where γ_- is the tunneling rate from dot to reservoir, whereas γ_+ is the tunneling rate from reservoir to dot.

Variations in the SEB complex impedance arise when the dot potential is driven cyclically around $n_\mathrm{g} = 0.5$ by an AC excitation with amplitude $V_\mathrm{g}^{RF}\sin(\omega_\mathrm{rf}t)$. The origin of such variations depends on the relation between the excitation frequency, ω_rf, and the tunneling rate away from the degeneracy, γ_0.

Fig. 2.3.5e describes the case for which $\gamma_0 \sim \omega_\mathrm{rf}$. Starting in $n_\mathrm{g} < 0.5$ in the state E_0, the AC excitation drives the system rapidly to $n_\mathrm{g} > 0.5$ (I). When an electron tunnels into the dot, the system dissipates energy $\Delta E = E_1 - E_0$ (II). Then, the system is driven back to $n_\mathrm{g} < 0.5$ (III), where an electron tunnels out from the dot dissipating energy (IV). The average power dissipated during a cycle is related to a resistance as $P_\mathrm{dis} = (V_\mathrm{g}^{RF})^2/2R_\mathrm{sis}$ [176]. This resistance is called Sisyphus resistance due to its similarity to the Greek myth.

At the same time, the tunneling of electrons produced by the AC excitation creates an excess capacitance in the SEB called tunneling capacitance, $C_\mathrm{t} = \alpha_\mathrm{SEB}\frac{\partial\langle ne\rangle}{\partial V_\mathrm{g}^{RF}}$, where $\langle ne\rangle$ is the average charge in the island [179]. If the tunneling rates are small compared with the thermal energy ($\hbar\gamma_0 < k_\mathrm{B}T_\mathrm{e}$), the tunneling capacitance and Sisyphus resistance are given by [180]:

$$C_\mathrm{t} = \frac{e^2\alpha_\mathrm{SEB}^2}{4k_\mathrm{B}T_\mathrm{e}}\frac{1}{1+{\omega_\mathrm{rf}}^2/{\gamma_0}^2}\cosh^{-2}\left(\frac{\epsilon}{2k_\mathrm{B}T_\mathrm{e}}\right) \tag{2.23}$$

and

$$R_\mathrm{sis} = \frac{2k_\mathrm{B}T_\mathrm{e}}{e^2\alpha_\mathrm{SEB}^2}\frac{1+{\gamma_0}^2/\omega_0^2}{\gamma_0}\cosh^{-2}\left(\frac{\epsilon}{2k_\mathrm{B}T_\mathrm{e}}\right), \tag{2.24}$$

where α_SEB is the SEB lever arm.

As described by these equations, if $\gamma_0 << \omega_\mathrm{rf}$, the tunneling capacitance tends to zero, whereas the Sisyphus resistance tends to infinity. The system is driven so fast that it is locked in one state, so that there is no tunneling and, therefore, no dissipation (see Fig. 2.3.5f). In the opposite situation, where $\gamma_0 >> \omega_\mathrm{rf}$, the system tunnels so fast that the energy dissipation is neglectable ($R_\mathrm{sis} \to \infty$). On the other hand the tunneling capacitance tends to $\frac{e^2\alpha_\mathrm{SEB}^2}{4k_\mathrm{B}T_\mathrm{e}}$.

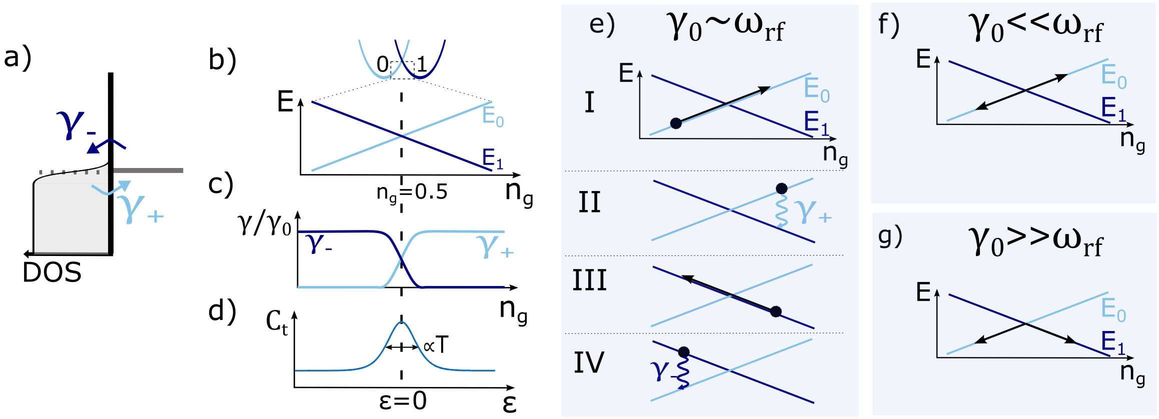

Figure 2.3.5: Working principles of the SEB. a) Sketch of a SEB, formed by a quantum dot tunnel coupled to a reservoir with tunnel rates γ_- and γ_+. b) Energy diagram of the dot zoomed in around the degeneracy point as a function of the reduced gate voltage, n_g. c) Tunneling rates from dot to reservoir, γ_-, and from reservoir to dot γ_+ as a function of n_g. d) Tunneling capacitance as a function of the detuning, ϵ. e) When the system is driven at a frequency similar to its tunneling rates, energy is dissipated as the electron tunnels inelastically from dot to reservoir and vice-versa. f) System driven with a fast AC excitation ($\gamma_0 << \omega_\mathrm{rf}$). g) System driven with a slow AC excitation ($\gamma_0 >> \omega_\mathrm{rf}$). Adapted from [179, 181]

If the tunneling rates are larger than the thermal energy ($\hbar\gamma_0 > k_\mathrm{B}T_\mathrm{e}$), the tunnel capacitance follows the lorentzian:

$$C_\mathrm{t} = \frac{e^2\alpha_\mathrm{SEB}^2}{\pi}\frac{\hbar\gamma_0}{(\hbar\gamma_0)^2+\epsilon^2}, \tag{2.25}$$

while the fast tunneling leads to no dissipation ($R_\mathrm{sis} = \infty$).

The SEB can be used as a charge sensor, since any perturbation of the dynamic equilibrium leads to a change in its complex impedance. To measure changes in the SEB impedance, a resonator is connected either to the gate forming the quantum dot or the reservoir. In this readout method, the rf-tone used to test the reflection coefficient acts as well as the AC excitation that drives the system. Usually, the main contribution to the signal is capacitive due to the fast tunneling rates with the reservoir, although using the Sisyphus resistance variations can increase your signal in some cases. However, the advantage of having no dissipation in the sensor is that the noise produced by the system reduces significantly.

Charge sensing with a SEB has achieved similar charge sensitivities to rf-SETs and rf-QPCs [175, 179, 182, 183], being the minimum 0.25 μeHz$^{-1/2}$ [183]. This readout is not limited by shot noise but by the temperature of the amplifier which can be reduced to 200-250 mK using a Josephson parametric amplifier (see Sec. 2.4).

2.3.5 In-situ readout

In-situ readout does not require an additional charge sensor because the dot charge state is directly measured by connecting the resonator to the gate electrode that controls it. The Sisyphus resistance and tunneling capacitance that arise at the charge states degeneracy points can be used to map the dot occupancy.

In-situ readout is particularly useful for singlet-triplet readout in a quantum dot. In the inter-dot transitions, the system in dynamic equilibrium presents not only the extra contributions from the Sisyphus resistance and tunneling capacitance, but also an additional quantum capacitance, C_Q, that arises from the system being driven through an energy band diagram with non-zero curvature [184, 185].

Singlet-triplet readout is possible because when the system is cyclically driven from the (1,1) to the (2,0) state, tunneling between dots is possible in the singlet state, $S(1,1)$, producing a change in impedance. However, the triplet state $T_0(1,1)$ is stuck in the (1,1) configuration, so that the impedance remains constant.

In-situ readout has demonstrations with charge sensitivities as low as $1.3\mu e/\sqrt{\text{Hz}}$ [175]. Moreover, it has the advantage that it does not require any additional reservoir.

Fig. 2.3.6 summarises the different charge sensors that work with rf-reflectometry, where the blue rectangles represent the leads required by each sensor.

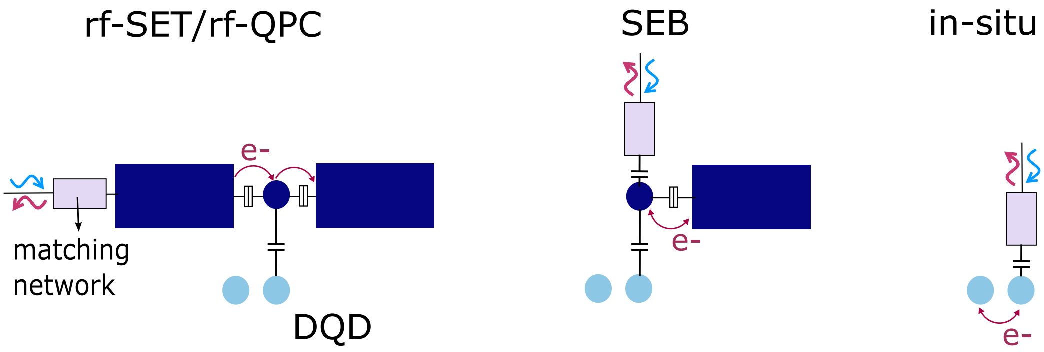

Figure 2.3.6: Charge sensor schematic. Scheme of the different charge sensors used with rf-reflectometry. The blue rectangles represents the reservoirs, whereas the light blue circles are the quantum dots whose charge state is being measured.

2.4 AMPLIFICATION

The delicate nature of quantum effects requires experiments to work with very weak probe signals. Inevitably, the readout signal is, as well, very weak and needs to be amplified. However, amplification comes with a toll: amplifiers not only amplify the signal and its original noise but also add extra noise due to the amplification, reducing the SNR. This section deals with the noise generated due to amplification and its limits for the readout of quantum devices. We deepen into the study of linear parametric amplifiers, like the one used for the experiments performed in this thesis. These kinds of amplifiers are widely popular in the superconducting community [16, 186–190], and further information can be found in theses from the superconducting qubit field [191–193]

2.4.1 NOISE IN AMPLIFIERS

In a linear amplifier, the power of the output signal is linearly proportional to the input signal with a factor G_s ($\sqrt{G_\mathrm{s}}$ in amplitude). If a signal with power P_s^in and corresponding noise P_n^in is fed to a linear amplifier, the associated output signal has a power of $P_\mathrm{s}^\mathrm{out} = G_\mathrm{s} P_\mathrm{s}^\mathrm{in}$ and a noise of $P_\mathrm{n}^\mathrm{out} = G_\mathrm{s}(P_\mathrm{n}^\mathrm{in} + P_\mathrm{n}^\mathrm{amp})$ as is depicted in Fig. 2.4.1.

Noise is characterised by the energy spectral density $S(\omega) \equiv |x(\omega)|^2$, where $x(\omega)$ is the Fourier transform of a noisy time trace ($x(\omega) = \frac{1}{2\pi}\int_{-\infty}^{\infty} x(t)e^{-i\omega t}dt$) [194]. Depending on the source of the noise, its corresponding $S(\omega)$ has a different frequency spectrum. The most common noise in amplifiers is thermal noise, also called white noise. This noise arises due to the thermal excitations of the charge carriers in a conductor and it is constant at every frequency.

We can consider the amplifier as an impedance at temperature T_n that is connected to a matched load, so that the power dissipated by the amplifier is [195]:

$$P_\mathrm{n} = Bk_\mathrm{B}T_\mathrm{n}, \tag{2.26}$$

with a noise spectral density

$$S(\omega) = k_\mathrm{B}T_\mathrm{n}. \tag{2.27}$$

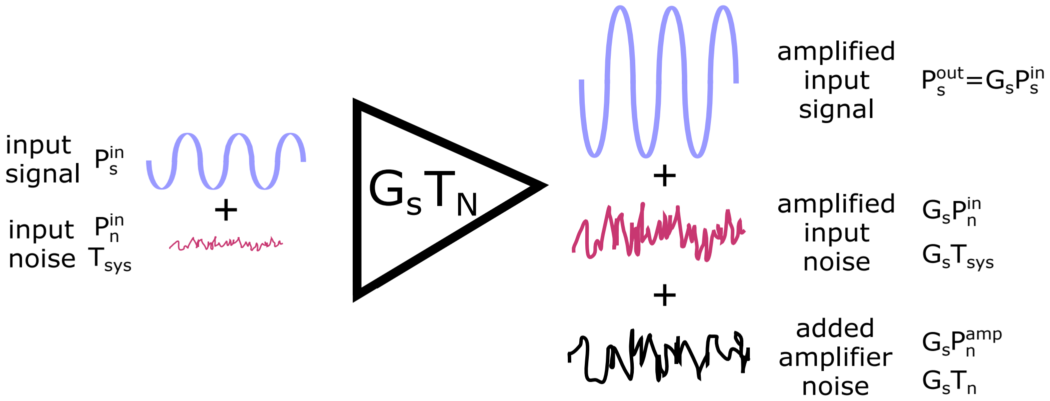
input signal P_s^{in}
input noise P_n^{in} T_{sys}
+
G_sT_N
amplified input signal $P_s^{out}=G_sP_s^{in}$
+
amplified input noise $G_sP_n^{in}$ G_sT_{sys}
+
added amplifier noise $G_sP_n^{amp}$ G_sT_n

Figure 2.4.1: Noise in an amplification process. A linear amplifier creates a copy of the input signal with its amplitude increased by $\sqrt{G_\mathrm{s}}A_\mathrm{signal}$. However, not only the input signal and its corresponding noise are amplified, but also the amplifier adds a noise characterise by T_n, so that the SNR of the amplified signal is smaller than the original signal.

Here, B is the given bandwidth and k_B is the Boltzman constant. This way, the noise at the output of an amplifier is:

$$P_\mathrm{n}^\mathrm{out} = G_\mathrm{s}k_\mathrm{B}(T_\mathrm{sys} + T_\mathrm{n})B, \tag{2.28}$$

where T_sys is the noise temperature of the signal before being amplified.

In cryo-measurements, several amplifiers are put in series to achieve sufficient gain. For two amplifiers in series, the noise power increases as,

$$P_\mathrm{n}^\mathrm{out} = G_\mathrm{s,2}(G_\mathrm{s,1}k_\mathrm{B}(T_\mathrm{sys} + T_\mathrm{n,1}) + k_\mathrm{B}T_\mathrm{n,2})B. \tag{2.29}$$

This way, the effective noise of a large series of amplifiers with respective gain $G_\mathrm{s,i}$ and noise temperature $T_\mathrm{n,i}$ is:

$$T_\mathrm{noise} = \frac{P_\mathrm{n}^\mathrm{out}}{k_\mathrm{B}BG_\mathrm{s,1}G_\mathrm{s,2}G_\mathrm{s,3}...} = T_\mathrm{sys} + T_\mathrm{n,1} + \frac{T_\mathrm{n,2}}{G_\mathrm{s,1}} + \frac{T_\mathrm{n,3}}{G_\mathrm{s,1}G_\mathrm{s,2}} + ... \tag{2.30}$$

For large gains, $G_\mathrm{s,i}$, the noise temperature depends mainly on the temperature from the first amplifier, which shows the importance of using a first amplifier that does not add much extra noise and can work at very low temperatures. For this purpose, cryo-experiments commonly use commercial high-electron-mobility-transistors amplifiers (HEMTs), which work at 4K, limiting the system noise temperature to a few Kelvin. Alternatively, superconductor parametric amplifiers can operate at lower temperatures thanks to their dissipation-less transport [187, 190]. These kinds of amplifiers, and specifically the Josephson parameter amplifier (JPA), are discussed in the following sections.

Other amplifiers can also work at hundreds of milliKelvin by exploiting different physical properties. Some examples are the quantum varying capacitance of semiconducting quantum dots [196], photon detectors [197], non-linear cavities [198], and SETs [199, 200] and QPCs coupled to planar superconducting resonator [201].

2.4.2 Noise quantum limits

Eq. 2.27 seems to reflect that, as we reduce the amplifier temperature, the amplification noise is also decreased. This holds up to a point, in which the amplification noise is dominated not by the temperature, but by quantum effects. Such effects can be modelled with the fluctuation and dissipation model [202], leading to a noise power density [203]:

$$S(\omega) = \frac{\hbar\omega}{2}\coth\left(\frac{\hbar\omega}{2k_\mathrm{B}T}\right) \tag{2.31}$$

with an equivalent noise temperature

$$T_\mathrm{eff} = \frac{S(\omega)}{k_\mathrm{B}} = \frac{\hbar\omega}{2k_\mathrm{B}}\coth\left(\frac{\hbar\omega}{2k_\mathrm{B}T}\right) \tag{2.32}$$

For experiments at high temperatures, we find that $T_\mathrm{eff} = T$. However, in cryo-experiments the noise effective temperature approaches to $T_\mathrm{eff} = \frac{\hbar\omega}{2k_\mathrm{B}}$ as it is shown in Fig. 2.4.2. When the amplification noise is equal to the effective temperature, the amplifier reaches the quantum limit. Amplification below the quantum limit is still possible under certain circumstances, as is exemplified in Sec. 2.4.4. In the experiments performed in this thesis, the frequency is 600-800 MHz. Consequently, the effective temperature is $T_\mathrm{eff} \approx 13 - 17$mK, similar to the real temperature ($T \approx$ 10mK). However, for higher frequency experiments, quantum effects dominate.

The quantum noise limit can be understood in terms of Heisenberg's uncertainty principle. Two non-commutating operators can only be measured up to a certain level of accuracy given by Heisenberg's inequality [204]. The most common example is the position and momentum of a particle, whose uncertainties Δx and Δp follow

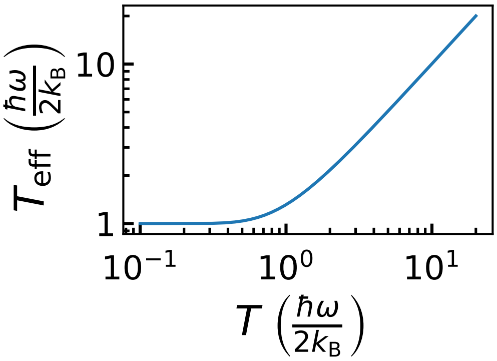

Figure 2.4.2: Effective temperature. Effective temperature as a function of the physical temperature in units of $\frac{\hbar\omega}{2k_{\mathrm{B}}}$. For $T < \frac{\hbar\omega}{2k_{\mathrm{B}}}$, the effective temperature tends to $\frac{\hbar\omega}{2k_{\mathrm{B}}}$. On the other hand for $T > \frac{\hbar\omega}{2k_{\mathrm{B}}}$, $T_{\mathrm{eff}} \sim T$

the inequation:

$$\Delta x \Delta p \geq \frac{\hbar}{2}. \tag{2.33}$$

In the quantum mechanical formulation of the electromagnetism, $\hat{I}$ and $\hat{Q}$ are non-commuting operators $[\hat{I}, \hat{Q}] = i$ and, therefore, cannot be accurately known at the same time. So, quantum fluctuations can be thought of as an area of uncertainty in the I/Q-plane [205, 206]. The additional quantum noise added by the amplifier can be understood as a process in which the amplifier measures both quadratures to create an amplified copy.

In the case of phase-sensitive amplification, only one of the quadratures is amplified, reaching noise temperatures below the quantum limit (See 2.4.4). Phase-sensitive amplification is useful when all the information can be projected in a single quadrature.

2.4.3 PARAMETRIC AMPLIFICATION

In parametric amplification, one parameter is varied harmonically in a non-linear medium to create some gain. The energy used to modulate the parameter is called the pump. One easy example of a parametric amplifier is a child on a swing. The legs of the child would act as the pump that varies its centre of gravity at twice the resonant frequency of the swing. The pump energy is then transferred to both of the degenerate normal modes of the swing ($e^{\pm i\omega t}$), increasing the swing oscillation amplitude.

This way, a parametric amplifier works as a mixer, in which part of the pump energy couples with two frequency modes (signal and idler) [207]. Depending on the frequency relation between pump, signal and idler, parametric amplifiers are classified as three-wave amplifiers and four-wave amplifiers. In three-wave amplifiers, one photon from the pump is transferred to the signal and idler and their frequencies follow the relationship:

$$\omega_{\text{pump}} = \omega_{\text{signal}} + \omega_{\text{idler}}. \tag{2.34}$$

On the other hand, in a four-wave amplifier, two photons from the pump are transferred to the signal and idler, so

$$\omega_{\text{pump}} + \omega_{\text{pump}} = \omega_{\text{signal}} + \omega_{\text{idler}}. \tag{2.35}$$

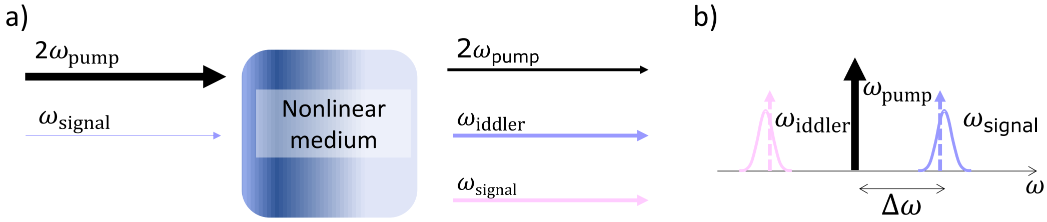

Figure 2.4.3: Four-wave amplifier. a) Sketch of a parametric amplifier working in a four-wave mode, where 2 photons of the pump mode are transferred to the weak signal mode and an extra idler mode is created for energy conservation. b) Fourier transform of the amplified output, with idler and signal placed symmetrically with respect to ω_{pump}.

In terms of quantum mechanics, the relation between the frequency modes is equivalent to the conservation of energy, being $E = \hbar\omega$, where $\hbar$ is the reduced Planck's constant.

In the following sections, we will focus on the four-wave amplifier, since most resonant-JPAs work in this mode. In the case where $\omega_{\text{signal}} = \omega_{\text{idler}}$, the amplifier is called degenerate. Such amplifiers are phase sensitive meaning that only the part of the signal that is in phase with the pump is amplified. This effect is called "squeezing" and leads to amplification beyond the quantum limit. On the other hand, if $\omega_{\text{signal}} \neq \omega_{\text{idler}}$ the amplification is phase preserving, so the shape of the signal wave is conserved, but the amplification will generate necessarily some noise due to quantum fluctuations.

2.4.4 JOSEPHSON PARAMETRIC AMPLIFIER (JPA)

To create a parametric amplifier, we need a resonator that includes a non-linear element. This is the case of the Lumped Josephson Parametric Amplifier (JPA), which in its simplest model is formed by two Josephson junctions forming a SQUID in parallel with a fixed capacitance as is shown in Fig. 2.4.4. The SQUID is modelled as a single Josephson junction with critical current I_0 whose inductance can be modulated by the flux applied to the loop. The model includes the shunted capacitance, C, and Z_0 accounting for the impedance of the microwave environment.

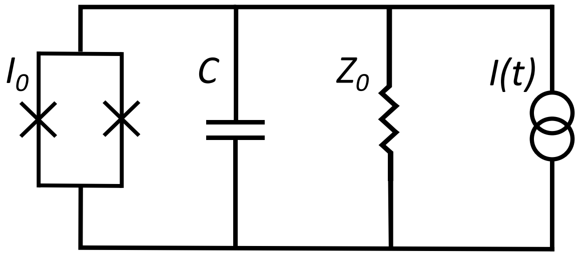

Figure 2.4.4: Schematics of the LJPA. Model of a LJPA consisting on a SQUID that is included in the equations as a single Josephson junction with tunable frequency, a shunted capacitance C and an impedance Z_0. To study its dynamics, the LJPA is connected to a current source with output $I(t)$.

The inductance from the Josephson junction goes as $L_\mathrm{J} = \frac{h/2e}{2\pi I_0 cos(\delta)}$, where δ is the phase difference across the Josephson junction. This way, when applying some power at the pump frequency mode ω_pump, the JPA inductance is varied at a rate $2\omega_\mathrm{pump}$ (See Appendix B for the whole mathematical description). Changes in the inductance modify the JPA resonant frequency since $\omega_\mathrm{JPA} = \frac{1}{\sqrt{L_\mathrm{J} C}}$.

For low powers applied to the JPA, ($P_\mathrm{JPA} \propto {I_\mathrm{d}}^2 << {I_0}^2$) the resonant frequency is constant and equal to $\omega_\mathrm{JPA,0}$. As the pump power is increased, the ω_JPA moves to lower frequencies and the resonance becomes sharper (See Fig.2.4.5). This is the regime in which parametric amplification can be performed, where the Josephson junction inductance creates a non-linear dependency between the reflected phase and the driving power.

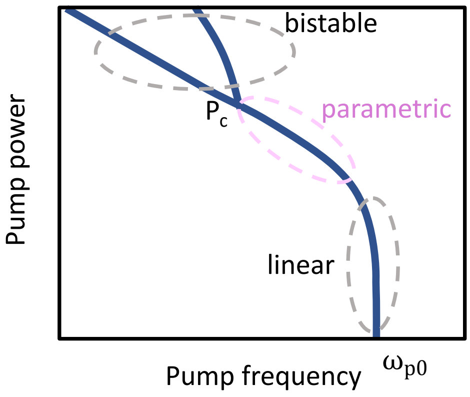

Figure 2.4.5: LJPA working principle. At low pump powers the JPA resonant frequency is constant as a function of the power. As the power increases, the resonant frequency bends to lower frequencies due to the non-linearity of the Josephson inductance. This is the power range at which parametric amplification can be realised. Above P_c, the resonance becomes bistable.

Above a certain critical power, P_c, the system becomes bistable. This corresponds to the conditions in which the equation that describes the JPA behaviour (Eq.B.5 in Appendix B) has three real solutions. This is the working regime of the Josephson Bifurcation Amplifier (JBA) [186].

JPA PARAMETRIC AMPLIFIER REGIME

Amplifiers are normally characterised by their transfer function, in which a small modulation of some input parameter leads to a large modulation of another. For example, in the case of field-effect transistors, a small modulation of the gate voltage can lead to a proportional large modulation in the source/drain current [208].

The JPA can work as an amplifier when connected to a transmission line in reflection (See Fig.2.4.9). Opposite to common resonators, in which the reflected phase is constant as a function of the power applied, in a JPA, the non-linear Josephson junction makes ω_JPA dependent on the pump power. This dependency produces the JPA transfer function, that correlates the input pump power with its reflected phase (See Fig. 2.4.6).

If the pump power is set at the steepest point of the transfer function, any modulation of the pump power leads to a large response in its reflected phase. If the variations of the pump power are small, the reflected phase response is proportional to them (See Fig. 2.4.6a). However, for larger power variations, the JPA saturates,

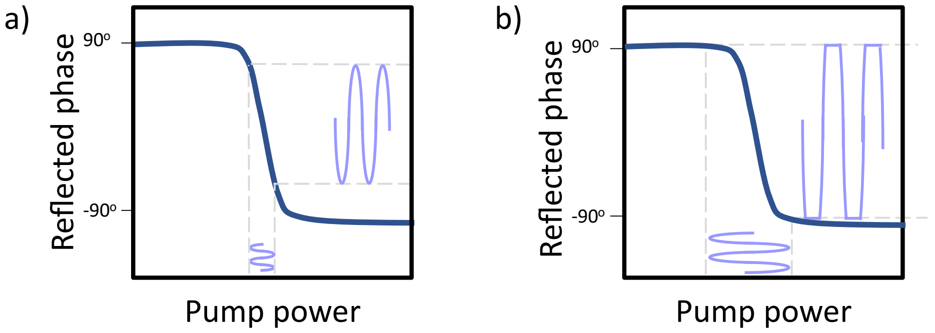

Figure 2.4.6: JPA transfer function. a) For small signal powers within the dynamic range, the input power signal is amplified linearly. b) For powers larger than the dynamic range, the JPA saturates cutting off the edges of the output reflected phase.

leading to a reflected phase that is cut off at the edges of the transfer function (See Fig. 2.4.6b). The range of power for which the response is linearly proportional to the input modulation is called the dynamic range.

If the signal power is larger than the dynamic range, the gain defined as $G_\mathrm{s} = \frac{P^\mathrm{out}_\mathrm{signal}}{P^\mathrm{in}_\mathrm{signal}}$ decreases, since there is not enough pump energy to be transferred from the pump to the signal and idler. This effect can be observed in Fig. 4.4.3a). For this reason, the dynamic range is also defined as the $P^\mathrm{in}_\mathrm{signal}$ at which the G_s decreases by 1dB.

Phase preserving and phase sensitive amplification

To explain the amplification process in terms of the I/Q-plane, we first explore the case in which the JPA works as a doubly degenerate amplifier ($\omega_\mathrm{pump} = \omega_\mathrm{idler} = \omega_\mathrm{signal}$). If the signal is in phase with the pump mode, changes in the signal amplitude will lead to changes in the pump amplitude of the same magnitude (see Fig. 2.4.7a). On the other hand, if the signal is in quadrature with the pump mode, their amplitudes need to be added in quadrature, so that changes in the signal amplitude produce a smaller variation in the pump (see Fig. 2.4.7c). Consequently, while the signal in phase with the pump tone is amplified, the signal in quadrature is de-amplified. Any noise that the signal has, will only be amplified in one of the quadratures so that the SNR will be the same before and after amplification. Therefore, phase-sensitive amplification can go below the quantum limit, being virtually possible to amplify without adding any extra noise (noiseless amplification). The only issue with phase-sensitive amplification is that it is only applicable in situations where the information encoded in the signal can be projected into one axis.

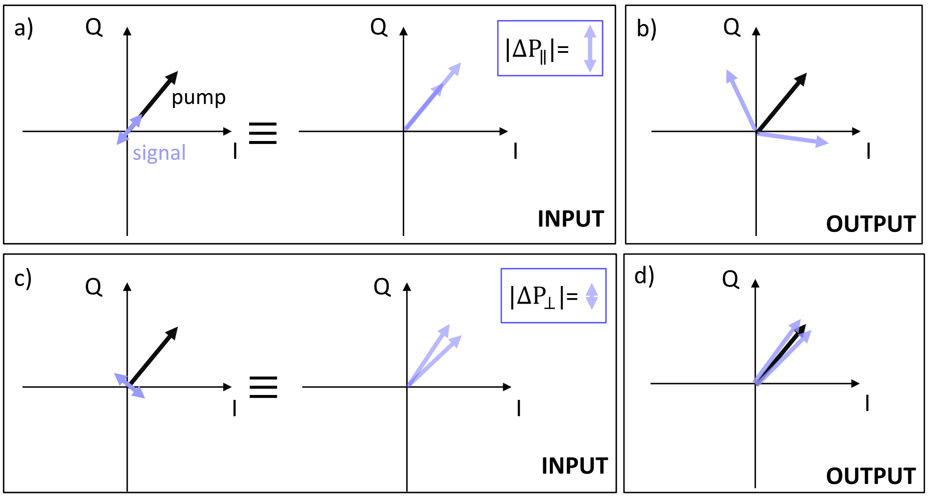

Figure 2.4.7: Phase sensitive amplification. a) Left: signal (purple) and pump (black) in parallel. Right: pump vector modified by the signal. The changes in pump power $\Delta P_{||}$ due to the signal are of the same magnitude as the signal. b) Signal amplification is achieved since the distance between vectors after the amplification is much larger than before. c) Left: signal and pump in quadrature. d) Addition of signal and pump. The variation of the pump power, $\Delta P_{\perp}$ is smaller, so there is no amplification in the output shown in d).

In the case where $\omega_{\text{pump}} \neq \omega_{\text{signal}}$ the amplification is phase preserving and extra noise will be added due to quantum fluctuations. If the pump and signal modes are presented in the I/Q-plane using the pump tone rotating frame, the signal tone will look like a vector that rotates counterclockwise with an angular velocity $\Delta\omega t$. When $\Delta\omega$ is small enough so the signal frequency is within the JPA amplification bandwidth [192], the signal is added as a slow modulation of the pump tone and can be amplified. At any moment, the signal can be separated into two quadratures in parallel and perpendicular to the pump mode whose magnitude fluctuates in time as $\cos(\Delta\omega t)$ and $\sin(\Delta\omega t)$. One could argue that the amplification can also be noiseless since only the part of the signal parallel to the pump is amplified. However, since $\omega_{\text{pump}} \neq \omega_{\text{signal}}$, there is also an idler mode that is amplified, which rotates at $-\Delta\omega t$ (see Fig. 2.4.8). The output amplified signal includes the amplified vacuum fluctuations at the idler and signal frequency, being, therefore, not noiseless. Phase preserving mode cannot go below the quantum limit but the output signal retains

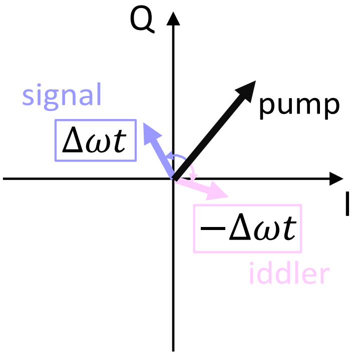

Figure 2.4.8: Phase preserving amplification. I/Q-plane in the rotating frame of the pump tone. The signal mode rotates at a rate $\Delta\omega t$. At any time, only the part of the signal that is parallel to the pump is amplified. At the same time, energy conservation requires the creation of an idler mode, since $\omega_{\text{pump}} \neq \omega_{\text{signal}}$. Such a mode rotates at a rate $-\Delta\omega t$ and it is also amplified, creating noise in the amplification process.

both its phase and amplitude information.

2.4.5 Superconducting parametric amplifiers for qubit readout

This is a quick review of the use of Josephson parametric amplifiers, their current challenges and possible applications for semiconducting spin qubits. For more complete reviews on superconducting parametric amplifiers, we direct the reader to Refs. [16, 190] and the slightly older review [187]

Parametric amplification using Josephson junctions has been known since the 60-70s [209, 210], but it was not until the creation of the dispersive readout in superconducting qubits [211] that it became popular [186, 212–214]. Such readout, and its posterior application to semiconductor qubits, requires a microwave amplification chain that adds the minimum extra noise to the signal.

As explained in the previous section, the first amplifier is the one that determines the noise added by the amplification chain. Therefore, the goal is to place it at the lowest temperature stage. However, in the coldest part of a dilution fridge ($\sim$ 10 mK) the cooling power is very low ($<<$ 1 mW), posing hard restrictions on the electronics heating. The most common amplifier, with the advantage of being completely straightforward to use, is the High- electron-mobility-transistor (HEMT). Nevertheless, HEMTs dissipate heat, making their operation at such low temperatures impossible. On the other hand, superconducting parametric amplifiers are perfect to tackle this challenge due to their dissipation-less transport.

Most Josephson parameter amplifiers are based on the reflection resonant-JPA set-up laid out in [215], in which pump and signal are input and output through the same port (See Fig. 2.4.9a). The Josephson junctions are normally placed in a SQUID configuration so the JPA resonant frequency ($\omega_{\mathrm{JPA},0}$) can be tuned by the magnetic flux through the SQUID [213]. Such amplifiers, are not only relatively easy and cheap to design and fabricate, but also routinely achieve amplification near and below the quantum limit [216]. Some of the active work in resonant-JPAs is trying to increase the bandwidth for linear amplification, which at the moment, for a gain of $G_{\mathrm{s}} \sim 20$ dB, has typical values of 10 MHz [190], although, using alternative Josephson junction circuit topologies, bandwidths of up to 700 MHz have been demonstrated [217]. A different option to increase the space in amplifiable frequency is to include different resonances in the JPA [218], as depicted in Fig. 2.4.9b.

Another challenge in using resonant-JPAs for qubit readout is the signal power that the JPA can handle before the gain starts decreasing (dynamic range). Usual values are -120 dBm [190], but ongoing work is trying to increase such numbers [219–222], reaching a maximum of -90 dBm [219].

Moreover, resonant-JPAs require isolation between the device under test and the JPA input port. Therefore, cryo-circulators of non-neglectable physical size need to be placed in the very demanded fridge space, which also increases the insertion losses of the already weak input signal.

The narrow amplification bandwidth in resonant-JPAs due to the presence of a cavity motivated the development of travelling wave parametric amplifiers (TWPAs). TWPAs have the advantage of having higher bandwidths, not requiring a specific circulator and having higher saturation powers. For example [223] demonstrated a bandwidth of 4 GHz with a saturation power of -52dBm at a Gain of 10dB.

The main reason why TWPAs are not yet the standard superconducting amplifier is because of their rather daunting design and fabrication. Their complexity makes TWPAs noisier than their resonant-JPAs counterparts, being the minimum noise reported two times the standard quantum limit [224]. There are two kinds of TWPAs depending on whether the parametric amplification is based on the non-linearity of high kinetic inductance in disordered superconducting materials (KTWPAs) [223], or on Josephson junctions (JTWPAs) [225]. Fig. 2.4.9d shows the sketch of a JTWPA

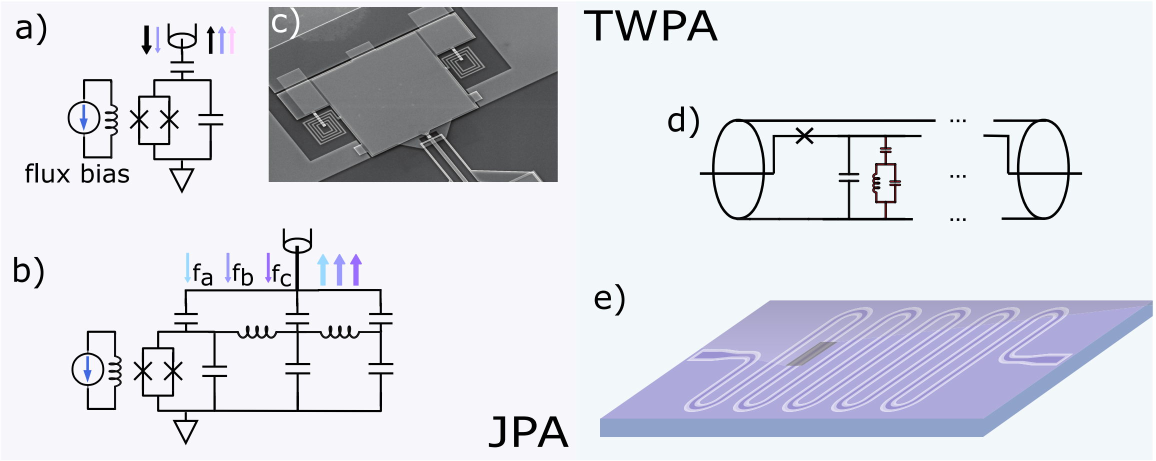

Figure 2.4.9: Josephson junction based amplifiers. a) Sketch of a basic resonant-JPA with a flux tunable resonant frequency. b) Same with three resonant frequencies (f_a, f_b and f_c) for multiqubit readout. c) Scanning electron micrograph of the device in b) showing the Nb wiring that forms the Josephson junctions and inductors. Image retrieved from [218]. d) Sketch of a TWPA with Josephson junctions in series. Signal and idler are amplified as they travel along the TWPA e). Image retrieve from [190].

made as a chain of Josephson junctions.

APPLICATIONS OF SUPERCONDUCTING PARAMETRIC AMPLIFIERS IN SEMICONDUCTOR QUBITS

The development of Josephson based amplifiers has been driven in academia as a means to an end. For this reason, they are more difficult to use than HEMTs, which can be added as a black-box to a given setup, requiring its own dedicated setup (for an example of JPA tuning for amplification Sec. 4.4.1).

The main limitation when using a JPA in a dispersive readout for semiconductor qubits is that the dynamic range of JPAs is lower than the signal powers commonly used in previous reflectometry measurements (−90 to −80 dBm)[179]. Resonators with higher Q-factor reduce the necessary power of the probe signal for readout, making JPAs compatible with dispersive readout (See Sec. 4.2.3 for more information).

JPAs in conjunction with a SEB have been used for charge sensing in semiconductors in [226] and [86], improving the SNR by a factor of x2000 and x10, respectively.

We would like to emphasise that, using an ultra-low noise amplifier, such as JPA or a TWPA, would only increase the SNR if the main source of noise comes from the first amplifier. If the noise is dominated by shot-noise in the device (as with rf-SETs [147]), there will not be any observable change. On the other hand, SEBs show Sisyphus noise, which vanishes when the tunneling between the SEB and the reservoir occurs adiabatically ($\gamma_0 >> f_{\mathrm{rf}}$) [179]. In this case, the noise is dominated by the first amplifier and the addition of the JPA has a real impact on the SNR.

3

Experimental methods

This chapter introduces the experimental techniques applied in this work. It includes a brief explanation of the silicon nanowire devices, followed by a description of the setup, including the method employed for performing rf-measurements. The chapter finishes describing the approach followed to generate fast pulses and reduce the setup noise.

3.1 DEVICE DESCRIPTION

The devices used in this thesis are field-effect MOS transistors made of a fully depleted silicon nanowire. The transistors were fabricated in an industrial cleanroom (CEA-Leti) using 300-mm silicon on insulator (SOI) wafers with a 145-nm-thick buried oxide [74, 155, 227, 228]. The active silicon is shaped into a nanowire using active mesa patterning. To create the transistor gates, the active silicon is firstly thermally oxidised to act as the gate dielectric (6 nm of thermal SiO_2/Si). Then, the gates are deposited with a stack consisting of 50 nm Poly-Si and 5 nm TiN. After this process, a 7 nm thickness silicon nanowire remains below the gate.

To shape the gates, a hybrid Deep Ultra Violet/Electron Beam Lithography and etching of the gate hard mask was performed before transferring the dense pattern into the rest of the stack. The simplest gate pattern design is made of a single wrap-around gate split in two (see Fig. 3.1.1a). This design can be extended by replicating the split-gate shape along the nanowire, forming a 2D array of quantum dots as shown in Fig. 3.1.1b.

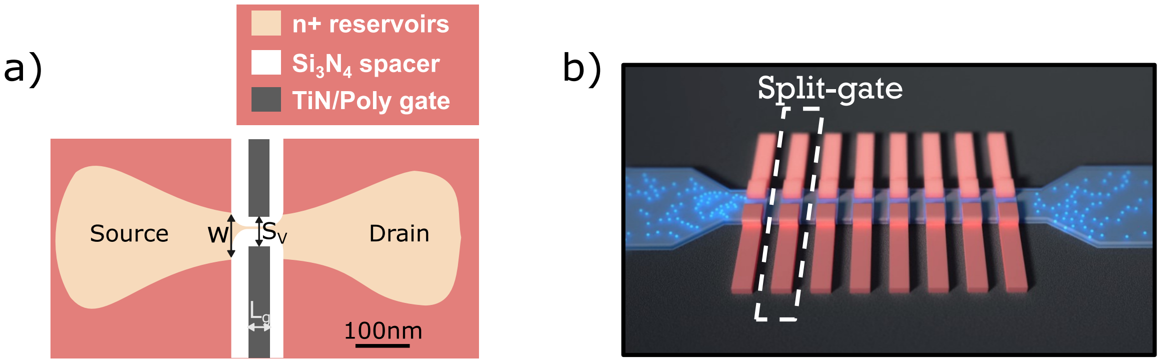

Figure 3.1.1: Device. a) False-color transmission electron micrograph of a silicon nanowire with a pair of split gates fabricated and designed in CEA-Leti. One of the gates is larger than the other due to a systematical misalignment of 7 ± 3 nm in the placement of the gates on the Si channel b) Artistic representation of a multiple split-gate nanowire.

After gate-etching, the nanowire is covered by 34 nm-wide Si_3N_4 spacers. On one hand, the spacer separates the reservoirs from the central part of the intrinsic nanowire, protecting the intrinsic silicon from the posterior ion implantation, which defines the reservoirs. And, on the other hand, it also covers the split between the independent gates since the spacer length is larger than half of the inter-gate gap. The reservoirs are then n-doped by Arsenic/Phosphorus implantation. The process is completed after an activation spike anneal, salicidation (NiPtSi), contacts and metallisation (see Fig. 3.1.2 for a summary of the device fabrication).

At low temperatures, quantum dots are formed on the upper corners of the nanowire, whose electrochemical potential can be independently controlled by the voltage applied to the gates above them. Although, in order to reach single electron confinement, the gate pitch is required to be of the order of 50 nm. The transistors characterised during this thesis were single and double split gate transistors with the

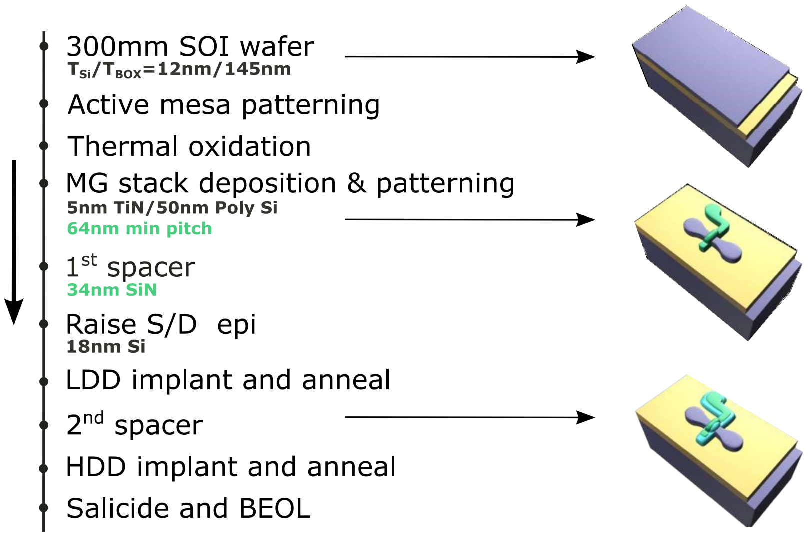
300mm SOI wafer
T_{Si}/T_{BOX}=12nm/145nm
Active mesa patterning
Thermal oxidation
MG stack deposition & patterning
5nm TiN/50nm Poly Si
64nm min pitch
1st spacer
34nm SiN
Raise S/D epi
18nm Si
LDD implant and anneal
2nd spacer
HDD implant and anneal
Salicide and BEOL

Figure 3.1.2: Device fabrication. Simplified process flow for the device fabrication and images of the initial wafer (up), the patterned nanowire with a wrap around gate without (middle) and with (down) spacers. Image adapted from [229]

dimensions summarised in table. 3.1.1.

For further control, the silicon substrate can be used as a back-gate and an overarching metal line as a top gate. These two gates modify the dot electron wave function [107, 230] and, therefore, the tunnel rates between dots and dots to reservoir. Changes in the voltage applied to the metal line require stabilisation for a few days, however, the new properties remain constant and stable for extended periods.

Finally, half of the nanowire along its longitudinal axis is lightly Bi doped with a dose of $6 \cdot 10^{10}$ at/cm^2. This gives an average of approximately one Bi dopant per window of 40 nm $\times$ 40 nm. However, the Bi donors were not used in the experiments presented here.

3.1.1 Device advantages

One of the advantages of these devices is that they have moved from bespoke processes in university cleanrooms to well-controlled facilities operating with 300-mm fabrication techniques, which could satisfy the demand to create uniform and reproducible quantum dots.

Moreover, the nanowire geometry is especially relevant since modern CMOS foundries

Single split gate devices		
W (nm)	L_{g} (nm)	S_{V} (nm)
80	**40**	**50**
70	**40**	**40**
80	60	50
70	50	40

Double split gate devices			
W (nm)	L_{g} (nm)	S_{V} (nm)	S_{H} (nm)
70	**50**	**40**	**50**
70	40	40	40
80	60	50	60
70	40	60	40
70	60	40	50

Table 3.1.1: Device dimensions. Dimensions of the devices characterised during this thesis in which a quantum dot was formed under each gate. Each row corresponds to a given device and W is the nanowire width, L_{g} is the gate length, S_{V} is the separation between the gates facing each other and S_{H} is the separation between parallel gates (see Fig. 3.1.1). The devices with their dimensions in bold are the ones in which spin readout was performed.

like Samsung, TSMC or Intel, have moved from planar MOS to patterned Si technology such as finFET, nanowireFET or Gate-All-Around structures [231–233]. Furthermore, this design is highly scalable, being able to form quantum dots with a single gate, (as opposed to combinations of depletion/accumulation gates required in planar structures) and, as we shall see later, still gives electron spin relaxation times of the same order of planar structures.

3.1.2 PCB

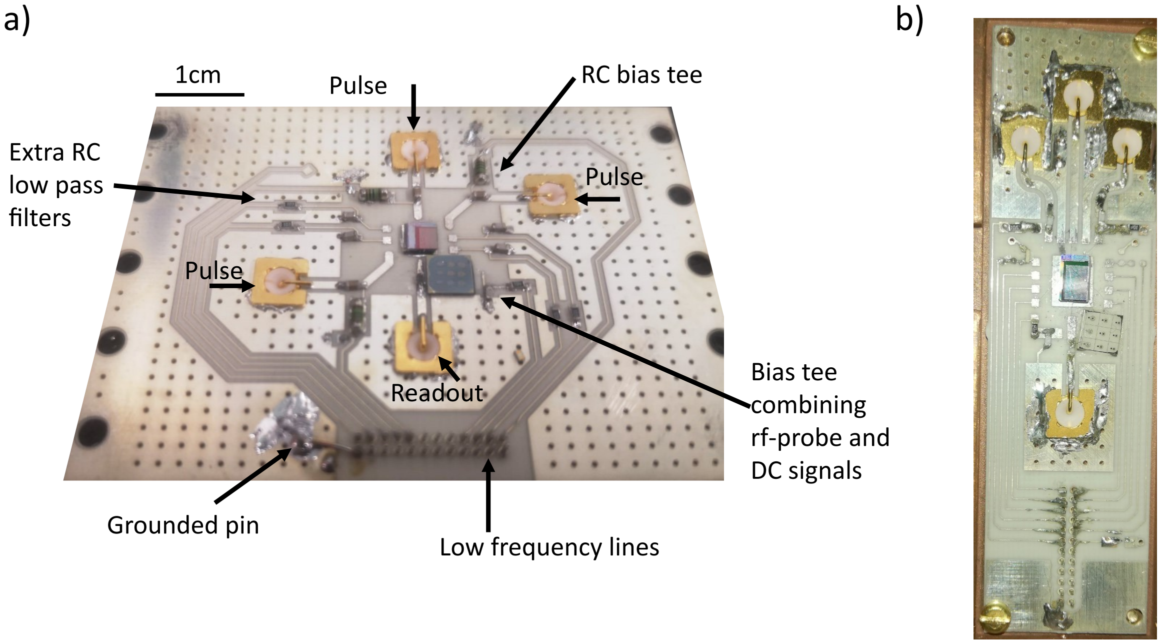
a)
1cm
Pulse
RC bias tee
Extra RC low pass filters
Pulse
Pulse
Readout
Bias tee combining rf-probe and DC signals
Grounded pin
Low frequency lines
b)

Figure 3.1.3: PCBs. a) PCB with three fast lines for pulsing and one fast line for readout. The fast lines are combined to low frequency lines using bias tees. The bias tee used in the readout line has a large capacitance (C_{G} =100 nF with model CC0603JRNPO9BN101) to provide a fast path to ground for the rf-probe frequency. This PCB can provide DC voltages to up to 8 gates. All of the low-frequency lines include extra low pass filters (~1-10kHz) to protect the device from EST during bonding and loading. b) Similar PCB without the extra low pass filters for source and drain.

The silicon wafer in which the devices are located is conveniently cut into chips with dimensions of the order of 10x10 mm^2. The chip, with around 50 transistors, is stuck on a printed circuit board (PCB) with silver paste. Since this glue is also conductive, DC voltages can be applied to the transistors back gate. To provide electrical connections between the device gates and the fridge lines, the transistor electrodes are connected to the PCB contacts via on-chip aluminium bond wires.

The PCB is made from 0.8 mm thick RO4003C for improved high-frequency performance and the tracks have an immersion silver finish to facilitate bonding. The design consists of multiple low-frequency lines connected to the fridge using simple Molex pin connectors and high-frequency lines terminated in SMP connectors. The high-frequency lines are coplanar waveguides matched to 50 Ω. The line used to carry the radio-frequency readout signal has the shortest length to reduce the parasitic capacitance.

High-frequency and DC signals were combined using on-PCB bias tees formed by multilayer ceramic capacitors of 100 nF (TDK CGA3E2C0G1H103J080AA) and thin-film resistors of between 100 kΩ-1 MΩ for the device gates and 10 kΩ for source and drain (Panasonic ERA3APB104V). All the low-frequency lines, included the ones connected to source and drain, have this RC configuration that acts as an extra on-PCB low pass filter (∼1-10kHz). This filter offers protection against electrostatic discharges (EST), a common cause of device malfunction when bonding and connecting the PCB to the chip.

The PCB also holds the elements that form the resonator such as the inductor chip and the coupling capacitor, which is made of a surface-mount thin-film silicon capacitor of 50 fF (Kyocera AVX 04021JR05Z4STR\500).

3.2 MEASUREMENT SETUP

Measurements were performed at base temperature (17 mK) in a Bluefors LD dilution refrigerator. As shown in Fig. 3.2.1, the fridge has different cooling stages, each one with a different cooling power. The device sits on the coldest stage of the cryostat where the cooling power is < 1 mW.

The control signals generated at room temperature need to be carefully attenuated and filtered in their way to the device to not perturb the quantum state. The DC voltages and slow signals are delivered through twisted pairs forming a loom, which is thermalised at different stages to reduce its noise temperature and filtered with RF and RC Qfilters in the mixing chamber to remove high-frequency noise. These lines can carry DC and low-frequency signals of up to 100 kHz.

The radio-frequency signal for gate-based readout and the fast pulses are delivered through semi-rigid coaxial lines. The fast pulses are sent through CuNi-CuNi coaxial wiring with SMA connectors and can transport signals up to 18 GHz. On the other hand, the rf-probe used for reflectometry travels through flexible grapho coaxial wires, which work well up to a few GHz. All the fast lines are thermalised at different cooling stages using attenuators mounted to the thermal plate (see Fig. 3.2.1). Moreover, additional attenuators can be added at room temperature to reduce the noise from the rf-source, which is usually larger than room temperature.

3.2.1 RF-REFLECTOMETRY SETUP

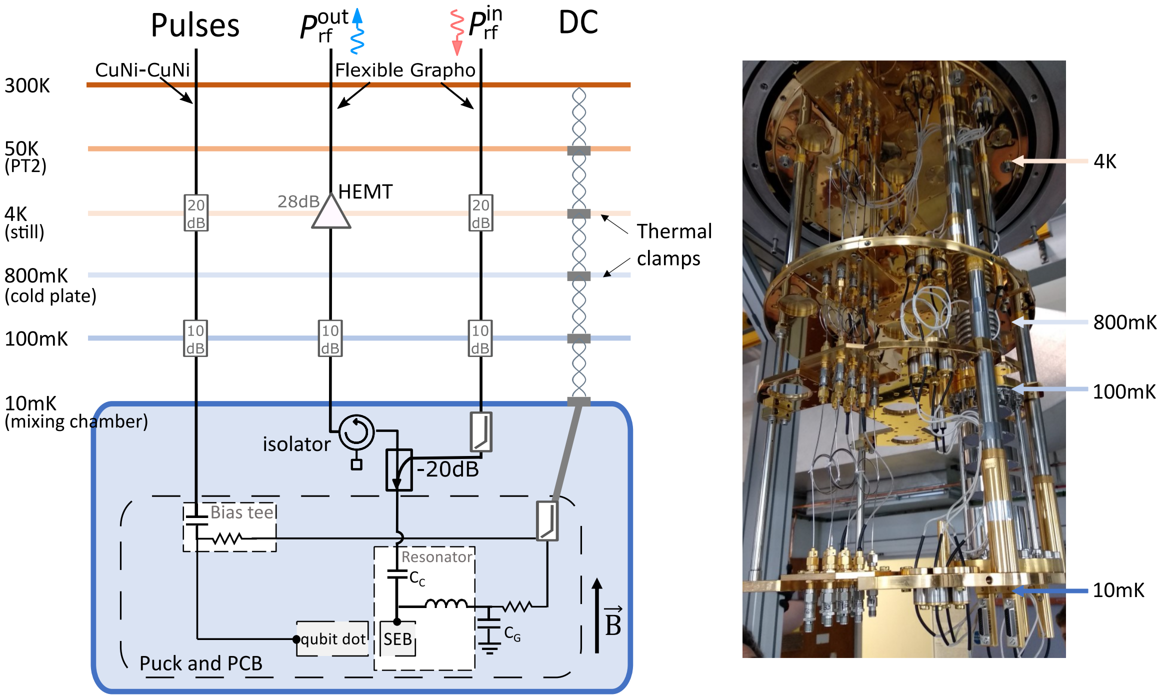
Pulses
P_{rf}^{out}
P_{rf}^{in}
DC
CuNi-CuNi
Flexible Grapho
300K
50K
(PT2)
4K
(still)
800mK
(cold plate)
100mK
10mK
(mixing chamber)
20 dB
28dB
HEMT
20 dB
Thermal clamps
10 dB
10 dB
10 dB
isolator
-20dB
Bias tee
Resonator
C_C
C_G
qubit dot
SEB
Puck and PCB
$\vec{B}$
4K
800mK
100mK
10mK

Figure 3.2.1: Measurement setup. (Left) Fridge wiring for semiconductor spin readout. Signals are sent through a cryogenic loom (DC signals) and fast coaxial lines. It includes a typical setup for readout with reflectometry and an additional fast line for pulsing. (Right) Picture of the different cooling stages in an LD Bluefors dilution fridge.

Two fast lines are dedicated to rf-measurements. Firstly, the radio-frequency signal is delivered through an attenuated and filtered coaxial line into the mixing chamber. There, a cryogenic directional coupler (Krytar 158020-810) combines the incident and reflected waves. The reflected wave comes back through a different path to avoid self-resonances and amplify the signal. On its way out of the fridge, the rf-signal is first amplified by 26 dB at 4 K (LNF-LNC0.6_2A) and further amplified at room temperature. Moreover, an isolator is added to prevent that the noise generated in the amplifier arrives at the device.

Measurements performed with a JPA require an additional fast line, as explained in Sec. 4.4.1.

3.2.2 HOMODYNE DETECTION

The magnitude that has the information from changes in the sensor impedance is the reflection coefficient, Γ. This section introduces wave notation to later explain how to extract Γ from the reflected signal.

PHASORS AND WAVE QUADRATURES

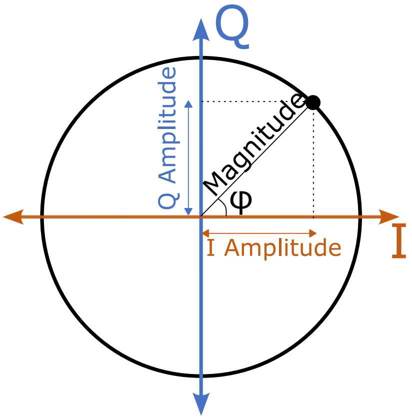

Figure 3.2.2: IQ phasor diagram. Wave representation as a point in a 2D plane, where I and Q are the cartesians coordinates. The point can also be defined in a phasor form using the polar coordinates: magnitude and phase.

Periodic signals with frequency $f = 2\pi\omega$, like the ones used in reflectometry, have the shape:

$$V = A\cos(\omega t + \phi), \tag{3.1}$$

where A is the wave amplitude and ϕ is the phase delay. This way, if the frequency is known, the only other parameters that characterise a wave are the magnitude and phase delay. These two factors can be used as polar coordinates to represent the wave as a point in a 2-dimensional plane. Due to its similarity with the complex plane, the wave can be represented as a complex number called **phasor** as $Ae^{i\phi}$ (see Fig. 3.2.2). Additionally, the cartesian coordinates of the wave point (X, Y) can also be used to represent the waves. These terms are the quadrature terms I and **Q**, where

$$V_{\mathrm{I}} = A\cos(\phi) \tag{3.2}$$

$$V_{\mathrm{Q}} = A\sin(\phi). \tag{3.3}$$

The terms I and Q are also sometimes called X and Y or the 'in-phase' and 'out of phase' quadratures. The wave can be rewritten in terms of its quadrature as

$$V = V_{\mathrm{I}}\cos(\omega t) - V_{\mathrm{Q}}\cos(\omega t). \tag{3.4}$$

Reflected wave

As explained in Sec. 2.3.2, a wave travelling trough a lossless transmission line with frequency ω has a shape:

$$V_{\mathrm{in}}(z,t) = |V_0^+|\cos(\omega t - \beta z + \phi^+), \tag{3.5}$$

where z is the position on the line, β is the propagation constant, $|V_0^+|$ is the voltage amplitude and ϕ^+ is the initial phase. In the phasor represenation the above wave looks like:

$$V_{\mathrm{in}}(z) = V_0^+\mathrm{e}^{j(-\beta z+\phi^+)}, \tag{3.6}$$

which is related to the reflected wave coming from the PCB by the reflection coefficient as

$$V_{\mathrm{out}}(z) = |\Gamma|V_0^+\mathrm{e}^{j(-\beta z_2+\phi^+ +\angle\Gamma)}. \tag{3.7}$$

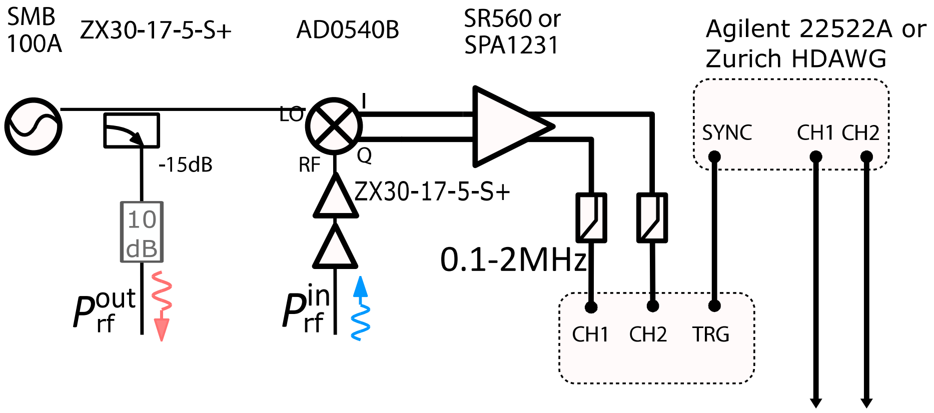

Figure 3.2.3: Room temperature reflectometry setup. The input and reflected wave are compared using homodyne detection to obtain the quadratures of the reflected wave and, in turn, variances in the SEB impedance.

DEMODULATION

Obtaining the reflection coefficient directly from the reflected wave would be a difficult task since it requires measuring changes in the phase and magnitude of a high frequency wave. Instead, quadrature demodulation simplifies the measurement greatly since it converts the wave into DC components carrying the wave quadratures. To do so, demodulation makes use of a mixer to compare the input and reflected wave and a low pass filter.

The input wave is divided into two paths. The first one goes inside the fridge to excite the device, whereas the second one is fed into the LO port of an IQ demodulator (Polyphase AD0540B) as seen in Fig. 3.2.3. On the other hand, the incoming reflected wave is connected to the RF port of the IQ demodulator.

The IQ demodulator separates the RF signal into two DC components corresponding to its quadrature (see [158] for the working principles of the IQ demodulator), which are related to the reflection coefficient as $\sqrt{V_\mathrm{I}^2 + V_\mathrm{Q}^2} \propto |\Gamma|$ and $\arctan V_\mathrm{I}/V_\mathrm{Q} \propto \angle\Gamma$.

Finally, the I and Q components are further amplified and filtered before being measured with a digitiser (Spectrum M4i.4451-x4).

3.3 SETUP OPTIMISATION

This section includes modifications in the setup to optimise the fast pulses used for spin readout and reducing noise.

3.3.1 FAST PULSE GENERATION

The on−PCB bias tee that combines low and high-frequency signals acts as a high pass filter on the fast pulses sent to the qubit dot. Ideally, pulses are composed of different stages of constant voltage (see Fig. 3.3.1a), however, the high pass filter deforms the wave shape as shown in Fig. 3.3.1b. Since the filter is simply an RC first order filter, its transfer function is given by:

$$H(\omega) = \frac{RCj\omega}{1 + RCj\omega}, \tag{3.8}$$

where R and C are the values of the resistance and capacitance mounted to the PCB.

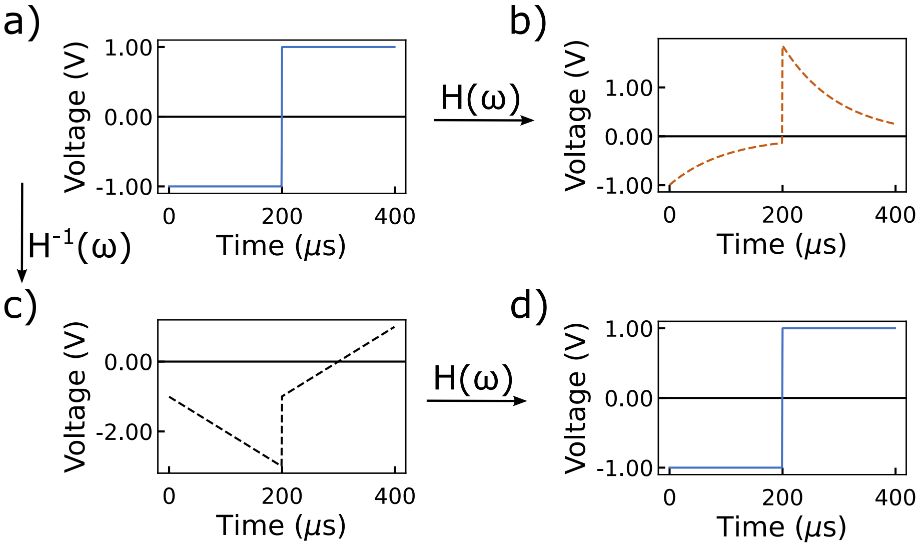

Figure 3.3.1: Fast pulses. a) Desired line-shape of the voltage pulse. b) Voltage arriving to the device without using compensation. c) Compensated pulse. d) The pulse arriving to the device has the desire shape using compensation.

The high pass filter was compensated with the help of pulse engineering. We use the python package ScyPy to apply the inverse of the filter transfer function to the desired wave shape. This way, after passing through the bias tee, the pulses acquired the desired line shape again. Mathematically, this can be expressed as:

$$\underbrace{H(\omega)}_{\text{filter}}\underbrace{(H^{-1}(\omega)V(\omega))}_{\text{pulse sent}} = V(\omega), \tag{3.9}$$

where $V(\omega)$ is the desired voltage line shape in the frequency domain.

3.3.2 Reducing setup interferences

Noise can have different sources such as dissipation in the device or the resonator, the amplification chain and the room temperature setup. This section focus on the latter. Here, we identified two kinds of noise produced by interferences in the room temperature setup that were detrimental to the SNR.

The first one is 50-100-150 Hz noise in sync with the power supply. 50 Hz noise is often present as a result of ground loops. Ground loops are the electrical situation produced when there is more than one conductive path between two electrical nodes. If one of these nodes is the zero-reference line, the voltage produced by the current going through the loop is added to the measured signal, resulting in noise. Moreover, the loop can act as an antenna and couple with the magnetic flux produced by the transformers. These interferences introduce noise at 50 Hz, 150 Hz and their harmonics.

In order to avoid ground loops, the fridge should have one solely low-resistance connection to the ground. To avert ground loops produced by the low-frequency connections, we used a QDAC for the DC bias of the device gates. The QDAC has their outputs galvanically isolated so that it provides a signal without any ground connection. For the fridge fast lines, we used DC-blockers (ground and signal) to isolate the ground connection between the rf-source, the fridge, the IQ mixer and the pre-amplifiers. The only connection for which the ground could not be isolated was between the AWG and the fridge fast line to send fast pulses. However, it did not seem to have a big effect in terms of noise.

Ground loops can also be produced by hoses that connect the gas handling system and the fridge. The Bluefors fridge design already includes isolation in the hoses clamps that prevent these extra ground connections. However, if the hose is in contact

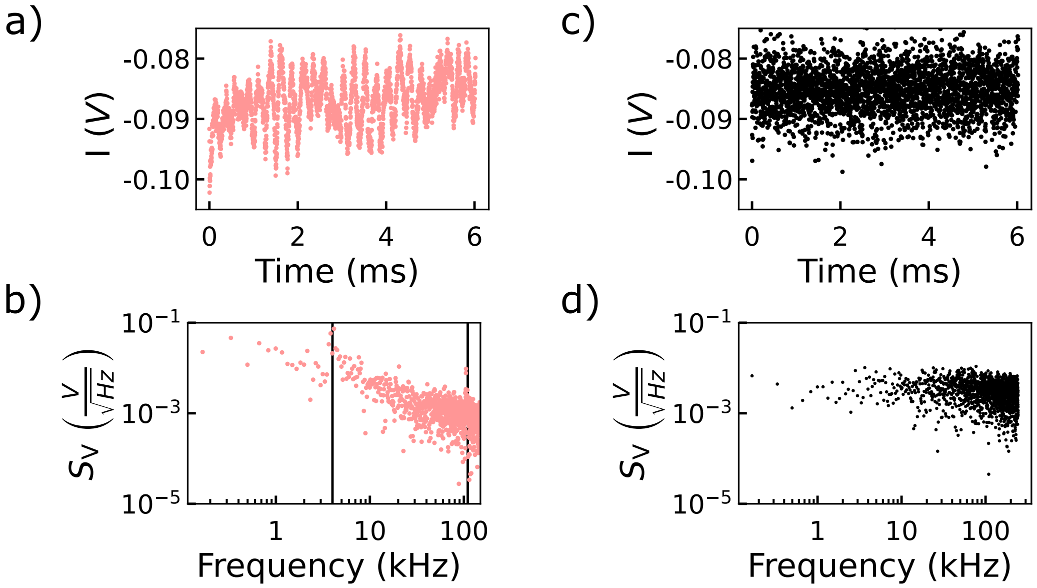

Figure 3.3.2: Noise characterisation. a) Measurement trace over time acquire with the digitiser. b) Corresponding noise power density. Besides low-frequency noise, a spike at ∼ 4kHz is observed. This can correspond with the frequency of the pulse tube cryocooler [234] that is picked up by a ground loop produced by ground connections between the fridge fast lines, the rf-source and the IQ demodulator. Moreover, there is an extra spike around 100kHz that is attributed to the demodulator power supply. c) Same measurement taken after including DC blockers (signal and ground) between the demodulator bridge, the rf-source and the fridge input and output ports. At the same time, the IQ demodulator and the pre-amplifiers power supply was modified. In a) they are powered with a commercial switching mode power supply, whereas in c) the noise is eliminated by powering them with an analogue bench power supply.

with any conductive surface, it can produce unwelcome noise.

The second source of noise that was identified and removed was a spike with a frequency around the ∼100 kHz. It was produced by the switched-mode power supply that was feeding the IQ demodulator and room temperature amplifiers. The noise disappeared when the power supply was changed by a constant voltage analogue bench power supply (see Fig. 3.3.2).

To summarise, the way to reducing noise related with interferences is a procedure consisting of characterising the noise after every change in the setup until most interferences disappear.

4

Optimisation of gate-based single electron box

A fast and highly sensitive charge sensor is paramount to achieving high fidelity qubit readout. This chapter summarises the advances in gate-based dispersive detection using a SEB. The optimisation of the resonator and the SEB, together with the addition of a Josephson parametric amplifier, improved the signal to noise ratio leading to the demonstration of a minimum integration time of $\tau_\mathrm{m} = 0.1$ μs. This result provides the route to combine high-fidelity readout with a compact and scalable architecture.

4.1 SNR and minimum integration time

As stated in the previous chapter, a good charge sensor is capable of detecting charge events fast and with a high fidelity. When using rf-reflectometry, the ultimate speed to measure a charge event is given by the resonator bandwidth, however, if the signal is not large enough compared with the noise, changes in the sensor impedance are not detectable. For this reason, optimising the signal to noise ratio (SNR) is a fundamental step towards having a fast readout with high fidelity.

To quantify the quality of a readout sensor, we use the minimum integration time, τ_{m}, defined as the minimum integration time to obtain a signal to noise ratio equal to one (SNR $= 1$). Another magnitude to characterise the sensor is the charge sensitivity, $\sqrt{S^{\mathrm{N}}_{\mathrm{QQ}}}$, which is related to τ_{m} as $\tau_{\mathrm{m}} = S^{\mathrm{N}}_{\mathrm{QQ}}/2e^2$ [158].

For an analytic expression of the SNR, we need to compute separately the magnitude of the signal and the noise. The signal is measured as the difference in reflected power produced by a charge event, calculated as [235]:

$$Signal = P_0|\Delta\Gamma|^2. \tag{4.1}$$

Here, P_0 is the applied power and $\Delta\Gamma$ is the change in reflection coefficient produced by a charge transient, which depends on the sensor and the matching network. In the case of SEBs, and specifically for this thesis, charge events modify only the SEB capacitance (the Sisyphus resistance is neglectable due to the high tunneling rates between SEB and reservoir in comparison with the rf-probe frequency). If these changes in the SEB capacitance are small[1], $\Delta\Gamma$ can be calculated considering only the first-order term as

$$\Delta\Gamma = \frac{\partial\Gamma}{\partial C_{\mathrm{D}}}\Delta C_{\mathrm{D}}, \tag{4.2}$$

where ΔC_{D}, the change in the SEB capacitance, is equal to the tunneling capacitance, C_{t}

To compute the SNR, we also need to quantify the noise. The noise can have different contributions, such as the power dissipated in the resonator, the power dissipated in the SEB due to the Sisyphus resistance or the noise generated in the amplification process. The combination of all noise sources can be expressed in terms of an effective temperature, T_{n}, as

$$P_{\mathrm{n}} = \frac{k_{\mathrm{B}}T_{\mathrm{n}}}{2\tau}, \tag{4.3}$$

where τ is the integration time defined as $\tau = 1/2B$, and B is the measurement bandwidth (this equation is equivalent to Eq. 2.26).

---

[1] Here, by small changes in the SEB capacitance we are referring to the small-signal regime characterised by $Q_{\mathrm{L}}\Delta C_{\mathrm{D}}/C_{\mathrm{tot}} << 1$, where C_{tot} is the total capacitance of the matching network and Q_{L} is the loaded quality factor.

This way, the expression for the signal to noise ratio reads as:

$$\mathrm{SNR} = \frac{P_0|\Delta\Gamma|^2}{P_\mathrm{n}}. \tag{4.4}$$

The following sections describe how to improve each of these factors. To do so, we need to, on one hand, design the matching network and SEB to maximise the signal power and, on the other hand, optimise the amplifier chain to minimise the noise.

4.2 MAXIMISING THE SIGNAL

This section goes through every aspect that can be optimised to maximise the signal. The first subsection describes how the strength of the capacitive coupling between SEB and the target dot affects the signal power. Then, the matching network is analysed, including how to characterise it and how to improve its design. Lastly, the text focus on the SEB properties that influences the SNR.

4.2.1 STRONG AND WEAK SENSITIVE REGIME

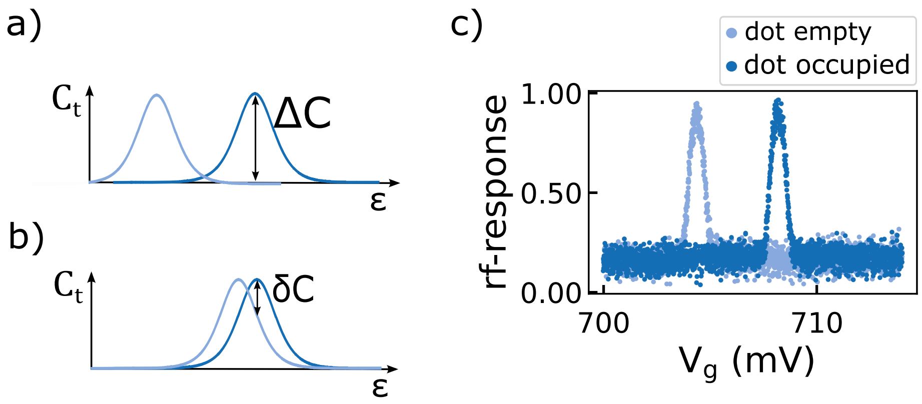

Figure 4.2.1: Strong and weak sensitive regime. a) The change in capacitance is maximum, ΔC, when the SEB is strongly sensitive to the target dot, so that the change in potential is larger than the linewidth of tunneling capacitance. The linewidth, given by Eqs. 2.23 and 2.25, has a different magnitude depending on the relation between $h\gamma$ and $k_\mathrm{B}T$, being $\epsilon_{1/2} = 2h\gamma$ if $h\gamma > k_\mathrm{B}T$ and $\epsilon_{1/2} = 3.53k_\mathrm{B}T$ if $h\gamma < k_\mathrm{B}T$. b) Change in SEB capacitance in the weakly sensitive regime. c) Measurements of the rf-reflectometry signal when the target dot is empty (light blue) and occupied (dark blue).

Charge sensing with a SEB is based on the fact that a charge event in the target dot produces a shift in the SEB potential, that modifies its capacitance. The magnitude of the potential shift depends on the capacitive coupling between SEB and the target dot. In the strong sensitive regime, the addition of one electron to the target dot causes a large shift in the SEB potential compared to the capacitance linewidth (see Fig. 4.2.1a). In this regime, the sensitivity on the target dot produces a maximal signal contrast, $\Delta C = C_\mathrm{t}$, being C_t the tunneling capacitance. On the other hand, if the SEB is weakly sensitive to the target dot, the SEB potential is weakly perturbed, producing smaller changes in capacitance: $\delta C < C_\mathrm{t}$ (see Fig. 4.2.1b).

The factor η characterises the decrement in capacitance change due to a weak coupling as

$$\eta = \frac{\delta C}{C_\mathrm{t}}. \tag{4.5}$$

The strong sensitive regime, for which $\eta = 1$, is desired since a weak coupling affects the SNR quadratically as:

$$\mathrm{SNR} = \eta^2 \mathrm{SNR}_\mathrm{strong}. \tag{4.6}$$

Here, $\mathrm{SNR}_\mathrm{strong}$ is the SNR that would have been obtained in the strong coupling regime. All the experiments performed in this thesis fall in the strong sensitive regime, as exemplified in Fig. 4.2.1c.

4.2.2 Circuit and simulations

This section discusses the configuration of the resonator (see Fig. 4.2.2) and its benefits for gate-based SEB readout. The resonator consists of a coupling capacitance C_c that connects the transmission line to a parallel configuration of an inductor, L, a resistor, R_D, representing the resonator and SEB losses, and a variable capacitance $C_0 = C_\mathrm{p} + C_\mathrm{D}$, where C_D is the SEB capacitance and C_p is the parasitic capacitance of the circuit. The equivalent impedance of such resonator is given by [175]:

$$Z_\mathrm{L} = R_\mathrm{D} \frac{j\omega\Delta\omega_0}{\omega_0^2 - \omega^2 + j\omega\Delta\omega_0} + \frac{1}{j\omega C_c}, \tag{4.7}$$

where $\Delta\omega_0 = \frac{1}{R_\mathrm{D} C_0}$ and $\omega_0 = 2\pi f_0 = \frac{1}{\sqrt{LC_0}}$ are the width and resonant frequency

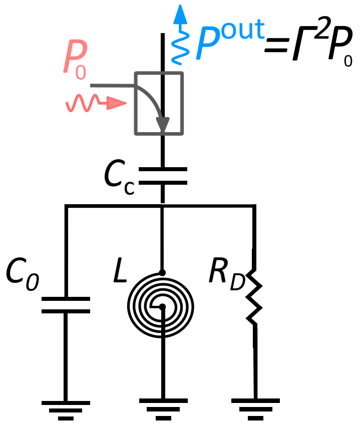

Figure 4.2.2: Parallel resonator. Resonator model including a coupling capacitor (C_c), followed by a resistance (R_D), inductor (L) and a capacitance ($C_0 = C_\mathrm{p} + C_\mathrm{D}$) in parallel.

of the unloaded parallel $LR_\mathrm{D}C_0$ circuit.

Following the calculations developed in [236], we can obtain the circuit parameters that will help us to interpret $|\Delta\Gamma|$, such as the resonance frequency, the quality factors and the coupling:

$$f_\mathrm{res} \approx \frac{1}{2\pi\sqrt{L(C_\mathrm{c}+C_0)}}, \tag{4.8}$$

$$Q_\mathrm{ext} = \frac{C_\mathrm{c}+C_0}{C_\mathrm{c}^2 Z_0}\sqrt{L(C_\mathrm{c}+C_0)}, \tag{4.9}$$

$$Q_\mathrm{int} = \sqrt{\frac{C_\mathrm{c}+C_0}{L}}R_\mathrm{D}, \tag{4.10}$$

$$\beta = \frac{Q_\mathrm{int}}{Q_\mathrm{ext}} = Z_0\frac{R_\mathrm{D}C_\mathrm{c}^2}{L(C_\mathrm{c}+C_0)}. \tag{4.11}$$

Knowing that $\Gamma = (Z_\mathrm{L} - Z_0)/(Z_\mathrm{L} + Z_0)$ and using Eq. 4.2, we can determine the absolute differential change in the reflection coefficient $|\Delta\Gamma|$ at the resonant frequency, f_res, arising from changes in the SEB capacitance [236]:

$$|\Delta\Gamma| = \left|\frac{\partial\Gamma}{\partial C_\mathrm{D}}\Delta C_\mathrm{D}\right| = \frac{2\beta}{(1+\beta)^2}Q_\mathrm{int}\frac{\Delta C_\mathrm{D}}{C_\mathrm{c}+C_0}. \tag{4.12}$$

This equation summarises the first guidelines for the resonator optimisation[2], which include (i) a large internal Q-factor, Q_{int}, (ii) a coupling to the line close to $\beta = 1$ and (iii) large fractional changes in the capacitance. Moreover, Eqs. 4.9 and 4.10 highlight the advantages of the resonator parallel topology. In this configuration, external and internal Q-factors can be varied independently by modifying the coupling capacitance, C_{c} and L, so that a good matching can be obtained ($Q_{\text{int}} \approx Q_{\text{ext}}$) at the same time as Q_{int} is kept high. This tunability does not exist in the traditional LCR series configuration, where Q_{int} and Q_{ext} scale with L and C in the same manner (see Eqs. 2.18 and 2.19). The rest of the parameters, C_{p} and R_{D}, are not tunable and account for the parasitic capacitance and losses from the PCB and the device.

4.2.3 POWER TO THE DEVICE

According to Eq. 4.4, increasing the power applied to the network, P_0, would indefinitely improve the SNR. In reality, this is not true since applying larger powers overdrives the SEB, making the SNR tend asymptotically to a maximum (see Sec. 4.2.4 for more details). To account for the SEB overdrive, the applied power, P_0, needs to be rewritten in terms of the voltage applied to the SEB gate connected to the resonator, V_{g}.

The power, P_0 is produced by the voltage, V_0, applied to a transmission line with characteristic impedance Z_0:

$$P_0 = \frac{|V_0|^2}{Z_0}. \tag{4.13}$$

Only a fraction of P_0 gets delivered to the matching network. That input power, P_{in}, is determined by the difference between the applied power, P_0, and the reflected power, P_{refl}:

$$P_{\text{in}} = P_0 - P_{\text{refl}} = \frac{|V_0|^2}{Z_0}(1 - |\Gamma|^2), \tag{4.14}$$

In turn, P_{in} is the power produced by the voltage difference, V_{g}, across the resistance R_{D}:

$$P_{\text{in}} = \frac{V_{\text{g}}^2}{R_{\text{D}}}. \tag{4.15}$$

---

[2] Although, here, we are not taking into account the input power, P_0, yet

Putting together the three previous equations and knowing that

$$1 - |\Gamma|^2 = 4\beta/(1+\beta)^2, \tag{4.16}$$

we obtain:

$$P_0 = \frac{V_\mathrm{g}^2}{R_\mathrm{D}} \frac{(1+\beta)^2}{4\beta}. \tag{4.17}$$

V_g, the power drop across the resistance R_D, is equivalent to the voltage applied to the SEB gate.

4.2.4 Device capacitance

The last term required to compute the signal power is the change in the SEB capacitance. Eq. 2.23 shows the importance of the SEB lever arm, α, the electron temperature and the tunneling rates between SEB and reservoir. However, this expression does not include the effect of overdriving the SEB with too much power. In [237], they study the effect of V_g on the tunneling capacitance using the adiabatic approximation ($\gamma_0 > \omega_\mathrm{rf}$), in which inelastic relaxation processes and excitation produced by the rf-probe are neglected. Assuming that the tunneling capacitance is thermally broadening ($\hbar\gamma_0 < k_\mathrm{B}T_\mathrm{e}$) they arrived to the expression:

$$\Delta C_\mathrm{D} = \eta \frac{2\alpha e}{\pi V_\mathrm{g}} \frac{1}{1 + (\omega_\mathrm{rf}/\gamma_0)^2} f_\mathrm{c}(x), \tag{4.18}$$

where $x = \frac{\alpha e V_\mathrm{g}}{k_\mathrm{B}T_\mathrm{e}}$, and f_c is a dimensionless function of the form

$$f_\mathrm{c}(x) = \pi f_\mathrm{rf} \int_0^{1/f_\mathrm{rf}} \frac{\sin(2\pi f_\mathrm{rf} t) dt}{1 + \exp\left[-x \sin(2\pi f_\mathrm{rf} t)\right]}, \tag{4.19}$$

which increases monotonically as a function of V_g until it saturates to the value of 1.

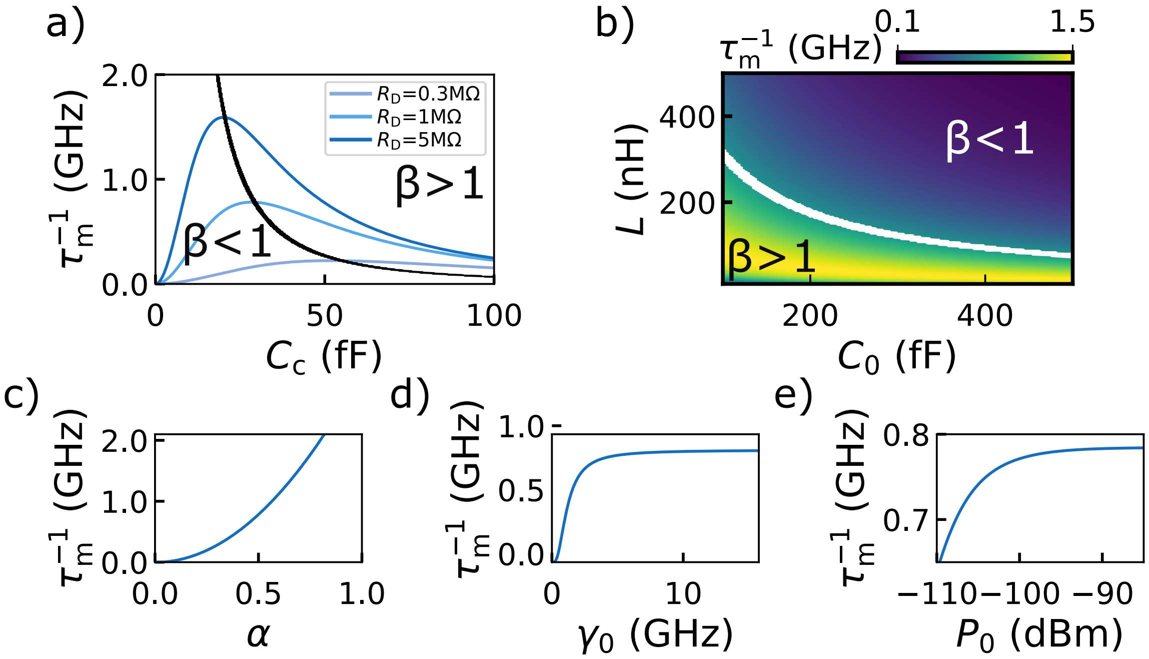

Figure 4.2.3: Signal dependency on the experimental parameters. a) Normalised signal as a function of the coupling capacitance, C_c for different R_D. The black line shows the signal at matching ($\beta = 1$) for different values of C_c and R_D. b) Signal as a function of L and C_0, where the white line are the values of L and C_0 for which $\beta = 1$. c) Signal as a function of α d) γ_0 and f) P_0. Here, we have not included the effect of the JPA, for which the minimum integration time should get eventually worse as the JPA overloads at high powers.

4.2.5 MINIMUM INTEGRATION TIME DEPENDENCY ON THE EXPERIMENTAL PARAMETERS

Substituting Eqs. 4.12, 4.17, 4.18 and 4.3 in Eq. 4.4, we find the analytic expression for inverse of the minimum integration time:

$$\tau_{\mathrm{m}}{}^{-1} = 32\eta^2 \frac{\beta}{(1+\beta)^2} \frac{(\alpha e)^2}{k_{\mathrm{B}} T_{\mathrm{n}}} Q_{\mathrm{int}} Z_{\mathrm{r}} f_{\mathrm{res}}{}^2 \left[1 + (2\pi f_{\mathrm{res}}/\gamma_0)^2\right]^{-2} f_{\mathrm{c}}^2(x). \tag{4.20}$$

Here, $Z_{\mathrm{r}} = \sqrt{L/(C_{\mathrm{c}} + C_0)}$ is the resonator impedance and the system is tested with a probe rf-frequency equal to the resonant frequency ($2\pi f_{\mathrm{res}} = \omega_{\mathrm{rf}}$).

This formula allows a quantitative analysis of the effect from different experimental parameters on τ_{m}. Fig. 4.2.3 provides a guideline to optimise τ_{m} using typical values of L = 100nH, C_{c} = 25fF, R_{D} = 1 MΩ, C_0 = 400fF, α = 0.5, $P_0 = -90$dBm, γ_0 =3GHz, η = 1 and T_{e} = 130mK and a noise dominated by the amplifier with T_{n} =2.5K. Fig. 4.2.3a shows that increasing R_{D} leads to a better SNR, which can be further improved by tuning the coupling capacitance C_{c} to achieve perfect matching (black line). As shown in Fig. 4.2.3b, the best SNR is achieved with low parasitic capacitance, C_0, and inductor, L. They both have a similar effect: higher values of any of them produce an undercoupled resonator with lower resonant frequency f_{res}, which affects negatively to the SNR. For this reason, the best results are achieved for values of L and C_0 below perfect matching, marked by the white line. In summary, an optimise resonator would have a high R_{D}, low L and C_0, and a C_c tuned for perfect matching.

Fig. 4.2.3c and d summarise the effect of the SEB characteristics on τ_{m}. The value of the SEB gate lever arm is specially important, with a dependence of $1/\tau_{\mathrm{m}} \propto \alpha^2$. Another parameter that affect τ_{m} is the SEB to reservoir tunneling rates, γ_0, which should be larger than the resonant frequency f_{res} for an optimal readout. Lastly, the SNR improves with the power applied, P_0 although it saturates at high powers (see Fig. 4.2.3e).

4.3 SETUP AND IMPLEMENTATION

This section introduces the setup used during this thesis and describes how to extract the experimental parameters introduced in the previous section. Fig. 4.3.1a and b show the top and bottom of a PCB with the components that form the lumped-element resonator. The inductor is a planar spiral inductor fabricated by depositing a NbN film on top of a Sapphire subtract using DC sputtering. The NbN film is later patterned into a spiral shape using optical lithography and etching [175]. The number of spiral turns sets the inductance value between 30 to 600nH (see Fig. 4.3.1c). The low-loss Sapphire substrate produces an inductor with low losses and self-capacitance, leading to a resonator with high R_D and low C_0.

The inductor is wirebonded to the PCB, which is designed to minimise the parasitic capacitance, C_0. To do so, the metal of the bottom layer is removed around the resonator area (See Fig. 4.3.1a) leading to a parasitic capacitance of $C_0 = 400-600$ fF. Lastly, the coupling capacitance, C_c, is a source mounted element whose value is selected to achieve perfect matching or, failing that, a slightly overcoupled resonator.

With this setup, a resonant frequency of 600-800MHz is achieved. Although higher resonant frequencies are beneficial for the SNR, the losses in the interconnections between resonator and device increase at high rf-probe frequencies. Moreover, the SNR deteriorates as f_res gets closer to the tunneling rate, γ_0, due to a reduction of the tunneling capacitance.

In terms of the device, the SEB is implemented in a silicon nanowire transistor fabricated in industrial cleanrooms at the scale of 300-mm wafers (see Sec. 3.1 for fabrication details and dimensions). Fig. 4.3.2 shows a transversal view of the nanowire where, at low temperatures, electrons are trapped in its upper corners forming two quantum dots, whose potential is controlled individually by the two gates wrapped onto the nanowire, in a face-to-face arrangement [227]. The two quantum dots are tunnel-coupled (in a parallel configuration) to self-aligned, heavily implanted, n-type source and drain electron reservoirs, and capacitively coupled to each other. The device is notionally symmetric; however, the gate of the dot that will act as a SEB is connected to an LC resonator for gate-based reflectometry. The nanowire geometry is specially beneficial for gate-based readout since the larger surface of wrap-around gates and the thin gate oxide (6 nm of SiO_2) increase the lever arm with respect to planar structures, leading to an alpha-factor in the range of $\alpha = 0.25 - 0.7$.

By monitoring the phase of the reflected RF signal, while the SEB and the other dot (so-called qubit dot) potentials are swept, it is possible to map out charge transitions for the two quantum dots (see Fig.4.3.3a for a full stability diagram and

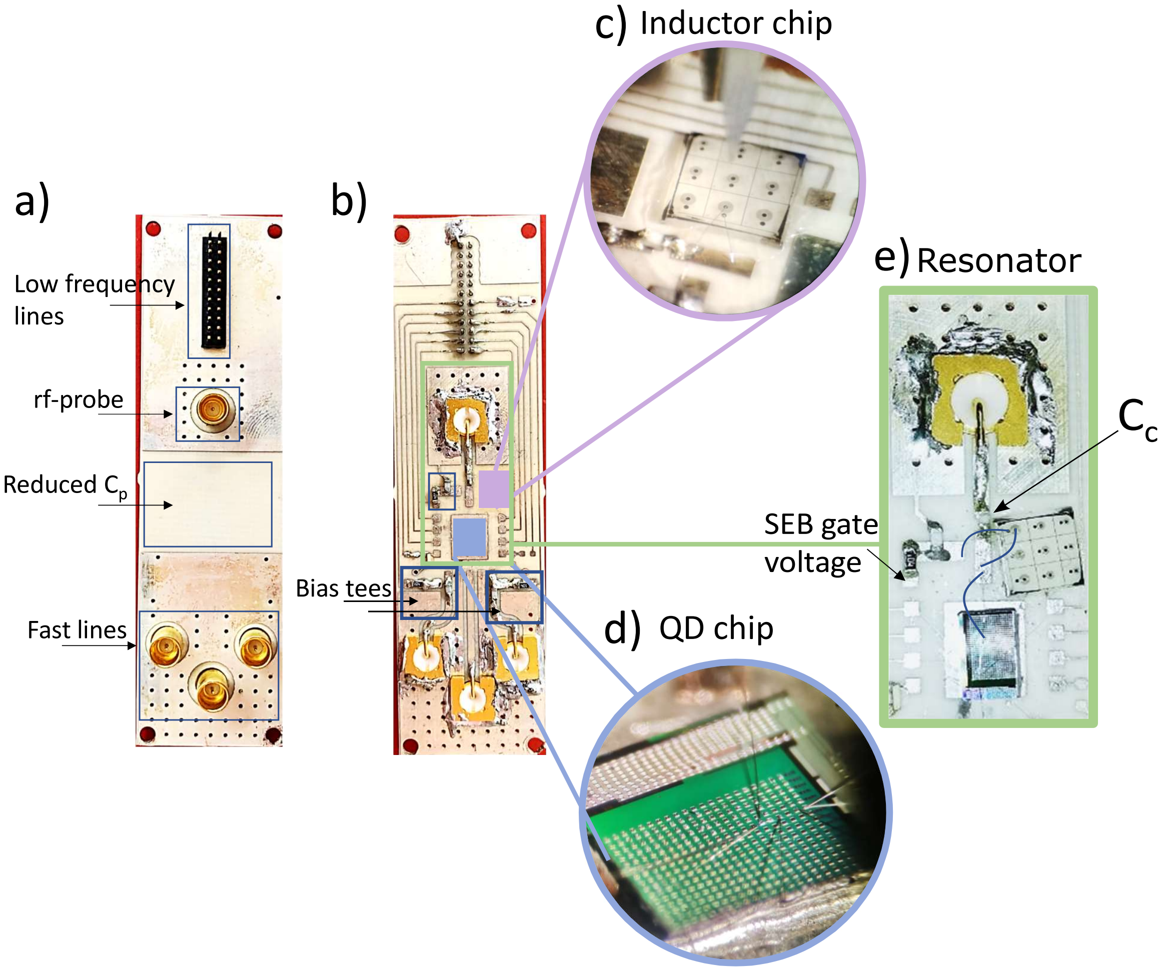
a)
Low frequency lines
rf-probe
Reduced C_p
Fast lines
b)
Bias tees
c) Inductor chip
d) QD chip
e) Resonator
C_c
SEB gate voltage

Figure 4.3.1: PCB and resonator. a) Bottom b) and top of the PCB with components soldered. The purple and blue square show the position of the inductor chip and QD chip, respectively, whereas the green rectangle encompass the part of the PCB where the resonator is implemented. The PCB was designed by previous PhD. student Simon Schaal. c) Inductor chip. The NbN films were provided by Dr. N. Stelmashenko and Dr. J. A. W. Robbinson. On the other hand, Dr. D.J.Ibberson and Dr. L. Ibberson manufactured the spiral NbN inductors. d) Wirebonded QD chip. e) Close-up of the resonator section, where the rf-probe signal comes from a SMP connector. The blue lines indicate the bondwires that connect the PCB with the inductor and the SEB in a parallel configuration. The gate voltage is delivered to the SEB gate through the inductor and combined with the rf-probe tone using a bias tee.

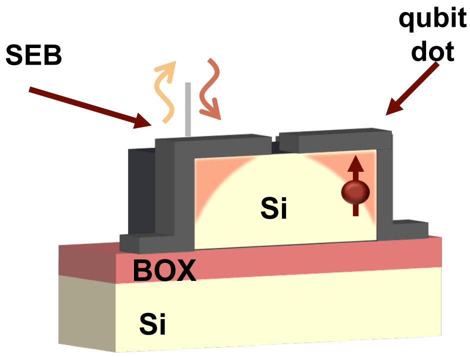

Figure 4.3.2: SEB transversal view. Sketch of a transversal view of the Silicon nanowires with a split wrap-around gate.

Fig. 4.3.3b for detail). The number of electrons in the qubit dot, n_q, can be measured using the inter-dot capacitive coupling with the SEB: each change in n_q shifts the SEB electrochemical potential (see Fig. 4.3.3b) allowing us to ensure complete depletion in the qubit dot by reducing the voltage applied to the qubit dot gate, V_Q, until no further shifts are observed by the SEB (see Fig. 4.3.3a). On the other hand, because the reflectometry signal is a function of the tunnelling rate between SEB and reservoir, and this rate depends on the SEB occupancy, n_s, it is not straightforward to assign an electron occupation for the SEB. Nevertheless, n_s is not central to the charge sensing employed here.

4.3.1 SEB characterisation

This section shows how to extract the parameters from the SEB that affect the SNR, such as the lever arm α, the tunneling rates, γ_0, the electron temperature T_e and the power applied to the resonator, P_0.

SEB lever arm

As mentioned before, the nanowire is notionally symmetric, however, selecting the dot with the highest gate alpha factor is critical for the SNR since SNR $\propto \alpha^2$. The following paragraphs describe how to quantify the lever arms from the dot on the right side and left side of the nanowire, finding that a systematical misalignment of 7 ± 3 nm in the placement of the gates on the Si channel produces an asymmetry in the gates lever arm.

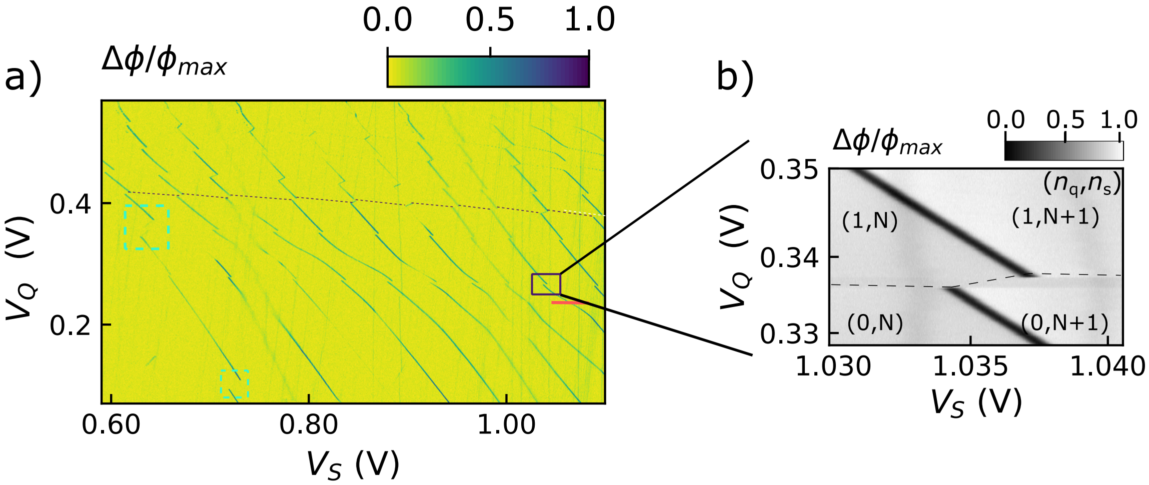

Figure 4.3.3: Stability diagram. a) Stability map of the SEB and qubit dot measured with gate-based reflectometry. A solid square indicates the readout area corresponding to the first electronic transition of the qubit dot since no other shifts are visible for a large range of smaller V_Q. The dashed square indicates dot-donor transitions. The donor is presumed to be bismuth since the sample was bismuth-doped. The black dashed line helps the eye to follow one of the qubit dot electronic transitions. The red horizontal line marks the dot to lead transition where Coulomb diamonds are measured in Fig. 4.3.4a b) Close-up of the first electronic transition of the qubit dot. The SEB potential shifts when the first electron is added to the dot, changing the rf-response from a maximum to some minimum, background level.

The gate lever arms map the voltage applied to each gate to the electrostatic energy at the dot. In this system, where two quantum dots are placed in parallel, the Coulomb diamonds of each dot can be measured independently. The right and left dots lever arm (α_{RR}, α_{LL}) can be calculated with their Coulomb diamonds measured in current or with reflectometry (See Fig. 4.3.4). At $V_{\mathrm{sd}} \neq 0$, the transition splits in two. These two lines with slope m_1 and m_2, delimit the set of voltages at which the dot level is in the bias window and the lever arm can be calculated as the inverse of the slope difference: $\alpha_{\mathrm{RR}}(\mathrm{LL}) = 1/|1/m_1 - 1/m_2|$ [123]. In addition, the voltage applied to one of the dots can influence the other, such that, in general, there is a lever arm matrix [126]:

$$\begin{pmatrix} \Delta\mu_{\mathrm{R}} \\ \Delta\mu_{\mathrm{L}} \end{pmatrix} = \begin{pmatrix} \alpha_{\mathrm{RR}} & \alpha_{\mathrm{RL}} \\ \alpha_{\mathrm{LR}} & \alpha_{\mathrm{LL}} \end{pmatrix} \begin{pmatrix} V_{\mathrm{R}} \\ V_{\mathrm{L}} \end{pmatrix} \tag{4.21}$$

where $\Delta\mu_{\mathrm{R}}$ and $\Delta\mu_{\mathrm{L}}$ are the electrochemical potentials of the right and left dot, respectively. The effect of the cross terms is visible in the stability diagram, where the slope of dot-to-lead transitions is given by the ratio between lever arms. This way, the cross lever arms were found to be: $\alpha_{\mathrm{RL(LR)}} = \frac{\Delta V_{\mathrm{R(L)}}}{\Delta V_{\mathrm{L}}(\mathrm{R})} \cdot \alpha_{\mathrm{RR(LL)}}$.

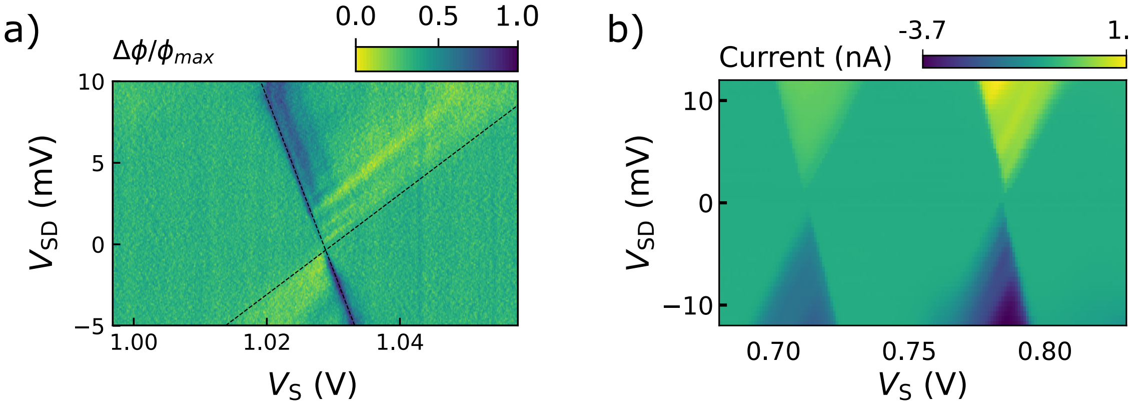

Figure 4.3.4: Lever arm and device characterisation. a) Coulomb diamond of the SEB from the SEB dot-to-lead transition indicated in red in Fig. 4.3.3 measured in reflectometry. The slopes used for calculating $\alpha_{\mathrm{RR}}(\mathrm{LL})$ are marked with dashed black lines. b) Coulomb diamonds measured in current.

The lever arms values for three different devices called device A, B and C are summarised in Table 4.3.1. They reflect that the left dot has systematically larger

	XX	α_{XX}	$\sigma_{\alpha_{\mathrm{XX}}}$
Device A	**RL**	0.070	0.006
	LL	0.58	0.03
Device B	**RR**	0.239	0.004
	LR	0.078	0.004
	RL	0.121	0.002
	LL	0.478	0.008
Device C	**RR**	0.23	0.02
	LL	0.35	0.06

Table 4.3.1: Lever arms. XX refers to the subindex of the alpha factor which can take the values *RR*, *RL*, *LL* or *RL*. $\sigma_{\alpha_{\mathrm{XX}}}$ refers to the standard error in the extracted values. Device A and B are single split nanowires. Device A has a gate length of $L_{\mathrm{g}} = 50$ nm and a width of $W = 80$ nm, whereas device B has $L_{\mathrm{g}} = 40$ nm and $W = 70$ nm. The splitting between gates is $S_{\mathrm{v}} = 50$ nm for device A and $S_{\mathrm{v}} = 40$ nm for device B. On the other hand, device C is a double split nanowire (4 dots) with a width of W=80 nm and a gate length of $L_{\mathrm{G}} = 50$ nm. The separation between parallel gates is $S_{\mathrm{H}} = 50$ nm, whereas between the gates facing each other is $S_{\mathrm{V}} = 40$ nm.

α factors than the right dot, which coincides with similar asymmetries reported for nominally identical devices [238, 239]. This means that the SNR can be increased by a factor of 4 simply by swapping the assignment of SEB and qubit dot.

EFFECT OF POWER, TEMPERATURE AND TUNNELING RATES

The broadening of the SEB to reservoir transition has three different sources: 1) the reservoir electron temperature, 2) the perturbations in its potential produced by the rf-carrier via cross capacitance to the sensor dot gate and 3) the dot state broadening due to tunneling. When power broadening is dominant (See Fig. 4.3.5), the linewidth increases as

$$\epsilon_{\frac{1}{2}} = \epsilon_{\frac{1}{2}0}\sqrt{1 + \frac{P}{P_{\mathrm{i}}}}, \tag{4.22}$$

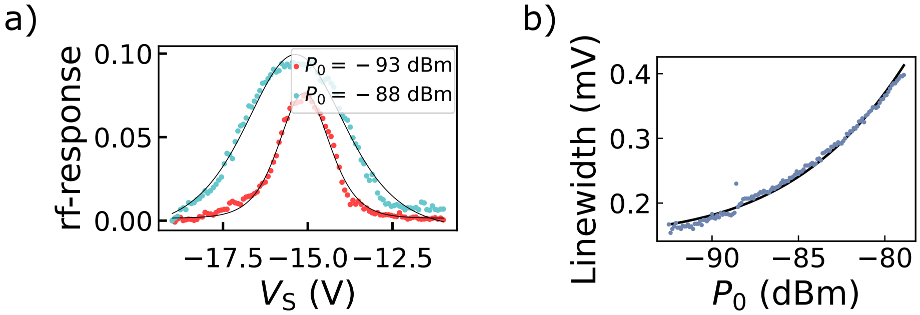

Figure 4.3.5: Power broadening. a) SEB to reservoir dot transition measured in reflectometry as a function of the voltage applied to the SEB gate, V_S. b) Linewidth broadening as the power applied, P_0, increases.

where $\epsilon_{\frac{1}{2}0}$ is the natural width due to electron temperature or tunnelling rates and P_i is the power at which the power starts dominating the transition width.

As shown in Fig. 4.2.3e, increasing the power, at first instance, improves the SNR. However, if the power broadening is larger than the difference in voltage produced by a charge transition in the qubit dot, the SNR would decrease due to a reduction of η. Fortunately, as shown in Fig. 4.3.3b, the potential shift is so large compared with the linewidth that this will not be the case. Nevertheless, the power broadening can also affect the potential of the qubit dot in the same way a higher temperature would do, which can affect the spin readout fidelity.

For small rf-powers, the linewidth of the transition is set by the electronic temperature as long as the thermal energy, k_BT_e, is larger than the QD level broadening, $\hbar\gamma_0$, where γ_0 is the tunneling rate. In this case, the tunneling capacitance is proportional to $\Delta C_d \propto \frac{1}{\cosh^2(\epsilon/2k_BT_e)}$, where ϵ is the quantum dot level detuning with the reservoir (see Eq. 2.23). On the other hand, if $k_BT_e \ll \mathrm{h}\gamma$, the width is set by γ_0 and the parametric capacitance follows a Lorentzian shape: $\Delta C_d \propto \frac{\hbar\gamma_0}{(\hbar\gamma_0)^2+\epsilon^2}$(see Eq. 2.25). These shapes are very similar and difficult to distinguish, however, they can give a upper limit for γ_0. With this method, tunneling rates raging from $\gamma_0 = 5 - 74$ GHz were obtained.

The relation between the broadening and the temperature can be very useful to accurately calculate the lever arm since, at higher temperatures, where the electron temperature is similar to the measurable mixing chamber temperature, the linewidth in voltage scales proportionally with respect to the temperature and the factor that relates both magnitudes is the lever arm, α.

4.3.2 Resonator characterisation

Experimentally, the reflection coefficient is extracted by measuring S_{21} between the lines driving the input power, $P_{\mathrm{rf}}^{\mathrm{in}}$, and output power, $P_{\mathrm{rf}}^{\mathrm{out}}$, with a network analyzer as $\Gamma = \sqrt{S_{21}} = \sqrt{\frac{P_{\mathrm{rf}}^{\mathrm{out}}}{P_{\mathrm{rf}}^{\mathrm{in}}}}$ (see Fig. 4.4.1). Fig. 4.3.6a shows a measurement of Γ, which differs from the expected constant resistance circle due to the effect of the environment and instead follows the equation [240]:

$$S_{21} = ae^{j\alpha}e^{-2\pi jf\tau}\left(1 - \frac{Q_{\mathrm{L}}/|Q_{\mathrm{ext}}|e^{j\phi}}{1 + 2iQ_{\mathrm{L}}\left(f/f_{\mathrm{res}} - 1\right)}\right). \tag{4.23}$$

Here, the constant a takes into account that the amplitude of the outcoming wave has been modified by the attenuators and amplifiers present in the system. Moreover, due to the cable length, the wave has an electrical length characterised by $e^{j\alpha}$ and it acquires a delay, τ, that makes the phase proportionally dependent on the frequency as $e^{-j2\pi f\tau}$ [240].

Fig. 4.3.6c shows in grey a resonator at B=0T once the effect of the environment has been removed. The additional phase offset, ϕ, is what produces an asymmetry in the absolute value of the reflection coefficient (See Fig.4.3.6d). Only when the resistance circle is rotated to it is right position, the resonant frequency coincides with the minimum in the absolute value of the reflection coefficient (see purple circle in Fig. 4.3.6d). The term $e^{j\phi}$ comes from asymmetries of the resonator's transmission signal due to different input and output impedances at the two ports of the resonator [241] or from standing waves in the transmission line connected to the resonator [242].

The rotated circle (purple in Fig. 4.3.6c) corresponds to a constant resistance circle, which has the equation [169, 243]:

$$\Gamma = o_{\mathrm{c}} + \left(1 - \frac{2}{1 + j2Q_{\mathrm{L}}(\frac{f}{f_{\mathrm{res}}} - 1)}\right) r_{\mathrm{c}}. \tag{4.24}$$

Here, $o_c = \frac{r_{\mathrm{L}}}{1+r_{\mathrm{L}}}$ is the center of the circle, $r_c = \frac{1}{1+r_{\mathrm{L}}}$ is the radius, $r_{\mathrm{L}} = \frac{1}{\beta}$ is the real part of the normalised resonator impedance $\left(\frac{Z_{\mathrm{L}}}{Z_0} = r_{\mathrm{L}} + jy_L\right)$, f_{res} is the resonant frequency and Q_{L} is the loaded quality factor defined as the ratio of the total energy stored in the resonator to the average energy dissipated per cycle multiplied by 2π. The data was fitted to a circle using the tools python library found in [244].

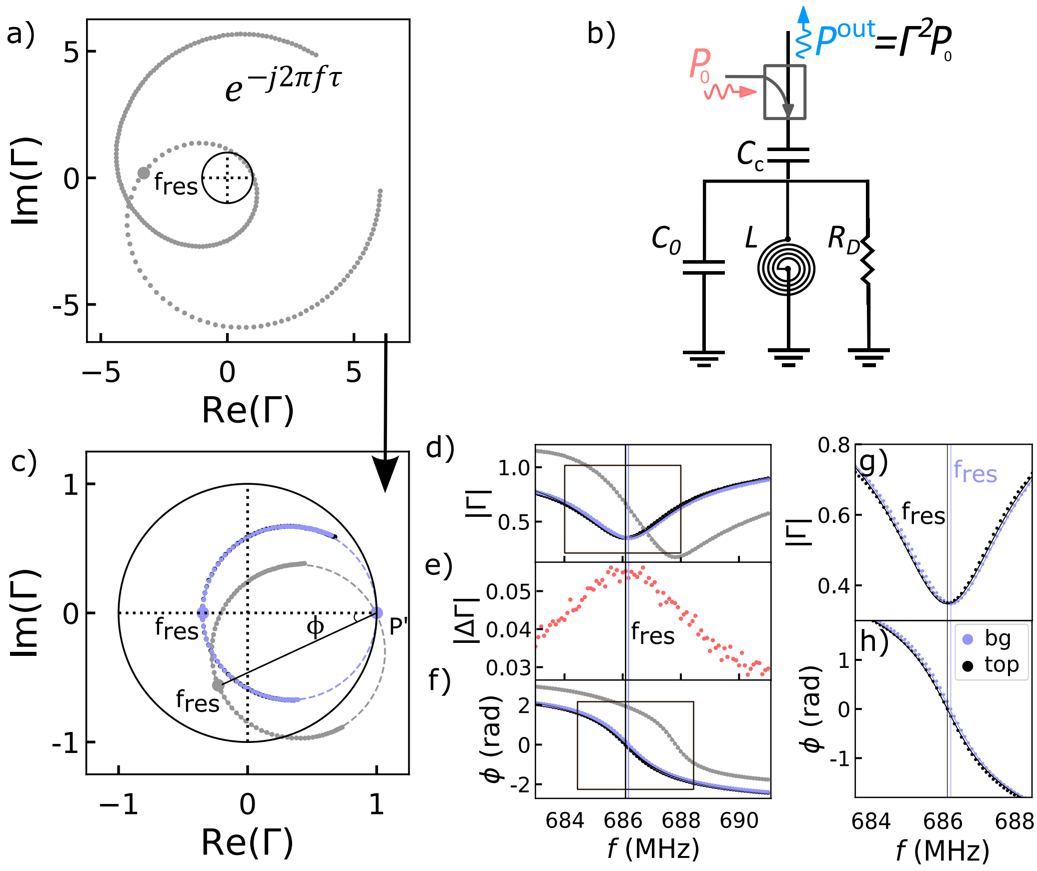

Figure 4.3.6: Resonator characterisation. a) Γ raw data acquired from a $\sqrt{S_{21}}$ measurement between the ports $P_{\mathrm{rf}}^{\mathrm{in}}$ and $P_{\mathrm{rf}}^{\mathrm{out}}$ shown in b for B=0 T. b) Resonator model including a coupling capacitor (C_{c}), followed by a resistance (R_{D}), inductor (L) and a capacitance ($C_0 = C_{\mathrm{p}} + C_{\mathrm{D}}$) in parallel. c) Measured reflection coefficient and fit before (grey) and after (purple/black) removing the offset angle ϕ. The point of resonant frequency is marked as f_{res}, whereas the off-resonant point corresponding to $f \to \infty$ is marked as P'. d) Absolute value of the reflection coefficient against the frequency, showing that the minimum of the raw data, does not correspond to the resonant frequency. e) Absolute value of the reflection coefficient variation when the SEB is at a charge instability at different frequencies. The maximum variation and, therefore SNR, occurs at f_{res}. f) Phase of the reflection coefficient with respect to the frequency. g), h) Absolute value and phase of the reflection coefficient on top of an SEB charge transition (top) and out of it (bg) and its respective resonant frequencies shown as vertical lines in their corresponding color. $|\Gamma|$ remains mostly the same, whereas the resonant frequency changes by 70kHz, revelling that the SEB impedance shift at a charge instability is mostly capacitive.

If the circle centre is then transported to the origin, the change in phase is related to the frequency as

$$\phi(\omega) = \theta_0 + 2\arctan\left[2Q_\mathrm{L}\left(1 - \frac{f}{f_\mathrm{res}}\right)\right], \tag{4.25}$$

where θ_0 is an offset angle. This is considered one of the most accurate ways to obtain the Q-factor and resonant frequency of a resonator [243].

Fig. 4.3.6g and h show the magnitude and phase of the reflection coefficient with respect to the frequency at the top of an SEB charge instability (black) and out of it (purple). We found that the resonant frequency is $f_\mathrm{res}^\mathrm{top} = 686.099 \pm 0.017$ MHz at the charge transition degeneracy point and $f_\mathrm{res}^\mathrm{bg} = 686.168 \pm 0.016$ MHz away from it. The change in resonant frequency is linked to an increment in the SEB capacitance to ground as $f_\mathrm{res} = \frac{1}{2\pi\sqrt{L(C_\mathrm{c}+C_\mathrm{p}+C_\mathrm{D})}}$, being the change in capacitance $\Delta C_\mathrm{D} = 0.09 \pm 0.03$ fF.

We observed that the system is overcoupled as the phase completes a 2π rotation but the circle does not cross the origin. The matching, calculated as $\beta = \frac{Z_0}{R} > 1$, is barely changed by the SEB, being $\beta^\mathrm{top} = 2.064$, $\beta^\mathrm{bg} = 2.061$ at and away from the charge degeneracy point, respectively, and, neither is the loaded Q-factor: ${Q_\mathrm{L}}^{top} = 125.3 \pm 0.5$ and ${Q_\mathrm{L}}^{bg} = 125.7 \pm 0.5$. This means that the charge instability in the SEB produces a capacitive change.

Because we are measuring a small change in the SEB capacitance, the maximum change in $|\Delta\Gamma|$ and, therefore SNR, occurs at the resonant frequency [175], where the slope in phase is maximum (See Fig. 4.3.6e).

4.4 REDUCING NOISE

NOISE TEMPERATURE

The noise power(conveniently characterised by the equivalent noise temperature T_n) contains contributions from the system itself T_sys (SEB and resonator) as well as the amplification chain (see Fig. 4.4.1a). In rf measurements of semiconductor QDs, high-mobility electron transistors (HEMTs) are typically used as the first amplifier, limiting the noise temperature to a few Kelvin. Here, the addition of an amplifier with lower noise temperature, a JPA, with gain G_{JPA}, reduces T_{n} accordingly:

$$T_{\mathrm{n}} = T_{\mathrm{sys}} + T_{\mathrm{JPA}} + \frac{T_{\mathrm{HEMT}}}{G_{\mathrm{JPA}}}. \tag{4.26}$$

where $T_{\mathrm{HEMT(JPA)}}$ is the noise temperature of the HEMT(JPA). The use of a JPA is only advantageous if the noise is dominated by the HEMT instead of the system. This is not the case for rf-SETs where shot noise may be comparable or in excess of that of the HEMT [147]. For SEBs, if the tunneling rate γ_0 between SEB and reservoir is greater than f_{rf}, electrons tunnel adiabatically, and the Sisyphus noise vanishes [179] leaving predominantly the noise contribution of the HEMT .

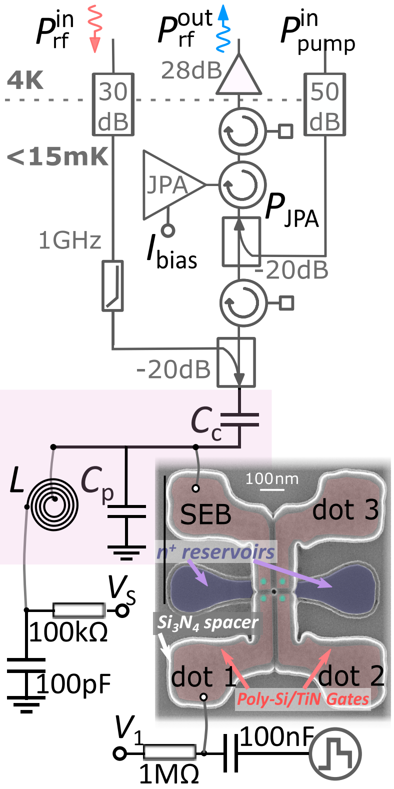
$P_{\mathrm{rf}}^{\mathrm{in}}$
$P_{\mathrm{rf}}^{\mathrm{out}}$
$P_{\mathrm{pump}}^{\mathrm{in}}$
4K
30 dB
28dB
50 dB
<15mK
JPA
P_{JPA}
1GHz
I_{bias}
-20dB
-20dB
C_{c}
L
C_{p}
100nm
SEB
dot 3
n^{+} reservoirs
V_{S}
100kΩ
Si_3N_4 spacer
100pF
dot 1
dot 2
Poly-Si/TiN Gates
V_1
100nF
1MΩ

Figure 4.4.1: Device and measurement setup. False-colour scanning electron micrograph of a silicon nanowire transistor with two pairs of split gates (red). The green dots indicate the location of the QDs under each gate. The blue regions are electron reservoirs. The SEB is connected to a lumped-element resonator that is excited with $P_{\mathrm{rf}}^{\mathrm{in}}$. The reflected signal is amplified as it travels through the middle line, and then the difference in phase and magnitude between the input and output wave is measured using homodyne detection. The third line is used to apply the pump power attenuated at different temperatures.

In the devices measured during this thesis, the tunneling rate γ_0 between SEB and reservoir is in the range $\gamma_0 = 5 - 74$ GHz (see Sec.4.3.1), well in excess of $f_{\rm rf} \sim 0.6 - 0.8$ GHz, such that we are in the regime of negligible Sisyphus dissipation in the SEB. This is confirmed by noise temperature measurements yielding $T_{\rm n} = 2.5^{+1.4}_{-0.9}$ K [183] with the JPA off, reducing to $T_{\rm n} = 0.25^{+0.14}_{-0.09}$ K with the JPA . The fact that the latter falls below typical shot noise levels [147] demonstrates one of the major advantages of SEBs over SETs.

4.4.1 JPA SETUP

To produce amplification, the JPA needs to be pumped applying some power $P_{\rm JPA}$ at frequency $\omega_{\rm pump}$ close to the JPA resonant frequency. This requires the addition of an extra fast line in the setup that delivers the pump tone to the JPA. This way, the setup includes three fast lines. The first one delivers the attenuated rf-tone into the device. Then a directional coupler is used so the reflected wave travels through a different line that includes the amplification chain. Finally, an extra line delivers the pump tone to the JPA. To avoid disturbing the device with the pump tone, an extra circulator is included between the JPA and the resonator (see Fig. 4.4.1).

The JPA used in this thesis was designed and fabricated by Dr A. Hasheem and Dr I. Siddiqi. It consists of a SQUID loop array shunted by a fixed capacitance, $C_{\rm JPA}$ [186] (See Fig. 4.4.2a). This configuration creates a low-quality factor ($Q_{\rm JPA} < 100$) superconducting resonator, whose resonant frequency, $\omega_{\rm JPA}$, can be tuned from 550-750MHz (See black line in Fig. 4.4.2b) by passing a current, $I_{\rm bias}$, through a nearby coil that modifies the flux through the SQUIDs.

4.4.2 JPA TUNING

Fig. 4.4.2c shows the variation of $\omega_{\rm JPA}$ as a function of the power applied to the JPA, $P_{\rm JPA}$. As $P_{\rm JPA}$ increases, $\omega_{\rm JPA}$ is firstly constant, but then it shifts to lower frequencies. Parametric amplification can be achieved in the power range in which $\omega_{\rm JPA}$ varies as a function of $P_{\rm JPA}$. The JPA amplification transfer function is exemplified in Fig. 4.4.2d, where small variations of the power arriving at the JPA due to the signal tone, $f_{\rm rf}$, are translated into large changes in the reflected phase. When the JPA is tuned at even higher pump powers, it becomes bistable [186].

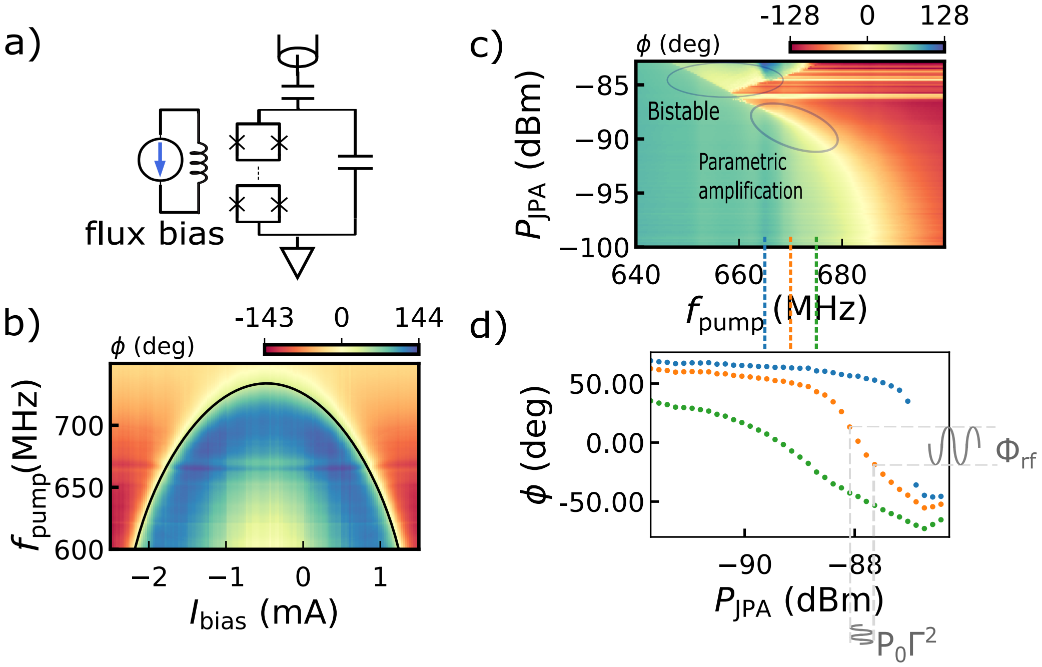

Figure 4.4.2: JPA tuning. a) Sketch of the JPA as a SQUID loop array in parallel with a shunted capacitance connected in reflection to the setup by a coupling capacitance. b) Reflected phase as a function of the pump frequency and I_{bias}. The resonant frequency, ω_{JPA}, is fitted to a function proportional to $\cosh^2(I_{\text{bias}})$ shown as a black line. c) Reflected phase as a function of the pump frequency and the power applied to the JPA. d) Amplification transfer function at 3 different frequencies (663 MHz in blue, 668 MHz in orange and 673 MHz in green). A small variation in the power arriving at the JPA leads to a large variation of the reflected phase, producing a gain.

.

There is a trade-off between the width of powers for which the amplification is linear (dynamic range) and the gain, given by the steepness of the transfer function. As observed in Fig. 4.4.2d, higher P_{JPA}s lead to a higher gain but a smaller dynamic range.

4.4.3 JPA AND LC RESONATOR

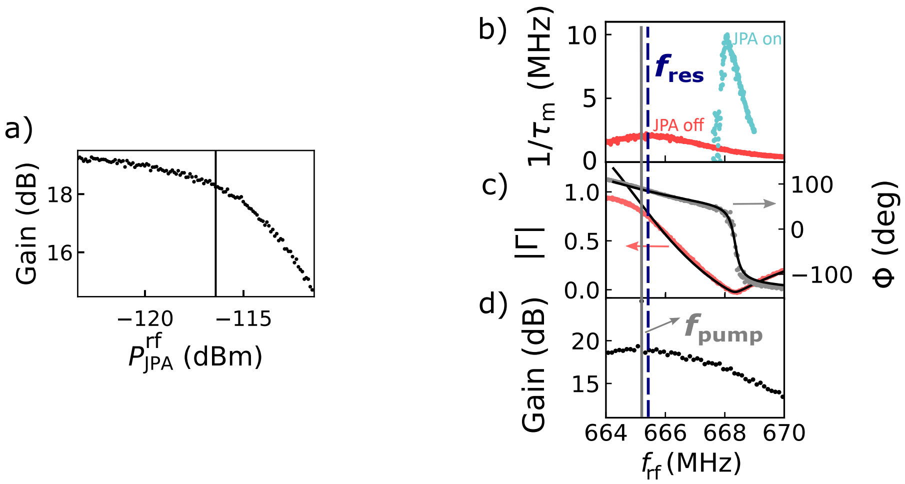

Figure 4.4.3: JPA and LC resonator. a) Gain as a function of the rf-probe power arriving to the JPA.The back vertical line at -116 dBm denotes the rf-power for a 1dB compression in gain. b) Inverse of the minimum integration time $1/\tau_{\mathrm{m}}$ as a function of f_{rf} without and with the JPA (red and blue respectively). The blue dashed line indicates the natural frequency of the resonator, f_{res}, which optimises sensitivity without the JPA. c) The reflection coefficient (magnitude $|\Gamma|$ (red) and phase Φ (grey)) at $B = 2$ T, shows a minimum at the frequency which optimises sensitivity with the JPA. d) The JPA gain decreases as f_{rf} moves away from the JPA pumping frequency, ω_{pump}, solid grey line, as determined by the JPA bandwidth of 19.2 MHz.

When implementing together rf measurements with a JPA the main factors to take into account are the JPA bandwidth, resonant frequency and dynamic range. The JPA is used in a phase preserving mode, for which the signal frequency, f_{rf}, is very similar but not equal to the pump frequency, $\omega_{\mathrm{pump}} = 2\pi f_{\mathrm{pump}}$. To produce amplification the rf-tone, $f_{\mathrm{rf}} \sim f_{\mathrm{res}}$, needs to fall within the JPAs bandwidth, B_{JPA}, so that $\Delta f = f_{\mathrm{pump}} - f_{\mathrm{rf}} < B_{\mathrm{JPA}}$. At the same time, this difference in frequency, Δf, can limit the measurement bandwidth, since noise at Δf appears in homodyne detection and needs to be filtered out with a low pass filter.

In terms of the dynamic range, Fig. 4.4.3a shows how increasing the power of the signal tone arriving at the JPA, $P_{\mathrm{JPA}}^{\mathrm{rf}} = P_0|\Gamma|^2$, leads to a gain reduction, since there is not enough pump energy to be transferred from the pump to the signal and idler. The power at which the gain is compressed by 1dBm is the JPA dynamic range (-116 dBm).

The importance of the small dynamic range is exemplified in Fig. 4.4.3b and c. When measuring at $f_{\mathrm{rf}} = 668$ MHz, where the reflection coefficient of the resonant circuit is at a minimum, we find $\tau_{\mathrm{m}} = 1$ μs and $\tau_{\mathrm{m}} = 100$ ns, for JPA off and on, respectively. Operating at this f_{rf}, where the reflected power, $P_0|\Gamma|^2$, is minimum becomes necessary to avoid driving the JPA beyond its 1 dB compression point, $P_{1\mathrm{dB}} = -116$ dBm. However, as can be seen in Fig. 4.4.1c, τ_{m} with the JPA off can be decreased by approximately a factor of two by adjusting the drive frequency f_{rf} to match f_{res}, which differs from the point of minimum reflected power in the total circuit (see Sec. 4.3.2). The overall achievable reduction in τ_{m} achieved using the JPA is, therefore, a factor of 4.5. These results emphasise the importance of a well-matched and high-Q resonator to minimise the reflected power to avoid saturating the JPA [183].

As explained above, the limit in measurement bandwidth is set by the difference Δf between the JPA pump frequency ($f_{\mathrm{pump}} = 665.2$ MHz) and f_{rf}, while the JPA gain falls as this difference increases (see Fig. 4.4.1d). For this specific experiment, a $\Delta f = 2.9$ MHz was selected, for which $G_{\mathrm{JPA}} = 17$ dB.

JPA back-action

In this subsection, we examined whether the effective electron temperature is increased when a JPA is included in our system. The JPA relies on a rf-frequency source that is used as a pump to amplify the signal ($P_{\mathrm{pump}}^{\mathrm{in}}$ in Fig. 4.4.1). The power from the rf-pump could potentially arrive at the SEB gate and act as a driving excitation. Such perturbation in its potential could affect the qubit dot due to the capacitive coupling between the SEB and the qubit dot.

Fig. 4.4.4 shows that the JPA does not have any effect on the SEB by looking at the width of the rf-response of a SEB electronic transition.

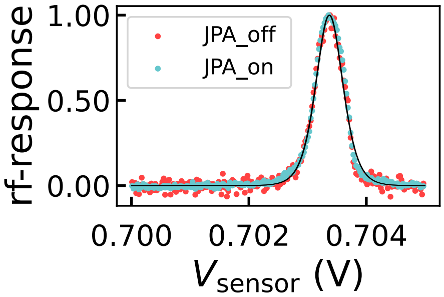

Figure 4.4.4: JPA back-action. Normalised rf response from a SEB as a function of the voltage applied to its gate obtained using a low rf-tone power, $P_0 = -91$ dBm. The width of the transition is related to the SEB-to-reservoir tunneling rate, leading to an upper limit of $\gamma \leq 74 \pm 12$ GHz. The same result is obtained with and without a JPA.

4.5 EFFECT OF THE EXTERNAL MAGNETIC FIELDS

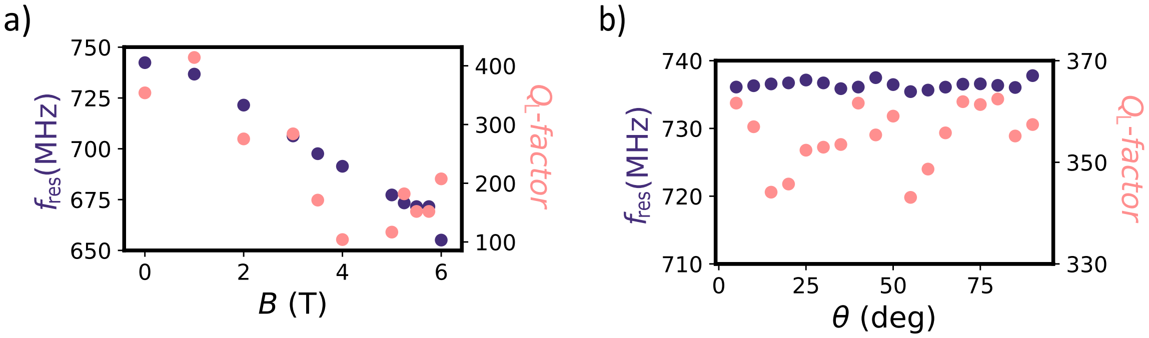

Figure 4.5.1: Resonator dependency on external field. a) Q_{L}-factor and resonant frequency of the resonator at different magnetic fields applied in the $[\bar{1}, 1, 0]$ crystallographic direction of the QD (see Sec. 5.1.1 for more information). The error bars are smaller than the scatter dots. b) Q_{L}-factor and inductance when 1 Tesla was applied in different directions. θ is the angle of the magnetic field with respect to $[\bar{1}, 1, 0]$ in the plane of the device.

Measurements of the electronic spin require static magnetic fields applied to the device. This magnetic field could potentially affect the behaviour of both the inductor used in the resonator and the JPA since both are made of superconducting materials. The inductor is glued to the PCB, close to the QD, where the magnetic field is maximum. Generally, as the magnetic field increases so does the inductance, L, affecting the matching and decreasing the loading factor (see Fig. 4.5.1a). However, charge measurements with rf-reflectometry were still performed at $B_z = 6$ T. The direction of the magnetic field (if applied parallel to the spiral inductor) does not modify the resonator drastically as shown in Fig. 4.5.1b.

The JPA is placed at 40cm from the centre of the magnetic field. In that location, the magnetic field reaches a maximum of 500G when a magnetic field of $B_z = 6$ T is applied to the QD. To protect the JPA and circulators from this magnetic field, they are enclosed on cryoperm shields that can repel fields of up to 1500 G.

4.6 SNR IMPROVEMENTS

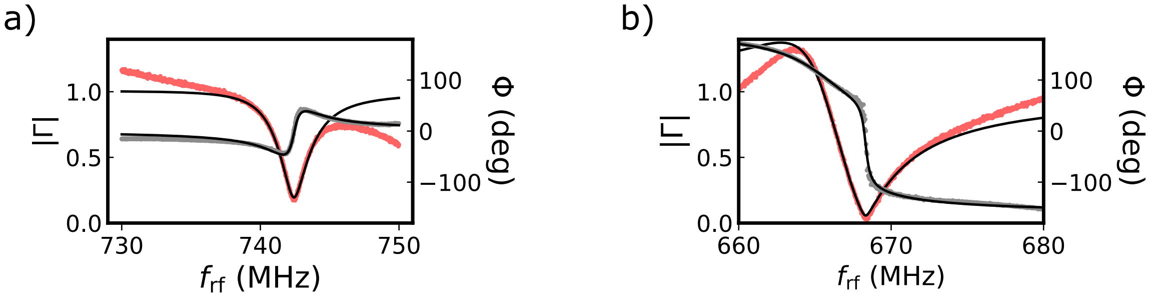

Figure 4.6.1: Resonator comparison. a) Reflection coefficient (magnitude $|\Gamma|$ (red) and phase ϕ (grey)) of the resonator used in [99](2020). b) Same for the resonator used in [98](2022).

This section compares the minimum integration time obtained in two different papers ([99] and [98]) measured during this thesis. Improvements in the signal-to-noise ratio (SNR) of the gate-based reflectometry were achieved by further optimising the resonator design to detect capacitance changes [239] and by lowering the noise floor through the use of a quantum-limited amplifier [183].

Fig.4.6.1 shows the resonators used in each experiment, whose extracted parameters are summarised in Table. 4.6.1. The results can be analysed in terms of the analytic expression for the minimum integration time (Eq. 4.20). The reduction of the parasitic capacitance due to a new PCB design and having a slightly overcoupled resonator improves the τ_{m} by a factor of 4 (See Table 4.6.1). Moreover, a careful assignment of the SEB and qubit dot based on the results from Table. 4.3.1 increased the SEB lever-arm from $\alpha_{\mathrm{SEB}} = 0.24$ to $\alpha_{\mathrm{SEB}} = 0.35$, improving τ_{m} by another x2 factor. The total theoretical improvement of τ_{m} is of a factor x7 due to a slight

Type	**Parameter**	Ciriano2020 [99]	Oakes&Ciriano2022 [98]	
			JPA off	**JPA on**
Resonator	β	0.7	2.5	2.5
	$C_{\text{tot}}(\text{fF})$	574	461	461
	$C_{\text{c}}(\text{fF})$	50	50	50
	$Q_{\text{int}}Z_{\text{r}} = R_{\text{D}}(\text{M}\Omega)$	0.25	1.15	1.15
	$f_{\text{r}} = \frac{1}{2\pi\sqrt{LC_{\text{tot}}}}(\text{MHz})$	742	668	668
SEB	α	0.24	0.35	0.35
	η	1	1	1
	γ (GHz)	5	74	74
	$T_{\text{e}}(\text{mK})$	230	137	137
Noise	$T_{\text{n}}(\text{K})$	2.5	2.5	0.25(0.56*)
Sensor	$\tau_{\text{m}}(\mu\text{s})$	9	0.45	0.1

Table 4.6.1: Summary of parameters relevant for SEB charge sensing. *Although the noise temperature with the JPA is 0.25K, the optimal SNR requires to work at a rf-frequency for which the SEB capacitance change is smaller, so that the effective temperature noise is 0.56K instead.

difference in the resonant frequencies.

However, the measured reduction of τ_{m} was larger, going from $\tau_{\text{m}} = 9$ μs to an optimised $\tau_{\text{m}} = 0.45$ μs. This is because, not only the resonator and lever-arm were optimised, but also the noise generated by the readout setup was systematically studied and reduced (see Sec. 3.3.2 for more information).

Finally, the addition of a JPA in the setup improved τ_{m} by an extra x4.5 factor by reducing the temperature noise, achieving a $\tau_{\text{m}} = 100$ ns, with a measurement bandwidth of B=0.49MHz. This optimised and compact charge sensing method allowed to achieve high-fidelity single-shot measurements of an electron spin in the qubit dot.

4.7 SNR AND τ_{m} EXTRACTION

To evaluate the readout performance, we send a 2-level pulse that varies the I-Q response between the top of the SEB to reservoir transition and the background (marked with red dots in Fig. 4.7.1a). A histogram of the pulse rf-response in the quadrature plane shows two separated circular distributions, each one corresponding to the top and background of the transition (See Fig. 4.7.1b).

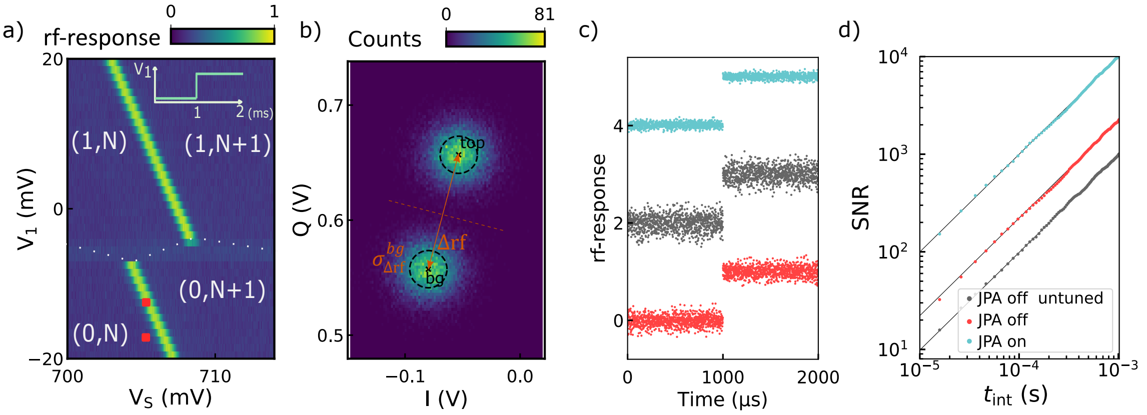

Figure 4.7.1: SNR extraction. a) Normalised rf-response showing the stability diagram of the SEB versus the qubit dot where the occupation of the SEB and the qubit dot is displayed as (qubit dot, SEB). Due to their cross capacitance, the rf-response has a shift in voltage when an electron is added to the qubit dot. The inset shows the pulses sent to *dot* to jump on and off the dot-to-reservoir transition, which corresponds to the red points. b) I-Q histogram from 1,000 data traces collected by pulsing between the red points marked in a). The histogram shows 2 distinct distributions corresponding to the background and the top of the SEB charge instability for data taken without a JPA. The signal is collapsed into 1D using the axis between the centre of the so-called Fresnel lollipops. c) Normalised rf response in the 1D-projection for JPA on, off and optimised JPA off for a measurement bandwidth $f_{\mathrm{eff,BW}} = 12$ kHz. d) SNR as a function of the integration time.

Since the noise is Gaussian and equal in every direction, most of the information is in the axis that joins the centres of the so-called Fresnel lollipops, whereas its perpendicular axis carries just noise. Therefore, we project our data on the optimal axis and use the SNR definition SNR $= \frac{\Delta\mathrm{rf}^2}{(\sigma_0^2+\sigma_1^2)/2}$, where Δrf is the distance between the lollipop centers and and $\sigma_{0(1)}$ is the 1-dimensional standard deviation of the background(peak).

Figure 4.7.1d shows SNR as a function of integration time with the JPA off tuned at its optimal point (red), JPA on (blue) and JPA off with the same settings used for the JPA on (grey). Using an extrapolation (black straight lines) we infer the integration time to have an SNR=1. These times are ${\tau_{\mathrm{m}}}^{\mathrm{off\,tuned}} = 451.1 \pm 0.1\,\mathrm{ns}$, ${\tau_{\mathrm{m}}}^{\mathrm{off}} = 1.015 \pm 0.001\,\mu\mathrm{s}$, ${\tau_{\mathrm{m}}}^{\mathrm{on}} = 100.4 \pm 0.8\,\mathrm{ns}$. This way, the noise temperature is reduced by a factor of x10 when switching the JPA on. However, the frequency at which this is achieved is not the optimal frequency, i.e. the natural frequency of the oscillator. The SNR when the JPA is off can be improved by a factor of x4.5 by choosing the optimal f_{rf} as it is showed in Fig.4.4.3b. This is a consequence of the higher reflected power at f_{res} that saturates the JPA reducing its gain.

4.7.1 Experimental bandwidth

The minimum integration time, τ_{m}, can be calculated as $\tau_{\mathrm{m}} = \tau_{\mathrm{int}}/\mathrm{SNR}$. The previous section explained how to obtain the SNR, whereas this section describes how to determine the bandwidth, and in turn the integration time, of a given measurement. To do so, the results and setup from [98] are used as an example.

Although the bandwidth of an rf experiment is ultimately limited by the resonator bandwidth ($\frac{f_{\mathrm{r}}}{Q_{\mathrm{L}}} = 6.18 \pm 0.04$ MHz), a low-pass filter can be introduced to reduce high-frequency noise, improving the SNR at the cost of reducing the measurement bandwidth.

To characterise the measurement bandwidth, we can obtain the effective noise bandwidth as

$$\omega_{\mathrm{eff,BW}} = \int_0^\infty \left|\frac{H(j\omega)}{H_{\max}}\right|^2 d\omega, \tag{4.27}$$

which corresponds to the bandwidth of a brick-wall filter that produces the same integrated noise power. Here, $H(j\omega)$ is the filter transfer function, and $H_{\max}$ is its maximum.

In this experiment, a (minicircuits BLP-1.9+) low pass filter was used, whose transfer function was obtained from its insertion loss provided by the manufacture as

$$\text{Insertion loss (dB)} = 10\log_{10}\left|\frac{V_{\mathrm{i}}}{V_{\mathrm{f}}}\right|^2 = -20\log_{10}|H_{\mathrm{MC}}(j\omega)|, \tag{4.28}$$

where V_{i} and V_{f} are the filter input and output voltage, respectively.

After that filter, a digital boxcar filter that averages every ten points (N=10) is applied, followed by a decimation process, to reduce the sample rate from 10 MHz to 1 MHz. This way, the total transfer function is equal to $|H_{\mathrm{total}}(j\omega)| = |H_{\mathrm{MC}}(j\omega)H_{\mathrm{BC}}(j\omega)|$, where H_{BC} is the transfer function of the boxcar filter. The combination leads to the filter depicted in Fig. 4.7.2, with an effective noise bandwidth of $f_{\mathrm{eff,BW}} = \frac{\omega_{\mathrm{eff,BW}}}{2\pi} = 0.49$ MHz.

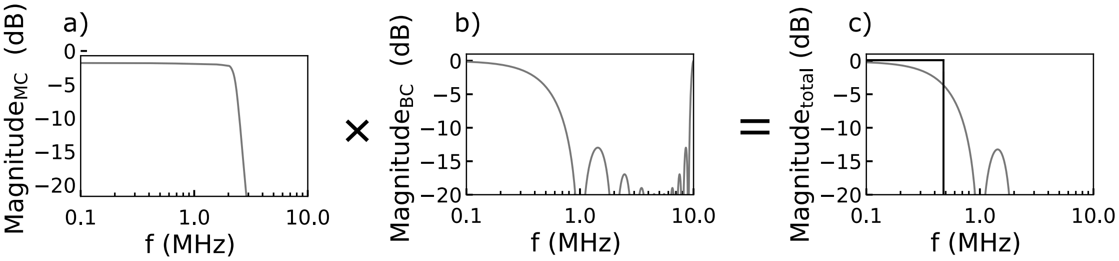

Figure 4.7.2: a) Bode diagram of the magnitude of the 8th-order minicircuits BLP-1.9+ filter utilised in our measurements. b) Same for the boxcar filter used to downsample the sample rate from 10 MHz to 1 MHz. c) Combination of the effects from both filters and equivalent brickwall filter with the same integrated noise power, showing an effective noise bandwidth of $f_{\mathrm{eff,BW}} = 0.49$ MHz.

Moving average filter

The SNR can be increased in post-processing by adding an additional low-pass filter, which removes high-frequency noise. From the many digital filters available, we used the rolling average filter which takes the average over N points recursively. The first point of the filtered signal corresponds to the mean of the first N points from the original signal and the subsequent points are obtained by shifting forwards by one time step the subset of N points that are averaged. This additional filter modifies the total transfer function as $|H_{\mathrm{total}}(j\omega)| = |H_{\mathrm{MC}}(j\omega)H_{\mathrm{BC}}(j\omega)H_{\mathrm{RF}}(j\omega)|$, where $H_{\mathrm{RF}}(j\omega)$ is the rolling average transfer function.

Although the rolling average has a complicated frequency dependence (See Fig. 4.7.2b), it is ideal for this application since it has one of the lowest computation times and is optimal for reducing random noise while retaining a sharp step response [245].

4.8 CONCLUSIONS

The culminating result of this chapter demonstrates a gate-based SEB with a $\tau_{\mathrm{m}} = 100$ ns and a measurement bandwidth of B=0.49 MHz, providing a route to combine high-fidelity charge sensing of semiconductor-based qubits with the demands of a compact and scalable architecture. To maximise the SNR, two strategies were followed: minimising the noise power and maximising the signal power. The parameters that have the highest impact on the signal power, with a quadratic dependence, are the charge sensing regime (quantified by η, the fractional change in ΔC due to a charge sensing event), the gate lever arm of the SEB, α, and the operation frequency, $f_{\mathrm{rf}} \sim f_{\mathrm{res}}$ (although f_{rf} cannot be increased indefinitely, otherwise electron tunneling to and from the SEB may not occur). Moreover, low-loss, high-impedance resonators close to critical coupling are desired for a large signal power.

Resonators with large resonant frequencies and high impedance can be achieved by reducing the parasitic capacitances and parasitic losses. To do so, this implementation included a superconducting spiral inductor together with an optimised PCB. However, to further minimise C_{p}, the resonator topology can be swapped for a resonator with inductive coupling [239]. Moreover, the surface mount resonator can be replaced by an on-chip microwave resonator, in which the smaller size of the components and wire bonds creates a lower C_{p}. Furthermore, in the case of superconducting on-chip resonators, the losses are dominated by the device semiconductor substrates, producing resonators with larger Q-factors of around $Q_{\mathrm{L}} \sim 2000$ [226, 246]. However, despite the aforementioned advantages, on-chip resonators add complexity to the fabrication and implementation.

At the device level, the key parameter is the lever arm, which can be increased by reducing the gap between the gate and the quantum dot using a small gate oxide thickness (like the 6 nm of $\mathrm{SiO_2}$ from the devices used in this thesis) or using thin high-k dielectrics, although charge traps in the interface between the gate and the high-k dielectric might affect negatively to the device reproducibility. Another route for improvement is to use thin silicon on insulator (SOI), like in these devices, in which the active region is a thin layer of material so that the dot is created in close proximity to the gate. An additional increment in α can be achieved with a device geometry that makes the gate surface near the SEB maximal. An example of an optimal geometry is the nanowire geometry used here, where the gates are wrapped around the SEB.

The second strategy to optimise the SNR is to reduce the noise power created during amplification with the help of quantum-limited amplifiers. In this front, SEBs demonstrate a major advantage over SETs since the noise can be reduced below the typical values of the shot noise levels that limit SETs [147]. Concerning the results presented in this chapter, the noise performance could be further enhanced by using the JPA in phase-sensitive mode, reaching the quantum limit. Moreover, incorporating a TWPA would eliminate the JPA power restrictions due to its smaller dynamic range, allowing it to operate at the f_{rf} for higher sensitivity, leading to an x2 SNR improvement.

In terms of scalability, SEBs, consisting of just two terminals (charge island and a single reservoir), have gained considerable traction [107, 155, 177, 178] as a more scalable alternative to the standard three-terminal charge sensors (QPCs and SETs). However, the size of the resonator, which must be placed close to the device, will pose a challenge as the number of sensors increases [77]. Currently, the resonator footprint has a lower limit of 100x100μm^2 given by the inductor size [246], although it could potentially be reduced to sub μm using high-inductance-density materials [247, 248].

5

Readout of a single spin using a SEB

Qubit readout can become the bottleneck in quantum computation since the fidelity of any qubit operation is limited by the quantum state readout. Moreover, QEC requires the constant readout of qubits with high fidelity. This chapter shows a demonstration of spin readout of a single electron in a quantum dot through spin-dependent tunnelling, detected using an adjacent SEB as a charge sensor.

The experiments were performed in three different devices that we call devices A, B and C and which dimensions are summarised in Table 3.1.1 and 4.3.1. Devices A and B were fully characterised in [99]. To do so, we performed excited state spectroscopy of the quantum dot and measured the spin relaxation time (T_1) as a function of the magnetic field magnitude and orientation. We measured T_1 up to 9 ± 3 seconds — to our knowledge the longest measured so far for silicon quantum dots (at the time of publication). The experiments performed in device C are published in [98] and focus on single-shot spin readout. In this latter experiment, single-shot was possible due to the improvements in the charge sensor SNR explained in Chapter 4.

5.1 Spin readout

The quantum dots are formed on opposite corners of a silicon split-gate NW-FET, fabricated using CMOS-compatible processes in CEA-Leti. One of them acts as a SEB that is used to read the electron spin in the other dot, so-called 'qubit' dot. As shown in Fig. 5.1.1, the two quantum dots are tunnel-coupled (in a parallel configuration) to self-aligned, heavily implanted, n-type source and drain electron reservoirs, and capacitively coupled to each other. The number of electrons in the qubit dot is defined as n_{q} and the one in the SEB as n_{s}.

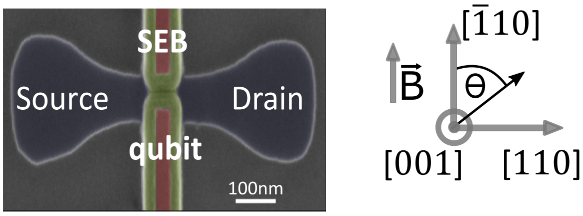

Figure 5.1.1: Device and measurement setup. False-colour transmission electron micrograph of a silicon nanowire with a pair of split gates. Quantum dots are formed under each gate, referred to as SEB and 'qubit' dot, and controlled respectively by V_{S} and V_{Q}. To lift the spin degeneracy, a magnetic field is applied in the [$\bar{1}$10] crystallographic direction, perpendicular to the nanowire. The magnetic field orientation can be rotated in the plane of the device, making an angle θ to [$\bar{1}$10].

Once the qubit dot is depleted to its last electron (see Sec. 4.3 for more information), the spin degeneracy is lifted by applying a magnetic field in the plane of the device and perpendicular to the nanowire, in the [$\bar{1}$10] crystallographic direction. To measure the spin orientation, we apply a 3-level voltage pulse to the qubit dot gate (see Fig. 5.1.2a). First, the qubit dot is emptied so an electron with a random spin polarisation can be loaded from the reservoir. Then, at the readout stage, the reservoir Fermi energy, E_{F}, lies in between the spin $|\uparrow\rangle$ and $|\downarrow\rangle$ states, so a spin $|\uparrow\rangle$ electron can tunnel out from the dot to the reservoir and be subsequently replaced by a spin $|\downarrow\rangle$ electron, whereas a spin $|\downarrow\rangle$ electron remains in the qubit dot [145]. This spin-dependent tunnelling is detected using the SEB when tuned to a point in the stability diagram where the reflectometry signal depends on the qubit dot electron occupation.

Useable 'read' points are those where the SEB rf-response is strongly dependent on the qubit dot electronic occupation. Two such points can be identified in Fig. 5.1.2d labelled ‘AR’ and ‘BR’. At ‘BR’, a reflectometry signal is visible only when the qubit dot is empty. In this case, the signature of a spin $|\uparrow\rangle$ electron on the qubit dot is the brief emergence of a reflectometry signal at the read point, as the electron tunnels out of the dot (and a new spin $|\downarrow\rangle$ tunnels in). Conversely, at ‘AR’, a reflectometry signal is visible only when the qubit dot is occupied, in which case the signature of spin $|\uparrow\rangle$ is a transient reduction in the signal. Experiments on devices B and C used point ‘BR’ for readout, while those on device A used the point ‘AR’. Fig. 5.1.2c shows the ideal one-shot traces and the measured spin readout traces averaged over 1024 ‘ELR’ cycles at both ‘AR’ and ‘BR’ (see sec. 5.5 for device C single shot traces).

Detecting the spin-dependent transient signals requires that the tunneling rate Γ_0 between the qubit dot and reservoir falls within the resonator bandwidth. The resonator Q-factor in these experiments was magnetic field-dependent leading to a detection bandwidth in the range of 1.4–5.0 MHz. Dot-to-reservoir tunnelling rates in these devices can be tuned by applying a voltage to a global metal top-gate (not shown in Fig. 5.1.1a) or to the substrate [107, 230]. We applied 0 V and -10 V to the metal top gate for Devices A and B respectively, with the substrate at 0V, to achieve suitably low tunnelling rates: $\Gamma_{0,\mathrm{g_A}} = 0.62(1)$ MHz for device A and $\Gamma_{0,\mathrm{g_B}} = 0.97(1)$ MHz for device B. On the other hand, Device C had tunneling rates of around $\Gamma_{0,\mathrm{g_C}} = 0.005(1)$ MHz with a top gate voltage of 7 V. The slower tunneling rates in device C and the improvement in the SNR made single-shot possible.

5.1.1 READOUT OFFSET TUNING

Observing spin-dependent tunnelling requires careful tuning of the qubit gate offset voltage, V_Q. Figs. 5.1.3a and 5.1.3e show the time-dependent normalised demodulated phase at the ‘read’ stage of the 3-level sequence, for different V_Q, each averaged 1024 times. For low offsets, the electron tunnels out of the qubit dot regardless of the spin state (Fig. 5.1.3d), whereas for higher offset voltages it always remains in the dot (Fig. 5.1.3 b). At intermediates offsets, only electrons with spin-up can tunnel out, producing the observed spin-dependent feature. Due to the choice of different readout points in the stability diagram, the rf signal for device A is maximal when an electron is present in the qubit dot, while for device B the rf signal is maximal for

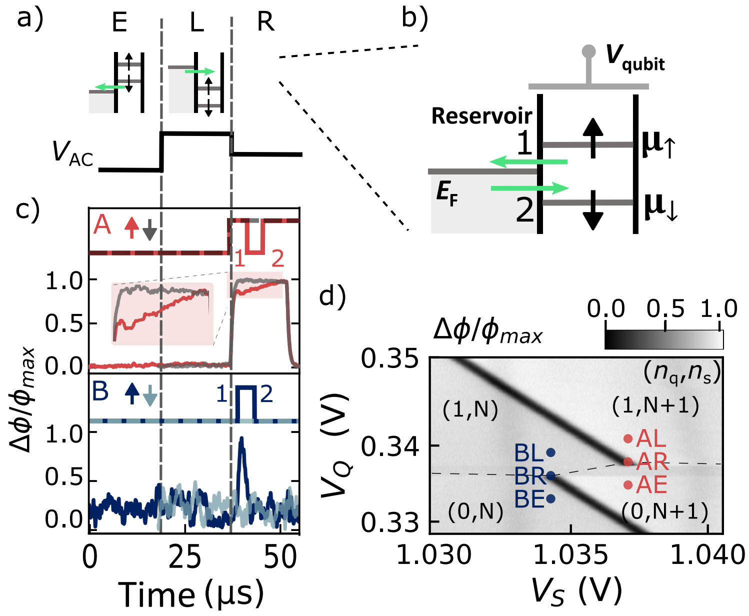

Figure 5.1.2: Spin readout. a) 3-level pulse sequence applied to the qubit dot gate: first emptying the dot (E), then loading an electron with a random spin orientation into the dot (L) and finally reading the spin state (R). b) For spin readout, the qubit dot potential is tuned so its spin-up and spin-down states straddle the reservoir Fermi energy. A spin-down electron remains in the qubit dot, whereas a spin-up electron tunnels out (1) followed by a spin-down electron entering the dot (2). c) Single shot schematics and time-averaged measured phase response (1024 averages) for device A (red), and B (blue), where the spin up signature is respectively a dip or a peak in the phase response. d) Charge stability diagram of the double quantum dot near the $(n_q, n_s) = (1, N) \leftrightarrow (0, N + 1)$ charge transition for device B (device A measurements used a nominally identical charge transition).

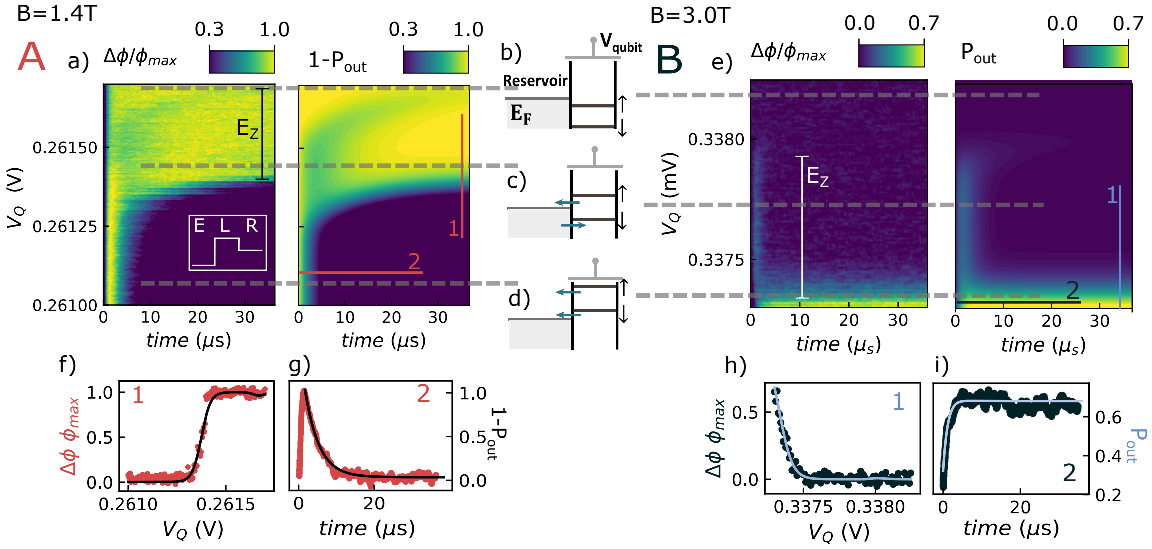

Figure 5.1.3: Readout offset tuning. a) Left: Normalised phase response of the resonator over time in the readout stage at different V_Q offsets for device A. The pulse sequence is depicted in the inset. Right: Simulation for an applied magnetic field of 1.4 T. The simulation takes into account the mismatch between the bias tee cutoff frequency and the compensated pulse. b) Same for device B at B=3T. b),c) and d) diagrams of the qubit dot electrochemical potential as a function of the lead Fermi energy at three different offsets. At offset b) The electron remains in the dot. In c) only spin up electrons can tunnel out from the dot and, shortly afterwards, an electron with spin down comes back to the dot. In d) the electron always tunnels out. f) Dot occupation number along line *1* comparing measurement (dotted) with simulation (line) for device A. g) Dot occupation number as a function of time at low offsets along line *2*. The phase rise time due to the resonator bandwidth corresponds to the first microsecond of the graph. Panels e), h) and i) show corresponding data and simulation for device B.

the empty qubit dot.

SPIN-READOUT SIMULATIONS

We now simulate the qubit dot tunneling events to try to obtain the same behaviour as the one pictured in Fig. 5.1.3a and e. The averaged demodulated signal during the readout stage is proportional to the expected number of electrons in the qubit dot [249]. We model the qubit dot occupancy using a rate equation that considers three possible states: spin up (in the qubit dot), spin down (in the qubit dot), or no electron in the qubit dot. The ratio at which the levels are populated/emptied is given by their respective tunnel rates. The tunnelling rates depend on V_Q, the electron temperature and the natural tunnel rate Γ_0 which we take to be spin-independent. Assuming elastic tunnelling and that the reservoir has a continuous energy spectrum, the dot to reservoir tunnelling rate follows a Fermi-Dirac distribution [250]:

$$\Gamma_{\mathrm{in(out)}} = \frac{\Gamma_0}{1 + \exp\left[+(-)\Delta E / k_\mathrm{B} T\right]}. \tag{5.1}$$

Here, k_B is Boltzmann's constant and ΔE is the energy difference between the relevant dot state and the lead Fermi energy. $\Delta E = |e|\alpha_\mathrm{QQ}(V_\downarrow - V_\mathrm{Q})$ for the spin down state and $\Delta E = |e|\alpha_\mathrm{QQ}(V_\downarrow + E_\mathrm{z} - V_\mathrm{Q})$ for the spin up state, where $V_\downarrow$ is the voltage at which the $|\downarrow\rangle$ state and reservoir potentials align, e is the electron charge, α_QQ is the lever arm of the qubit gate on the qubit dot, and E_z is the Zeeman energy. Therefore, four different tunneling rates can be defined: $\Gamma_\downarrow^\mathrm{in}$,$\Gamma_\downarrow^\mathrm{out}$,$\Gamma_\uparrow^\mathrm{in}$ and $\Gamma_\uparrow^\mathrm{out}$, i.e. two per dot state.

During the read stage, the sum of the probabilities of finding the electron in the dot with a spin up, $N_\uparrow$, with a spin down, $N_\downarrow$, or out of the dot, N_out, remains constant (and equal to one) such that the time dependent derivative of the total electronic number is equal to zero: $\frac{dN_\mathrm{total}}{dt} = \frac{dN_\mathrm{out}}{dt} + \frac{dN_\uparrow}{dt} + \frac{dN_\downarrow}{dt} = 0$.

The rate equation can be summarised by the following system of differential equations:

$$\begin{aligned}\frac{dN_\uparrow}{dt} &= -\Gamma_\uparrow^{\text{out}} N_\uparrow + \Gamma_\uparrow^{\text{in}} N_{\text{out}} \\ \frac{dN_\downarrow}{dt} &= -\Gamma_\downarrow^{\text{out}} N_\downarrow + \Gamma_\downarrow^{\text{in}} N_{\text{out}} \\ \frac{dN_{\text{out}}}{dt} &= \Gamma_\uparrow^{\text{out}} N_\uparrow + \Gamma_\downarrow^{\text{out}} N_\downarrow - (\Gamma_\downarrow^{\text{in}} + \Gamma_\uparrow^{\text{in}}) N_{\text{out}}\end{aligned} \tag{5.2}$$

When the system of differential equations is rewritten as a matrix, its solution has the general form:

$$\begin{pmatrix} N_\uparrow \\ N_\downarrow \\ N_{out} \end{pmatrix} = x e^{v_1 t} \vec{v}_1 + y e^{v_2 t} \vec{v}_2 + z e^{v_3 t} \vec{v}_3, \tag{5.3}$$

where $\vec{v}_1$, $\vec{v}_2$ and $\vec{v}_3$ are the matrix eigenvectors and v_1, v_2 and v_3 their correspondent eigenvalues given by:

$$\begin{aligned} v_1 &= 0 \\ v_2 &= \frac{1}{2}(-4\Gamma_0 - \sqrt{(4\Gamma_0)^2 - 4(\Gamma_\uparrow^{\text{in}}\Gamma_\downarrow^{\text{out}} + \Gamma_\uparrow^{\text{out}}(\Gamma_\downarrow^{\text{out}} + \Gamma_\downarrow^{\text{in}}))}) \\ v_3 &= \frac{1}{2}(-4\Gamma_0 + \sqrt{(4\Gamma_0)^2 - 4(\Gamma_\uparrow^{\text{in}}\Gamma_\downarrow^{\text{out}} + \Gamma_\uparrow^{\text{out}}(\Gamma_\downarrow^{\text{out}} + \Gamma_\downarrow^{\text{in}}))}). \end{aligned} \tag{5.4}$$

x, y and z are the constants determined by the initial conditions. Here, it is assumed that the qubit dot is always emptied during the empty stage and populated after the load stage such that the readout initial conditions include an electron in the dot with a random spin polarisation:

$$\begin{aligned} N_\uparrow(t=0) &= 1/2 \\ N_\downarrow(t=0) &= 1/2 \\ N_{\text{out}}(t=0) &= 0. \end{aligned} \tag{5.5}$$

These assumptions are based on the fact that the measured tunnelling times are much shorter than the duration of the pulses. The averaged demodulated phase is proportional to the expected dot occupation number, $1 - N_{\text{out}}$, for device A and to N_{out} for device B.

Properties of the system can be obtained by examining the behaviour in particular regimes where the dynamics can be simply understood. First, at low offsets the dot state is well above the lead Fermi energy (see line-cut 2 in Fig. 5.1.3a). In this regime, $\Gamma_{\downarrow}^{\text{in}}$ and $\Gamma_{\uparrow}^{\text{in}}$ tend to zero, whereas $\Gamma_{\downarrow}^{\text{out}}$ and $\Gamma_{\uparrow}^{\text{out}}$ reach their maximum value, Γ_0, which can thus be obtained by fitting the demodulated phase over time to an exponential decay (See Figs. 5.1.3g and 5.1.3i). In this way, we obtain tunneling rates $\Gamma_{0,\text{A}} = 0.624 \pm 0.011$ MHz for device A and $\Gamma_{0,\text{B}} = 0.970 \pm 0.012$ MHz for device B.

Second, by observing the demodulated phase as a function of V_{Q} after some time has passed (line-cut 1 in Fig. 5.1.3a), the *effective* temperature in the qubit dot can be inferred. The dynamics are initially described by the complete model described in Eq. 5.3, however, the effect of the negative eigenvalues fades away over time and the term $\vec{N} = x\vec{v}_1$ dominates the dot occupation. For the given initial conditions, this steady-state term reads:

$$N_{\text{out}}(t = \infty) = \frac{\Gamma_{\uparrow}^{\text{out}}\Gamma_{\downarrow}^{\text{out}}}{\Gamma_{\uparrow}^{\text{in}}\Gamma_{\downarrow}^{\text{out}} + \Gamma_{\uparrow}^{\text{out}}(\Gamma_{\downarrow}^{\text{out}} + \Gamma_{\downarrow}^{\text{in}})}, \tag{5.6}$$

which for the condition $\frac{E_z}{k_B T} >> 1$ simplifies to $N_{\text{out}}(t = \infty) = \frac{\Gamma_{\downarrow}^{\text{out}}}{\Gamma_0}$. Therefore, the demodulated phase with respect to V_{Q} was fitted to $1 - \Gamma_{\downarrow}^{\text{out}}/\Gamma_0$ for device A and $\Gamma_{\downarrow}^{\text{out}}/\Gamma_0$ for device B (See Figs. 5.1.3f and 5.1.3h). From these fits we found an effective temperature of 0.157 ± 0.012 K for device A and 0.275 ± 0.022 K for device B (see Sec.5.1.2 for full discussion of the origin of this effective temperature and noise sources).

The Zeeman splitting, E_{z}, was calculated from the width in voltage of the spin-dependent 'tail' seen in Figs. 5.1.3. The Zeeman splitting is plotted for different magnetic fields in Fig. 5.1.5.

To improve the fit to the data, the simulations of device A (Figs. 5.1.3b and 5.1.4) include a voltage drift over time due to a cutoff frequency miscalculation of the bias tee high pass filter (nominally taken to be 16 kHz, but fitted to be 15.915 kHz). This small frequency mismatch does not affect measurements of the spin relaxation time.

Readout tests

Here, we perform several tests to ensure that we were measuring the electron spin and it was not a different effect.

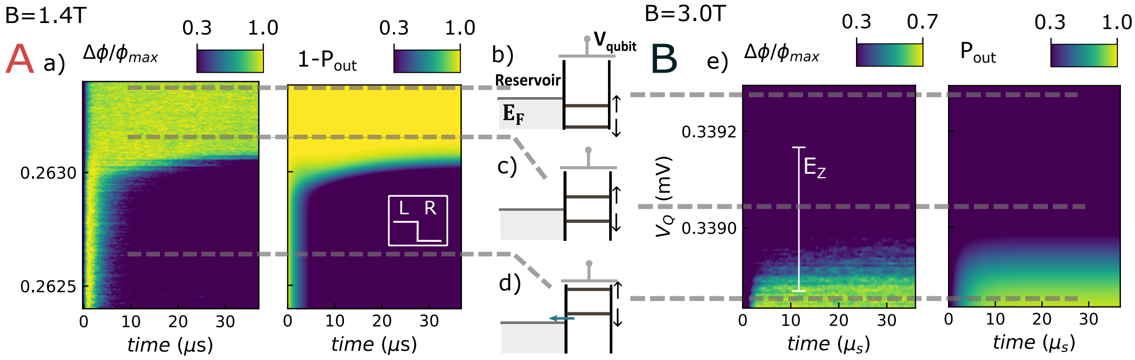

Figure 5.1.4: Two-level pulse sequence Two-level pulse sequence based on 'load' and 'read'. a) Demodulated phase over time in the readout stage normalised at each V_Q offset for device A (left) and its simulation (right) for an applied magnetic field of 1.4T. The pulse sequence is depicted in the inset. It can be observed how the 2-level pulse does not generate a spin tail. b), c) and d) show diagrams of the qubit dot electrochemical potential with respect to the lead Fermi energy at three different pulse offsets, V_Q. e) Same as for panel (a), but for device B at $B = 3$ T.

Two-level pulse sequence (load-read only). First, we sent a modified version of the pulse sequence with which the spin signature should disappear. In this version, the 'empty' stage is removed from the pulse sequence to leave just the 'load' and 'read' steps. This way, the dot remains occupied unless the electron tunnels out during the read stage. In this two-level pulse sequence, the electron in the dot eventually decays to the spin-down ground state, so that no spin up signature is observed (see Fig. 5.1.4 for measurements and simulations). This way the initial conditions

$$\begin{aligned} N_{\uparrow}(t=0) &= \frac{\Gamma_{\downarrow}^{\text{out}}}{2\Gamma_0} \\ N_{\downarrow}(t=0) &= 1 - N_{\uparrow}(t=0) \\ N_{out}(t=0) &= 0, \end{aligned} \tag{5.7}$$

used input in the system of equations from Eq. 5.2 to obtain the simulations presented in Fig. 5.1.4.

Magnetic field dependence. To further test the spin readout measurements, we measure the Zeeman splitting as a function of the magnetic field. The Zeeman splitting is related to the width in voltage of the spin-dependent 'tail' from Figs. 5.1.3a and 5.1.3e as $E_{\mathrm{Z}} = g\mu_{\mathrm{B}}B = e\alpha_{\mathrm{QQ}}\Delta V_{\mathrm{Q}}$, where g is the g-factor, μ_{B} is the Bohr magnetron, B is the magnetic field, α_{QQ} is the qubit alpha factor and ΔV_{Q} is the spin tail length in voltage.

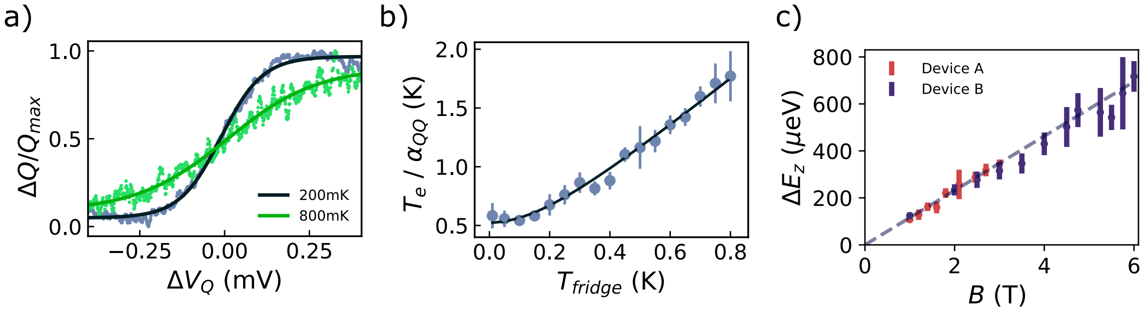

Figure 5.1.5: Qubit dot lever arm from temperature measurements. a) Homodyne I/Q voltage as a function of ΔV_Q, at fridge temperatures of 200 and 800 mK for device B. b) Width of the Fermi-Dirac distribution measured in a) as a function of the fridge temperature and fit. c) Zeeman energy obtained as $\Delta E_{\mathrm{z}} = e\alpha_{\mathrm{QQ}}V_{\mathrm{Q}}$ from Fig. 5.1.3a, where QQ is the lever arm calculated in b). Dashed line shows the Zeeman energy for $g = 2$.

We observed that, as expected, ΔV_{Q} is proportional to the magnetic field applied. Moreover, to obtain the g-factor (which should be similar to $g \sim 2$) we first calculate the qubit dot lever arm, α_{QQ}. The qubit dot lever arm is determined with a temperature study in which the qubit dot occupation number is fitted as a function of V_{Q} to a Fermi distribution at different fridge temperatures, as in Figs. 5.1.5a. At low temperatures, the broadening is constant and, as the temperature in the fridge is raised, it increases linearly as a function of the fridge temperature (see Fig. 5.1.5b). In this way, the temperature can be related to the transition broadening as $k_{\mathrm{B}}T_{\mathrm{e}} = e\alpha_{\mathrm{QQ}}V_{\mathrm{Q}}$ and can be fitted to $T_{\mathrm{e}} = \sqrt{T_0^2 + T_{\mathrm{fridge}}^2}$ [251]. We obtained a base electron effective temperature $T_0 = 230 \pm 9$ mK and a $\alpha_{\mathrm{QQ}} = 0.478 \pm 0.008$.

The relation between Zeeman energy and magnetic field is shown in Fig. 5.1.5, leading to a g-factor $g = 1.92 \pm 0.11$.

5.1.2 Effect of the rf-carrier on spin readout

To differentiate between spin states and achieve spin readout, the Zeeman splitting, $E_z = g\mu_{\mathrm{B}}B$ must be greater than the broadening of the $0 \rightarrow 1$ charge transition in the qubit dot depicted in Fig. 5.1.5a. The same as with a SEB, the broadening of the transition has at least two different sources: 1) the reservoir electron temperature and 2) the perturbations in its potential produced by the rf-carrier via cross capacitance to the SEB gate. These noise sources limit the minimum magnetic field at which the spin state can be accurately determined.

Here, we study how the power from the rf-carrier sent to the SEB gate affects the ‘qubit’ dot potential. The RF readout tone applied to the SEB can be transferred to the qubit dot due to the cross capacitance between dots or a direct capacitance between the sensor gate and the qubit dot: $\mu_{\mathrm{Q}} = \frac{\alpha_{QS}}{\alpha_{SS}}\Delta\mu_{\mathrm{S}}$. In Fig. 5.1.6 we compare i) the broadening measured on the SEB that has been converted to an expected qubit dot broadening, with ii) a direct measurement of the qubit dot broadening as in Fig. 5.1.5a. We observe that increasing the RF readout power, increases the perturbation for both methods, however, they lead to a different natural width. This suggests that the predominant broadening at lower power does not come from the electron temperature, since it should be the same under both measurements, but from the tunneling rates which are higher in the SEB (5 GHz for the SEB versus $\sim$ 0.5 MHz for the qubit dot). At higher powers, such as the one used for spin readout ($P_0 =$ -83 dBm), we can deduce that the major contribution to line broadening (and thus effective temperature) comes from the RF tone used for readout. The contribution from the RF tone can be reduced by optimising the resonator so less power is needed to show a measurable phase shift [175] and/or using cryogenic amplifiers with lower noise temperature such as a Josephson parametric amplifier [183] allowing operation at lower RF power due to a decreased noise level. Moreover, although the coupling capacitance between dots is necessary for this readout, the cross capacitance between the sensor gate and the quantum dot should be as small as possible.

The reflectometry signal was optimised by selecting the power that gave the highest visibility of the spin-up fraction. Fig. 5.1.6b shows a comparison of the spin-up fraction for two RF powers. The spin-up signature is more visible at higher powers up to a point where the power broadening counteracts the increment in the signal.

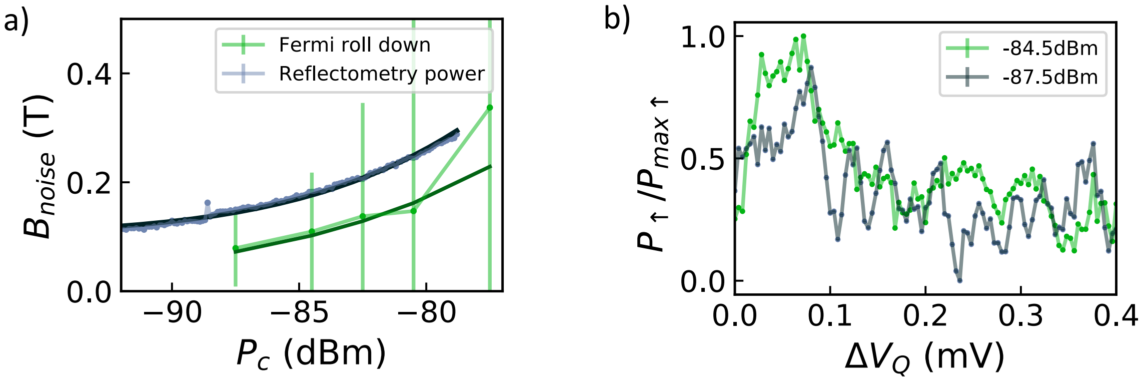

Figure 5.1.6: Effect of the rf-carrier power on spin readout. Perturbation of the qubit dot electrochemical potential, given in Tesla, due to the rf-carrier power, P_0. a) Blue: Electronic transition half width maximum, $\epsilon_{\frac{1}{2}}$ of the SEB, converted to a qubit dot potential using the cross lever arm α_{QS}. Error bars are smaller than the dot size. Green: A direct measurement of broadening obtained by sweeping the qubit dot voltage (see Fig. 5.1.5a). b) Spin-up fraction for different powers at 1 T.

5.2 Spin relaxation

We next consider the effect of spin relaxation by varying the duration of the 'load' period in the 3-level pulse sequence. The spin of the loaded electron relaxes from its initial randomised state into the spin $|\downarrow\rangle$ ground state with a time constant T_1. Once an electron is loaded to the dot, the probability of finding a spin-up state decreases exponentially with respect to the time waited before reading its state following $\frac{P_\uparrow(t_{\mathrm{wait}})}{P_\uparrow(0)} = e^{-(t_{\mathrm{wait}}/T_1)}$. Figs. 5.2.1a and 5.2.1b show the exponential fitting for several magnetic fields in device A and device B. We also test whether the rf-carrier affects the relaxation during the 'wait' period. Fig. 5.2.1c shows a comparison of the relaxation times measured in device B when the RF readout tone remains on throughout the 3-level pulse (purple) versus switching off the rf-carrier during the waiting time (red). The similar values can be explained because the RF voltage only introduces an effective level broadening corresponding with a voltage drive at the frequency of the rf-carrier (742 MHz). Although this broadening is measured as an *effective* temperature, it is unrelated to the bath electron temperature and unlikely to affect the spin of the electron, with a Zeeman splitting larger than 28 GHz (B=1 T).

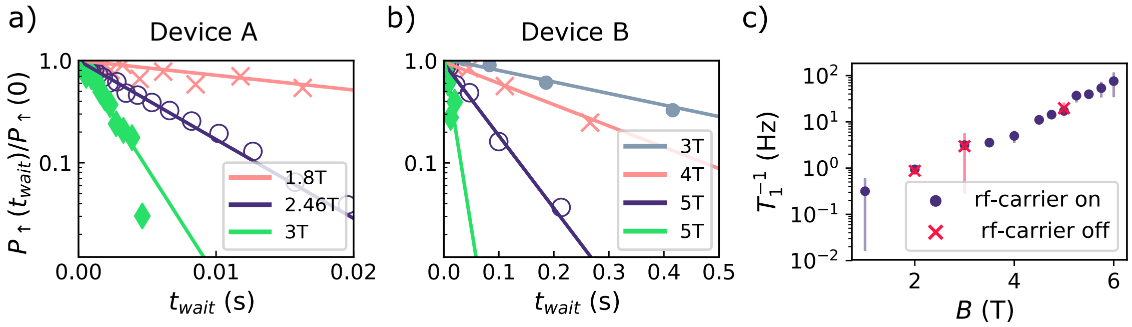

Figure 5.2.1: Spin relaxation. a) and b) respectively show the normalised spin up fraction with respect to the waiting time for devices A and B, fitted to an exponential decay for different magnetic fields. c) Comparison between the relaxation time measured with the rf-readout tone continuously on, or switched off during the waiting time.

5.2.1 T_1 DEPENDENCE ON THE MAGNETIC FIELD

We now study T_1 as a function of the magnetic field strength and orientation (see Fig. 5.2.2). In both devices, we observe an increament in T_1 as the magnetic field decreased up to a maximum of $T_1 = 0.28(3)$ s (device A) and $T_1 = 9(3)$ s (device B) at $B = 1$ T.

DEPENDENCE OF T_1 ON MAGNETIC FIELD STRENGTH

The magnetic field dependence of T_1 varies according to the relaxation mechanism and the direction of the field with respect to crystal axes. For the measurements presented in Fig. 5.2.2a the magnetic field was parallel to $[\bar{1}10]$. Spin relaxation may arise from magnetic noise at the spin Zeeman frequency or, more commonly and given some spin-orbit coupling (SOC) that mixes the spin degree of freedom with orbital or valley states, from phonon-induced electric field noise or Johnson noise. At this field orientation, and far from any anti-crossing with higher-lying excited states [101], the primary contributions from phonons to the relaxation rate ${T_1}^{-1}$ are proportional to B^7 [253, 254], while those from Johnson Nyquist noise are proportional to B^3 [253]. We therefore fit the data in Fig. 5.2.2a to a combination of such processes: ${T_1}^{-1} = c_{\mathrm{ph}} B^7 + c_{\mathrm{J}} B^3$, obtaining the coefficients summarised in Table. 5.2.1. The large uncertainties are due to the high correlation between the two terms.

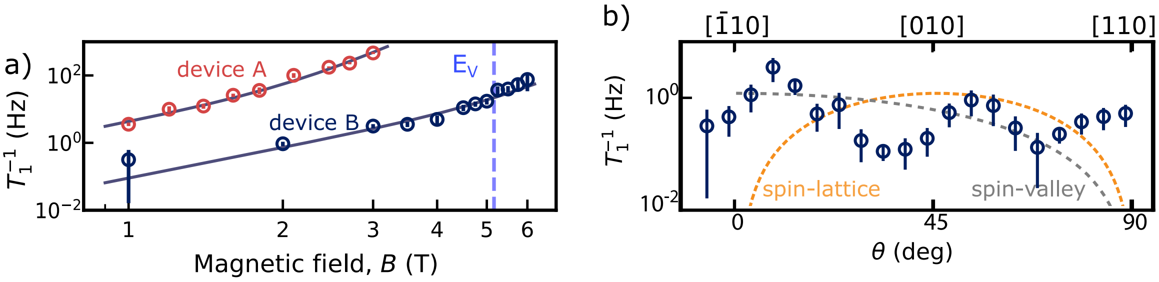

Figure 5.2.2: Spin relaxation rates and their magnetic field dependence. a) Relaxation rate measured with the magnetic field applied perpendicular to the nanowire, in the plane of the device, in the [$\bar{1}$10] crystallographic direction. Curves are fit to a general model described in the text, and E_V marks the field at which the Zeeman splitting matches the measured valley splitting in device B. b) Dependence of ${T_1}^{-1}$ on magnetic field orientation at 1 T for device B, where θ is the angle between the magnetic field and the [$\bar{1}$10] crystallographic direction for device B in the nanowire plane. The angular dependence expected from spin-valley mixing in an ideal corner dot (dashed grey curve) is insufficient to explain the observed trend. Spin-lattice relaxation mechanisms can, however, give rise to higher-order angular modulations [252] in quantum dots with high symmetry.

Device A	c_{jh}	4.1 ± 0.5 Hz/T^3
	c_{ph}	0.171 ± 0.018 Hz/T^7
Device B	c_{jh}	0.089 ± 0.012 Hz/T^3
	c_{ph}	$(10 \pm 4)\ 10^{-5}$ Hz/T^7

Table 5.2.1: Fitting parameters for the relaxation rate magnetic field dependence.

DEPENDENCE OF T_1 ON MAGNETIC FIELD ORIENTATION

We studied the angular dependence of the spin relaxation rate in device B, rotating a 1 T field in the plane of the device. A minimum in the relaxation rate is expected as the magnetic field is parallel to the direction of the nanowire, aligned along the [110] crystallographic direction since there is no spin-valley mixing (a typically dominant spin-orbit mixing mechanism) when the magnetic field is perpendicular to a mirror symmetry plane of the device [254, 255]. Although we see a downward trend towards [110], we find that the usual models for spin-orbit driven relaxation [252–254, 256] (see dashed lines in Fig. 5.2.2b) are not able to account for all features in the angular dependence.

In general, though, spin-lattice relaxation can produce higher-order harmonics in the dependence on magnetic field orientation, especially in quantum dots with high in-plane symmetry (see Appendix C). Such a high symmetry in device B would also suggest a weak spin-valley which would lead to a weak or absent hot spot in the relaxation rate when the Zeeman splitting approaches the valley splitting.

5.3 EXCITED STATES SPECTROSCOPY (QUBIT DOT)

To gain further insights into the spin relaxation mechanism for this device, we move on to study the excited states of the quantum dot by sweeping the voltage of the 'load' stage, $V_{\mathrm{Q,L}}$. The rate at which an electron loads from the reservoir into some dot state $|i\rangle$ depends on the difference in electrochemical potential, ΔE_{i}, between $|i\rangle$ and the reservoir Fermi energy. Here, we consider four dot states, $i \in \{g_\downarrow, g_\uparrow, e_\downarrow, e_\uparrow\}$, where g and e are respectively the ground and excited z-valley states, each with spin-up and spin-down states. Assuming elastic tunnelling and a constant reservoir density of states, the loading rate follows a Fermi-Dirac distribution centred at $\Delta E_{\mathrm{i}} = 0$, when dot and lead potentials are aligned [250, 257]:

$$\Gamma_i^{\mathrm{load}} = \frac{\Gamma_{0,i}}{1 + e^{\Delta E_{\mathrm{i}}/k_{\mathrm{B}}T}}, \tag{5.8}$$

where $\Gamma_{0,i}$ is the natural tunnel rate for each state $|i\rangle$, k_{B} is the Boltzmann constant and T the effective temperature. We assume here that the natural tunnel rates are spin-independent (i.e. for the ground states $g_\downarrow$ and $g_\uparrow$ they are equal to $\Gamma_{0,g}$, and similarly for the excited state natural tunnel rate $\Gamma_{0,e}$), as well as independent of

$V_{\mathrm{Q,L}}$ over the small (~ 1 mV) range of voltages studied here. The energy separation ΔE_i can be tuned with $V_{\mathrm{Q,L}}$ as $\Delta E_{\mathrm{i}} = |e|\alpha_{\mathrm{QQ}}(V_{\mathrm{i}} - V_{\mathrm{Q,L}})$, where V_{i} is the voltage at which the dot state $|i\rangle$ and reservoir potential align and α_{QQ} is the gate lever arm of the 'qubit gate' to the qubit dot. From Eq. 5.8, tunnelling rates tend to zero for load voltages smaller than V_i, and towards the natural tunnelling rate, $\Gamma_{0,i}$, for higher voltages. As a result, varying the 'load' voltage $V_{\mathrm{Q,L}}$ changes the tunnelling rates into the various dot states, and thus the probability of loading a spin-up, which we detect using the spin-readout described above.

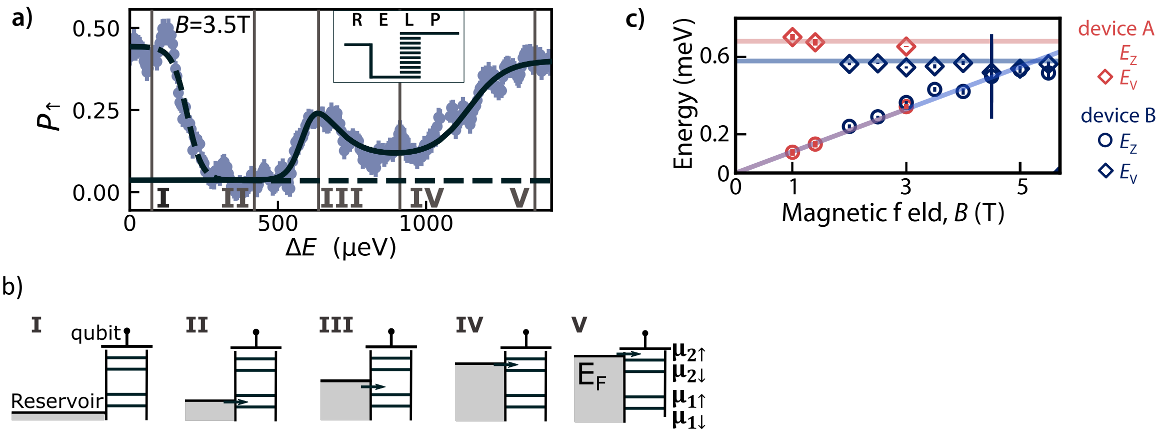

Figure 5.3.1: Excited state spectroscopy. a) Measured spin-up fraction for different load levels obtained using energy-selective loading in a 4-level pulse scheme as shown in the inset and fit. b) Illustration of different loading level regimes. (I) When the load level is too low, no electrons are loaded, and an electron with random spin tunnels in during the plunge stage. (II) If the reservoir E_{F} is placed between the spin-up and down state, only spin-down electrons tunnel in. (III) At higher load levels, an electron with a random spin polarisation tunnels in during the load stage. (IV) When E_{F} lies between the spin-up and down levels of the excited state, an electron can occupy any spin state of the ground state and the spin-down excited state. Assuming fast spin-conserving relaxation from the excited to the ground state, most electrons are found with spin-down. (V) For even higher load levels, the electron tunnels into any possible state. c) Zeeman splitting E_{Z} and excited-state energy E_{V} obtained by fitting a) to Eq. 5.10 at different magnetic fields for devices A and B.

To perform excited state spectroscopy on the qubit dot we use a 4-level pulse-sequence ('empty'-'load'-'plunge'-'read') applied to the qubit dot gate [146], where the additional 'plunge' stage ensures that an electron is always loaded for any cycle, while the loading voltage is swept between the 'empty' and 'plunge' levels (see inset in Fig. 5.3.1a). We define a spin-up fraction $P_\uparrow$ based on the integrated spin-up signal, baseline-corrected, and normalised to obtain $P_\uparrow = 0.5$ in the limit of zero load time (to neglect relaxation) and random loading using only the 'plunge' phase. The dependence of $P_\uparrow$ on the 'load' voltage (converted to energy) is shown in Fig. 5.3.1a, and can be understood by considering the schematics in Fig. 5.3.1b. In the limit (I) of low $V_{\mathrm{Q,L}}$, no electron tunnels into the qubit dot during the 'load' phase and an electron of random spin is loaded during 'plunge'. When the Fermi energy, E_{F}, of the reservoir lies between the spin-up and spin-down states (II), only spin-down electrons tunnel into the dot, and $P_\uparrow$ drops to zero. Assuming the duration of the 'load' period in the pulse sequence is long compared to the natural tunnelling rates $\Gamma_{0,i}$, the transition between regions I and II is characterised by the spin-down ground state loading rate, $\Gamma_{\mathrm{load},g\downarrow}$:

$$P_\uparrow = \frac{1}{2}\left(1 - \frac{\Gamma^{\mathrm{load}}_{g\downarrow}}{\Gamma_{0,\mathrm{g}}}\right), \tag{5.9}$$

used to generate dashed curve in Fig. 5.1.2a.

As the 'load' voltage is further increased (III), both spin states can be loaded and the measured spin-up fraction increases. Excited states can also be measured in this way provided their decay rates to the ground state are sufficiently high [253, 258]. Once the spin-down excited state becomes available during the load process (IV), the measured spin-up fraction again reduces, since the excited state rapidly decays in a spin-conserving manner [251]. Finally, in region (V), an electron of either spin orientation can be loaded into the excited state. In regions II–V, the measured spin-up fraction can be modelled by combining all relevant rates [251]:

$$P\uparrow(\mathrm{V}_{\mathrm{Q,L}}) = \frac{\Gamma_{\mathrm{load,g}\uparrow} + \Gamma_{\mathrm{load,e}\uparrow}}{\Gamma_{\mathrm{load,g}\uparrow} + \Gamma_{\mathrm{load,e}\uparrow} + \Gamma_{\mathrm{load,g}\downarrow} + \Gamma_{\mathrm{load,e}\downarrow}}, \tag{5.10}$$

By fitting the data to Eq. 5.10 (see solid line in Fig.5.3.1a) we can extract several parameters: i) The Zeeman splitting E_{Z} between the spin-up and spin-down states (fixed to be the same for the ground and excited valley states), related to the width of regions II and IV; ii) The valley splitting E_{V}, related to the separation of regions II and IV; iii) The ratio between ground and excited state natural tunnelling rates, $A_1 = \Gamma^{\mathrm{e}}_0/\Gamma^{\mathrm{g}}_0$, related to the amplitude in region IV; and iv) the effective temperature

Device A	$\boldsymbol{E_\mathrm{V}}$	681 ± 23 μeV
	$\boldsymbol{T_\mathrm{g}}$	370 ± 200 mK
	$\boldsymbol{T_\mathrm{e}}$	510 ± 160 mK
	$\boldsymbol{A_1}$	2.0 ± 0.3
Device B	$\boldsymbol{E_\mathrm{V}}$	571 ± 27 μeV
	$\boldsymbol{T_\mathrm{g}}$	300 ± 30 mK
	$\boldsymbol{T_\mathrm{e}}$	710 ± 200 mK
	$\boldsymbol{A_1}$	7.7 ± 0.9

Table 5.3.1: Fitting parameters extracted from excited state spectroscopy.

T, related to the sharpness of transitions between various regions, which can be seen to be different for the ground states (T_g) and the excited state (T_e). The effective temperature of the excited states, T_e, was left as a fitting parameter to include effects arising from the finite excited state lifetime. In contrast, any lifetime broadening of $|g_\uparrow\rangle$ is neglected based on the long measured T_1 times (> 1 ms).

5.3.1 The spin-valley mixing impact on the relaxation time

Extracted values for E_Z and E_V for both devices are shown in Fig. 5.3.1c as a function of the magnetic field. As expected, E_Z shows a linear dependence with respect to the field with a g-factor of 1.91(10), while E_V is field-independent and measured to be 0.68(2) meV (device A) and 0.57(3) meV (device B). These values are broadly similar (within a factor of two) to those measured in similar nanowire devices [155] — furthermore, a large valley splitting is beneficial for spin qubits to remain within the computational basis states and maximise spin relaxation times [259]. The valley splitting in device B is shown as an equivalent magnetic field in Fig. 5.2.2. When $E_\mathrm{Z} \sim E_\mathrm{V}$, there is a finite inter-valley spin-orbit matrix element leading to spin-valley mixing that should produce a ‘hot-spot’ in the relaxation rate. The absence of such ‘hot-spot’ within our measurement resolution (250 mT) sets an upper limit for the ‘hot-spot’ linewidth, and, in turn, for the spin-valley mixing strength [260]. Several previous studies have reported wider linewidths, corresponding to stronger spin-valley mixing [101, 261, 262], however, similar [263], and narrower [259] linewidths have been observed: this places our measurements amongst the lowest in terms of spin-valley mixing strength.

A possible explanation for the weak spin-valley mixing is that the corner dot has greater symmetry than expected, with two orthogonal quasi-symmetry planes [255] — this would be consistent with the complex magnetic field-orientation dependence of T_1 discussed above. Another possible explanation is phase cancellations between the valley coupling and spin-orbit coupling matrix elements strongly suppressing spin-valley mixing [264, 265]. In both cases, this interesting regime warrants investigation of further devices to ascertain the relationship between these conditions and the device geometry, growth conditions, and electrostatic environment.

In the case of device A, we could not confirm the strength of the spin-valley mixing since the excited state lies above our magnet range (6 T). However, a larger spin-valley mixing would explain the shorter relaxation times measured. Given that both devices were measured with the same setup, we suspect that the different relaxation times could arise from the fact that device B was measured with a higher voltage applied to the sensor gate, pulling the qubit dot wavefunction outwards from the edge making it more symmetrical. Also consistent with a more symmetric wavefunction dot is that device B is shorter than device A (L_g=40 nm against L_g=50 nm). Moreover, we cannot discard that the source of the extra symmetry in device B is due to some fabrication inhomogeneity.

5.3.2 EXCITED STATE NATURE

So far, we have assumed that the excited state probed in the devices is a valley excitation, however, now we explore the possibility that such excited state is instead an orbital excitation. If so, the valley excitation must lie at low energy ($\lesssim$ 110 μeV in device A and $\lesssim$ 280 μeV in device B), below the lowest magnetic field explored in the experiments since no signs of such a valley state were found in measurements like the one shown in Fig. 5.3.1a. Although very small valley splittings have indeed been measured in specific devices [255], larger valley splittings, closer to the excited state energies we measure, would be more consistent with recent measurements in the few electrons regime [155]. Furthermore, according to effective mass calculations, orbital excitations would rather be expected in the few meV range [266], larger than the values we measure. Therefore, an orbital excitation cannot be ruled out but is definitely not the most likely assumption. Nonetheless, the main conclusions of this work and discussion would be little affected in principle. The experiments indeed probe the spin degree of freedom as long as the Fermi level of the contacts lies between the pair of spin up and the pair of spin-down valley states at readout; also, as valley relaxation is presumably much faster than spin relaxation, and little dependent on the magnetic field orientation, the angular dependence of the relaxation time shall be globally the same as discussed below.

5.4 RESERVOIR EXCITED STATES

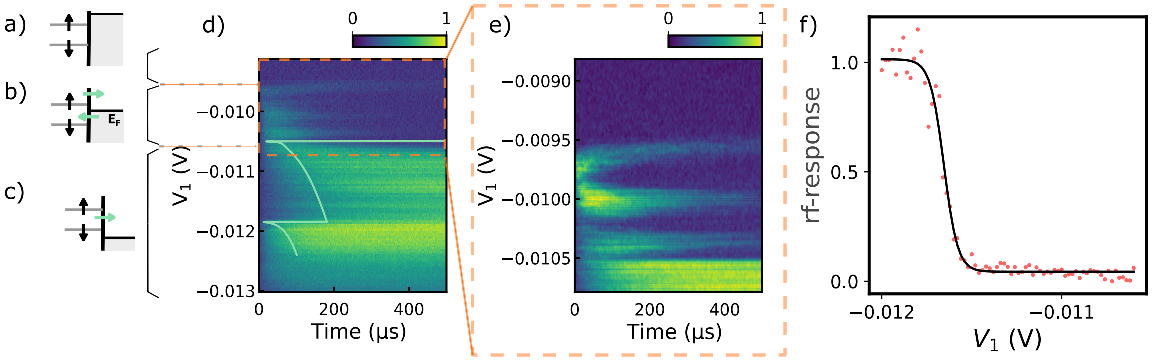

Figure 5.4.1: Reservoir 1-D nature. a,b and c) show diagrams of qubit dot electrochemical potential with respect to the lead Fermi energy at different voltages applied to the qubit dot gate, V_Q. d) Time-averaged and normalised rf response over time at different V_Q in Device C. At the voltages described by the situation in c), any loaded electron tunnels out during the readout stage. This corresponds with a low value of the rf response that rises on time as the electron leaves the qubit dot. The superposed green line is the calculated tunneling times from a quasi-1D reservoir to a 0D dot. At higher V_Q, we encounter the situation pictured in b), where the reservoir Fermi energy is in between the dot spin $|\uparrow\rangle$ and $|\downarrow\rangle$. This regime is shown with more detail in e), where we can observe how the quasi 1D density of states from the lead shape the dependency of $1/\Gamma_\uparrow^\mathrm{out} = t_\mathrm{out}^\uparrow$ and $1/\Gamma_\downarrow^\mathrm{in} = t_\mathrm{in}^\downarrow$ with respect to V_Q. f) rf response after the transient as a function of V_Q, following a Fermi-Dirac distribution.

As we have discussed before, the tunneling rates in device C were much slower than in devices A and B. This fact made it possible to observe the characteristic features of a quasi-one-dimensional reservoir. The tunneling rate between a 0-dimensional (qubit dot) and a 1-dimensional system (reservoir) depends on the energy as $\Gamma^\mathrm{out} \propto \frac{1}{\sqrt{E-E_\mathrm{n}}}$, being E_n the position in energy of the reservoir 1D subbands. Such behaviour is embodied in Fig. 5.4.1d, which shows a 2D-map similar to the one in Fig. 5.1.3e, where a simulation of the tunneling rates based on the $\frac{1}{\sqrt{E-E_{\mathrm{n}}}}$ dependency is superposed as a green line.

Around the Fermi level, the reservoir density of states follows a Fermi-Dirac distribution, so that the tunneling rate is a combination of the 1-D subbands and the Fermi-Dirac distribution:

$$\Gamma^{\mathrm{out}}(E) = \frac{2\pi}{\hbar}|\Gamma_0| \left(\sum_n \frac{1}{\sqrt{E - E_{\mathrm{n}}}} \right) (1 - f(E - E_{\downarrow})). \tag{5.11}$$

Here, $E = -|e|\alpha_{\mathrm{QQ}}V_{\mathrm{Q}}$, and $1 - f(E - E_{\downarrow})$ is the distribution of empty states in the qubit dot. The electronic temperature, $T_{\mathrm{e}} = 137 \pm 18$ mK, is extracted by fitting the rf response as a function of V_{Q} to the Fermi-Dirac distribution (See Fig. 5.4.1f).

5.5 SINGLE SHOT SPIN READOUT FIDELITY

Fault-tolerant quantum computing requires high-fidelity readout performed in the minimum readout time, Δt. Qubits need to be measured fast in comparison to the decoherence time and with a high fidelity in order to implement error correction codes. Therefore, the desirable conditions are to have the maximum amount of spin polarisation correctly identified in the minimum readout time, Δt. This section describes how we performed single-shot spin readout, including the steps followed to quantify the fidelity and what parameters are limiting it. First, we include how to calculate the electrical fidelity, F_{E}, given by the ability of the sensor to correctly identifying a given spin trace. We then combine it with the spin to charge fidelity, F_{STC}, defined as the probability that a spin electron polarisation generates its corresponding readout trace. Combining F_{STC} and F_{E}, we reach a maximum measurement fidelity of 99.54% in $\Delta t = 250\mu$s. We finally discuss a different method to identify whether a measurement trace corresponds to a spin-up or spin-down electron and its repercussions on the fidelity.

5.5.1 SINGLE-SHOT SPIN-DEPENDENT TUNNELING READOUT TRACES

The readout is based on spin-dependent tunneling using a SEB as described in Sec. 5.1. Depending on the spin polarisation, we obtain two different readout traces. A readout trace from a spin $|\downarrow\rangle$ state is a constant noisy background (the grey and black traces in Fig. 5.5.1). On the other hand, a spin $|\uparrow\rangle$ readout trace is characterised by a top hat shape that starts when the spin $|\uparrow\rangle$ electron leaves the dot ($t_{\text{out}}^{\uparrow}$), and lasts until a spin $|\downarrow\rangle$ electron tunnels back into the dot ($t_{\text{in}}^{\downarrow}$). Spin $|\uparrow\rangle$ single-shot traces taken without the JPA are displayed in red in Fig. 5.5.1, whereas the ones using a JPA in blue, show a noticeable ×4.5 SNR improvement. In both cases, the traces are taken with a sample rate of $\Gamma_s = 1$ MHz and a measurement bandwidth of $f_{\text{eff,BW}} = 25$ kHz

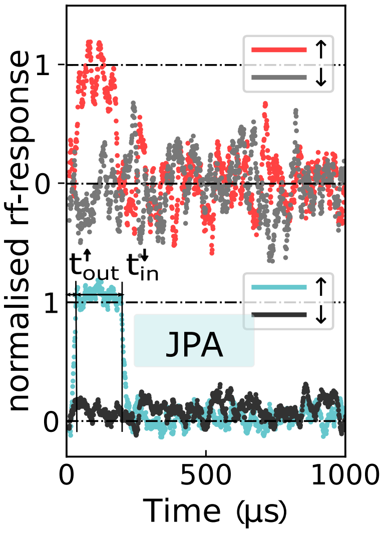

Figure 5.5.1: Single-shot readout traces. Top: spin $|\uparrow\rangle$ (red) and $|\downarrow\rangle$ (grey) traces taken without the JPA. The rf-response is normalised so it is 0 when the dot is occupied and 1 when it is empty. The bottom panel shows spin $|\uparrow\rangle$ (blue) and spin $|\downarrow\rangle$ (black) traces taken with a JPA. .

5.5.2 TRACE IDENTIFICATION AND ELECTRICAL FIDELITY

We identify the spin polarisation of a given trace by setting a threshold in the rf-response that is compared against the trace maximum. If the threshold is exceeded, the trace is labeled as a spin $|\uparrow\rangle$ and if not, as $|\downarrow\rangle$. The trace maxima follow a bimodal probability distribution, as shown in Fig. 5.5.2a and b, with one peak corresponding to spin $|\uparrow\rangle$ traces and the other to $|\downarrow\rangle$ traces. To determine the readout fidelity, we model the histograms as $N_{\text{tot}}(V_{\text{rf}}) = N_{\text{tot}}[n_{\uparrow}(V_{\text{rf}}) + n_{\downarrow}(V_{\text{rf}})]V_{\text{bin}}$, where $n_{\uparrow(\downarrow)}$ is the probability density of the maxima of spin $|\uparrow\rangle$ ($|\downarrow\rangle$) traces, V_{rf} is the normalised rf-response, N_{tot} is the total number of traces and V_{bin} is the width of the rf-response bins [267]. The fidelity of correctly labelling an individual readout trace, ${F_E}^{\uparrow(\downarrow)}$, is called the electrical fidelity and can be calculated as:

$$ {F_E}^{\downarrow} = 1 - \int_{V_T}^{\infty} n_{\downarrow}(V_{rf})\, dV_{rf} \qquad {F_E}^{\uparrow} = 1 - \int_{-\infty}^{V_T} n_{\uparrow}(V_{rf})\, dV_{rf}, \tag{5.12} $$

where the integral of $n_{\downarrow(\uparrow)}$ from $V_T(-\infty)$ to $\infty(V_T)$ is the cumulative probability of having labeled spin $|\downarrow\rangle$ ($|\uparrow\rangle$) trace wrongly [267].

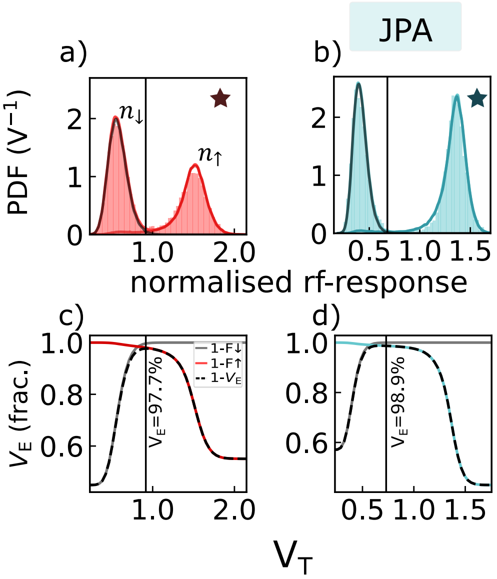

Figure 5.5.2: Electrical fidelity. a) Histogram of the maximum values of the normalised rf-response from 10,000 single-shot measured data traces taken without a JPA. The red line is the simulated histogram created using the parameters $A = 0.50$, $\Gamma_s = 1$ MHz, $t^{\uparrow}_{out} = 53\ \mu$s, $t^{\downarrow}_{in} = 440\ \mu$s and Gaussian noise with standard deviation $\sigma_{high} = 1.09$ for the top of the blip and and $\sigma_{low} = 1.03$ for the background. Both the measurement bandwidth and readout time used to create this histogram corresponds with the optimal $\Delta t = 434\ \mu$s and measurement bandwidth $f_{eff,BW} = 25$ kHz. b) Same as a) for measurement taken with a JPA. In this case, the parameters used for the simulation are $A_{JPA} = 0.46$, $\Gamma_{s,JPA} = 1$ MHz, $t^{\uparrow}_{out,JPA} = 31\ \mu$s, $t^{\downarrow}_{in,JPA} = 186\ \mu$s and Gaussian noise with standard deviation $\sigma_{high,JPA} = 0.38$ for the top of the blip and $\sigma_{low,JPA} = 0.36$ for the background. The post-processing parameters are chosen to be the ones that maximises the visibility ($\Delta t = 268\ \mu$s and $f^{JPA}_{eff,BW} = 122$ kHz). c) Electrical visibility, V_E, as a function of the threshold voltage used to discriminate between spin down and up. d) Same for traces obtained using a JPA.

The experimental data results in the bimodal distribution as a whole. However, to obtain $n_\uparrow$ and $n_\downarrow$ separately, we numerically generate 100,000 readout traces, where each trace is assigned a spin polarisation with probability A of being spin $|\downarrow\rangle$ and $1-A$ of being spin $|\uparrow\rangle$. Readout traces are completely determined by a few experimental parameters that can be extracted from the data traces: the sample rate Γ_s, the measurement bandwidth, $f_\mathrm{eff,BW}$, the sensor SNR, the tunneling times $t^\uparrow_\mathrm{out}$, and $t^\downarrow_\mathrm{in}$, and the duration of the readout trace, called readout time, Δt (See Sec. 5.5.2 for a description of the parameter extraction).

We fit the simulated histogram to 10,000 experimental shots using least squares regression, see Fig. 5.5.2a and b. In Fig. 5.5.2b, $n_\uparrow$ (solid black curve) and $n_\downarrow$ (solid blue curve) are comparatively narrower due to the reduced noise enabled by the JPA. As shown in Fig. 5.5.2c and d, the electrical visibility, $V_\mathrm{E} = 1 - {F_\mathrm{E}}^\uparrow - {F_\mathrm{E}}^\downarrow$, depends on the selected threshold voltage, V_T. We obtain a maximum $V_\mathrm{E} = 97.7\%$ without a JPA and of ${V_\mathrm{E}}^\mathrm{JPA} = 98.9\%$ using a JPA.

PARAMETER EXTRACTION FOR READOUT TRACE SIMULATIONS

As explained in the previous section, the electrical fidelity for spin-dependent measurements is calculated by simulating single-shot histograms like the ones shown in Fig. 2b and c. To create them, we need to reproduce single-shot traces equivalent to the ones measured. An example of a spin $|\uparrow\rangle$ trace is depicted in Fig. 5.5.3a with a blip starting at $t^\uparrow_\mathrm{out}$, lasting for $t^\downarrow_\mathrm{in}$. The background and blip have values $E(\mathrm{low})$ and $E(\mathrm{high})$, with its respective noise, σ_low and σ_high. This example can be labelled as a spin $|\uparrow\rangle$ trace since it surpasses the threshold voltage, V_T.

The experimental parameters that ultimately determine those traces can be separated into the ones that depend on the SEB and the ones that depend on the qubit dot. The SEB parameters are independent of the readout method and are the rf response at the background, $E(\mathrm{low})$, and at the blip, $E(\mathrm{high})$, and their respective noise level.

In order to extract these parameters, 10,000 single-shot spin readout traces like the one displayed in Fig. 5.5.3a were registered. The average of the rf response at the blip and the background are equal to the expectation values $E(\mathrm{high})$ and $E(\mathrm{low})$, respectively. To characterise the noise level of the background, we obtain the noise spectral density, $S_\mathrm{V}(f)$ of the rf response (see Fig. 5.5.4a and b). For lower frequencies, the background noise spectral density is obtained using the last

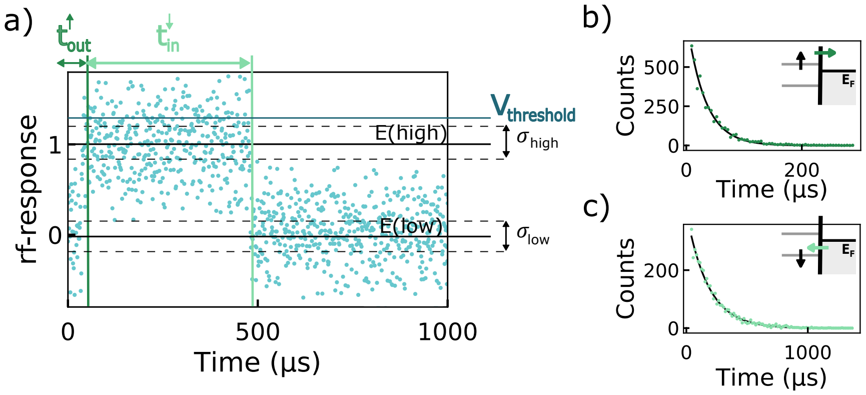

Figure 5.5.3: Trace parameter extraction. a) Normalised rf response of a spin $|\uparrow\rangle$ data trace taken with a JPA using a sample rate of Γ_s=1 MHz and a measurement bandwidth of $f_{\mathrm{eff,BW}} = 0.49$ MHz. The blip starts when the spin $|\uparrow\rangle$ electron leaves the dot at $t_{\mathrm{out}}^{\uparrow}$ and lasts until a spin $|\downarrow\rangle$ electron replaces it ($t_{\mathrm{in}}^{\downarrow}$). When the qubit dot is occupied the rf response has an estimated value E(low) with a standard deviation σ_{low}, whereas when it is empty the estimated value and standard deviation are E(high) and σ_{high}, respectively. We have also indicated the $V_{\mathrm{threshold}}$ above which the trace is labeled as a spin $|\uparrow\rangle$. b) Histogram of the starting point of the pulse and exponential fit. c) Histogram of the pulse duration and fit.

data point of all the consecutive readout traces (see Fig. 5.5.4a), whereas for higher frequencies we calculate S_{V} of a single spin $|\downarrow\rangle$ trace (see Fig. 5.5.4b). Comparing the noise spectrum with the one generated by a Gaussian random number generator, we concluded that the noise of the background has a Gaussian profile with variance σ_{low}^2 for the whole set of measurements.

The noise at E(high) can include additional sources of noise such as charge noise, where the noise spectral density typically depends on the frequency as $1/f$. This noise originates from the collective behaviour of defects or charge traps that act as charge fluctuators as they trap and release electrons [164]. The charge fluctuations slightly modify the potential around the sensor modifying its bias point, so that their effect is more noticeable at the slope of a SEB electronic transition than at the top. Figure 5.5.5a shows the SEB dot-to-reservoir transition as a function of the voltage applied to the qubit dot, where the signal at each point has been averaged over 2 ms. Figure 5.5.5b displays their corresponding standard deviations. It is very clear how the standard deviation is higher on the slope than on the offset and top of the peak.

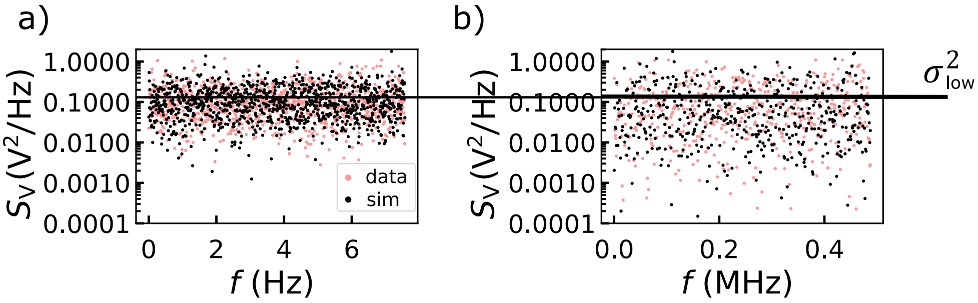

Figure 5.5.4: Noise spectral density. Noise spectral density of the rf response at E(low) at low frequencies (a) and high frequencies (b) for the acquired data (pink) and the simulations created with Gaussian noise (black).

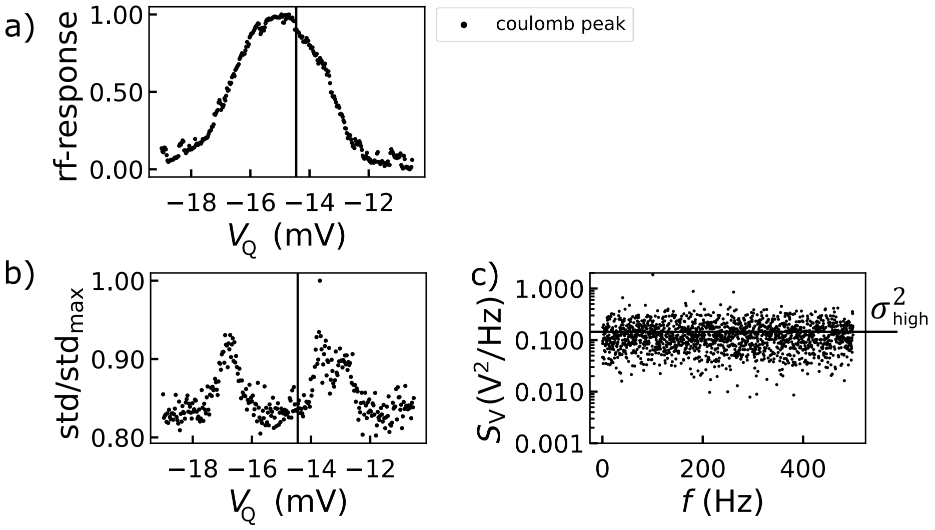

Figure 5.5.5: Noise as a function of SEB potential. a) Average of the normalised rf response for a SEB electronic transition with respect to the voltage applied to the qubit dot gate, V_Q. The vertical line indicates the voltage for spin readout. b) Standard deviation over 2 ms of rf response at E(high) at different voltages. c) S_V at the blip.

We observe that the readout position – marked as a black vertical line in Fig. 5.5.5 – is at the maximum of the rf response. This has two benefits, on one hand, the contrast between qubit dot empty and occupied is maximum (E(low) and E(high)) and, on the other hand, the charge noise is minimised. Fig. 5.5.5c shows that the noise spectral density at the top of the rf response is also constant over the range of frequencies with a variance σ^2_{high} very similar to σ^2_{low}.

The rest of parameters ($t^{\uparrow}_{\mathrm{out}}$, $t^{\downarrow}_{\mathrm{in}}$ and A) are set by the qubit dot. $t^{\uparrow}_{\mathrm{out}}$ is the time constant for a spin $|\uparrow\rangle$ electron to leave the dot. Such time corresponds with the start time of the blip and can be determined as the time at which the rf response reaches a certain threshold voltage, V_{T}. Registering the number of times that the rf response exceeds such threshold voltage at a given readout time follows an exponential trend whose time constant is $t^{\uparrow}_{\mathrm{out}}$. $t^{\downarrow}_{\mathrm{in}}$ is obtained following a similar analysis, where the blip duration probability is fitted to an exponential function (See Fig. 5.5.3 b and c).

The simulated traces for a spin $|\downarrow\rangle$ were created as a set of points with a sample rate of Γ_{s} =1 MHz (as the one of the experiment) and constant value E(low) to which it is added a Gaussian noise characterised by σ_{low}. Spin $|\uparrow\rangle$ traces are generated as a constant value E(low) with Gaussian noise σ_{low} and a blip with a constant value of E(high) and a standard deviation of σ_{high}. The blip starting time and duration follow exponential distributions with time constant $t^{\uparrow}_{\mathrm{out}}$ and $t^{\downarrow}_{\mathrm{in}}$, respectively.

5.5.3 MEASUREMENT FIDELITY, F_{M}

Depending on the readout time, Δt, spin mapping errors can diminish the readout fidelity. If Δt is of the order or smaller than $t^{\uparrow}_{\mathrm{out}}$, spin $|\uparrow\rangle$ electrons will not leave the qubit dot during the readout time, leading to a false spin $|\downarrow\rangle$ measurement (See Fig. 5.5.6a). On the other hand, if Δt is increased, a spin $|\uparrow\rangle$ may relax to the ground state before leaving the qubit dot, resulting in a false spin $|\downarrow\rangle$ (See Fig. 5.5.6b), or a spin $|\downarrow\rangle$ could be thermally excited out of the qubit dot, leading to a false spin $|\uparrow\rangle$ (See Fig. 5.5.6c). The spin readout fidelity, F_{M}, is the product of the electrical fidelity, F_{E}, which determines the probability of label correctly a given readout trace (as discussed earlier) and the spin-to-charge fidelity, F_{STC}, setting the probability that a spin state generates the trace that it is expected to. In our case, F_{E} also includes the false negatives derived from a slow $t^{\uparrow}_{\mathrm{out}}$, since the simulated traces have a finite length, Δt (See Sec. 5.5.3 for a full description).

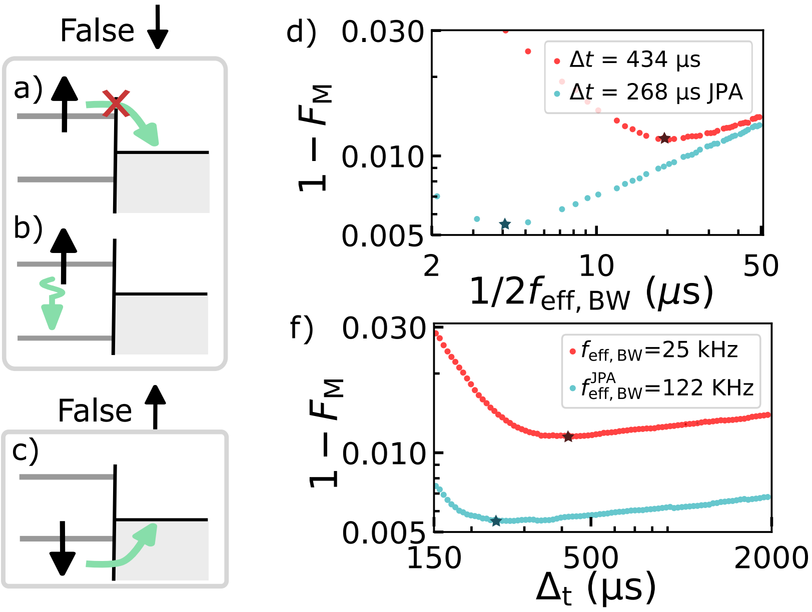

Figure 5.5.6: Measurement fidelity. Spin mapping errors due to a short readout time with respect to $t^{\uparrow}_{\mathrm{out}}$ (a), relaxation processes (b) or thermal excitations (c). d) Measurement infidelity $(1 - F_{\mathrm{M}})$ taken with (blue) and without (red) a JPA as a function of the integration time, which is equal to $1/2f_{\mathrm{eff,BW}}$. e) Measurement infidelity versus measurement time, Δt. The stars mark the optimal integration times and measurement times.

Quantification of the measurement fidelity

The probability of correctly recognising a spin $|\uparrow\rangle$ electron, ${F_{\mathrm{M}}}^{\uparrow}$, is given by the sum of the probability that such electron truthfully generates a spin $|\uparrow\rangle$, ${F_{\mathrm{STC}}}^{\uparrow}$, and that the sensor detects the corresponding blip, ${F_{\mathrm{E}}}^{\uparrow}$, plus the probability of generating a false spin $|\downarrow\rangle$ trace, $1-{F_{\mathrm{STC}}}^{\uparrow}$, that is misidentified as a spin $|\uparrow\rangle$ electron, $1-{F_{\mathrm{E}}}^{\downarrow}$. This way,

$$ {F_{\mathrm{M}}}^{\uparrow} = {F_{\mathrm{STC}}}^{\uparrow}{F_{\mathrm{E}}}^{\uparrow} + (1-{F_{\mathrm{STC}}}^{\uparrow})(1-{F_{\mathrm{E}}}^{\downarrow}). \tag{5.13}$$

Equivalently, the probability of correctly recognise a spin $|\downarrow\rangle$ electron is:

$$ {F_{\mathrm{M}}}^{\downarrow} = {F_{\mathrm{STC}}}^{\downarrow}{F_{\mathrm{E}}}^{\downarrow} + (1-{F_{\mathrm{STC}}}^{\downarrow})(1-{F_{\mathrm{E}}}^{\uparrow}). \tag{5.14}$$

Both independent fidelities can be combined as

$$ F_{\mathrm{M}} = \frac{{F_{\mathrm{M}}}^{\downarrow} + {F_{\mathrm{M}}}^{\uparrow}}{2} \tag{5.15}$$

to calculate the overall measurement fidelity. The electrical fidelity is calculated via Monte-Carlo simulations as described in Sec. 5.5.2, whereas the F_{STC} fidelity uses an analytic expression to take into account the errors coming from relaxation and thermal processes. The probability of not having a thermal excitation, so a spin $|\downarrow\rangle$ does not produce a false spin $|\uparrow\rangle$ trace, is given by:

$$ {F_{\mathrm{STC}}}^{\downarrow} = e^{-t/t^{\downarrow}_{\mathrm{out}}}. \tag{5.16}$$

The other infidelity source is the relaxation process of a spin $|\uparrow\rangle$ electron that has not tunneled out of the dot. That can be calculated as the conditional probability $P(A|B)$, being $P(A) = 1 - e^{-t/T_1}$ the probability that a spin $|\uparrow\rangle$ has decayed at time t, and $P(B) = e^{-t/t^{\uparrow}_{\mathrm{out}}}$, the probability that an electron with spin $|\uparrow\rangle$ has not left the dot at time, t. Since both events are independent the probability of having a false spin $|\downarrow\rangle$ trace due to a relaxation process is:

$$ P(A|B) = \frac{P(A\cap B)}{P(B)} = \frac{P(A)P(B)}{P(B)} = P(A) = 1 - e^{-t/T_1}, \tag{5.17}$$

Therefore, the probability of not having a relaxation process is e^{-t/T_1}. To calculate the fidelity, we have to add the probability that an spin $|\uparrow\rangle$ relaxes and, subsequently the spin $|\downarrow\rangle$ electron tunnels down the dot:

$$F_{\mathrm{STC}}{}^{\uparrow} = e^{-t/T_1} + (1 - e^{-t/T_1})(1 - e^{-t/t^{\downarrow}_{\mathrm{out}}}) \tag{5.18}$$

Here, the relaxation time T_1 depends on the magnetic field applied [268], which in this experiment was 5.1 ± 0.4 s, at B=2 T. On the other hand, $t^{\downarrow}_{\mathrm{out}}$ depends on the temperature and the difference in energy between the spin $|\downarrow\rangle$ and the reservoir Fermi Energy at the readout stage.

5.5.4 F_{M} DEPENDENCE ON Δt AND THE MEASUREMENT BANDWIDTH

Having taken spin mapping errors into consideration, we investigate the dependence of F_{M} on Δt, and $f_{\mathrm{eff,BW}}$. Figure 5.5.7a and b show how decreasing $f_{\mathrm{eff,BW}}$ leads to an improved fidelity as the noise is reduced, up to a point in which the additional filtering deforms the spin $|\uparrow\rangle$ top hat, smoothing the edges and reducing its maximum value. The optimal measurement bandwidth is different for measurements taken with and without the JPA not only because of the SNR improvement but also because of the different tunneling rates in each data set, caused by a shift of the readout point and the 1-dimensional nature of the reservoir (See Sec. 5.4).

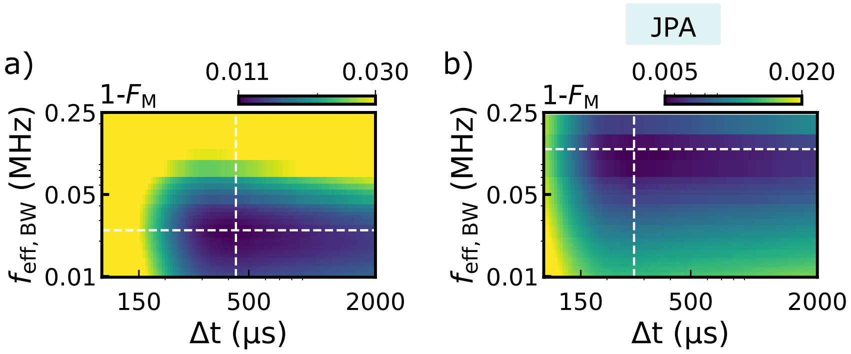

Figure 5.5.7: Fidelity as a function of measurement parameters. a). Dependence of the measurement infidelity $1 - F_{\mathrm{M}}$, with respect to the measurement bandwidth and the readout time. The dashed white lines pass through the maximum fidelity point. b) Same for measurements taken using JPA.

F_{M} also increases with Δt, since more blips can be captured as the readout time duration is longer. However, beyond an optimal value, the fidelity worsens because of the additional opportunities for the background noise to surpass the threshold. For this reason, the optimal readout time with a JPA is shorter, having faster tunneling times $t^{\uparrow}_{\mathrm{out,JPA}}$ and $t^{\downarrow}_{\mathrm{in,JPA}}$. Spin mapping errors due to thermal excitation and relaxation are negligible due to their large time constant, being the relaxation time $T_1 = 5.2$ s and the time constant for a thermal excitation $t^{\downarrow}_{\mathrm{out}} = 309$ s and 70 s without and with the JPA, respectively. The white dashed lines in Fig. 5.5.7 pass through the maximum in F_{M} and correspond with the 1D-plots presented in Fig. 5.5.6d and e.

We obtain a maximum spin readout fidelity $F_{\mathrm{M}} = 98.85\%$ without the JPA at $\Delta t = 434$ μs and $f_{\mathrm{eff,BW}} = 25$ kHz and $F_{\mathrm{M,JPA}} = 99.45\%$ for measurements obtained with a JPA using $\Delta t_{\mathrm{JPA}} = 268$ μs and $f^{\mathrm{JPA}}_{\mathrm{eff,BW}} = 122$ kHz. We note $F_{\mathrm{M,JPA}} = 99\%$ is already achieved at $\Delta t_{\mathrm{JPA}} = 131$ μs. We further explore machine learning-based approaches to improve readout fidelity [269, 270]. Here, by using Neural Networks, we report an increased fidelity of $F_{\mathrm{M}} = 99.1\%$ in $\Delta t = 500$ μs, and $F_{\mathrm{M,JPA}} = 99.54\%$ in $\Delta t = 250$ μs without and with a JPA respectively (See Sec. 5.5.5 for more information).

5.5.5 MACHINE LEARNING SPIN LABELLING APPROACH

The previous sections describe how to obtain the electrical fidelity using the probability density function of the rf response peak values (Eq. 5.12). However, when using other spin identification methods, the fidelity can be calculated with an equivalent method that relies on the number of simulated traces wrongly identified, being:

$$F_{\mathrm{E}}{}^{\uparrow} = 1 - n^0_{\uparrow}/N_{\mathrm{tot}} \qquad F_{\mathrm{E}}{}^{\downarrow} = 1 - n^1_{\downarrow}/N_{\mathrm{tot}}. \tag{5.19}$$

Here, $n^0_{\uparrow}$ is the number of spin $|\uparrow\rangle$ traces misidentified as $|\downarrow\rangle$ traces, and the opposite holds for $n^1_{\downarrow}$. We use this method to calculate the measurement fidelity when using a neural network method to label the readout traces.

The neural network method summarised in Fig. 5.5.8a was developed and programmed by David F. Wise. It uses the deep learning architecture known as InceptionTime, a state of the art approach to time series classification. The InceptionTime network involves a series of convolutional layers which apply learned filters to the time series to extract its features [271]. The features extracted from Fig. 5.5.8b spin traces are shown in Fig. 5.5.8c. These features are fed into a fully connected or dense

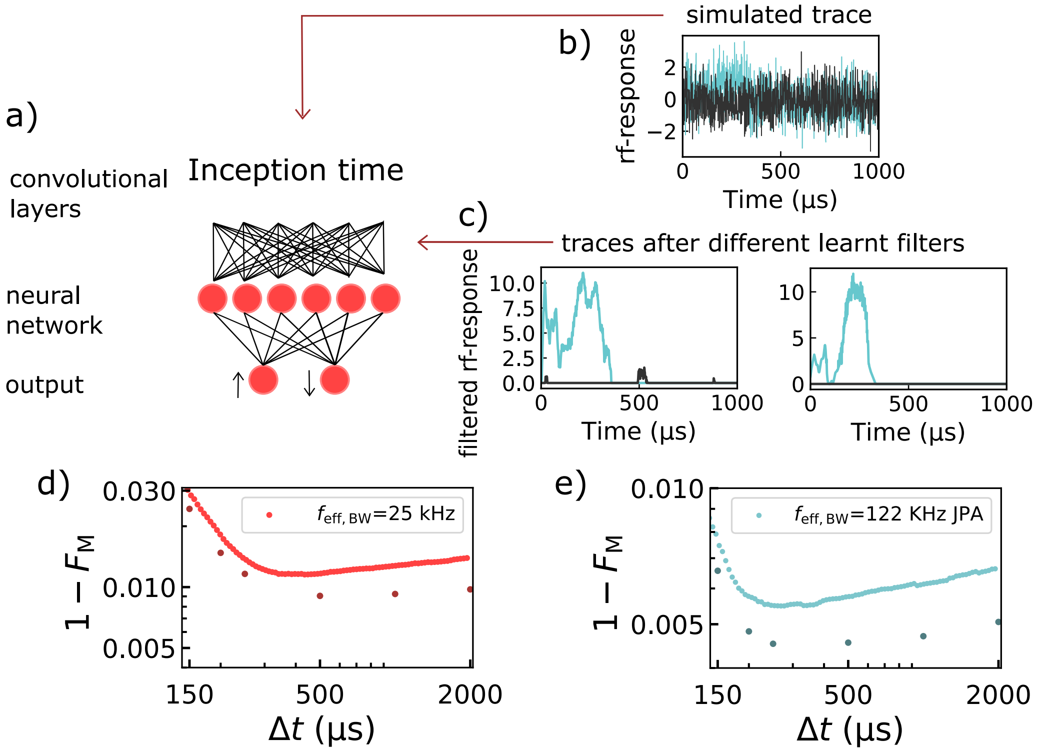

Figure 5.5.8: Machine learning fidelity extraction. a) Working protocol of the machine learning spin-classification approach. b) Simulated spin $|\uparrow\rangle$ and $|\downarrow\rangle$ trace using the parameters for JPA on. c) Output of the InceptionTime convolution layers with the blip edges enhanced to facilitate trace classification. d) Measurement fidelity without a JPA using the threshold method approach (light red) and the machine learning approach (dark red). d) Same for measurements using a JPA, with threshold (light blue) and machine learning (dark blue) labelling methods.

layer which assigns one of two classes to the input time series (spin up or down). The network was trained using the same body of data that the thresholding method described in the main text, with it divided into training, validation, and test sets. The training set is used to train the model via gradient descent and the validation set is monitored during training to avoid overfitting. If the network learns to recognise the training set too well, then that can compromise its performance on unseen data. The network that produces the best validation accuracy is selected and is applied to the test set, which gives the final accuracy data reported here. The approach used here uses the TSAI package for instantiating the networks and records training metrics using the Weights and Biases library, which is also used for hyperparameter optimisation [272, 273].

Figure 5.5.8d and e show an improvement of the fidelity for measurements taken with and without a JPA. Here, the spin to charge errors is also included as described in Sec. 5.5.3. We find a maximum fidelity F_M = 99.1% for $\Delta t = 500$ μs without using a JPA and $F_\mathrm{M}^\mathrm{JPA}$ = 99.54% with a JPA for $\Delta t_\mathrm{JPA} = 250$ μs. We observed that, when using the machine learning classification method, the measurement fidelity stays almost constant as the readout time, Δt, increases. This is because the optimised filters enhance the blip edges features, mitigating the errors that appeared in the threshold method when the background noise surpasses the threshold.

5.6 CONCLUSIONS

In this chapter, we have demonstrated spin-dependent tunneling readout using a SEB. The results indicate that CMOS-compatible fabrication methods and the nanowire geometry with its corner quantum dots hold considerable promise for high-quality qubits compatible with scalable manufacture. On one hand, although the spin coherence time, T_2, ultimately limits qubit lifetime, the long spin relaxation times we measure (up to 9 s) are particularly encouraging for these devices. Moreover, the large valley splittings guarantee that the spin qubits will remain on their computational basis.

We also performed single-shot spin readout achieving a measurement fidelity F_M =99.54% in $\Delta t = 250\mu$s. The results presented here are one of the few demonstrations of spin-dependent tunneling readout with a fidelity above the fault-tolerant threshold for the surface code (99%), having the additional advantage of using a compact charge sensor (SEB). As a downside, the readout time is relatively long compared to silicon spin coherent times ($T_2 \sim 120\mu$s [62]).

The long readout time is a consequence of the spin-dependent tunneling readout. In this method, spin $|{\uparrow}\rangle$ and $|{\downarrow}\rangle$ cannot be differentiated until the spin $|{\uparrow}\rangle$ leaves the dot, characterised by the tunneling time $t^{\uparrow}_{\text{out}}$, which in our experiments was $t^{\uparrow}_{\text{out}} > 31\mu$s. A long $t^{\uparrow}_{\text{out}}$ adds an idle time to Δt and, therefore, slows down the readout. This is not the case for Pauli Spin Blockade, in which the idle time, given by the spin tunneling time between dots, is usually minimal. For this reason, the next chapter is focused on PSB readout.

In terms of scalability, the reduced footprint of the SEB compared to standard dissipative charge sensors, like the SET, will facilitate the development of highly-connected quantum dot-based quantum processors. As an example, these split-gate nanowire devices can be naturally scaled to produce 2xn arrays of corner quantum dots [178, 229] — such devices could represent a 1D spin qubit array along one edge of the nanowire, where end qubits have charge sensors used for readout based on the approach presented here. 1D qubit arrays are well-suited for certain quantum simulation problems, such as a variational quantum eigensolver approach to the Hubbard model [274, 275]. Spin shuttling [276] or qubit SWAPping [88] could transport qubits to the ends of the array, however, for some algorithms readout of an end-qubit ancilla is sufficient [277].

6

Towards singlet-triplet readout using a SEB

This chapter summarises the efforts towards singlet-triplet readout using a SEB as a charge sensor. We first compare Pauli spin blockade and spin-dependent tunneling as spin-to charge conversion methods. Then, we describe how to use the SEB as a charge sensor for multiple target dots and show some evidence of Pauli spin blockade.

6.1 MOTIVATION FOR PAULI SPIN BLOCKADE READOUT

In the previous chapter, we concluded that the readout time, Δt, was limited by the spin-to-charge conversion method. Spin-dependent tunneling has an idle time in which the spin states are indistinguishable, given by the time that a spin $|\uparrow\rangle$ electron takes to leave the dot, $t_{\text{out}}^{\uparrow}$. This sets the ideal parameters for a fast and high fidelity readout: a short $t_{\text{out}}^{\uparrow}$ that minimises the idle time and a long $t_{\text{in}}^{\downarrow}$ to better distinguish between spin states. However, $t_{\text{in}}^{\downarrow}$ and $t_{\text{out}}^{\uparrow}$ are usually of the same order and cannot be tuned independently.

Singlet-triplet readout offers an alternative that minimises the delay without influencing the period in which the spin configurations are distinguishable. As explained in Sec. 2.2.3, singlet-triplet readout is based on Pauli spin blockade. If the system is in the singlet state $S(1,1)$, it can tunnel to $S(2,0)$, whereas if the system is in one of the triplet states $T(1,1)$, it will stay in the (1,1) configuration, until it relaxes to $S(1,1)$ in a time given by T_1. Changes in the charge configuration produced by an electron tunneling are registered using a charge detector.

We can make a parallelism between the traces generated using spin-dependent tunneling and Pauli spin blockade (PSB). In both cases, there is a delay time, t_{delay}, in which the spin traces are indistinguishable. In the case of spin-dependent tunneling this is given by $t_{\text{out}}^{\uparrow}$, whereas for Pauli spin blockade, this time is characterised by the inter-dot tunneling rate Γ_{t}. Both methods also share a time in which the spin states are distinguishable, t_{detect}. For spin-dependent tunneling this time corresponds to $t_{\text{in}}^{\downarrow}$, whereas for Pauli spin blockade this time is given by the relaxation time, T_1. Γ_{t} is normally much faster than T_1 (sometimes even faster than the sensor bandwidth), making PSB a more advantageous spin to charge conversion method since $t_{\text{delay}} << t_{\text{detect}}$ (See Fig. 6.1.1).

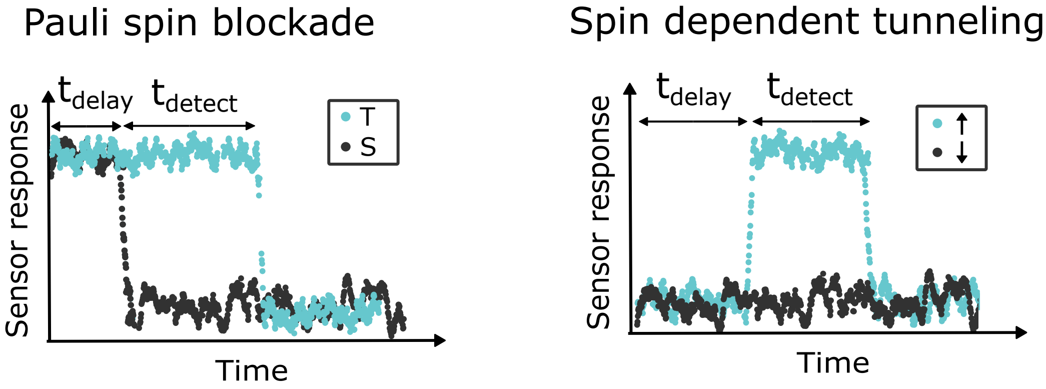

Figure 6.1.1: Charge sensor simulated readout traces. From the point of view of a charge sensor a spin readout trace is characterised by two times: a delay time in which the two spin states are indistinguishable and a detect time which is used for spin detection. For Pauli spin blockade the delay time is the inter-dot tunneling and T_1 is the sum of the delay and detect time (left). For spin dependent tunneling the delay time is $t_{\text{out}}^{\uparrow}$ and the detect time is $t_{\text{in}}^{\downarrow}$ (right).

6.1.1 Measurement fidelity for asymmetric tunneling rates

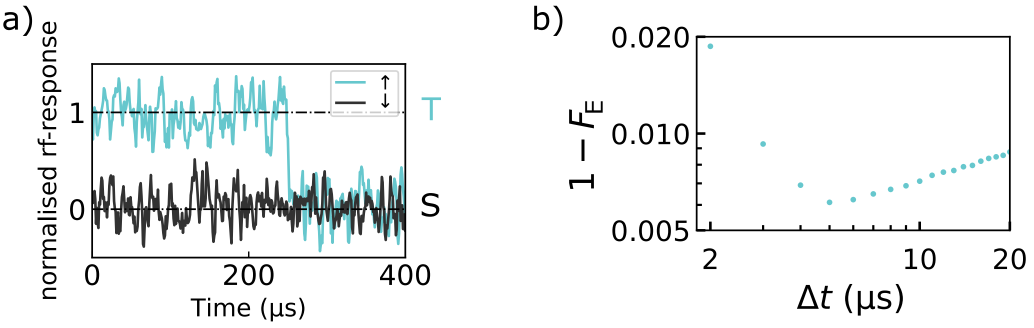

Figure 6.1.2: Simulated PSB readout traces. a) Spin $|\uparrow\rangle$ and $|\downarrow\rangle$ traces simulated using the experimental parameters of measurements taken with a JPA, with the exception of $t^{\uparrow}_{\text{out}}$ and $t^{\downarrow}_{\text{in}}$ that are modified to emulate triplets and singlets. The spin $|\uparrow\rangle$ is equivalent to a triple trace and, in the same way, the spin $|\downarrow\rangle$ is equivalent to a singlet trace. The traces shown have a readout bandwidth of $f_{\text{eff,BW}} = 122$ kHz. b) $1 - F_{\text{E}}$ as a function of the readout time.

Here, we investigate the measurement fidelity for asymmetric tunneling rates – a fast t_{delay} whereas t_{detect} remains long – to reduce the readout time necessary to achieve a fidelity above 99%. These kinds of traces are shown in Fig. 6.1.2a and are very similar to the ones from singlet and triplet traces.

To obtain the fidelity, we simulate traces like in Sec. 5.5.2 using the experimental values from measurements taken with a JPA (E(high), E(low), σ_{high}, σ_{low}, Γ_{s} and proportion of spin $|\downarrow\rangle$). The tunneling rates are modified in order to emulate triplet/singlet traces. We chose $t^{\uparrow}_{\text{out}} = 0.01$ μs and $t^{\downarrow}_{\text{in}} = 228$ μs, so that $t^{\downarrow}_{\text{in}}$ is equal to the triplet relaxation time T_1 from the Pauli Spin blockade experiment described in [98].

The average of the trace during Δt is compared against a threshold, which is varied to obtain the maximum fidelity. Figure 6.1.2b has the fidelity at different readout times, Δt. We obtain a maximum $F_{\text{E}} = 99.3\%$ for a readout time $\Delta t = 4$ μs. This result shows that the SEB could assign a spin label in much shorter timescales with equivalent fidelity if a spin-to-charge conversion mechanism with these tunneling characteristics could be used.

6.2 SEB as a DQD charge sensor

The following sections describe our attempt to measure Pauli spin blockade between two dots, so-called *dot* 1 and *dot* 2, placed in the same nanowire. We use a device like the one sketched in Fig. 6.2.1a that can hold up to four quantum dots, one under each gate. We select the dots facing each other for PSB to ensure a higher inter-dot tunneling rate, since the distance between them ($S_\mathrm{V} = 40$ nm) is smaller than the distance between consecutive dots ($S_\mathrm{H} = 50$ nm). From the remaining dots, one is coupled to a resonator to act as a SEB, whereas the other is not used during this experiment. The dummy dot is completely depleted by applying a negative voltage on the gate above it ($V_3 = -300$ mV).

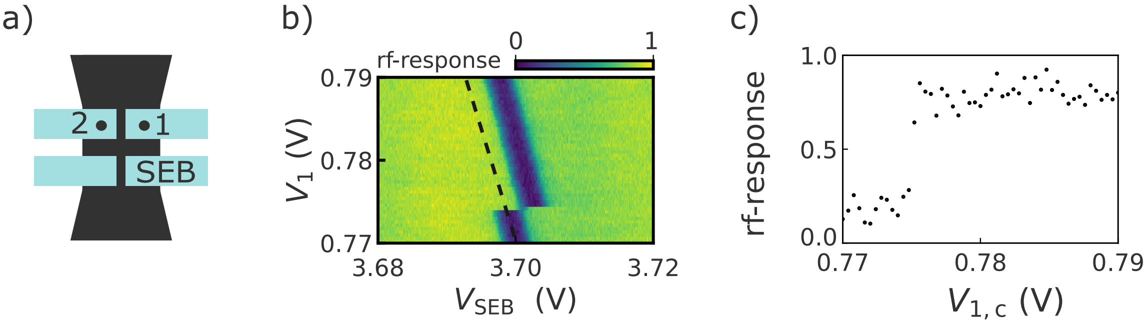

Figure 6.2.1: DQD charge sensor. a) Sketch of the four qubit nanowire. b) Stability diagram between the SEB and *dot* 1. c) rf-response along the compensated gate $V_{1,\mathrm{c}}$ that follows the dashed blacked line from b).

The potential in *dot* 1, *dot* 2 and the SEB can be tuned independently by the voltage applied on the gates above them (V_1 , V_2 and V_SEB, respectively). However, as shown in Fig. 6.2.1b, the voltage applied to the target dots also weakly affects the SEB due to their capacitive coupling. To use the SEB as a charge sensor, V_SEB is linearly compensated as [107]:

$$V_\mathrm{SEB,c} = V_\mathrm{SEB} - \alpha_\mathrm{SEB,1}\Delta V_1 - \alpha_\mathrm{SEB,2}\Delta V_2, \tag{6.1}$$

where ΔV_1 and ΔV_2 are the increment on the gates voltage and $\alpha_\mathrm{SEB,1}$ and $\alpha_\mathrm{SEB,2}$ are the cross lever arms as described in Sec. 4.3.1. Fig. 6.2.1c shows how using linear compensation rf-response is maintained constant as $V_{1,\mathrm{c}}$ is swept until a new electron is added to the target dot. With this method, we can characterise the absolute electron number in *dot* 1 and *dot* 2 and uncover voltage sections with a constant charge configuration, as observed in Fig. 6.2.2.

For PSB we are interested in charge fluctuations between *dot* 1 and *dot* 2. We observed that, although the SEB is weakly sensitive to *dot* 2, due to the long distance between them, it is strongly sensitive to charge transitions in *dot* 1 and between *dot* 1 and *dot* 2 (see Fig. 6.2.2). For this reason, to maximise the rf-response, the sensor is tuned to be at the top of the SEB electronic transition. The SEB transition is also power broadened so that small errors in the cross lever arm have a minimal effect on the measurement.

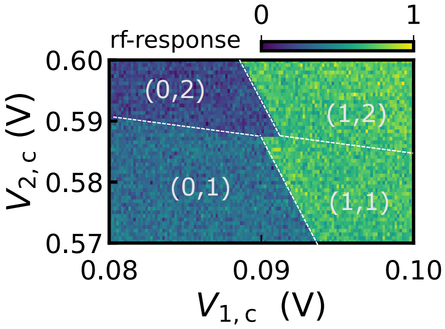

Figure 6.2.2: Compensated DQD stability diagram. Charge stability diagram of the double quantum dot. The electron number is shown as (N_1, N_2), where N_1 is the number of electrons in *dot* 1 and N_2 is the number of electrons in *dot* 2 and

6.3 Evidence of Pauli Spin blockade

Using the SEB as a charge sensor for *dot* 1 and *dot* 2, we identify the (1,1)-(0,2) transition. If PSB is observable, the inter dot charge transition (ICT) should look different depending on whether is obtained sweeping from the (2,0) to the (1,1) region (see Fig. 6.3.1a) or from the (1,1) to the (2,0) configuration (see Fig. 6.3.1b).

Sweeping $V_{2,c}$ slowly from the (2,0) to the (1,1) region, an electron should tunnel between the dots independently of the spin configuration. We observed that the system remains in the (2,0) configuration after passing the ICT, and uses the reservoirs to do a (0,2)-(0,1)-(1,1) transition. We identify that this is produced due to a slow inter-dot tunneling rate with respect to the voltage sweep (20 Hz). We measure the same behaviour when sweeping from (1,1) to (2,0). In this case, the singlet state $S(1,1)$ can tunnel directly to $S(0,2)$, whereas, the triplet states remain in the $T(1,1)$ configuration until they relax to a singlet state or until the triplets $T(0,2)$ become available. Since the inter-dot tunneling rate is so slow, triplets and singlets both remain in the (1,1) configuration until they can tunnel to the (0,2) region using the reservoir as (1,1)-(1,2)-(0,2). Having slow inter-dot tunneling rates is a disadvantage for PSB readout because it increases the t_{delay} in which singlet and triplet states are indistinguishable.

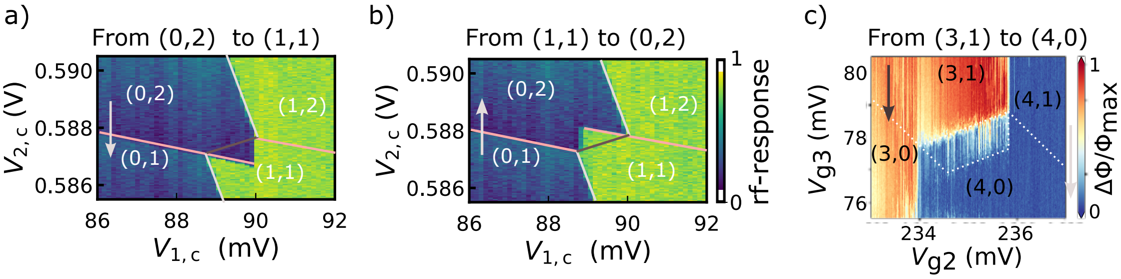

Figure 6.3.1: Interdot charge transition. a) Interdot charge transition (ICT) in which $V_{2,\mathrm{c}}$ is swept downwards from (0,2) to (1,1). b) Same ICT from (1,1) to (2,0). The brown line indicates where the inter dot transition should be. Tunneling only occurs once the system has passed the reservoir transition due to the slow inter dot tunneling rates. c) ICT measured from (3,1) to (2,0) in which PSB observed. Image courtesy of Giovanni Oakes [98].

As a comparison, Fig. 6.3.1c shows a successful implementation of PSB in a similar device performed by Giovanni Oakes. In that demonstration, the inter-dot tunneling rates are $\Gamma_{\mathrm{t}} > 1\mathrm{MHz}$. So that singlet states can rapidly tunnel between dots. The size of the trapezoidal region, in which PSB occurs, is dictated by the value of the excited valley state.

To measure Γ_{t}, we send a 2-level pulse that switches the system between the positions marked as orange circles in Fig. 6.3.2a. First, the system rapidly tunnels to (2,0) using the reservoirs and goes slowly to (1,1) through the inter dot transition. By fitting an average of the second part of the pulse to an exponential we obtain $1/\Gamma_{\mathrm{t}} = 720 \pm 190$ ms (see Fig. 6.3.2b for the equivalent (4,0)-(3,1) transition).

Now, we want to test whether we see any kind of asymmetry when pulsing in the opposite direction. In this case, the system tunnels quickly to (1,1) using the reservoirs

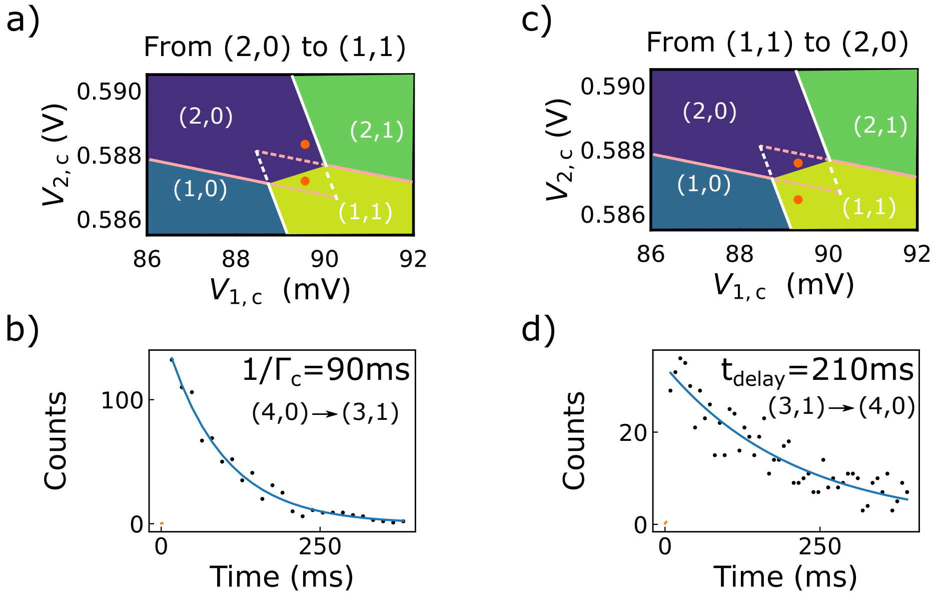

Figure 6.3.2: Asymmetries in the inter dot tunneling rates. a) Sketch of the inter dot charge transition (ICT). The dot to reservoir transitions have been extended with dashed lines to indicate the area in which the electrons cannot use the reservoirs to tunnel to the other dot. The orange circles marked the position of the two-level pulse used to measure the inter dot tunneling rate. b) Histogram and exponential fit of the time that the system takes to pass from the (4,0) to the (3,1) configuration using the protocol pictured in a). c) The orange circles show the position of the two-level pulsed used to measure the tunneling time from (3,1) to (4,0). d) Histogram and exponential fit of the time that the system takes to tunnel from (3,1) to (4,0).

and through the inter dot transition to (2,0) (see Fig. 6.3.2c). If the relaxation time between the triplet and singlet is larger than $1/\Gamma_{\mathrm{t}}$, we should observe that the system decays from (1,1) to (2,0) slower than what we measured before. The exponential decay will be a combination of Γ_{t} and T_1 related to the initial proportion of singlet and triplets, which is unknown. For comparison, we just fit the decay to a single exponential obtaining a decay constant $t_{\mathrm{Decay}} = 1.735 \pm 0.056$ s. The difference in decay times indicates that the device shows signs of Pauli spin blockade when a magnetic field of $B = 1$ T is applied. However, the readout time to distinguish between triplets and singlets should be at least longer than $1/\Gamma_{\mathrm{t}}$, hindering fast single-shot readout.

We tried two different approaches to increase the coupling between dots and, in turn, Γ_{t}. The first one was to try the same experiment in the (3,1)-(4,0) transition. Dots with more electrons have a larger size so that the distance between dots decreases. We obtained a $1/\Gamma_{\mathrm{t}} = 90 \pm 4$ ms, which is faster than before, but still too slow for fast high-fidelity single-shot readout. The second approach was to increase the top gate from $V_{\mathrm{top}} = 5\mathrm{V}$ to $V_{\mathrm{top}} = 10\mathrm{V}$. A higher voltage in the top gate should pull the dots together, increasing Γ_{t}. However, the top gate increased the device charge noise to the point that it made PSB readout problematic.

6.4 CONCLUSIONS

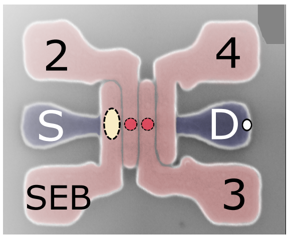

Figure 6.4.1: Wrap-around gate nanowire with four dots. False coloured scanning electron micrograph of a silicon nanowire transistor with wrap around gates, under which QDs form. One of the dots was used as a SEB, whereas PSB was measured between the dots formed under the gates 2 and 3. Image courtesy of Giovanni Oakes [98].

In this chapter we have demonstrated some signature consistent with Pauli spin blockade: there is an asymmetry in the measured tunneling rates from the (2,0) to the (1,1) configuration and vice versa. However, the slow inter dot tunneling rates prevent differentiation between triplet and singlet states. The devices could benefit from a barrier gate running along the nanowire that allows fine control of the tunneling rates between facing dots.

Although single-shot readout of singlet-triplet states could not be realised during the duration of this thesis, the project was taken over by another student from the same group that was able to achieve PSB with a fidelity of $F_{\mathrm{M}} = 99.2\%$ in $\Delta t = 6\mu\mathrm{s}$ (Giovanni Oakes). The device used for that experiment had four wrap-around gates (not split in the middle) as shown in Fig. 6.4.1. We suspect that, in that device, dots were formed in the middle of the nanowire instead of in the corners, which increased the tunneling coupling between neighbour dots.

7

Conclusions and outlook

The results presented in this thesis provide substantial encouragement for silicon quantum computing because they demonstrate that industrial manufacturing processes can provide an appropriate platform for long-lived electron spins. Moreover, the optimisation of a compact charge sensing method led to the successful demonstration of a fast and high-fidelity readout. This chapter summarises the main achievements of this thesis and identifies future research directions and questions that arise from the results obtained.

7.1 Achievements

7.1.1 CMOS foundry-based quantum devices

Quantum dot fabrication is moving from bespoke processes in university clean-rooms to industrial semiconductor foundries. This transition holds the promise of creating homogeneous and reproducible dots that are required for large-scale quantum architectures. The devices presented in this thesis were fabricated in CEA-Leti and have a design adapted for quantum applications that can still be fabricated in an industrial clean-room at the scale of 300mm wafer (see Sec. 3.1). The transistors are stable over time and have high rates of yield and reproducibility, forming single, double and four quantum dots in a nanowire (Chapters 3, 4 and 5). There is the possibility of forming even more dots in the same nanowire, however, those devices were not measured in the work presented here.

Their low complexity, with a low number of gates, generate dots well suited for large scale implementation, in which the single-electron regime is easily achievable. However, their simplicity is granted at the expense of a low tunability, which is slightly compensated by the overarching top metal gate for the global control of the tunneling rates.

One of the achievements in this thesis is the measurement of exceptionally long relaxation times in Chapter 5, which together with the high lying valley splitting, put the nanowire corner dots in an advantageous position, with the promise of a fruitful future.

7.1.2 Highly sensitive compact charge sensing

This thesis presents the single electron box (SEB) as a scalable alternative to traditional charge sensors such as single electron transistors (SETs) and quantum point contacts (QPCs). SETs and QPCs are three-terminal charge sensors that require two charge reservoirs near the qubit. On the other hand, SEBs consists of just two terminals and requires only one single reservoir.

For charge sensing, radio-frequency gate-based measurements are used to monitor the SEB complex impedance. Chapter 4 offers a complete study of the SEB and radio-frequency working principles. From that analysis, we extract that the performance is optimised using a SEB with a large lever arm that is strongly sensitive to the target dot ($\eta = 1$). In terms of the resonator, the signal power improves quadratically as the operating frequency increases. Moreover, the signal can be further optimised using a well-matched, low-loss and high impedance resonator. Additionally, the noise generated in the amplification chain can be reduced by a factor of x10 by using a Josephson parameter amplifier as the first amplifier instead of a HEMT. This noise reduction only translates into an improvement in the sensor signal to noise ratio (SNR) if the main source of the noise comes from the amplification chain, as is the case for SEBs, and not from the sensor.

The experimental application of the aforementioned steps led to the demonstration of a SEB with a minimum integration time of $\tau_\mathrm{m} = 100$ ns and a maximum measurement bandwidth of $B = 0.49$ MHz. These results place the SEB as a leading candidate for charge sensing due to its competitive signal to noise ratio and low footprint.

7.1.3 Single-shot readout

High-fidelity single-shot spin readout is a prerequisite for large-scale semiconductor spin-based quantum computers. Retrieving the qubit state with high fidelity and faster than the coherence time is paramount for error correction. In Chapter 5, the highly optimised SEB is put to use as a charge sensor to measure the spin state in a neighbour dot. In this implementation, the SEB and the target dot are integrated with the same technology, being the quantum dots formed in the opposite corners of the same nanowire.

Chapter 5 shows a demonstration of spin readout using spin-dependent tunneling with a measurement fidelity above the fault-tolerant threshold for the surface error correction code, $F_\mathrm{M} = 99.54\%$. The duration of the measurement trace, Δt, needs to be $\Delta t = 250\mu$s to achieve that fidelity. The length of Δt is set by the waiting time inherit from spin-dependent tunneling. We explore Pauli spin blockade as a different method for spin-to-charge conversion and predict that, with the same sensor, we could achieve a spin readout with a fidelity $F_\mathrm{M} = 99.3\%$ in $\Delta t = 4\mu$s. Chapter 6 shows the work towards realising Pauli spin blockade using a SEB as a charge sensor. Although such demonstration was not completed during this thesis, the high and fast readout prediction is confirmed by the results presented in [98], in which Giovanni Oakes (a member from the same research group) achieved Pauli spin readout with a SEB achieving a fidelity $F_\mathrm{M} = 99.2\%$ in $\Delta t = 6\mu$s.

7.2 Next steps

7.2.1 CMOS devices

Nanowire architecture

The nanowires presented here can be extended to produce a 2xn array of qubits. For the readout, a SEB can be placed at each end of the nanowire (see Fig. 7.2.1a). In this implementation, the qubits would have to be read sequentially like in a serial shift register, which would require the implementation of SWAP gates, increasing the computation time. Alternatively, the dots on one column could store qubits, whereas the dots on the other column could be used as sensors for Pauli spin blockade readout using in-situ readout(see Fig. 7.2.1b).

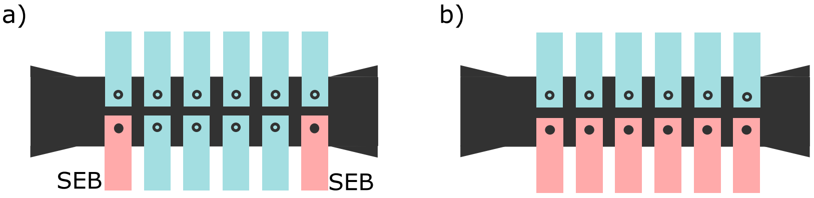

Figure 7.2.1: Nanowire architecture. a) Double column of dot arrays terminated in a SEB that is used as a sensor. Here, the blue gates with empty circles represent the qubits and the red gates with fill circles the charge sensors. b) In this implementation each qubit has a nearby sensor that reads the qubit state using in-situ readout.

One-qubit operations can be performed by applying a global ac magnetic field, in which qubits would be tuned in and out of the resonance by electrically controlling their Stark shift. For two-qubit gates, nearest neighbours can interact via exchange coupling.

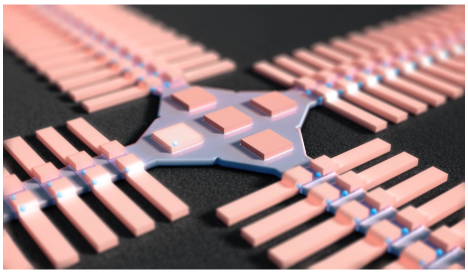

Figure 7.2.2: 2d architecture. Artistic representation of a two-dimensional spin qubit architecture formed by nanowires arranged in a grid. The hardware junctions can couple up to four qubits. Image retrieved from [82].

To create a 2-dimensional qubit processor, the nanowires can be set forming a grid. At the points where the nanowires cross, a new junction structure can be included to couple up to four qubits via SWAP operations and spin shuttling. This architecture is depicted in Fig. 7.2.2.

RELAXATION TIME

The intriguing results concerning the relaxation time warrant further investigations to ascertain how the device geometry, surface defects and growth conditions affect the dot shape, which in turn, determines the spin-valley coupling and relaxation time. At the same time, the utilisation of ^{28}Si as opposed to natural silicon would enhance the quality of any spin qubit produced with these devices, as it has been already included in industrially fabricated device [75]

INTER-DOT TUNNELING RATE

Based on the results presented in Chapter 6, Pauli spin readout was prevented by the slow tunneling rates between dots, which could not be sufficiently increased by the overarching gate. Including a barrier gate between dots could increase the control over the inter-dot tunneling. Moreover, if such a gate was compatible with fast pulses, it would allow a rapid control of the exchange interaction to perform exchange gates with a symmetric operation.

7.2.2 SENSOR IMPROVEMENTS

The SNR of the sensor presented here is limited by the JPA dynamic range. To avoid the overloading of the JPA, the reflectometry measurements had to be taken at the frequency corresponding with the minimum $|\Gamma|$ of the resonator. This prevented operating at the optimal frequency with a corresponding detriment of a factor of x2 in the SNR. Using a TWPA, whose dynamic range is superior to the JPAs, could avoid this issue. Moreover, if the JPA/TWPA was operated in the phase sensitive mode, the noise included by amplification could be reduced below the quantum limit.

Another factor that negatively affects the SNR is the parasitic capacitance, which sets an upper limit for the resonant frequency and reduces the percentage of the tunneling capacitance from the total capacitance. To reduce it, the resonator could be inductively coupled rather than capacitively coupled. In this scenario, perfect matching could be achieved by using an array of SQUIDs as tunable inductances. Additionally, the parasitic capacitance can also be reduced by utilising on-chip microwave resonators with smaller components.

In terms of the SEB, further improvements in the SNR can be achieved by creating devices with smaller equivalent oxide thickness, and hence larger lever arms (α).

Finally, another line of research could be to explore the suitability at cryogenic temperatures of other methods to measure capacitance that could eliminate the effect of the parasitic capacitance [278].

7.2.3 Scalability

There are two parallel paths to face the increasing number of sensors. The first one, followed in this thesis, consists of reducing the footprint and terminals that the sensor requires. The second one is based on reducing the number of sensors. This can be done by extending the range one sensor can cover. Both routes are not mutually exclusive and their combination could be the solution to stop an exponential increment in the processor complexity.

As the number of qubits increases, so does the number of sensors and resonators. On one hand, the number of resonators can be reduced by using time-division multiple access (TDMA), in which the qubits are readout sequentially using a single resonator. In addition, several qubits could be read simultaneously, reducing the number of required fast lines per sensor. This is possible thanks to frequency-domain multiple access (FDMA), in which a resonator chip has many resonant frequencies since it includes several inductors.

Additionally, one of the main issues for reflectometry measurements is the large size of the resonator, which is normally not integrable together with the quantum layer. The resonator dimensions are limited to 100x100 μm^2 due to the inductor size. Further research on high-inductance-density materials is indispensable to reduce the inductance size.

Appendices

A

Silicon qubit readout benchmarking

Readout method	Paper	spin qubit	sensor	F_{M}	Δt	T_1
SDT	Morello2010 [146]	Donor P	SET	96	100 μs	100 ms
	Watson2015 [166]	Donor P	SET	99.6	55 μs	7 s
	Veldhorst2014 [62]	MOS	SET	92	2 ms	1 ms
	Watson2018 [68]	Si/SiGe	SET	73	65 μs	3.7 ms
	Keith2019 [147]	Donor P	RF-SET	97.8	1.5 μs	20 s
	Oakes&Ciriano2022 [98]	**MOS NW**	**SEB**	**99.54**	**250 μs**	**5 s**
	Hogg2022 [279]	Donor P	SEB	95	66 μs	9 s
PSB	Broome2017 [280]	Donor P	SET	98.4	20 ms	500 ms
	Fogarty2018 [154]	MOS	SET	70	200 μs	
	Zhao2018 [149]	MOS	SET	99.3	120 μs	22 ms
	Harvey-Collard2018 [150]	MOS	SET	99.3	150 μs	15 ms
	Connors2019 [156]	Si/SiGe	RF-SET	82.9	2.1 μs	11 μs
	Borjans2021 [281]	Si/SiGe	SEB	99.2	100 μs	1.17 ms
	Oakes&Ciriano2022 [98]	MOS NW	SEB	99.2	6 μs	230 μs
	Pakkiam2018 [282]	Donor P	in-situ	82.9	300 μs	620 μs
	West2019 [283]	MOS	in-situ	73	2.6 ms	4.5 ms
	Zheng2019 [246]	Si/SiGe	in-situ	98	6 μs	160 μs
LPSB	Fogarty2018 [154]	MOS	SET	99	200 μs	2.8 ms
	Harvey-Collard2018 [150]	MOS	SET	99.8	65 μs	40 ms
	Curry2019 [157]	MOS	SET	99.9	6 μs	
	Connors2019 [156]	Si/SiGe	RF-SET	99	1.6 μs	52 μs
	Urdampilleta2019 [155]	MOS NW	in-situ	98	500 μs	900 μs

Table A.0.1: Spin readout with charge sensors in silicon Measurement fidelity, F_{M} achieved during a readout time, Δt with a blockade time T_1. The readout can be realised either via spin dependent tunneling (SDT), Pauli spin blockade (PSB) or latched Pauli spin blockade (LPSB). On the other hand, the charge sensors are divided in single electron box (SEB), in-situ readout with a resonator, quantum point contacts (QPC) and single electron transistor (SET) in its DC or RF versions (RF-QPC and RF-SET). The final results of this thesis are included in bold format.

B

LJPA mathematical description

The simplest model of a Lumped Josephson Parameter Amplifier (LJPA) is formed by two Josephson junctions forming a SQUID in parallel with a fixed capacitance as it's shown in Fig. B.0.1. The SQUID is modelled as a single Josephson junction with critical current I_0 whose inductance can be modulated by the flux applied to the loop. The model includes the shunted capacitance, C, and Z_0 accounting for the impedance of the microwave environment.

To simulate the behaviour of the JPA, we apply a current $I(t)$ as an external source. Using Kirchhoff's current law, we know that the current apply by the source

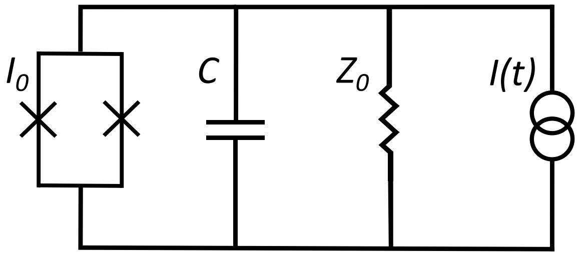

Figure B.0.1: Schematics of the LJPA. Model of a LJPA consisting on a SQUID that is included in the equations as a single Josephson junction with tunable frequency, a shunted capacitance C and an impedance Z_0. To study its dynamics, the LJPA is connected to a current source with output $I(t)$.

is equal to the sum of the current's through the JPA's equivalent circuit as:

$$I(t) = C\frac{dV}{dt} + \frac{V}{Z_0} + I_{\mathrm{J}}, \tag{B.1}$$

where $I_{\mathrm{J}} = I_0 \sin(\delta t)$ is the current though the Josephson junction. The voltage across the Josephson junction relates to the gauge-invariant phase different δ as $V = \frac{\Phi_0}{2\pi}\frac{\mathrm{d}\delta}{\mathrm{d}t}$ and $\Phi_0 = 2\pi\frac{\hbar}{2e}$ is the magnetic flux quantum. This way, by Kirchoff's voltage law, Eq. B.1 can be converted to:

$$C\frac{\Phi_0}{2\pi}\frac{d^2\delta(t)}{dt^2} + \frac{1}{Z_0}\frac{\Phi_0}{2\pi}\frac{d\delta(t)}{dt} + I_0\sin(\delta(t)) = I(t), \tag{B.2}$$

For the current source, we use a small pump tone of frequency ω_{pump} that varies sinusoidally so that $I(t) = I_{\mathrm{d}}\cos(\omega_{\mathrm{pump}}t)$, where $I_{\mathrm{d}} < I_0$. Moreover, by substituting $\sin(\delta(t))$ by its Taylor expression we obtain [284]:

$$\frac{d^2\delta(t)}{dt^2} + 2\Gamma_d\frac{d\delta(t)}{dt} + \omega_{\mathrm{JPA},0}^{2}\left(\delta(t) + \frac{\delta(t)^3}{6}\right) = \frac{2\pi}{\Phi_0 C}I_{\mathrm{d}}\cos(\omega_{\mathrm{pump}}t). \tag{B.3}$$

This equation corresponds to a soft damped non-linear resonator that can be modeled as a Duffling oscillator [191] with a resonant frequency $\omega_{\mathrm{JPA},0} = \sqrt{2\pi I_0/\Phi_0 C} = 1/\sqrt{L_{\mathrm{J}0}C}$ and damping rate $\Gamma_d = 1/2Z_0C$.

Eq. B.3 can be solved using the ansatz $\delta(t) = \delta_0\cos(\omega_{\mathrm{pump}}t - \theta)$. The solution leads to a general situation in which three possible values of δ_0 and θ can solve the differential equation [192]. For small I_{d} only one real-valued solution exists but, as I_{d} is increased, there are some values of ω_{pump} for which three different real solutions exist (See Fig. 2.4.5). This is called the bistable regime, where the Josephson bifurcation amplifier operates [186]. However, for parametric amplification we restrict ourselves to the regime where the solutions are single valued.

To observe the amplification effect, we can add a weak signal slightly detuned from the pump frequency $I_{\mathrm{s}}(t) = I_{\mathrm{s}}\cos((\omega_{\mathrm{pump}}+\Delta\omega)t)$, where $I_{\mathrm{s}} << I_{\mathrm{d}}$ and $\Delta\omega << \omega_{\mathrm{pump}}$. We can predict that the signal will affect the solution with a small perturbation so:

$$\delta(t) = \delta_0\cos(\omega_{\mathrm{pump}}t - \theta) + \epsilon(t) \tag{B.4}$$

Inputting the new ansatz into Eq. B.3 leads to:

$$\begin{aligned}\frac{d^2\epsilon(t)}{dt^2} + 2\Gamma_d\frac{d\epsilon(t)}{dt} + \epsilon(t)\omega_{\mathrm{JPA},0}^{2}\left(1 - \frac{\delta_0^2}{4} - \frac{\delta_0^2}{4}\cos(2\omega_{\mathrm{pump}}t - 2\theta)\right) = \\ \frac{2\pi}{\Phi_0 C}I_{\mathrm{s}}\cos(\omega_{\mathrm{pump}}t + \Delta\omega t),\end{aligned} \tag{B.5}$$

where we have used that $\delta_0 \cos(\omega_{\text{pump}} t - \theta)$ is a solution of the equation and we have neglected all the terms with higher dependencies on $\epsilon(t)$.

Eq. B.5 is a parametrically driven harmonic oscillator whose resonant frequency is being modified at $2\omega_{\text{pump}}$. The modulation of ω_{JPA} happens at $2\omega_{\text{pump}}$ even though the pump frequency is ω_{pump}. This is due to the fact that the Josephson inductance is an even function of δ [192]. This way, the LJPA works as a four-wave amplifier, in which the energy of two pump photons is transferred to a signal photon with frequency $\omega_{\text{signal}} = \omega_{\text{pump}} + \Delta\omega$ and an idler mode is created symmetrically with respect to the pump frequency $\omega_{\text{idler}} = \omega_{\text{pump}} - \Delta\omega$ as it's graphically portrayed in Fig. 2.4.3b.

C

Dependence of Spin relaxation (T_1) on magnetic field

This appendix includes the theory developed by Yann Michel Niquet and Jing Li published as part of the supplementary information in [99]. The theory focuses on explaining the relaxation dependence on the magnetic field, with a special emphasis on the high harmonics that we observed in the angular dependency and the weak hot-spot.

Here, we discuss the angular dependence of the spin relaxation rate in the Z valleys of silicon. We consider a silicon quantum dot under a finite magnetic field $\vec{B}$. We note $|n,\sigma\rangle$ and $E_{n,\sigma} = E_n \pm \frac{1}{2}g_0\mu_b B\sigma$ the eigenstates and eigenenergies of the dot in the absence of spin-orbit coupling, with $\sigma = \pm 1$ the spin quantized along the magnetic field axis, g_0 the bare gyromagnetic factor of the electron and μ_b Bohr's magneton. In these assumptions, the orbitals $\varphi_n(\vec{r}) = \langle \vec{r}|n\rangle$ can be chosen real at $\vec{B} = \vec{0}$.

In the Fermi Golden rule approximation, the relaxation rate between states $|\mathbb{0}\rangle \equiv |0,-1\rangle$ and $|\mathbb{1}\rangle \equiv |0,+1\rangle$ is typically proportional to the squared matrix element(s) $|\langle \mathbb{1}|\,O\,|\mathbb{0}\rangle|^2$ of one or more observable(s) O [253, 254, 260]. We assume that O is invariant under time-reversal symmetry, and does not couple spins directly [O is, e.g., a local potential $V(\vec{r})$ (Johnson-Nyquist noise), an electric dipole operator x, y, or z (phonons), etc...]. There must, therefore, be a mechanism such as spin-orbit coupling (SOC) mixing spins in $|\mathbb{0}\rangle$ and $|\mathbb{1}\rangle$ in order to achieve non-zero $\langle \mathbb{1}|\,O\,|\mathbb{0}\rangle$'s.

Since SOC is weak in the conduction band of silicon, we can deal with it to first order in perturbation. Let H_{so} be the SOC Hamiltonian. The first-order $|\mathbb{0}\rangle$ and $|\mathbb{1}\rangle$

states read:

$$\begin{aligned}|\tilde{\mathbb{0}}\rangle &= |\mathbb{0}\rangle + \sum_{n\neq 0} \frac{\langle n,-1|\, H_{\rm so}\, |0,-1\rangle}{E_0 - E_n} |n,-1\rangle \\ &\quad + \sum_{n} \frac{\langle n,+1|\, H_{\rm so}\, |0,-1\rangle}{E_0 - E_n - g_0\mu_b B} |n,+1\rangle\end{aligned} \tag{C.1a}$$

$$\begin{aligned}|\tilde{\mathbb{1}}\rangle &= |\mathbb{1}\rangle + \sum_{n\neq 0} \frac{\langle n,+1|\, H_{\rm so}\, |0,+1\rangle}{E_0 - E_n} |n,+1\rangle \\ &\quad + \sum_{n} \frac{\langle n,-1|\, H_{\rm so}\, |0,+1\rangle}{E_0 - E_n + g_0\mu_b B} |n,-1\rangle \ .\end{aligned} \tag{C.1b}$$

Hence, since O only couples same spins,

$$\begin{aligned}\langle\tilde{\mathbb{1}}|\, O\, |\tilde{\mathbb{0}}\rangle &= \sum_n \frac{\langle 0,+1|\, O\, |n,+1\rangle \langle n,+1|\, H_{\rm so}\, |0,-1\rangle}{E_0 - E_n - g_0\mu_b B} \\ &\quad + \sum_n \frac{\langle 0,+1|\, H_{\rm so}\, |n,-1\rangle \langle n,-1|\, O\, |0,-1\rangle}{E_0 - E_n + g_0\mu_b B} \,.\end{aligned} \tag{C.2}$$

We will further develop this expression to first order in $\vec{B}$, assuming $g_0\mu_b B \ll E_1 - E_0$. Neglecting the action of the vector potential on the orbital motion of the electrons in a first place, the only B-dependent terms are the Zeeman energies on the denominators:

$$\frac{1}{E_0 - E_n \pm g_0\mu_b B} = \frac{1}{E_0 - E_n} \mp \frac{g_0\mu_b B}{(E_0 - E_n)^2} \tag{C.3}$$

Then, making use of the time-reversal symmetry relations:

$$\langle 0,+1|\, O\, |n,+1\rangle = \langle 0,-1|\, O\, |n,-1\rangle^* = \langle n,-1|\, O\, |0,-1\rangle \tag{C.4a}$$

$$\begin{aligned}\langle n,+1|\, H_{\rm so}\, |0,-1\rangle &= -\, \langle n,-1|\, H_{\rm so}\, |0,+1\rangle^* \\ &= -\, \langle 0,+1|\, H_{\rm so}\, |n,-1\rangle\end{aligned} \tag{C.4b}$$

we get:

$$\langle\tilde{\mathbb{1}}|\, O\, |\tilde{\mathbb{0}}\rangle = 2g_0\mu_b B \sum_n \frac{\langle 0,+1|\, O\, |n,+1\rangle \langle n,+1|\, H_{\rm so}\, |0,-1\rangle}{(E_n - E_0)^2} \,. \tag{C.5}$$

With a SOC operator of the form $H_{\rm so} = \sum_k P_k \sigma_k$, where P_k are real-space operators (e.g., velocity operators) and σ_k are the Pauli matrices (for a spin quantized along the reference axis z),

$$\langle\tilde{\mathbb{1}}|\,O\,|\tilde{\mathbb{0}}\rangle = iB(\alpha_x\,\langle +1|\,\sigma_x\,|-1\rangle + \alpha_y\,\langle +1|\,\sigma_y\,|-1\rangle \tag{C.6}$$

$$+\,\alpha_z\,\langle +1|\,\sigma_z\,|-1\rangle)\,, \tag{C.7}$$

where the α_i's depend on the orbital motion of the electrons. As expected, the matrix elements $\langle\tilde{\mathbb{1}}|\,O\,|\tilde{\mathbb{0}}\rangle$ are proportional to B, since time-reversal symmetry must be broken by the magnetic field for O to couple opposite spin states.

The orbitals $\varphi_n(\vec{r})$ being real, the matrix elements of the P_k's must be imaginary and those of O must be real according to the time-reversal symmetry relations, Eqs. (C.4) (this is obvious if the P_k's are linear combinations of velocity operators and O is one of the examples given above). Therefore, α_x, α_y and α_z are real, and:

$$\langle\tilde{\mathbb{1}}|\,O\,|\tilde{\mathbb{0}}\rangle = iB\,\langle +1|\,\vec{\alpha}\cdot\vec{\sigma}\,|-1\rangle = iB|\vec{\alpha}|\,\langle +1|\,\vec{\sigma}_{\vec{\alpha}}\,|-1\rangle\ , \tag{C.8}$$

where $\vec{\sigma}_{\vec{\alpha}}$ is the spin along axis $\vec{\alpha} = (\alpha_x, \alpha_y, \alpha_z)$. Since $|-1\rangle$ and $|+1\rangle$ are defined with respect to the magnetic field axis, $|\,\langle +1|\,\vec{\sigma}_{\vec{\alpha}}\,|-1\rangle\,| = |\sin\theta_\alpha|$, where θ_α is the angle between the magnetic field and the vector $\vec{\alpha}$. Hence,

$$|\,\langle\tilde{\mathbb{1}}|\,O\,|\tilde{\mathbb{0}}\rangle\,|^2 \propto \sin^2\theta_\alpha\,. \tag{C.9}$$

This gives rise to the simple uniaxial dependence measured for example in Ref. [137]. In that reference, the effects of SOC are dominated by "spin-valley" mixing, that is by the $n = 1$ term in Eq. (C.5) (same orbital in the other valley). In an ideal corner dot with a (110) mirror symmetry plane, θ_α shall be the angle with the [110] axis.

The above considerations may not, however, apply when the action of the vector potential is taken into account. Indeed, in the presence of a vector potential, time-reversal symmetry transforms $\varphi_n(\vec{B}, \vec{r})$ into $\varphi_n^*(-\vec{B}, \vec{r})$, breaking Eqs. (C.4) and the resulting cancellations. This is not expected to make much difference for spin-valley mixing as the ground-states of both valleys effectively behave as zero (or, more generally, identical) angular momentum states and are, therefore, weakly coupled by the vector potential. Yet the effects of the vector potential may become relevant when spin-valley mixing is not dominant.

In order to go further, we can write Eq. (C.2) under the form:

$$\langle\tilde{\mathbb{1}}|\,O\,|\tilde{\mathbb{0}}\rangle = \langle +1|\,H_c\,|-1\rangle\ , \tag{C.10}$$

where the effective Hamiltonian H_c is:

$$H_c = \sum_{n,k}\left(\frac{\langle 0|\,O\,|n\rangle\,\langle n|\,P_k\,|0\rangle}{E_0 - E_n - g_0\mu_b B} + \frac{\langle 0|\,P_k\,|n\rangle\,\langle n|\,O\,|0\rangle}{E_0 - E_n + g_0\mu_b B}\right)\sigma_k\,, \tag{C.11}$$

then expand H_c to first order in $\vec{B}$ (being understood that E_n, $|n\rangle$ and possibly the

P_k operators depend on $\vec{B}$):

$$H_{\mathrm{c}} = iB\vec{\alpha}\cdot\vec{\sigma} + \sum_{i,j} \lambda_{ij} B_i \sigma_j \,, \tag{C.12}$$

where λ_{ij} are real scalars. Symmetry considerations may put constraints on the λ_{ij}'s.

Assuming $\vec{B} = B(\cos\theta, \sin\theta, 0)$, we may then sort out the angular dependence of the matrix element $\langle +1|\, H_{\mathrm{c}}\, |-1\rangle$. The $|+1\rangle$ and $|-1\rangle$ spin states are the eigenstates of the Zeeman Hamiltonian:

$$H_{\mathrm{z}} = \frac{1}{2} g_0 \mu_b B (\cos\theta\sigma_x + \sin\theta\sigma_y) = \frac{1}{2} g_0 \mu_b B \begin{bmatrix} 0 & e^{-i\theta} \\ e^{i\theta} & 0 \end{bmatrix} \tag{C.13}$$

Hence,

$$\begin{aligned} |-1\rangle &= \frac{e^{i\pi/4}}{\sqrt{2}} \left(e^{-i\theta/2} |\uparrow\rangle - e^{i\theta/2} |\downarrow\rangle \right) \\ |+1\rangle &= \frac{e^{-i\pi/4}}{\sqrt{2}} \left(e^{-i\theta/2} |\uparrow\rangle + e^{i\theta/2} |\downarrow\rangle \right) \,. \end{aligned} \tag{C.14}$$

The above phase factors have been chosen for convenience. Then,

$$\begin{aligned} \langle +1|\, \sigma_x \,|-1\rangle &= +\sin\theta \\ \langle +1|\, \sigma_y \,|-1\rangle &= -\cos\theta \\ \langle +1|\, \sigma_z \,|-1\rangle &= i \,. \end{aligned} \tag{C.15}$$

Therefore, after substitution in Eq. (C.10) and trigonometric manipulations,

$$\langle +1|\, H_{\mathrm{c}} \,|-1\rangle = B(a_0 + ic_1 \cos\theta + is_1 \sin\theta \tag{C.16}$$

$$+ c_2 \cos 2\theta + s_2 \sin 2\theta) \,, \tag{C.17}$$

where a_0, c_1, s_1, c_2 and s_2 are real. This matrix element does, therefore, feature $\sin n\theta$ and $\cos n\theta$ harmonics up to $n = 2$ – Hence the relaxation rate, which is $\propto |\langle \mathbb{1}|\, H_{\mathrm{c}}\, |\mathbb{0}\rangle|^2$, features $n = 0$, $n = 2$, and $n = 4$ harmonics. We may thus write, in general,

$$\Gamma = \gamma_0 + \gamma_2 \cos[2(\theta - \theta_2^0)] + \gamma_4 \cos[4(\theta - \theta_4^0)] \,. \tag{C.18}$$

Note that the relaxation rate is invariant under the transformation $\theta \to \theta + \pi$ ($\vec{B} \to -\vec{B}$), as expected. Competing relaxation mechanisms may yield different γ's and θ^0's; yet trigonometric relations easily show that the sum over mechanisms can always be refactored under that form.

Higher-order harmonics may result from the breakdown of one of the above assumptions [first-order developments in B and $H_{\rm so}$, validity of Fermi Golden Rule (multi-phonon/photon processes)...], or from extrinsic contributions. Also, the prefactors of the relaxation rates scale as a power of the Larmor frequency, ω (ω^3 to ω^5 for phonons, ω for Johnson Nyquist noise), which may introduce extra angular dependences through the anisotropy of the g-factors. However, the contribution of g-factors to the angular dependence of the relaxation rates is presumably very weak in silicon, as they remain usually very close to 2 whatever the orientation of the magnetic field.

Examples of pure $\cos[4(\theta - \theta_4^0)]$ dependences have for example been given in Ref. [252] (relaxation owing to phonon-induced shear strains in a highly symmetric dot). The enumeration of possible symmetry invariants in Eq. (C.12) suggests that the relative weight of $n = 4$ harmonics shall actually increase when the dot gets more symmetric [going, e.g., from a single mirror symmetry plane (C_s group) to a double mirror symmetry plane (C_{2v} group)].

In the present experiments, the angular dependence of the relaxation rate is indeed dominated by $n = 2$ and $n = 4$ harmonics, although significant $n = 6$ and $n = 8$ contributions may also be needed to reproduce the behavior around $\theta = 0$. Without further knowledge about the shape of that particular dot, it remains, however, difficult to make detailed predictions. Still, the presence of strong $n = 4$ harmonics suggests, as discussed above, that the relaxation is not dominated by spin-valley mixing at $B = 1$ T (nor at any field given the absence of measurable hot spot at the crossing between the ground valley spin up state and the excited valley spin down state). Both the weakness of spin-valley mixing effects and the presence of sizable $n > 2$ harmonics are consistent with a dot showing high in-plane symmetry [255].

Bibliography

1. Moore, G. E. *Cramming more components onto integrated circuits, Reprinted from Electronics, volume 38, number 8, April 19, 1965, pp.114 ff. IEEE Solid-State Circuits Soc. Newsl.* **11** (2006) (cit. on p. 7).
2. Waldrop, M. *The chips are down for Moore's law.* 2016 (cit. on p. 7).
3. Biamonte, J. *et al. Quantum machine learning. Nature* **549** (2017) (cit. on p. 7).
4. Grover, L. K. *A fast quantum mechanical algorithm for database search.* in *Proc. twenty-eighth Annu. ACM Symp. Theory Comput. - STOC '96* (ACM Press, New York, New York, USA, 1996) (cit. on pp. 7, 9).
5. Gisin, N., Ribordy, G., Tittel, W. & Zbinden, H. *Quantum cryptography. Rev. Mod. Phys.* **74** (2002) (cit. on p. 7).
6. McArdle, S., Endo, S., Aspuru-Guzik, A., Benjamin, S. C. & Yuan, X. *Quantum computational chemistry. Rev. Mod. Phys.* **92** (2020) (cit. on p. 7).
7. Schaal, S. *Scalable and high-sensitivity readout of silicon quantum devices Simon Schaal.* PhD thesis (UCL, 2019) (cit. on pp. 9, 11).
8. Montanaro, A. *Quantum algorithms: an overview. npj Quantum Inf.* **2** (2016) (cit. on pp. 10, 14).
9. Shor, P. W. *Polynomial-Time Algorithms for Prime Factorization and Discrete Logarithms on a Quantum Computer. SIAM J. Comput.* **26** (1997) (cit. on p. 10).
10. Harrow, A. W., Hassidim, A. & Lloyd, S. *Quantum Algorithm for Linear Systems of Equations. Phys. Rev. Lett.* **103** (2009) (cit. on p. 10).
11. Lo, C. C. & Morton, J. J. *Will silicon save quantum computing. IEEE Spectr.* **51** (2014) (cit. on p. 10).
12. Feynman, R. P. *Simulating physics with computers. Int. J. Theor. Phys.* **21** (1982) (cit. on p. 10).
13. Benioff, P. *The computer as a physical system: A microscopic quantum mechanical Hamiltonian model of computers as represented by Turing machines. J. Stat. Phys.* **22** (1980) (cit. on p. 10).

14. Deutsch, D. *Quantum theory, the Church–Turing principle and the universal quantum computer*. *Proc. R. Soc. London. A. Math. Phys. Sci.* **400** (1985) (cit. on p. 10).
15. Guerreschi, G. G., Hogaboam, J., Baruffa, F. & Sawaya, N. P. D. *Intel Quantum Simulator: a cloud-ready high-performance simulator of quantum circuits*. *Quantum Sci. Technol.* **5** (2020) (cit. on p. 10).
16. Esposito, M., Ranadive, A., Planat, L. & Roch, N. *Perspective on traveling wave microwave parametric amplifiers*. *Appl. Phys. Lett.* **119** (2021) (cit. on pp. 10, 51, 60).
17. DiVincenzo, D. P. *The Physical Implementation of Quantum Computation*. *Fortschritte der Phys.* **48** (2000) (cit. on p. 11).
18. DiVincenzo, D. P. *Two-bit gates are universal for quantum computation*. *Phys. Rev. A* **51** (1995) (cit. on p. 11).
19. Resch, S. & Karpuzcu, U. R. *Quantum Computing: An Overview Across the System Stack* (2019) (cit. on p. 11).
20. De Leon, N. P. *et al. Materials challenges and opportunities for quantum computing hardware*. *Science (80-.).* **372** (2021) (cit. on pp. 11, 14, 19).
21. Cross, A. W., Bishop, L. S., Sheldon, S., Nation, P. D. & Gambetta, J. M. *Validating quantum computers using randomized model circuits*. *Phys. Rev. A* **100** (2019) (cit. on p. 11).
22. Ladd, T. D. *et al. Quantum computers*. *Nature* **464** (2010) (cit. on p. 12).
23. Ball, P. *Ion-based commercial quantum computer is a first*. 2018 (cit. on p. 12).
24. Wright, K. *et al. Benchmarking an 11-qubit quantum computer*. *Nat. Commun.* **10** (2019) (cit. on p. 12).
25. Harty, T. P. *et al. High-Fidelity Preparation, Gates, Memory, and Readout of a Trapped-Ion Quantum Bit*. *Phys. Rev. Lett.* **113** (2014) (cit. on p. 12).
26. Ballance, C. J., Harty, T. P., Linke, N. M., Sepiol, M. A. & Lucas, D. M. *High-Fidelity Quantum Logic Gates Using Trapped-Ion Hyperfine Qubits*. *Phys. Rev. Lett.* **117** (2016) (cit. on p. 12).
27. Mehta, K. K. *et al. Publisher Correction: Integrated optical multi-ion quantum logic*. *Nature* **590** (2021) (cit. on p. 12).
28. Gibney, E. *Physicists propose football-pitch-sized quantum computer*. *Nature* **542** (2017) (cit. on p. 12).
29. Devoret, M. H. & Schoelkopf, R. J. *Superconducting Circuits for Quantum Information: An Outlook*. *Science (80-.).* **339** (2013) (cit. on p. 12).
30. Wang, Y. *Analysis on the Mechanism of Superconducting Quantum Computer*. *J. Phys. Conf. Ser.* **1634** (2020) (cit. on p. 12).

31. Jurcevic, P. *et al. Demonstration of quantum volume 64 on a superconducting quantum computing system. Quantum Sci. Technol.* **6** (2021) (cit. on p. 12).
32. IBM. *IBM Announces Advances to IBM Quantum Systems and Ecosystem.* 2017 (cit. on p. 12).
33. Intel. *IBM Unveils World's First Integrated Quantum Computing System for Commercial Use.* 2019 (cit. on p. 12).
34. Zeng, W. *Unsupervised Machine Learning on Rigetti 19Q with Forest 1.2.* 2019 (cit. on p. 12).
35. Arute, F. *et al. Quantum supremacy using a programmable superconducting processor. Nature* **574** (2019) (cit. on pp. 12, 14).
36. Cao, G. *et al. Ultrafast universal quantum control of a quantum-dot charge qubit using Landau–Zener–Stückelberg interference. Nat. Commun.* **4** (2013) (cit. on p. 12).
37. Loss, D. & DiVincenzo, D. P. *Quantum computation with quantum dots. Phys. Rev. A* **57** (1998) (cit. on p. 12).
38. Veldhorst, M., Eenink, H. G., Yang, C. H. & Dzurak, A. S. *Silicon CMOS architecture for a spin-based quantum computer. Nat. Commun.* **8** (2017) (cit. on pp. 12, 16).
39. Ciorga, M. *et al. Addition spectrum of a lateral dot from Coulomb and spin-blockade spectroscopy. Phys. Rev. B* **61** (2000) (cit. on p. 12).
40. Mailly, D., Chapelier, C. & Benoit, A. *Experimental observation of persistent currents in GaAs-AlGaAs single loop. Phys. Rev. Lett.* **70** (1993) (cit. on p. 13).
41. Mimura, T., Joshin, K., Hiyamizu, S., Hikosaka, K. & Abe, M. *High Electron Mobility Transistor Logic. Jpn. J. Appl. Phys.* **20** (1981) (cit. on p. 13).
42. Vandersypen, L. M. K. & Eriksson, M. A. *Quantum computing with semiconductor spins. Phys. Today* **72** (2019) (cit. on p. 13).
43. Petta, J. R. *et al. Coherent manipulation of coupled electron spins in semiconductor quantum dots. Science (80-.).* **309** (2005) (cit. on pp. 13, 33, 38).
44. Foletti, S., Bluhm, H., Mahalu, D., Umansky, V. & Yacoby, A. *Universal quantum control of two-electron spin quantum bits using dynamic nuclear polarization. Nat. Phys.* **5** (2009) (cit. on p. 13).
45. Malinowski, F. K. *et al. Notch filtering the nuclear environment of a spin qubit. Nat. Nanotechnol.* **12** (2017) (cit. on p. 13).
46. Camenzind, L. C. *et al. Hyperfine-phonon spin relaxation in a single-electron GaAs quantum dot. Nat. Commun.* **9** (2018) (cit. on p. 13).
47. Bluhm, H. *et al. Dephasing time of GaAs electron-spin qubits coupled to a nuclear bath exceeding 200 μs. Nat. Phys.* **7** (2011) (cit. on p. 13).

48. Zhong, H.-S. *et al.* *Quantum computational advantage using photons. Science (80-.).* **370** (2020) (cit. on p. 13).

49. Arrazola, J. M. *et al.* *Quantum circuits with many photons on a programmable nanophotonic chip. Nature* **591** (2021) (cit. on p. 13).

50. Kok, P. *et al.* *Linear optical quantum computing with photonic qubits. Rev. Mod. Phys.* **79** (2007) (cit. on p. 13).

51. Yin, J. *et al.* *Satellite-based entanglement distribution over 1200 kilometers. Science (80-.).* **356** (2017) (cit. on p. 13).

52. Franke, D., Clarke, J., Vandersypen, L. & Veldhorst, M. *Rent's rule and extensibility in quantum computing. Microprocess. Microsyst.* **67** (2019) (cit. on pp. 13, 14, 16).

53. Fowler, A. G., Mariantoni, M., Martinis, J. M. & Cleland, A. N. *Surface codes: Towards practical large-scale quantum computation. Phys. Rev. A* **86** (2012) (cit. on p. 14).

54. Harrow, A. W. & Montanaro, A. *Quantum computational supremacy. Nature* **549** (2017) (cit. on p. 14).

55. McClean, J. R., Romero, J., Babbush, R. & Aspuru-Guzik, A. *The theory of variational hybrid quantum-classical algorithms. New J. Phys.* **18** (2016) (cit. on p. 14).

56. Nam, Y. *et al.* *Ground-state energy estimation of the water molecule on a trapped-ion quantum computer. npj Quantum Inf.* **6** (2020) (cit. on p. 14).

57. Arute, F. *et al.* *Hartree-Fock on a superconducting qubit quantum computer. Science (80-.).* **369** (2020) (cit. on p. 14).

58. Kandala, A. *et al.* *Error mitigation extends the computational reach of a noisy quantum processor. Nature* **567** (2019) (cit. on p. 14).

59. Knill, E. *Quantum computing with realistically noisy devices. Nature* **434** (2005) (cit. on p. 15).

60. Chen, E. H. *et al.* *Detuning Axis Pulsed Spectroscopy of Valley-Orbital States in Si/SiGe Quantum Dots. arXiv* (2020) (cit. on p. 15).

61. Struck, T. *et al.* *Author Correction: Low-frequency spin qubit energy splitting noise in highly purified 28Si/SiGe. npj Quantum Inf.* **6** (2020) (cit. on p. 15).

62. Veldhorst, M. *et al.* *An addressable quantum dot qubit with fault-tolerant control-fidelity. Nat. Nanotechnol.* **9** (2014) (cit. on pp. 15, 18, 26, 29, 32, 145, 163).

63. Muhonen, J. T. *et al.* *Storing quantum information for 30 seconds in a nanoelectronic device. Nat. Nanotechnol.* **9** (2014) (cit. on p. 15).

64. Yoneda, J. *et al.* *A quantum-dot spin qubit with coherence limited by charge noise and fidelity higher than 99.9%. Nat. Nanotechnol.* **13** (2018) (cit. on pp. 15, 29).

65. Kawakami, E. *et al.* *Electrical control of a long-lived spin qubit in a Si/SiGe quantum dot*. *Nat. Nanotechnol.* **9** (2014) (cit. on pp. 15, 19).

66. Veldhorst, M. *et al.* *A two-qubit logic gate in silicon*. *Nature* **526** (2015) (cit. on pp. 15, 32, 34).

67. Zajac, D. M. *et al.* *Resonantly driven CNOT gate for electron spins*. *Science (80-.).* **359** (2018) (cit. on pp. 15, 19, 33, 34).

68. Watson, T. F. *et al.* *A programmable two-qubit quantum processor in silicon*. *Nature* **555** (2018) (cit. on pp. 15, 34, 37, 163).

69. Xue, X. *et al.* *Benchmarking Gate Fidelities in a Si/SiGe Two-Qubit Device*. *Phys. Rev. X* **9** (2019) (cit. on p. 15).

70. Xue, X. *et al.* *Quantum logic with spin qubits crossing the surface code threshold*. *Nature* **601** (2022) (cit. on pp. 15, 34).

71. Noiri, A. *et al.* *Fast universal quantum gate above the fault-tolerance threshold in silicon*. *Nature* **601** (2022) (cit. on pp. 15, 34).

72. Madzik, M. T. *et al.* *Precision tomography of a three-qubit donor quantum processor in silicon*. *Nature* **601** (2022) (cit. on p. 15).

73. Philips, S. *et al.* *Coherent multiqubit operations in a six quantum dot linear array*. *Bull. Am. Phys. Soc.* (2021) (cit. on p. 15).

74. Maurand, R. *et al.* *A CMOS silicon spin qubit*. *Nat. Commun.* **7** (2016) (cit. on pp. 15, 19, 64).

75. Zwerver, A. M. J. *et al.* *Qubits made by advanced semiconductor manufacturing* (2021) (cit. on pp. 15, 19, 159).

76. Camenzind, L. C. *et al.* *A spin qubit in a fin field-effect transistor* (2021) (cit. on p. 15).

77. Gonzalez-Zalba, M. F. *et al.* *Scaling silicon-based quantum computing using CMOS technology*. *Nat. Electron.* **4** (2021) (cit. on pp. 16, 110).

78. Li, R. *et al.* *A crossbar network for silicon quantum dot qubits*. *Sci. Adv.* **4** (2018) (cit. on p. 16).

79. Vandersypen, L. M. K. *et al.* *Interfacing spin qubits in quantum dots and donors—hot, dense, and coherent*. *npj Quantum Inf.* **3** (2017) (cit. on p. 16).

80. Hill, C. D. *et al.* *A surface code quantum computer in silicon*. *Sci. Adv.* **1** (2015) (cit. on p. 16).

81. Boter, J. M. *et al.* *A sparse spin qubit array with integrated control electronics*. in *2019 IEEE Int. Electron Devices Meet.* **2019-Decem** (IEEE, 2019) (cit. on p. 16).

82. Crawford, O., Cruise, J. R., Mertig, N. & Gonzalez-Zalba, M. F. *Compilation and scaling strategies for a silicon quantum processor with sparse two-dimensional connectivity* (2022) (cit. on pp. 16, 158).
83. Vahapoglu, E. *et al. Coherent control of electron spin qubits in silicon using a global field* (2021) (cit. on pp. 16, 29).
84. Van Diepen, C. J. *et al. Electron cascade for distant spin readout. Nat. Commun.* **12** (2021) (cit. on p. 16).
85. Duan, J. *et al. Remote Capacitive Sensing in Two-Dimensional Quantum-Dot Arrays. Nano Lett.* **20** (2020) (cit. on pp. 16, 47).
86. Schaal, S. *et al. A CMOS dynamic random access architecture for radio-frequency readout of quantum devices. Nat. Electron.* **2** (2019) (cit. on pp. 16, 62).
87. Ruffino, A. *et al. A cryo-CMOS chip that integrates silicon quantum dots and multiplexed dispersive readout electronics. Nat. Electron.* (2021) (cit. on p. 16).
88. Sigillito, A. J., Gullans, M. J., Edge, L. F., Borselli, M. & Petta, J. R. *Coherent transfer of quantum information in a silicon double quantum dot using resonant SWAP gates. npj Quantum Inf.* **5** (2019) (cit. on pp. 16, 145).
89. Yoneda, J. *et al. Coherent spin qubit transport in silicon. Nat. Commun.* **12** (2021) (cit. on p. 16).
90. Mills, A. R. *et al. Shuttling a single charge across a one-dimensional array of silicon quantum dots. Nat. Commun.* **10** (2019) (cit. on p. 16).
91. Mortemousque, P.-A. *et al. Enhanced Spin Coherence while Displacing Electron in a Two-Dimensional Array of Quantum Dots. PRX Quantum* **2** (2021) (cit. on p. 16).
92. Burkard, G., Gullans, M. J., Mi, X. & Petta, J. R. *Superconductor–semiconductor hybrid-circuit quantum electrodynamics. Nat. Rev. Phys.* **2** (2020) (cit. on p. 16).
93. Borjans, F., Croot, X. G., Mi, X., Gullans, M. J. & Petta, J. R. *Resonant microwave-mediated interactions between distant electron spins. Nature* **577** (2020) (cit. on p. 16).
94. Malinowski, F. K. *et al. Fast spin exchange across a multielectron mediator. Nat. Commun.* **10** (2019) (cit. on p. 16).
95. Yang, C. H. *et al. Operation of a silicon quantum processor unit cell above one kelvin. Nature* **580** (2020) (cit. on p. 16).
96. Petit, L. *et al. Universal quantum logic in hot silicon qubits. Nature* **580** (2020) (cit. on p. 16).
97. Zhao, R. *et al. Single-spin qubits in isotopically enriched silicon at low magnetic field. Nat. Commun.* **10** (2019) (cit. on p. 16).

98. Oakes, G. A. *et al.* *Fast high-fidelity single-shot readout of spins in silicon using a single-electron box.* *arXiv 2203.06608* (2022) (cit. on pp. 17, 38, 104, 105, 107, 112, 148, 151, 153, 157, 163).

99. Ciriano-Tejel, V. N. *et al.* *Spin Readout of a CMOS Quantum Dot by Gate Reflectometry and Spin-Dependent Tunneling.* *PRX Quantum* **2** (2021) (cit. on pp. 17, 19, 47, 104, 105, 112, 167).

100. Angus, S. J., Ferguson, A. J., Dzurak, A. S. & Clark, R. G. *Gate-Defined Quantum Dots in Intrinsic Silicon.* *Nano Lett.* **7** (2007) (cit. on p. 18).

101. Yang, C. H. *et al.* *Spin-valley lifetimes in a silicon quantum dot with tunable valley splitting.* *Nat. Commun.* **4** (2013) (cit. on pp. 18, 124, 129).

102. Lawrie, W. I. L. *et al.* *Quantum dot arrays in silicon and germanium.* *Appl. Phys. Lett.* **116** (2020) (cit. on p. 18).

103. Borselli, M. G. *et al.* *Undoped accumulation-mode Si/SiGe quantum dots.* *Nanotechnology* **26** (2015) (cit. on p. 18).

104. Zajac, D. M., Hazard, T. M., Mi, X., Nielsen, E. & Petta, J. R. *Scalable Gate Architecture for a One-Dimensional Array of Semiconductor Spin Qubits.* *Phys. Rev. Appl.* **6** (2016) (cit. on pp. 19, 47).

105. Watzinger, H. *et al.* *A germanium hole spin qubit.* *Nat. Commun.* **9** (2018) (cit. on p. 19).

106. Hendrickx, N. W. *et al.* *A four-qubit germanium quantum processor.* *Nature* **591** (2021) (cit. on p. 19).

107. Ansaloni, F. *et al.* *Single-electron operations in a foundry-fabricated array of quantum dots.* *Nat. Commun.* **11** (2020) (cit. on pp. 19, 47, 66, 110, 114, 149).

108. Maurya, R. K. & Bhowmick, B. *Review of FinFET Devices and Perspective on Circuit Design Challenges.* *Silicon* (2021) (cit. on p. 20).

109. Razavieh, A., Zeitzoff, P. & Nowak, E. J. *Challenges and Limitations of CMOS Scaling for FinFET and beyond Architectures.* *IEEE Trans. Nanotechnol.* **18** (2019) (cit. on p. 20).

110. Ladd, T. D. & Carroll, M. S. in *Encycl. Mod. Opt.* (Elsevier, 2018) (cit. on p. 20).

111. He, Y. *et al.* *A two-qubit gate between phosphorus donor electrons in silicon.* *Nature* **571** (2019) (cit. on pp. 20, 33).

112. McCallum, J. C., Johnson, B. C. & Botzem, T. *Donor-based qubits for quantum computing in silicon.* *Appl. Phys. Rev.* **8** (2021) (cit. on pp. 20, 21).

113. McCamey, D. R., Van Tol, J., Morley, G. W. & Boehme, C. *Electronic Spin Storage in an Electrically Readable Nuclear Spin Memory with a Lifetime >100 Seconds.* *Science (80-.).* **330** (2010) (cit. on p. 20).

114. Bienfait, A. *et al.* *Controlling spin relaxation with a cavity.* *Nature* **531** (2016) (cit. on p. 20).

115. Asaad, S. *et al.* *Coherent electrical control of a single high-spin nucleus in silicon.* *Nature* **579** (2020) (cit. on p. 20).

116. Stock, T. J. Z. *et al.* *Atomic-Scale Patterning of Arsenic in Silicon by Scanning Tunneling Microscopy.* *ACS Nano* **14** (2020) (cit. on p. 20).

117. Kobayashi, T. *et al.* *Engineering long spin coherence times of spin–orbit qubits in silicon.* *Nat. Mater.* **20** (2021) (cit. on p. 20).

118. Zwanenburg, F. A. *et al.* *Silicon quantum electronics.* *Rev. Mod. Phys.* **85** (2013) (cit. on pp. 20, 41).

119. Fuechsle, M. *et al.* *A single-atom transistor.* *Nat. Nanotechnol.* **7** (2012) (cit. on p. 21).

120. Pla, J. J. *et al.* *A single-atom electron spin qubit in silicon.* *Nature* **489** (2012) (cit. on p. 21).

121. Kouwenhoven, L. P. *et al.* in *Mesoscopic Electron Transp.* Kluwer (Springer Netherlands, Dordrecht, 1997) (cit. on pp. 21, 28).

122. Ingold, G.-L. & Nazarov, Y. V. in *Single Charg. Tunneling* chap. 2 (Springer, Boston, MA, 1992) (cit. on p. 22).

123. Ihn, T. *Semiconductor Nanostructures* (Oxford University Press, 2009) (cit. on pp. 25, 27, 28, 92).

124. Leon, R. C. C. *et al.* *Coherent spin control of s-, p-, d- and f-electrons in a silicon quantum dot.* *Nat. Commun.* **11** (2020) (cit. on p. 26).

125. Hanson, R., Kouwenhoven, L. P., Petta, J. R., Tarucha, S. & Vandersypen, L. M. K. *Spins in few-electron quantum dots.* *Rev. Mod. Phys.* **79** (2007) (cit. on pp. 27, 28).

126. Van der Wiel, W. G. *et al.* *Electron transport through double quantum dots.* *Rev. Mod. Phys.* **75** (2002) (cit. on pp. 28, 92).

127. Shulman, M. D. *et al.* *Demonstration of Entanglement of Electrostatically Coupled Singlet-Triplet Qubits.* *Science (80-.).* **336** (2012) (cit. on p. 28).

128. Medford, J. *et al.* *Quantum-Dot-Based Resonant Exchange Qubit.* *Phys. Rev. Lett.* **111** (2013) (cit. on p. 28).

129. Thorgrimsson, B. *et al.* *Extending the coherence of a quantum dot hybrid qubit.* *npj Quantum Inf.* **3** (2017) (cit. on p. 28).

130. Yang, C. H. *et al.* *Silicon qubit fidelities approaching incoherent noise limits via pulse engineering.* *Nat. Electron.* **2** (2019) (cit. on p. 29).

131. Gilbert, W. *et al.* *On-demand electrical control of spin qubits.* 2022 (cit. on p. 29).

132. Chatterjee, A. *et al. Semiconductor qubits in practice. Nat. Rev. Phys.* **3** (2021) (cit. on p. 30).

133. Lin, Z.-R., Guo, G.-P., Tu, T., Zhu, F.-Y. & Guo, G.-C. *Generation of Quantum-Dot Cluster States with a Superconducting Transmission Line Resonator. Phys. Rev. Lett.* **101** (2008) (cit. on p. 30).

134. Ono, K., Austing, D. G., Tokura, Y. & Tarucha, S. *Current Rectification by Pauli Exclusion in a Weakly Coupled Double Quantum Dot System. Science (80-.).* **297** (2002) (cit. on p. 31).

135. Meunier, T., Calado, V. E. & Vandersypen, L. M. K. *Efficient controlled-phase gate for single-spin qubits in quantum dots. Phys. Rev. B* **83** (2011) (cit. on p. 32).

136. Reed, M. D. *et al. Reduced Sensitivity to Charge Noise in Semiconductor Spin Qubits via Symmetric Operation. Phys. Rev. Lett.* **116** (2016) (cit. on p. 33).

137. Zhang, X. *et al. Semiconductor quantum computation. Natl. Sci. Rev.* **6** (2019) (cit. on pp. 33, 169).

138. Maune, B. M. *et al. Coherent singlet-triplet oscillations in a silicon-based double quantum dot. Nature* **481** (2012) (cit. on pp. 33, 38).

139. Nowack, K. C. *et al. Single-Shot Correlations and Two-Qubit Gate of Solid-State Spins. Science (80-.).* **333** (2011) (cit. on p. 33).

140. Huang, C. H., Yang, C. H., Chen, C. C., Dzurak, A. S. & Goan, H. S. *High-fidelity and robust two-qubit gates for quantum-dot spin qubits in silicon. Phys. Rev. A* **99** (2019) (cit. on p. 34).

141. Jeschke, A. & Schweiger, G. *Principles of Pulse Electron Paramagnetic Resonance.* (2001) (cit. on p. 35).

142. Probst, S. *et al. Inductive-detection electron-spin resonance spectroscopy with 65 spins/ Hz sensitivity. Appl. Phys. Lett.* **111** (2017) (cit. on p. 35).

143. Morton, J. J. & Bertet, P. *Storing quantum information in spins and high-sensitivity ESR. J. Magn. Reson.* **287** (2018) (cit. on p. 35).

144. Grinolds, M. S. *et al. Nanoscale magnetic imaging of a single electron spin under ambient conditions. Nat. Phys.* **9** (2013) (cit. on p. 35).

145. Elzerman, J. M. *et al. Single-shot read-out of an individual electron spin in a quantum dot. Nature* **430** (2004) (cit. on pp. 35, 113).

146. Morello, A. *et al. Single-shot readout of an electron spin in silicon. Nature* **467** (2010) (cit. on pp. 35, 127, 163).

147. Keith, D. *et al. Single-Shot Spin Readout in Semiconductors Near the Shot-Noise Sensitivity Limit. Phys. Rev. X* **9** (2019) (cit. on pp. 37, 63, 98, 99, 110, 163).

148. Fogarty, M. A. *Computing with Silicon MOS Spin-Based Quantum Quantum Dots. Thesis* (2018) (cit. on p. 37).

149. Zhao, R. *et al. Coherent single-spin control with high-fidelity singlet-triplet readout in silicon* (2018) (cit. on pp. 37, 163).

150. Harvey-Collard, P. *et al. High-Fidelity Single-Shot Readout for a Spin Qubit via an Enhanced Latching Mechanism. Phys. Rev. X* **8** (2018) (cit. on pp. 37, 38, 39, 163).

151. Jones, C. *et al. Logical Qubit in a Linear Array of Semiconductor Quantum Dots. Phys. Rev. X* **8** (2018) (cit. on p. 38).

152. Yang, C. H. *et al. Operation of a silicon quantum processor unit cell above one kelvin. Nature* **580** (2020) (cit. on p. 38).

153. Nakajima, T. *et al. Robust Single-Shot Spin Measurement with 99.5% Fidelity in a Quantum Dot Array. Phys. Rev. Lett.* **119** (2017) (cit. on p. 38).

154. Fogarty, M. A. *et al. Integrated silicon qubit platform with single-spin addressability, exchange control and single-shot singlet-triplet readout. Nat. Commun.* **9** (2018) (cit. on pp. 38, 163).

155. Urdampilleta, M. *et al. Gate-based high fidelity spin readout in a CMOS device. Nat. Nanotechnol.* **14** (2019) (cit. on pp. 38, 39, 47, 64, 110, 129, 130, 163).

156. Connors, E. J., Nelson, J. & Nichol, J. M. *Rapid High-Fidelity Spin-State Readout in Si/Si-Ge Quantum Dots via rf Reflectometry. Phys. Rev. Appl.* **13** (2020) (cit. on pp. 39, 163).

157. Curry, M. J. *et al. Single-Shot Readout Performance of Two Heterojunction-Bipolar-Transistor Amplification Circuits at Millikelvin Temperatures. Sci. Rep.* **9** (2019) (cit. on pp. 39, 40, 163).

158. Vigneau, F. *et al. Probing quantum devices with radio-frequency reflectometry* (2022) (cit. on pp. 40, 45, 73, 80).

159. Fulton, T. A. & Dolan, G. J. *Observation of single-electron charging effects in small tunnel junctions. Phys. Rev. Lett.* **59** (1987) (cit. on p. 40).

160. Field, M. *et al. Measurements of Coulomb blockade with a noninvasive voltage probe. Phys. Rev. Lett.* **70** (1993) (cit. on p. 40).

161. Vandersypen, L. M. K. *et al. Real-time detection of single-electron tunneling using a quantum point contact. Appl. Phys. Lett.* **85** (2004) (cit. on p. 40).

162. Korotkov, A. N. *Intrinsic noise of the single-electron transistor. Phys. Rev. B* **49** (1994) (cit. on p. 40).

163. Starmark, B., Henning, T., Claeson, T., Delsing, P. & Korotkov, A. N. *Gain dependence of the noise in the single electron transistor. J. Appl. Phys.* **86** (1999) (cit. on p. 40).

164. Kranz, L. *et al. Exploiting a Single-Crystal Environment to Minimize the Charge Noise on Qubits in Silicon. Adv. Mater.* **32** (2020) (cit. on pp. 40, 136).

165. Tracy, L. A. *et al. Single shot spin readout using a cryogenic high-electron-mobility transistor amplifier at sub-Kelvin temperatures. Appl. Phys. Lett.* **108** (2016) (cit. on p. 40).

166. Watson, T. F., Weber, B., House, M. G., Büch, H. & Simmons, M. Y. *High-Fidelity Rapid Initialization and Read-Out of an Electron Spin via the Single Donor D- Charge State. Phys. Rev. Lett.* **115** (2015) (cit. on pp. 41, 163).

167. Hayes, R. R. *et al. Lifetime measurements (T1) of electron spins in Si/SiGe quantum dots* (2009) (cit. on p. 41).

168. Schoelkopf, R. J., Wahlgren, P., Kozhevnikov, A. A., Delsing, P. & Prober, D. E. *The Radio-Frequency Single-Electron Transistor (RF-SET): A Fast and Ultrasensitive Electrometer. Science (80-.).* **280** (1998) (cit. on p. 41).

169. Pozar, D. *Microwave Engineering* 4th (John wiley and sons, 2011) (cit. on pp. 42, 95).

170. Korotkov, A. N. & Paalanen, M. A. *Charge sensitivity of radio frequency single-electron transistor. Appl. Phys. Lett.* **74** (1999) (cit. on p. 46).

171. Brenning, H., Kafanov, S., Duty, T., Kubatkin, S. & Delsing, P. *An ultrasensitive radio-frequency single-electron transistor working up to 4.2 K. J. Appl. Phys.* **100** (2006) (cit. on p. 46).

172. Kafanov, S. & Delsing, P. *Measurement of the shot noise in a single-electron transistor. Phys. Rev. B* **80** (2009) (cit. on p. 47).

173. Keith, D. *et al. Benchmarking high fidelity single-shot readout of semiconductor qubits. New J. Phys.* **21** (2018) (cit. on p. 47).

174. Reilly, D. J., Marcus, C. M., Hanson, M. P. & Gossard, A. C. *Fast single-charge sensing with a rf quantum point contact. Appl. Phys. Lett.* **91** (2007) (cit. on p. 47).

175. Ahmed, I. *et al. Radio-Frequency Capacitive Gate-Based Sensing. Phys. Rev. Appl.* **10** (2018) (cit. on pp. 47, 50, 82, 88, 97, 122).

176. Persson, F., Wilson, C. M., Sandberg, M., Johansson, G. & Delsing, P. *Excess Dissipation in a Single-Electron Box: The Sisyphus Resistance. Nano Lett.* **10** (2010) (cit. on pp. 47, 48).

177. House, M. G. *et al. High-Sensitivity Charge Detection with a Single-Lead Quantum Dot for Scalable Quantum Computation. Phys. Rev. Appl.* **6** (2016) (cit. on pp. 47, 110).

178. Chanrion, E. *et al. Charge Detection in an Array of CMOS Quantum Dots. Phys. Rev. Appl.* **14** (2020) (cit. on pp. 47, 110, 145).

179. Gonzalez-Zalba, M. F., Barraud, S., Ferguson, A. J. & Betz, A. C. *Probing the limits of gate-based charge sensing*. *Nat. Commun.* **6** (2015) (cit. on pp. 48, 49, 50, 62, 63, 98).

180. House, M. G. *et al.* *Radio frequency measurements of tunnel couplings and singlet-triplet spin states in Si:P quantum dots*. *Nat. Commun.* **6** (2015) (cit. on p. 48).

181. Ahmed, I. *et al.* *Primary thermometry of a single reservoir using cyclic electron tunneling to a quantum dot*. *Commun. Phys.* **1** (2018) (cit. on p. 49).

182. Colless, J. I. *et al.* *Dispersive readout of a few-electron double quantum dot with fast rf gate sensors*. *Phys. Rev. Lett.* **110** (2013) (cit. on p. 50).

183. Schaal, S. *et al.* *Fast Gate-Based Readout of Silicon Quantum Dots Using Josephson Parametric Amplification*. *Phys. Rev. Lett.* **124** (2020) (cit. on pp. 50, 99, 102, 104, 122).

184. Mizuta, R., Otxoa, R. M., Betz, A. C. & Gonzalez-Zalba, M. F. *Quantum and tunneling capacitance in charge and spin qubits*. *Phys. Rev. B* **95** (2017) (cit. on p. 50).

185. Esterli, M., Otxoa, R. M. & Gonzalez-Zalba, M. F. *Small-signal equivalent circuit for double quantum dots at low-frequencies*. *Appl. Phys. Lett.* **114** (2019) (cit. on p. 50).

186. Vijay, R., Devoret, M. H. & Siddiqi, I. *Invited Review Article: The Josephson bifurcation amplifier*. *Rev. Sci. Instrum.* **80** (2009) (cit. on pp. 51, 57, 60, 99, 165).

187. Roy, A. & Devoret, M. *Introduction to parametric amplification of quantum signals with Josephson circuits*. *Comptes Rendus Phys.* **17** (2016) (cit. on pp. 51, 53, 60).

188. Walter, T. *et al.* *Rapid High-Fidelity Single-Shot Dispersive Readout of Superconducting Qubits*. *Phys. Rev. Appl.* **7** (2017) (cit. on p. 51).

189. Naghiloo, M. *Introduction to Experimental Quantum Measurement with Superconducting Qubits* (2019) (cit. on p. 51).

190. Aumentado, J. *Superconducting Parametric Amplifiers: The State of the Art in Josephson Parametric Amplifiers*. *IEEE Microw. Mag.* **21** (2020) (cit. on pp. 51, 53, 60, 61, 62).

191. Angel, M., Beltran, C. & Castellanos-Beltran, M. a. *Development of a Josephson Parametric Amplifier for the Preparation and Detection of Nonclassical States of Microwave Fields*. *Thesis* (2010) (cit. on pp. 51, 165).

192. Slichter, D. H. *Quantum Jumps and Measurement Backaction in a Superconducting Qubit*. PhD thesis (2011) (cit. on pp. 51, 59, 165, 166).

193. Schackert, F. D. O. *A Practical Quantum-Limited Parametric Amplifier Based on the Josephson Ring Modulator*. PhD thesis (Yale University, 2013) (cit. on p. 51).

194. Stein, J. *Digital Signal Processing A Computer Science Perspective* (JOHN WILEY and SONS, INC., 2000) (cit. on p. 51).

195. Motchenbacher, C. D., Connelly, J. A. (A. & Motchenbacher, C. D. *Low-noise electronic system design* (Wiley, 1993) (cit. on p. 51).

196. Cochrane, L. *et al.* *Quantum Dot-Based Parametric Amplifiers* (2021) (cit. on p. 53).

197. Eisaman, M. D., Fan, J., Migdall, A. & Polyakov, S. V. *Invited Review Article: Single-photon sources and detectors*. *Rev. Sci. Instrum.* **82** (2011) (cit. on p. 53).

198. Laflamme, C. & Clerk, A. A. *Quantum-limited amplification with a nonlinear cavity detector*. *Phys. Rev. A* **83** (2011) (cit. on p. 53).

199. Devoret, M. H. & Schoelkopf, R. J. *Amplifying quantum signals with the single-electron transistor*. *Nature* **406** (2000) (cit. on p. 53).

200. Segall, K. *et al.* *A high-performance cryogenic amplifier based on a radio-frequency single electron transistor*. *Appl. Phys. Lett.* **81** (2002) (cit. on p. 53).

201. Kumbhakar, P., Shanmugam, A., Sharma, C. H., Reno, J. L. & Thalakulam, M. *Quantum point contact galvanically coupled to planar superconducting resonator: a shot-noise-limited broad-band electrical amplifier*. *Quantum Sci. Technol.* **6** (2021) (cit. on p. 53).

202. Callen, H. B. & Welton, T. A. *Irreversibility and Generalized Noise*. *Phys. Rev.* **83** (1951) (cit. on p. 53).

203. Clerk, A. A., Devoret, M. H., Girvin, S. M., Marquardt, F. & Schoelkopf, R. J. *Introduction to quantum noise, measurement, and amplification*. *Rev. Mod. Phys.* **82** (2010) (cit. on p. 53).

204. Braginsky, B. V. & Khalili, F. Y. *Quantum Measurement* Cambridge (New York, 1992) (cit. on p. 53).

205. Caves, C. M., Combes, J., Jiang, Z. & Pandey, S. *Quantum limits on phase-preserving linear amplifiers*. *Phys. Rev. A* **86** (2012) (cit. on p. 54).

206. Haus, H. A. & Mullen, J. A. *Quantum Noise in Linear Amplifiers*. *Phys. Rev.* **128** (1962) (cit. on p. 54).

207. Howson, D. P. & Smith, R. B. *Parametric amplifiers* (McGraw-Hill, 1970) (cit. on p. 55).

208. Chang, J. *et al.* *The Super-Lattice Castellated Field-Effect Transistor: A High-Power, High-Performance RF Amplifier*. *IEEE Electron Device Lett.* **40** (2019) (cit. on p. 57).

209. Zimmer, H. *Parametric amplification of microwaves in superconducting Josephson tunnel junctions*. *Appl. Phys. Lett.* **10** (1967) (cit. on p. 60).

210. Feldman, M. J., Parrish, P. T. & Chiao, R. Y. *Parametric amplification by unbiased Josephson junctions*. *J. Appl. Phys.* **46** (1975) (cit. on p. 60).

211. Macklin, C. *et al. A near–quantum-limited Josephson traveling-wave parametric amplifier*. *Science (80-.).* **350** (2015) (cit. on p. 60).

212. Castellanos-Beltran, M. A., Irwin, K. D., Hilton, G. C., Vale, L. R. & Lehnert, K. W. *Amplification and squeezing of quantum noise with a tunable Josephson metamaterial*. *Nat. Phys.* **4** (2008) (cit. on p. 60).

213. Yamamoto, T. *et al. Flux-driven Josephson parametric amplifier*. *Appl. Phys. Lett.* **93** (2008) (cit. on pp. 60, 61).

214. Vijay, R., Slichter, D. H. & Siddiqi, I. *Observation of Quantum Jumps in a Superconducting Artificial Atom*. *Phys. Rev. Lett.* **106** (2011) (cit. on p. 60).

215. Castellanos-Beltran, M. A. & Lehnert, K. W. *Widely tunable parametric amplifier based on a superconducting quantum interference device array resonator*. *Appl. Phys. Lett.* **91** (2007) (cit. on p. 61).

216. Zhong, L. *et al. Squeezing with a flux-driven Josephson parametric amplifier*. *New J. Phys.* **15** (2013) (cit. on p. 61).

217. Roy, T. *et al. Broadband parametric amplification with impedance engineering: Beyond the gain-bandwidth product*. *Appl. Phys. Lett.* **107** (2015) (cit. on p. 61).

218. Lecocq, F. *et al. Nonreciprocal Microwave Signal Processing with a Field-Programmable Josephson Amplifier*. *Phys. Rev. Appl.* **7** (2017) (cit. on pp. 61, 62).

219. Naaman, O., Ferguson, D. G. & Epstein, R. J. *High Saturation Power Josephson Parametric Amplifier with GHz Bandwidth* (2017) (cit. on p. 61).

220. Zhang, W., Huang, W., Gershenson, M. E. & Bell, M. T. *Josephson Metamaterial with a Widely Tunable Positive or Negative Kerr Constant*. *Phys. Rev. Appl.* **8** (2017) (cit. on p. 61).

221. Sivak, V. *et al. Kerr-Free Three-Wave Mixing in Superconducting Quantum Circuits*. *Phys. Rev. Appl.* **11** (2019) (cit. on p. 61).

222. Planat, L. *et al. Understanding the Saturation Power of Josephson Parametric Amplifiers Made from SQUID Arrays*. *Phys. Rev. Appl.* **11** (2019) (cit. on p. 61).

223. Ho Eom, B., Day, P. K., LeDuc, H. G. & Zmuidzinas, J. *A wideband, low-noise superconducting amplifier with high dynamic range*. *Nat. Phys.* **8** (2012) (cit. on p. 61).

224. O'Brien, K., Macklin, C., Siddiqi, I. & Zhang, X. *Resonant Phase Matching of Josephson Junction Traveling Wave Parametric Amplifiers. Phys. Rev. Lett.* **113** (2014) (cit. on p. 61).

225. White, T. C. *et al. Traveling wave parametric amplifier with Josephson junctions using minimal resonator phase matching. Appl. Phys. Lett.* **106** (2015) (cit. on p. 61).

226. Stehlik, J. *et al. Fast Charge Sensing of a Cavity-Coupled Double Quantum Dot Using a Josephson Parametric Amplifier. Phys. Rev. Appl.* **4** (2015) (cit. on pp. 62, 109).

227. Voisin, B. *et al. Few-electron edge-state quantum dots in a silicon nanowire field-effect transistor. Nano Lett.* **14** (2014) (cit. on pp. 64, 88).

228. Bertrand, B. *et al. Development of spin quantum bits in SOI CMOS technology. Proc. IEEE Conf. Nanotechnol.* **2018-July** (2019) (cit. on p. 64).

229. Hutin, L. *et al. Gate reflectometry for probing charge and spin states in linear Si MOS split-gate arrays.* in *2019 IEEE Int. Electron Devices Meet.* (IEEE, 2019) (cit. on pp. 66, 145).

230. Ibberson, D. J. *et al. Electric-field tuning of the valley splitting in silicon corner dots. Appl. Phys. Lett.* **113** (2018) (cit. on pp. 66, 114).

231. Bu, H. *FINFET technology a substrate perspective.* in *IEEE 2011 Int. SOI Conf.* (IEEE, 2011) (cit. on p. 68).

232. Intel. *Intel 22 nm Technology.* 2014 (cit. on p. 68).

233. Jeon, Y. *Making Semiconductor History.* 2019 (cit. on p. 68).

234. Kalra, R. *et al. Vibration-induced electrical noise in a cryogen-free dilution refrigerator: Characterization, mitigation, and impact on qubit coherence. Rev. Sci. Instrum.* **87** (2016) (cit. on p. 76).

235. Müller, T. *et al. A circuit analysis of an in situ tunable radio-frequency quantum point contact. Rev. Sci. Instrum.* **84** (2013) (cit. on p. 80).

236. Ahmed, I. *Radio-Frequency Capacitive Gate-based Sensing for Silicon CMOS Quantum Electronics. PhD Thesis, Cambridge* (2018) (cit. on p. 83).

237. Derakhshan Maman, V., Gonzalez-Zalba, M. F. & Pályi, A. *Charge Noise and Overdrive Errors in Dispersive Readout of Charge, Spin, and Majorana Qubits. Phys. Rev. Appl.* **14** (2020) (cit. on p. 85).

238. Lundberg, T. *et al. A Spin Quintet in a Silicon Double Quantum Dot: Spin Blockade and Relaxation. arXiv Prepr. arXiv1910.10118* (2019) (cit. on p. 93).

239. Ibberson, D. J. *et al. Large Dispersive Interaction between a CMOS Double Quantum Dot and Microwave Photons. PRX Quantum* **2** (2021) (cit. on pp. 93, 104, 109).

240. Probst, S., Song, F. B., Bushev, P. A., Ustinov, A. V. & Weides, M. *Efficient and robust analysis of complex scattering data under noise in microwave resonators*. *Rev. Sci. Instrum.* **86** (2015) (cit. on p. 95).

241. Khalil, M. S., Stoutimore, M. J. A., Wellstood, F. C. & Osborn, K. D. *An analysis method for asymmetric resonator transmission applied to superconducting devices*. *J. Appl. Phys.* **111** (2012) (cit. on p. 95).

242. Deng, C., Otto, M. & Lupascu, A. *An analysis method for transmission measurements of superconducting resonators with applications to quantum-regime dielectric-loss measurements*. *J. Appl. Phys.* **114** (2013) (cit. on p. 95).

243. Petersan, P. J. & Anlage, S. M. *Measurement of resonant frequency and quality factor of microwave resonators: Comparison of methods*. *J. Appl. Phys.* **84** (1998) (cit. on pp. 95, 97).

244. Porbst, S. *Resonator tools*. 2018 (cit. on p. 95).

245. Steven W. Smith. in. 2nd edition. Chap. 15 (California Technical Publishing, 1997) (cit. on p. 108).

246. Zheng, G. *et al. Rapid gate-based spin read-out in silicon using an on-chip resonator*. *Nat. Nanotechnol.* **14** (2019) (cit. on pp. 109, 110, 163).

247. Stockklauser, A. *et al. Strong Coupling Cavity QED with Gate-Defined Double Quantum Dots Enabled by a High Impedance Resonator*. *Phys. Rev. X* **7** (2017) (cit. on p. 110).

248. Samkharadze, N. *et al. High-Kinetic-Inductance Superconducting Nanowire Resonators for Circuit QED in a Magnetic Field*. *Phys. Rev. Appl.* **5** (2016) (cit. on p. 110).

249. Xiao, M., House, M. G. & Jiang, H. W. *Measurement of the spin relaxation time of single electrons in a silicon metal-oxide-semiconductor-based quantum dot*. *Phys. Rev. Lett.* **104** (2010) (cit. on p. 117).

250. MacLean, K. *et al. Energy-Dependent Tunneling in a Quantum Dot*. *Phys. Rev. Lett.* **98** (2007) (cit. on pp. 117, 126).

251. Simmons, C. B. *et al. Tunable Spin Loading and T1 of a Silicon Spin Qubit Measured by Single-Shot Readout*. *Phys. Rev. Lett.* **106** (2011) (cit. on pp. 121, 128).

252. Glavin, B. A. & Kim, K. W. *Spin-lattice relaxation in Si quantum dots*. *Phys. Rev. B* **68** (2003) (cit. on pp. 125, 126, 171).

253. Tahan, C. & Joynt, R. *Relaxation of excited spin, orbital, and valley qubit states in ideal silicon quantum dots*. *Phys. Rev. B* **89** (2014) (cit. on pp. 124, 126, 128, 167).

254. Bourdet, L. & Niquet, Y.-M. *All-electrical manipulation of silicon spin qubits with tunable spin-valley mixing*. *Phys. Rev. B* **97** (2018) (cit. on pp. 124, 126, 167).

255. Corna, A. *et al. Electrically driven electron spin resonance mediated by spin-valley-orbit coupling in a silicon quantum dot*. *npj Quantum Inf.* **4** (2017) (cit. on pp. 126, 130, 171).

256. Scarlino, P. *et al. Spin-Relaxation Anisotropy in a GaAs Quantum Dot*. *Phys. Rev. Lett.* **113** (2014) (cit. on p. 126).

257. Amasha, S. *et al. Spin-dependent tunneling of single electrons into an empty quantum dot*. *Phys. Rev. B* **78** (2008) (cit. on p. 126).

258. Friesen, M., Tahan, C., Joynt, R. & Eriksson, M. A. *Spin Readout and Initialization in a Semiconductor Quantum Dot*. *Phys. Rev. Lett.* **92** (2004) (cit. on p. 128).

259. Hollmann, A. *et al. Large, Tunable Valley Splitting and Single-Spin Relaxation Mechanisms in a SiSiGe*. *Phys. Rev. Appl.* **13** (2020) (cit. on p. 129).

260. Huang, P. & Hu, X. *Spin relaxation in a Si quantum dot due to spin-valley mixing*. *Phys. Rev. B - Condens. Matter Mater. Phys.* **90** (2014) (cit. on pp. 129, 167).

261. Zhang, X. *et al. Giant Anisotropy of Spin Relaxation and Spin-Valley Mixing in a Silicon Quantum Dot*. *Phys. Rev. Lett.* **124** (2020) (cit. on p. 129).

262. Petit, L. *et al. Spin Lifetime and Charge Noise in Hot Silicon Quantum Dot Qubits*. *Phys. Rev. Lett.* **121** (2018) (cit. on p. 129).

263. Borjans, F., Zajac, D., Hazard, T. & Petta, J. *Single-Spin Relaxation in a Synthetic Spin-Orbit Field*. *Phys. Rev. Appl.* **11** (2019) (cit. on p. 129).

264. Nestoklon, M. O., Golub, L. E. & Ivchenko, E. L. *Spin and valley-orbit splittings in SiGe/Si heterostructures*. *Phys. Rev. B* **73** (2006) (cit. on p. 130).

265. Veldhorst, M. *et al. Spin-orbit coupling and operation of multivalley spin qubits*. *Phys. Rev. B* **92** (2015) (cit. on p. 130).

266. Venitucci, B., Li, J., Bourdet, L. & Niquet, Y.-M. *Modeling Silicon CMOS devices for quantum computing*. in *2019 Int. Conf. Simul. Semicond. Process. Devices* **2019-Septe** (IEEE, 2019) (cit. on p. 130).

267. Barthel, C. *et al. Fast sensing of double-dot charge arrangement and spin state with a radio-frequency sensor quantum dot*. *Phys. Rev. B - Condens. Matter Mater. Phys.* **81** (2010) (cit. on p. 134).

268. Huang, P. & Hu, X. *Electron spin relaxation due to charge noise*. *Phys. Rev. B - Condens. Matter Mater. Phys.* **89** (2014) (cit. on p. 141).

269. Struck, T. *et al. Robust and fast post-processing of single-shot spin qubit detection events with a neural network*. *Sci. Rep.* **11** (2021) (cit. on p. 142).

270. Matsumoto, Y. *et al. Noise-robust classification of single-shot electron spin readouts using a deep neural network. npj Quantum Inf.* **7** (2021) (cit. on p. 142).
271. Ismail Fawaz, H. *et al. InceptionTime: Finding AlexNet for time series classification. Data Min. Knowl. Discov.* **34** (2020) (cit. on p. 142).
272. Oguiza, I. *tsai - A state-of-the-art deep learning library for time series and sequential data.* Github. 2020 (cit. on p. 144).
273. Biewald, L. *Experiment Tracking with Weights and Biases.* Software available from wandb.com. 2020 (cit. on p. 144).
274. Cai, Z. *Resource Estimation for Quantum Variational Simulations of the Hubbard Model: The Advantage of Multi-core NISQ Processing. arXiv Prepr. arXiv1910.02719* (2019) (cit. on p. 145).
275. Cade, C., Mineh, L., Montanaro, A. & Stanisic, S. *Strategies for solving the Fermi-Hubbard model on near-term quantum computers. arXiv Prepr. arXiv1912.06007* (2019) (cit. on p. 145).
276. Fujita, T., Baart, T. A., Reichl, C., Wegscheider, W. & Vandersypen, L. M. K. *Coherent shuttle of electron-spin states. npj Quantum Inf.* **3** (2017) (cit. on p. 145).
277. Yuan, X., Endo, S., Zhao, Q., Li, Y. & Benjamin, S. C. *Theory of variational quantum simulation. Quantum* **3** (2019) (cit. on p. 145).
278. Xu, L., Sun, S., Cao, Z. & Yang, W. *Performance analysis of a digital capacitance measuring circuit. Rev. Sci. Instrum.* **86** (2015) (cit. on p. 160).
279. Hogg, M. R. *et al. Single-shot readout of multiple donor electron spins with a gate-based sensor* (2022) (cit. on p. 163).
280. Broome, M. A. *et al. High-Fidelity Single-Shot Singlet-Triplet Readout of Precision-Placed Donors in Silicon. Phys. Rev. Lett.* **119** (2017) (cit. on p. 163).
281. Borjans, F., Mi, X. & Petta, J. R. *Spin Digitizer for High-Fidelity Readout of a Cavity-Coupled Silicon Triple Quantum Dot. Phys. Rev. Appl.* **15** (2021) (cit. on p. 163).
282. House, M. G. *et al. Single-Shot Single-Gate rf Spin Readout in Silicon. Phys. Rev. X* **8** (2018) (cit. on p. 163).
283. West, A. *et al. Gate-based single-shot readout of spins in silicon.* 2019 (cit. on p. 163).
284. Dykman, M. & Krivoglaz, M. *Fluctuations in nonlinear systems near bifurcations corresponding to the appearance of new stable states. Phys. A Stat. Mech. its Appl.* **104** (1980) (cit. on p. 165).